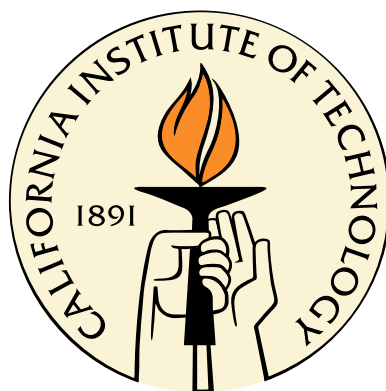


Exploring the Kinetics of Domain Switching in Ferroelectrics for Structural Applications

Thesis by
Charles Stanley Wojnar

In Partial Fulfillment of the Requirements
for the Degree of
Doctor of Philosophy



California Institute of Technology
Pasadena, California

2015
(Submitted June 5, 2015)

© 2015

Charles Stanley Wojnar

All Rights Reserved

may the force be with you

Acknowledgments

First and foremost, I acknowledge Professor Dennis Kochmann, my Ph.D. research advisor, from whom I have learned to always do the best I can and put as much effort as I can into everything I do, not only in research but also in my life. He is the best example of a great researcher, teacher, and mentor and is an example I hope to emulate in my future career. I thank my committee members. Professors Kaushik Bhattacharya and Ravi Ravichandran were generous enough to let me attend their group meetings (and eat their food) even though I was not in either of their groups. The meetings were always intellectually stimulating for me and I have learned a lot from my interactions with Kaushik and Ravi and their students, in particular Mike Rauls, Srivatsan Hulikal, Cindy Wang, Mauricio Ponga, Zubaer Hossain, Vinamra Agrawal, Jacob Notbohm, Gal Shmuel, and Bharat Penmecha. The meetings were also a great opportunity for me to get feedback on the work I was doing from my peers. Kaushik and Ravi have also been great resources for me as I went through my job application process. I am also grateful for Professor Pellegrino for serving on my committee. I have benefited tremendously from my interactions with his students, who have helped me get started with my experiments, namely Keith Patterson and John Steeves.

I wish to express my gratitude to Professor Ioannis Chasiotis, my undergraduate advisor, whose encouragement convinced me to apply to GALCIT for graduate school, even when I doubted myself. My decision to apply and later come here was the best decision I have made in my life. I have learned so much and have made so many great friends at Caltech. I would also like to thank Nikhil Karanjgaokar, who was my graduate mentor when I was working in Ioannis' lab as an undergraduate and who has continued to provide guidance and encouragement to me since he has come to Caltech as a postdoc.

I am grateful for having such great colleagues to work with in the Kochmann Research Group. I am glad to have had Yingrui Chang as my office mate and a great friend over the years. Jeff

Amelang is one of the nicest people I know and his great teaching abilities have inspired me to strive to improve my own. I wish to acknowledge Jean-Briac le Graverend, a great experimentalist, from whom I have learned so much and have received so much encouragement during his time in the group. Possibly the most important thing was that he helped me improve my golf game! I also wish to express my appreciation for everyone else in the group (and former members): Benjamin Klusemann, Neel Nadkarni, Ishan Tembhekar, Gabriela Venturini, and Alex Zelhofer.

There were many people from other groups at Caltech and elsewhere who were kind enough to take the time to help me with various aspects of my research. I thank Professor Sossina Haile and her student Chris Kucharczyk for training me and letting me use their equipment. Similarly, I thank Professor Julia Greer (whom I particularly thank for serving on my committee during my candidacy exam) and her students, Zach Aitken, Lucas Meza, and Lauren Montemayor for their help and for letting me use some of their equipment. I thank the students of Professor Ortiz, who have helped me through my many mathematical shortcomings. In particular, I am thankful for the help of Jonathan Chiang and Brandon Runnels. I am grateful for my interactions with Professor Chris Lynch and several of his students at UCLA. I could not have started my experiments without their guidance. I am glad to have the opportunity to work with Case Bradford at JPL. Through our collaborations I was actually able to see potential applications for my work.

I have had such a great experience being a part of the GALCIT family and have had great interactions with not only fellow students and faculty, but also staff. In particular, I would like to mention Denise Ruiz, who was one of the few people I could go to at Caltech to talk about something besides science. She continually exhibited professionalism in everything she did, even under the most demanding circumstances (such as when I screwed up my travel expenses). I also thank Francisco who was always willing to take the time to talk to me about anything that was on my mind. I am thankful for the lab support from Petros Arakelian and the machine shop staff, Joe, Brad, and Ali. Finally, I am extremely glad to have come to GALCIT with my fellow first-year students and would not have made it this far without their friendship and assistance on coursework: Neal Bitter, Peter Bridi, Subrahmanyam Duvvuri, Esteban Hufstedler, Cheikh Mbengue, Stephanie Mitchell, Nisha Mohan, Lauren Montemayor, Gina Olsen, Karen Oren, Vishagan Ratnaswamy, John Steeves, Dustin Summy, and Yuan Xuan.

I finally would like to acknowledge the Caltech Innovation Initiative, United Technologies Research Center, and NASA/JPL for financial support during my studies.

Abstract

The complex domain structure in ferroelectrics gives rise to electromechanical coupling, and its evolution (via domain switching) results in a time-dependent (i.e. viscoelastic) response. Although ferroelectrics are used in many technological applications, most do not attempt to exploit the viscoelastic response of ferroelectrics, mainly due to a lack of understanding and accurate models for their description and prediction. Thus, the aim of this thesis research is to gain better understanding of the influence of domain evolution in ferroelectrics on their dynamic mechanical response.

There have been few studies on the viscoelastic properties of ferroelectrics, mainly due to a lack of experimental methods. Therefore, an apparatus and method called Broadband Electromechanical Spectroscopy (BES) was designed and built. BES allows for the simultaneous application of dynamic mechanical and electrical loading in a vacuum environment. Using BES, the dynamic stiffness and loss tangent in bending and torsion of a particular ferroelectric, viz. lead zirconate titanate (PZT), was characterized for different combinations of electrical and mechanical loading frequencies throughout the entire electric displacement hysteresis. Experimental results showed significant increases in loss tangent (by nearly an order of magnitude) and compliance during domain switching, which shows promise as a new approach to structural damping.

A continuum model of the viscoelasticity of ferroelectrics was developed, which incorporates microstructural evolution via internal variables and associated kinetic relations. For the first time, through a new linearization process, the incremental dynamic stiffness and loss tangent of materials were computed throughout the entire electric displacement hysteresis for different combinations of mechanical and electrical loading frequencies. The model accurately captured experimental results.

Using the understanding gained from the characterization and modeling of PZT, two applications of domain switching kinetics were explored by using Macro Fiber Composites (MFCs). Proofs of concept of set-and-hold actuation and structural damping using MFCs were demonstrated.

Contents

Acknowledgments	iv
Abstract	vi
1 Introduction	1
1.1 Ferroelectrics	2
1.1.1 Physical properties	2
1.1.2 Origins of ferroelectricity	5
1.1.3 Microstructure: Domains and domain walls	10
1.1.4 Applications	15
1.2 Concepts of linear viscoelasticity	17
1.3 Motivation	19
1.4 Outline	22
2 Broadband Electromechanical Spectroscopy	24
2.1 Materials and methods used in Broadband Electromechanical Spectroscopy	27
2.1.1 Force control	30
2.1.2 Measuring the deflection and twist of the specimen	30
2.1.3 Electric field control	31
2.1.4 Vacuum chamber	33
2.1.5 Temperature control	35
2.2 Characterizing the material's response	38
2.2.1 Measuring viscoelastic properties	38
2.2.2 Frequency response of the Helmholtz coils	42

2.2.3	Approximate methods for extracting the material properties near resonance	44
2.2.4	Measuring electric displacement and electric field	48
2.3	Sources of error	49
2.3.1	Resolution of the laser detector	49
2.3.2	Effect of laser misalignment	50
2.3.3	Parasitic damping due to support loss	51
2.3.4	Electromagnetic coupling	52
2.3.5	Noise measurements	53
2.4	Validation	54
2.4.1	Viscoelastic characterization of PMMA	55
2.4.2	Loss tangent of aluminum	56
2.4.3	Electric displacement evolution in PZT	56
2.5	Summarizing the capabilities of BES	60
3	Experiments on Polycrystalline Lead Zirconate Titanate	62
3.1	Materials	63
3.2	Bending experiments	63
3.2.1	Different mechanical frequencies	65
3.2.2	Effect of electrical loading frequency	71
3.3	Torsion experiments	72
3.3.1	Different mechanical frequencies	73
3.3.2	Effect of electrical loading frequency	77
3.4	Discussion	79
3.4.1	Viscoelasticity of ferroelectrics	79
3.4.2	Parasitic damping due to surrounding air	80
3.4.3	Selecting the time constant of the lock-in amplifier	87
3.4.4	Frequency response of the Helmholtz coils	88
4	A Continuum Model of the Viscoelasticity of Ferroelectrics	92
4.1	Background and motivation	92
4.2	Review of electrostatics in a continuum	94
4.3	Constitutive equations	96

4.4	Kinetic relation	99
4.5	Variational principle	101
4.5.1	Potential energy of the electromechanical system	101
4.5.2	Euler-Lagrange equation	103
4.5.3	Uniqueness	104
4.6	Incremental complex moduli	104
4.7	Material model	106
4.7.1	Pure bending	106
4.7.2	Qualitative interpretation of stiffness and damping during domain switching	110
5	Set-and-Hold Actuation and Structural Damping via Domain Switching	115
5.1	Motivation	115
5.2	Materials	117
5.3	Quasistatic electromechanical testing	119
5.3.1	Experimental methods	119
5.3.2	Measuring longitudinal strain and charge	121
5.3.3	Demonstration of a set-and-hold actuator	125
5.4	Dynamic electromechanical testing	128
6	Conclusions	131
6.1	Broadband Electromechanical Spectroscopy	131
6.2	Viscoelastic characterization and modeling of PZT	132
6.3	Structural applications	133
6.4	Future work	135
	Appendix A Estimating Current Leakage	137
	Appendix B Selecting the Time Constant of the Lock-In Amplifier	140
	Appendix C Bending and Torsion Problems	143
C.1	Solution of the dynamic Euler-Bernoulli beam	143
C.2	Solution of the dynamic torsion of a bar	144

List of Figures

1.1	Illustration of a dielectric material being used as a capacitor. Applying a voltage V causes a polarization \bar{p} to form in the material and results in a charge Q on the surface. The relationship between applied voltage and charge is normally linear via the capacitance C	3
1.2	Evolution of the polarization (a) versus stress in a pyroelectric material where there is an initial, temperature-dependent spontaneous polarization p_s and (b) versus electric field in a ferroelectric material where the spontaneous polarization can be reversed when an opposing electric field exceeds the coercive field e_c leading to a hysteresis loop in addition to the linear dielectric behavior (arrows denote increasing time). . . .	4
1.3	Quartz is a piezoelectric material due to the lack of centrosymmetry of the crystal structure, which causes an electric dipole, \bar{p} , to form under the application of stress. That is, any reorientation of ions in a tetrahedra are not canceled out by an opposing tetrahedra. Under no applied stress, the overall electric dipole is zero due to the helical structure of oxygen-silicon tetrahedra (denoted by yellow arrows).	7
1.4	ZnS in its hexagonal form (wurtzite) is in point group 6mm and has a polar axis (i.e. zinc-sulfide tetrahedrons are aligned), which gives rise to pyroelectricity (with a spontaneous polarization \mathbf{p}_s).	8
1.5	Crystal unit cell of PZT. (a) Above the Curie temperature T_C , the unit cell is cubic and non-ferroelectric. (b) Below the Curie temperature, the unit cell is tetragonal and ferroelectric.	9
1.6	There are six equivalent directions of the spontaneous polarization in PZT: the four shown here as well as in and out of the page.	11

1.7	Images of the domain structure in PMN-PT at different length scales obtained from (a,b) PLM and (c,d) PFM. Images were adapted with permission from (Yao et al., 2011) © Wiley Materials. All rights reserved.	12
1.8	Images of the domain structure in PMN-PT obtained from TEM. Image was adapted with permission from (Yao et al., 2011) © Wiley Materials. All rights reserved.	13
1.9	Images of polycrystalline PZT showing (a) granular structure via SEM and (b) domain structure within individual grains via AFM. Fig. (a) was adapted with permission from King et al. (2007) Materials Forum Vol 31 – © Institute of Materials Engineering Australasia Ltd. Fig. (b): Wang et al. (2003c). Atomic force microscope observations of domains in fine-grained bulk lead zirconate titanate ceramics. Smart Materials and Structures 12, 217. URL: http://stacks.iop.org/0964-1726/12/i=2/a=309 . © IOP Publishing. Reproduced with permission. All rights reserved.	14
1.10	Images of the evolution of domain structure in PMN-PT upon application of an increasing electric field (a-d). Each image has the same scale. Snapshots were taken when the electric field was 0, 0.05, 0.067, and 0.083 MV/m in (a-d), respectively, in the horizontal direction. Images were obtained from PLM and adapted with permission from (Yao et al., 2011) © Wiley Materials. All rights reserved.	16
1.11	An example experiment to measure the viscoelastic properties of a material (i.e. the dynamic Young modulus and loss tangent) using harmonic loading in a DMA setup (an image of a Bose Electroforce is shown here).	19
1.12	Plot of Young’s modulus, loss tangent, and density of common engineering materials (including ceramics, metals, and polymers). Common engineering materials lack both a high Young modulus and high loss tangent (denoted by the shaded area). Values were obtained from (Callister and Rethwisch, 2009; Lakes, 1998).	21

2.1	Schematic of the apparatus showing the specimen gripped in the center. Above the specimen are the two pairs of Helmholtz coils used for bending and torsion tests as in BVS. The coils are shown in their raised position allowing for the specimen to be positioned. Once the specimen is gripped in place, the coils are lowered over the specimen such that the magnet is located at the intersection of the two coil axes. The specimen and coils are placed inside a vacuum chamber with a window for the laser beam to enter and reflect back to the position sensor outside. In the top-left corner appears the lock-in amplifier set-up connected to the position sensor with the applied voltage to the coils used as the reference signal. The bottom-right corner shows the Sawyer-Tower circuit used.	28
2.2	Pictures of the apparatus showing (a) the chamber in the operating position and how the laser enters the chamber, is reflected by the mirror, and is detected by the position sensor, (b) the chamber in the raised position, (c) the coils and their support structure, (d) the specimen and attached clamp holding the permanent magnet that applies the electromagnetic force generated by the coils to the specimen's free end, and a mirror used to reflect the incoming laser beam to measure specimen bending/twist, and (e) the specimen grip for the application of an electrical bias.	29
2.3	Ranges of specimen (a) Young modulus and (b) shear modulus that can be tested using the current BES setup (shaded region) versus specimen thickness. Several regions are shown for different lengths of the specimen.	32
2.4	Additional pictures of the apparatus: (a) shows the electronics rack containing the various instruments used during an experiment, (b) shows the primary pump sitting above the apparatus on a ceiling rack that is connected to the chamber via a hose, (c) shows the chamber viewed from the left hand side, and (d) shows the chamber viewed from the right hand side.	34
2.5	Evolution of the breakdown voltage in air as a function of the pressure p times the separation distance of the specimen electrodes d (Picot, 2000).	36

2.6 Drawing showing the approximate location of the two graphite resistive heaters on opposite sides of the inside wall of the vacuum chamber. Also shown are the approximate locations of cables for powering the Helmholtz coils, specimen surface electrodes, and heaters. It is important that the heater cables use a separate feed-through in the chamber wall on the opposite side to the feed-through for the coils and specimen electrodes to prevent electromagnetic interference due to the large heater current I creating a magnetic field B_{heat} 37

2.7 Illustration of the laser spot movement on the detector with components u_z and u_y due to applied bending and torsional moments M_z and M_y , respectively. 40

2.8 (a) Picture of the magnetometer made by coiling magnet wire and attaching it to the end of a pole so that it can be inserted between the Helmholtz coils. The diameter of the coiled wire was approximately 12 mm. (b) Illustrates how the magnetometer is placed in the Helmholtz coils and the current through it is measured via a resistor. 42

2.9 (a) Variation of the tangent of the phase between the applied voltage and magnetic field of the Helmholtz coils ($\tan \phi$) with the frequency of the applied voltage to the bending and torsion coils. (b) The change in the amplitude of the applied moment \hat{M} relative to the amplitude at 0 Hz (\hat{M}_0) versus the frequency of the applied voltage to the bending and torsion coils. 43

2.10 A cantilevered beam with tip deflection $w(L, t)$ due to an applied force F and with attached mass m is approximated by a spring-mass-dashpot system with stiffness k , mass m , and damping c 45

2.11 Comparison of the theoretical dynamic (a) compliance and (b) loss tangent (long dashed line) with their corrected response (solid line) using (2.15) and (2.16), respectively, for an Euler-Bernoulli beam. The parameters used are given in Tab. 3.2. The material compliance and loss tangent were taken to be constant and are shown by the short dashed line. 47

2.12 Illustration of how a polycrystalline specimen in a Sawyer-Tower circuit has spatially-varying polarization $\mathbf{p}(\mathbf{x})$ which gives rise to an average polarization $\bar{\mathbf{p}}$ that is reflected in the charge measured on the surface electrodes. 49

2.13 Illustration of the effect of the average laser position on the amplitude of the signal (not to scale). 51

2.14	Illustration of a cantilevered beam specimen attached to a grip modeled as an elastic half-space. Harmonic bending of the specimen generates elastic waves that travel away through the grip and cause energy loss (or damping).	52
2.15	Power spectral density of the laser position sensor output when applying a mechanical bending frequency of 75 Hz and 7.2 Vpp amplitude. The signal power at 75 Hz, due to the applied moment, is much higher than noise occurring at other frequencies. . . .	54
2.16	Viscoelastic response of a PMMA sample measured using BES with (a) showing the relative compliance and (b) showing the loss tangent in bending versus frequency. Blue points represent experimental data and solid black lines correspond to the dynamic Euler-Bernoulli solution using the parameters in Tab. 2.2.	55
2.17	Variation of the electric displacement versus electric field for different triangle-wave electric field frequencies ranging from 0.01 to 1.0 Hz while applying a bending moment at 75 Hz.	58
2.18	Variation of the electric displacement versus electric field for different triangle-wave electric field frequencies ranging from 0.01 to 1.0 Hz while applying a torsional moment at 75 Hz.	58
2.19	Electric displacement versus an applied cyclic electric field at 0.1 Hz: (a) effect of different mechanical bending frequencies (25-1000 Hz), (b) comparison between experiments performed in air and vacuum at a fixed mechanical frequency of 100 Hz. . .	59
2.20	Electric displacement versus an applied cyclic electric field at 0.1 Hz: (a) effect of different torsion frequencies (25-1000 Hz), (b) comparison between experiments performed in air and under vacuum at a fixed mechanical frequency of 100 Hz.	59
3.1	Drawing of the components of the imposed stresses and strains during bending and shearing, which are used to define the Young and shear moduli for the generally orthotropic material.	63

3.2 An image of a typical PZT specimen obtained from Scanning Electron Microscopy. Image is taken of the side of the specimen without the electrode (there was no surface preparation before imaging). Horizontal striations are due to the blade used by the manufacturer to cut specimens to size. Examining the surface reveals a granular structure with grains on the order of $2 \mu\text{m}$. The image was obtained under 20 kV with a working distance of 10.6 mm. The magnification is $2500\times$ 64

3.3 Relative Young modulus measured in air and under vacuum while applying a cyclic electric field at 0.1 Hz. Results for several mechanical frequencies are shown: (a) 25 Hz, (b) 100 Hz, (c) 400 Hz, and (d) 1000 Hz. The Young modulus during electrical cycling is normalized by the Young modulus when no electric field is applied, as presented in equation (2.7). 65

3.4 Loss tangent in bending measured in air and under vacuum while applying a cyclic electric field at 0.1 Hz. Several mechanical frequencies have been examined: (a) 25 Hz, (b) 100 Hz, (c) 400 Hz, and (d) 1000 Hz. 66

3.5 Transient behavior of the relative Young modulus at 25 Hz (a) versus time (along with the electric field) and (b) versus electric field (arrows indicate increasing time). Upon switching off the electric field, the relative dynamic Young modulus decays to a different steady-state value than that observed at zero electric field during electric field cycling. 67

3.6 Transient behavior of the loss tangent in bending at 25 Hz (a) versus time (along with the electric field) and (b) versus electric field (arrows indicate increasing time). Upon switching off the electric field, the loss tangent decays to a different steady-state value than that observed at zero electric field during cyclic electric fields. 68

3.7 The compliance (a) and the loss tangent (b) in bending are shown vs. mechanical frequency for two different values of the applied electric field (red and blue points) and are compared to the theoretical Euler-Bernoulli solution (red and blue dashed lines). 70

3.8 Summary of the results from Fig. 3.7 after applying the corrections in (2.15) and (2.16) to obtain the material response up to the first resonance frequency. 71

3.9	Experimental data of (a) relative Young modulus (normalized by the modulus without electric bias) and (b) loss tangent in bending vs. electric field for triangle-wave electric field (1.8 MV/m amplitude) frequencies of 0.01, 0.1, 0.5, and 1.0 Hz, and constant bending vibration at 75 Hz.	73
3.10	Relative shear modulus measured in air and under vacuum in torsion while applying a cyclic electric field at 0.1 Hz. Several mechanical frequencies are shown: (a) 25 Hz, (b) 100 Hz, (c) 400 Hz, and (d) 1000 Hz. The shear modulus during electrical cycling is normalized by the shear modulus when no electric field is applied, as presented in (2.7).	74
3.11	Loss tangent in torsion measured in air and under vacuum while applying a cyclic electric field at 0.1 Hz. Several mechanical frequencies are shown: (a) 25 Hz, (b) 100 Hz, (c) 400 Hz, and (d) 1000 Hz.	75
3.12	The compliance (a) and the loss tangent (b) in torsion are shown vs. mechanical frequency with and without an applied electric field (red and blue points) and are compared to the theoretical prediction (red and blue dashed lines).	76
3.13	Results from Fig. 3.12 after applying the correction in (2.17) to obtain the material response.	77
3.14	Experimental data of (a) relative shear modulus (normalized by the modulus without electric bias) and (b) loss tangent in torsion vs. electric field for triangle-wave electric field (2.0 MV/m amplitude) frequencies of 0.01, 0.1, 0.5, and 1.0 Hz and constant torsional vibration at 75 Hz.	78
3.15	Illustration of how the bending vibration of the specimen generates acoustic waves at the surface that propagate and thus transmit energy into the surrounding air causing parasitic damping. 1D acoustic wave theory is applied to quantify this effect using the geometry shown; each point on the surface of the specimen approximately oscillates in the x -direction giving rise to acoustic waves propagating in the same direction. The surface also oscillates in the normal direction during torsion due to the rectangular cross section of the specimens. Energy dissipated due to the generation of vortices from the edges of the specimen is neglected.	82

3.16 Relative damping error of the average maximum loss tangent in air compared to under vacuum as a function of the mechanical loading frequency of (a) bending and (b) torsion tests performed under cyclic electric fields with a frequency of 0.1 Hz. The theoretical relative error in bending and torsion is given by $D_{\text{bending}}/D_{\text{bending}}^0$, and $D_{\text{torsion}}/D_{\text{torsion}}^0$, respectively. 83

3.17 Relative damping error of the average maximum loss tangent in air compared to under vacuum as a function of the applied electric field frequency for (a) bending and (b) torsion tests performed with a mechanical loading at 75 Hz. 84

3.18 The effect of different lock-in amplifier time constants (10, 30, and 100 ms) on the measured viscoelastic stiffness (a) and damping (b). Results are shown for a bending frequency of 50 Hz and a cyclic electric field frequency of 0.1 Hz. 88

3.19 Comparison between the loss tangent in bending obtained using the applied voltage to the Helmholtz coils and the resulting current as the reference for the lock-in amplifier. By applying the phase correction measured beforehand, the results collapse. 89

3.20 Effect of different amplitudes of the applied voltage to the (bending) Helmholtz coils on the measured viscoelastic response. (a) and (b) show the relative Young modulus for mechanical frequencies of 25 and 1000 Hz, respectively. (c) and (d) show the bending loss tangent for mechanical frequencies of 25 and 1000 Hz, respectively. Each experiment was performed for a fixed electric field cycling frequency of 0.1 Hz. 90

3.21 Effect of different amplitudes of the applied voltage to the (torsion) Helmholtz coils on the measured viscoelastic response. (a) and (b) show the relative shear modulus for mechanical frequencies of 25 and 1000 Hz, respectively. (c) and (d) show the torsional loss tangent for mechanical frequencies of 25 and 1000 Hz, respectively. Each experiment was performed for a fixed electric field cycling frequency of 0.1 Hz. 91

4.1 Illustration of a volume enclosing an interface with charge per unit area σ and unit normal \mathbf{n} pointing from side 2 to side 1 with electric displacements \mathbf{d}_2 and \mathbf{d}_1 , respectively. 95

4.2 Longitudinal stress σ (arising from an applied moment M) and transverse electric field e give rise to changes in the transverse component of the macroscopic polarization p and strain ε 108

4.3 Results of bending experiments showing (a) the evolution of the electric displacement, (b) relative Young modulus, and (c) loss tangent versus applied electric field for different mechanical bending frequencies from 25-100 Hz and a fixed electric field frequency of 0.1 Hz. 109

4.4 Results of bending simulations showing the evolution of the electric displacement, relative Young modulus, and loss tangent versus applied electric field. The effect of different triangle-wave electric field frequencies from 0.01-1.0 Hz is shown in (a-c) while the effect of different mechanical bending frequencies from 25-100 Hz is shown in (d-f). 111

4.5 Relative dynamic Young modulus during domain switching versus mechanical frequency showing the affect of (a) increasing static Young modulus, (b) increasing ratio $\xi = \epsilon_s/p_s$, (c) increasing parameter κ , and (d) increasing viscosity parameter η . Unless specified in the figure, the parameters used were $\eta = 1$, $\xi = 1$, $E = 1$, and $\kappa = 1$ 113

4.6 Loss tangent in bending during domain switching versus mechanical frequency showing the affect of (a) increasing static Young modulus, (b) increasing ratio $\xi = \epsilon_s/p_s$, (c) increasing parameter κ , and (d) increasing viscosity parameter η . Unless specified in the figure, the parameters used were $\eta = 1$, $\xi = 1$, $E = 1$, and $\kappa = 1$ 114

5.1 Piezoelectric strain versus applied electric field shown for common piezoelectric ceramics (PZT and PMN-PT) as well as various single crystal compositions of PZN-PT demonstrating increased actuation. Experimental data was adapted from (Park and Shrout, 1997). 117

5.2 Illustration of the design of a MFC actuator. Planar view is shown on the left where the PZT fibers are covered by alternating positive and negative electrodes. A zoomed-in cross-sectional view is shown on the right revealing the electrodes on the reverse side. The electric field between positive and negative electrodes is nominally in the direction of the macroscopic polarization \bar{p} 118

5.3 Images showing (left) an MFC actuator with an applied speckle pattern and (right) full-field displacement measurements obtained from VIC-2D overlaid on the corresponding image taken by the camera. The dark and light vertical bands appearing in the camera image correspond to the slight protrusion of the PZT layer in the MFC actuator. The PZT layer was used as the area of interest for DIC. 121

5.4	Average longitudinal strain measured using DIC versus applied voltage. Different frequencies of 0.01 and 0.1 Hz as well as different peak-to-peak amplitudes of the applied voltage are shown.	123
5.5	Total charge accumulation on an MFC actuator versus an applied triangle-wave voltage with frequencies ranging from 0.01 to 10 Hz. To demonstrate the difference in response when operating the actuator within the manufacturer specifications and when going beyond the specifications, different voltage amplitudes of 1 kVpp and 5 kVpp, respectively, were applied.	124
5.6	Average longitudinal strain and total charge versus an applied triangle-wave voltage with a frequency of 0.1 Hz for a specimen with weakly-bonded paint. The specimens used in Figs. 5.4 and 5.5 had well-bonded paint.	125
5.7	Experimental setup used for demonstrating a set-and-hold actuator. An MFC actuator is adhered to a plexiglass substrate (a) and a voltage is applied causing the plexiglass to bend, which is observed by a camera (b). The plexiglass is held in place using a vise (c).	127
5.8	Before (left) and after (right) image of the free end of the specimen shown in Fig. 5.7(a) after applying a large voltage exceeding the normal operational range (i.e. ramping to 1800 V) and suddenly turning off the voltage. Applying a large voltage results in domain switching in the MFC actuator, which causes a permanent deflection of the specimen of 1 mm.	128
5.9	Evolution of the (a) charge accumulation and (b) bending loss tangent versus applied voltage for the double-sided actuator specimen. Different triangle-wave voltage frequencies of 0.01 Hz and 1 Hz were tested. The mechanical bending frequency was held constant at 25 Hz. Arrows indicate increasing time.	130
A.1	Sawyer-Tower circuit.	137
B.1	Example Bode magnitude plot of a (first order) low-pass filter. The relative magnitude of the output to the input is plotted versus the relative frequency (relative to the cutoff frequency).	142

List of Tables

1.1	Structural damping approaches and some of the typical loss tangents achieved.	20
2.1	Comparison of the various viscoelastic characterization methods with BES. BES is the only method that allows for a wide range of viscoelastic materials to be tested in a contactless fashion and in a vacuum environment while simultaneously controlling the temperature and applying electric fields.	26
2.2	Measured and fitted parameters of the PMMA specimen.	56
2.3	Amplitude of thermo-electromechanical loading and pressure that can be supplied by and the resolution of the material response that can be detected by the equipment used in the current BES apparatus and their associated bandwidths. Notes are provided that describe the particular limiting factor on the amplitude and/or bandwidth of some of the equipment.	61
3.1	Physical properties of the PSI-5A4E soft PZT ceramic at room temperature (obtained from Piezo Systems Inc., Woburn, MA, USA).	64
3.2	Measured and fitted parameters of the specimen.	70
3.3	Numerical values for STP air (Liepmann and Roshko, 1957).	85
4.1	Material parameters for polycrystalline PZT.	109
A.1	Approximate properties of circuit components used and voltages applied in experiments.	139

Chapter 1

Introduction

The multiscale nature of materials becomes evident upon their observation under the microscope. In metals, grain and twin boundaries are seen on the micro scale while smaller defects such as dislocations, stacking faults, and vacancies are observed on the nano and atomic level. Microstructure has a significant effect on the macroscopic properties of materials. For example, the interaction of dislocations and grain boundaries influences the macroscopic yield strength of metals. In other types of materials such as ceramics, different atomic bonding and crystal (or lack of crystal) structure generally lead to stiffer and more brittle behavior compared to metals. Thus, tailoring materials to exhibit desirable mechanical properties requires understanding their microstructure.

The microstructure of materials is normally unchanging. However, the evolution of microstructure over time (or kinetics) becomes important when materials are subjected to time-varying (dynamic) external forces including mechanical, thermal, and electrical loading. For example, cyclic mechanical loading causes fatigue through microcracking ([Alexopoulos et al., 2013](#)), thermal cycling changes the grain sizes in metals and effects their mechanical properties ([Callister and Rethwisch, 2009](#)), and cyclic electrical loading can degrade materials ([Wang et al., 2014](#)). The combined effects of microstructure and dynamic thermo-electromechanical loading clearly present a difficult challenge for understanding, predicting, and utilizing materials under these conditions. Some of these effects have been studied extensively, however, there exists a large gap in our understanding for the case of dynamic electromechanical loading of materials with microstructure evolution. Therefore, the goal of this thesis research is to investigate this particular piece of the puzzle.

The materials of interest are *ferroelectrics*. Although most materials are not affected by electric fields (at least at moderate levels), ferroelectrics are a special class of materials that exhibit

electromechanical coupling. Moreover, their electromechanical response is strongly influenced by their microstructure. Therefore, ferroelectrics present themselves as an ideal material for this study. While there are many ways dynamic loads are applied to materials, only the case of harmonic (i.e. cyclic) electromechanical loading will be considered. The response of materials under harmonic loading will be studied within the framework of *viscoelasticity* and, in particular, the dynamic stiffness and damping of ferroelectrics will be characterized. Therefore, an introduction to ferroelectric materials will first be given in Section 1.1. Then, a review of the relevant concepts from viscoelasticity will be presented in Section 1.2. Finally, the motivation for studying the viscoelasticity of ferroelectrics will be discussed in Section 1.3 and an outline of the thesis is given in Section 1.4.

1.1 Ferroelectrics

The possibility of electromechanical coupling in materials was first discovered by the Polish-French scientists Pierre and Marie Curie (1880a; 1880b). They observed that an electric field was generated when a stress was applied to quartz crystals. The converse is also true: application of an electric field results in a strain. This is known as the *piezoelectric* effect, or *piezoelectricity* (the word “piezo” hailing from the Greek word for pressure). A subset of materials that exhibit the piezoelectric effect also exhibit the *ferroelectric* effect (or *ferroelectricity*), which is of interest in the current study. Ferroelectricity was not discovered until later in the 1920s (for Rochelle Salt) by Valasek (1921). Such materials exhibit a spontaneous electric *polarization* that can be reoriented under application of large electric fields. The discovery of ferroelectricity occurred after the discovery of ferromagnetism and thus similar nomenclature was adopted (even though ferroelectrics need not be ferrous). Although technically correct but slightly misleading, ferroelectric materials are often colloquially called piezoelectric materials since, in many applications, only their piezoelectric property is utilized.

1.1.1 Physical properties

As mentioned previously, ferroelectrics can be classified as a subset of piezoelectrics. However a more precise distinction is that ferroelectrics are a subset of pyroelectrics, which are a subset of

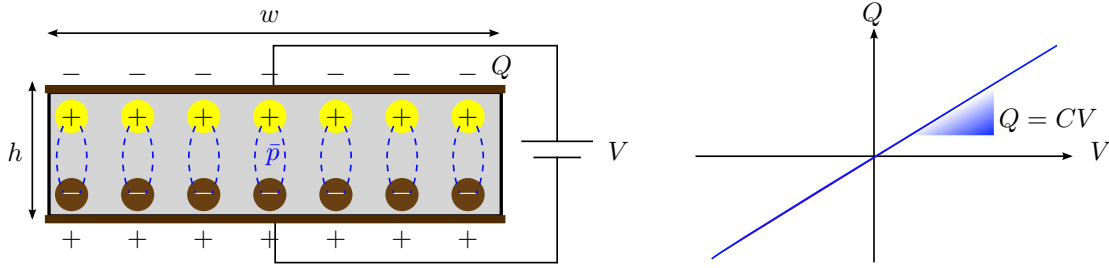


Figure 1.1: Illustration of a dielectric material being used as a capacitor. Applying a voltage V causes a polarization \bar{p} to form in the material and results in a charge Q on the surface. The relationship between applied voltage and charge is normally linear via the capacitance C .

piezoelectrics, which are a subset of dielectrics, that is,

$$\text{ferroelectrics} \subset \text{pyroelectrics} \subset \text{piezoelectrics} \subset \text{dielectrics} \subset \text{all materials.} \quad (1.1)$$

At the highest level, dielectric materials are electrically insulating (thus eliminating metals) and become electrically polarized upon application of an electric field. This phenomenon is used in capacitors to store charge as shown in Fig. 1.1. Due to electric field-dipole interaction, for example from the separation of ions in a polymer, a net electric dipole (or polarization) forms in dielectrics. Usually, the polarization changes linearly with the applied electric field. That is, the average¹ polarization per unit volume is $\bar{p} = \kappa e$, where κ is the dielectric constant of the material and e is the applied electric field. The total charge on the capacitor can be computed as the polarization multiplied by the electrode area, $Q = \bar{p}w$, where w is the width of the capacitor (assuming unit depth). Then, computing the electric field by dividing the applied voltage by the thickness h , the capacitor equation is obtained as $Q = CV$ where $C = \kappa w/h$ is the capacitance. From this relation, it is clear that the polarization returns to zero if the applied voltage is removed.

A subset of dielectrics are piezoelectrics, which behave as dielectrics do in response to electric fields but also in response to mechanical stresses. That is, in addition to the polarization being linearly dependent on the applied electric field, it is also linearly dependent on the applied stress. For example in the 1D case similar to Fig. 1.1, $\bar{p} = d\sigma + \kappa e$, where σ is an applied tensile/compressive stress, and d is the piezoelectric constant. Thus, the application of stress causes a separation of

¹The local polarization in a material may be homogeneous or spatially-varying. For a spatially-varying polarization, experiments typically measure the *apparent* or *effective* polarization that gives rise to the total charge Q , hence the use of the overbar on \bar{p} .

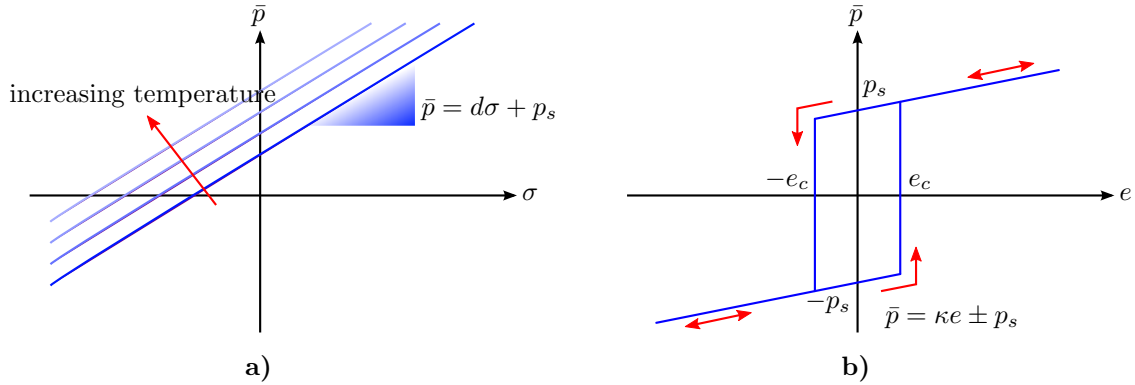


Figure 1.2: Evolution of the polarization (a) versus stress in a pyroelectric material where there is an initial, temperature-dependent spontaneous polarization p_s and (b) versus electric field in a ferroelectric material where the spontaneous polarization can be reversed when an opposing electric field exceeds the coercive field e_c leading to a hysteresis loop in addition to the linear dielectric behavior (arrows denote increasing time).

charges leading to an overall polarization.

Pyroelectric materials are piezoelectrics that exhibit a *spontaneous polarization*; the material is naturally polarized before stress or electric fields are applied. The linear variation of polarization with applied electric field and stress is then similar to Fig. 1.1 but the y -intercept of the curve for the 1D example is shifted up or down. The spontaneous polarization is typically dependent on temperature (hence the prefix “pyro-”) as shown in Fig. 1.2(a).

Finally, the unique property of ferroelectrics is that the spontaneous polarization arising from pyroelectricity can be reversed by applying a sufficiently large stress and/or electric field. For example, applying an increasing electric field as shown in Fig. 1.2(b) causes the spontaneous polarization to reverse direction (i.e. from $-p_s$ to $+p_s$ in the 1D example). The electric field at which the polarization reversal occurs is called the *coercive field*, which is denoted e_c . Reversing the electric field eventually causes the spontaneous polarization to revert to its original configuration (i.e. from $+p_s$ to $-p_s$ in the 1D example at $-e_c$). The process of polarization reorientation is referred to as *domain switching*. Since domain switching occurs at $\pm e_c$, applying sufficiently large, cyclic electric fields causes a *hysteresis* loop in the polarization.

1.1.2 Origins of ferroelectricity

To understand how the properties of ferroelectrics arise, we first consider piezoelectrics and pyroelectrics. The materials that will be studied later are ceramics, in particular polycrystalline materials, thus the following discussion focuses exclusively on ferroelectric ceramics. Polymers can be ferroelectric but the material structure is different and they are not the focus of this study. Ferroelectricity arises in a material due to the symmetry of (or lack of symmetry of) its crystal lattice.

When discussing the symmetry of crystal lattices, it is useful to have an understanding of crystallographic point groups. The online course by [Wuensch \(2005\)](#) provides a good introduction to the subject. A point group is a collection of symmetry operations (e.g. translations, rotations, mirror planes, and inversions) that can be performed about a point in space (e.g. Cartesian space); upon applying one of the symmetry operations, the resulting space looks the same. When talking about the symmetry of a crystal lattice, the “space” contains the lattice of atoms. By the definition of a lattice, this space is invariant upon applying the translation operation from one lattice point to another (i.e. crystal lattices are a regular periodic arrangement of atoms). If we require a space to contain a lattice, then there are a finite number of other possible operations (e.g. rotations, mirror planes, and inversions) that can be performed that are consistent with the lattice. For example, in 2D, the only possible rotations of a lattice are 180° , 90° , 60° , and 30° (can be shown using geometry) referred to as 2-fold, 4-fold, 3-fold, and 6-fold symmetry, respectively. Other rotations would violate the requirement of translational symmetry. In general, it has been shown for 3D lattices that there are only 32 sets of possible orientations (point groups); for a general space with no constraints there would be infinitely many possible point groups. This gives rise to the finite number of crystallographic classes: cubic, hexagonal, trigonal, tetragonal, monoclinic, and triclinic. Furthermore, 21 of these crystallographic point groups are non-centrosymmetric (i.e. they lack a point of inversion symmetry). That is, if you draw a line connecting a point to an object in the lattice (e.g. an atom), that object does not appear on the opposite side of the point at the same distance. Crystal lattices falling into one of these point groups are piezoelectric (except for the cubic class 432), which include the tetragonal, rhombohedral, or orthorhombic lattice structure ([Jaffe et al., 1971](#); [Lines and Glass, 1977](#); [Moulson and Herbert, 2003](#)). It is the lack of centrosymmetry that allows for a polarization in the material to form ([Abrahams et al., 1968](#)). Finally, of the 20 piezoelectric point groups, 10 can display pyroelectricity due to the presence of a polar axis. That

is, there exists a rotation axis whose normal plane is not a mirror plane.

The *polarization* of a material refers to an electric polarization (or electric dipole). Thus, the polarization is due to the separation of positive and negative charges. For the materials of interest we assume no free charges due to e.g. dopants such that the separation of charges is solely due to the arrangement of the atoms. Loosely, the overall polarization $\bar{\mathbf{p}}$ can be thought of as the volume-averaged summation over the product of the charge q_i and distance from a datum $\mathbf{r}_i - \mathbf{r}_0$ for all i ions,

$$\bar{\mathbf{p}} = \frac{1}{V} \sum_i q_i (\mathbf{r}_i - \mathbf{r}_0). \quad (1.2)$$

Thus, for a fixed set of charges in a material, as their separation increases (due to strain or electric field-dipole interactions) the polarization increases.

Quartz (a specific form of SiO_2) was one of the first widely-used piezoelectric materials. The ionic character of the bonding in quartz (and ceramics in general with ionic and covalent bonds) results in the atoms being charged. The structure of quartz (point group 32) contains tetrahedrons with a silicon atom inside and oxygen atoms on the vertices with each oxygen atom shared between two tetrahedrons. Thus, for charge neutrality, the oxygen atoms are 2− and the silicon atoms are 4+ and under stress free conditions, the charges balance out and do not generate a polarization. However, due to the non-centrosymmetric distribution of charges in the tetrahedron, uniaxial stretching of the material (e.g. due to an applied uniaxial stress) results in a loss of symmetry and gives rise to a net polarization as shown in Fig. 1.3, which is the piezoelectric effect. Note that since the charges balance out and the polarization becomes zero upon removing the stress, quartz is not pyroelectric.

A subset of the non-centrosymmetric point groups, called polar point groups, are those that exhibit pyroelectricity. An example of a pyroelectric (that is not ferroelectric) is zinc sulfide (ZnS), which is in point group 6mm as shown in Fig. 1.4. These structures have the specific characteristic that the plane normal to their rotation axis is not a mirror plane. Thus, in terms of charged atoms, there exists a plane where a charged atom on one side is not balanced out by a mirror-image atom with the same charge on the opposite side. Therefore, even in the absence of stresses, the charge imbalance gives rise to an overall polarization, \mathbf{p}_s . However, some pyroelectrics such as ZnS are not ferroelectric as the electric field required for polarization reversal exceeds the breakdown voltage. Therefore, domain switching is not possible in practice.

Finally, ferroelectrics are pyroelectrics that have a sufficiently low coercive field such that domain

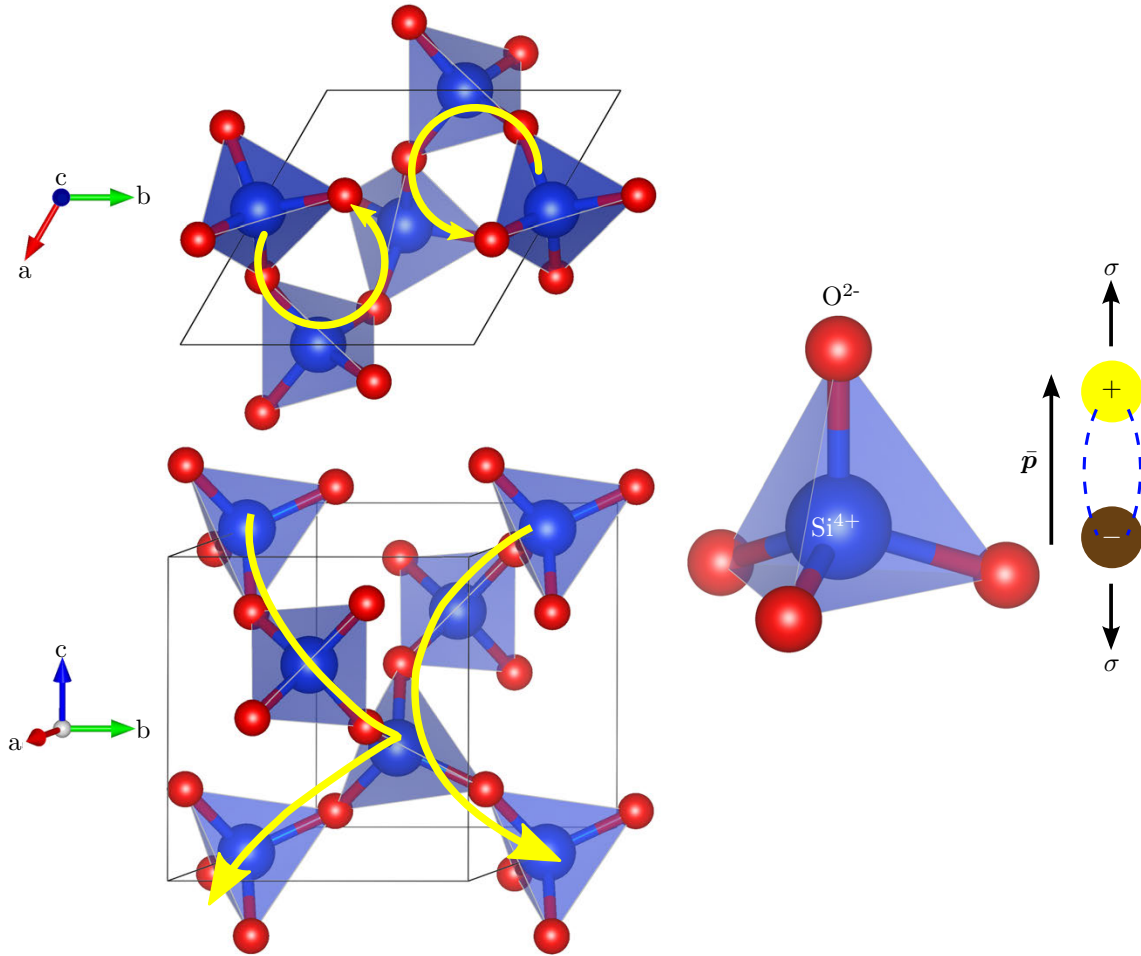


Figure 1.3: Quartz is a piezoelectric material due to the lack of centrosymmetry of the crystal structure, which causes an electric dipole, \bar{p} , to form under the application of stress. That is, any reorientation of ions in a tetrahedra are not canceled out by an opposing tetrahedra. Under no applied stress, the overall electric dipole is zero due to the helical structure of oxygen-silicon tetrahedra (denoted by yellow arrows).

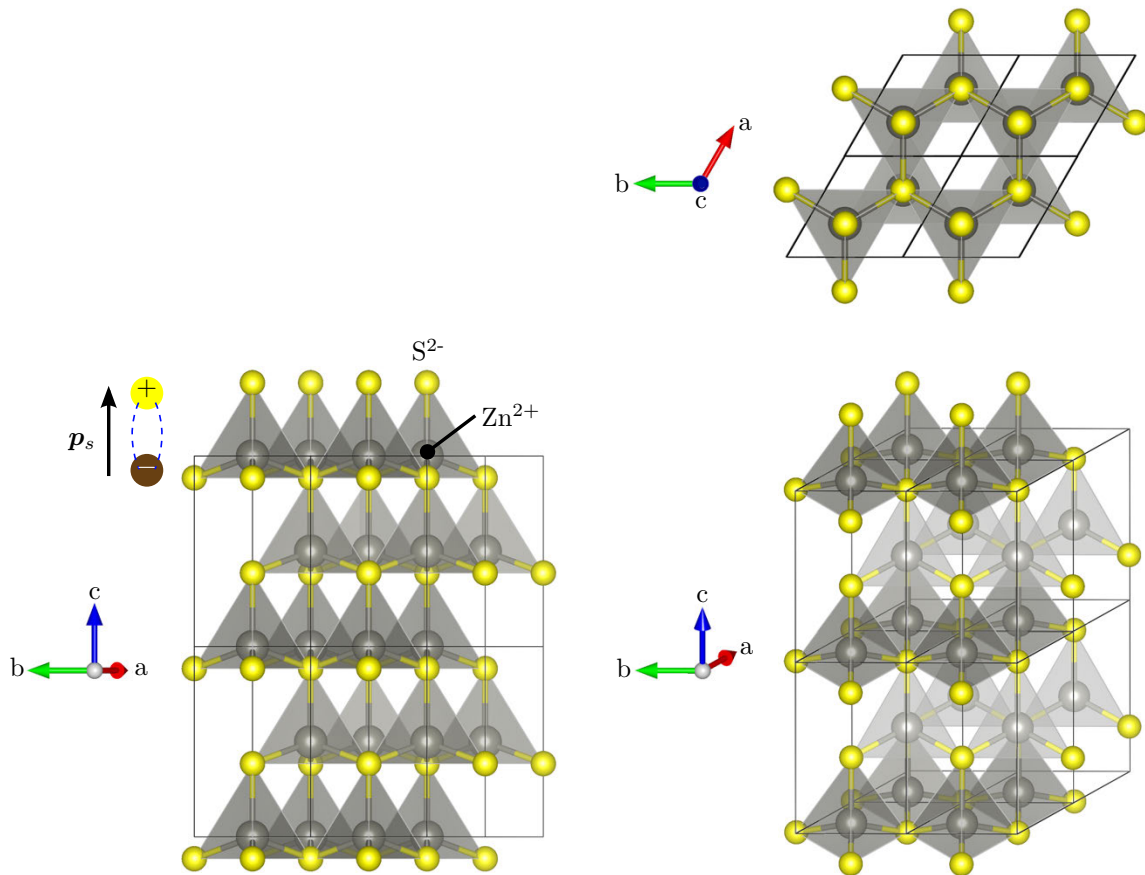


Figure 1.4: ZnS in its hexagonal form (wurtzite) is in point group $6mm$ and has a polar axis (i.e. zinc-sulfide tetrahedrons are aligned), which gives rise to pyroelectricity (with a spontaneous polarization \mathbf{p}_s).

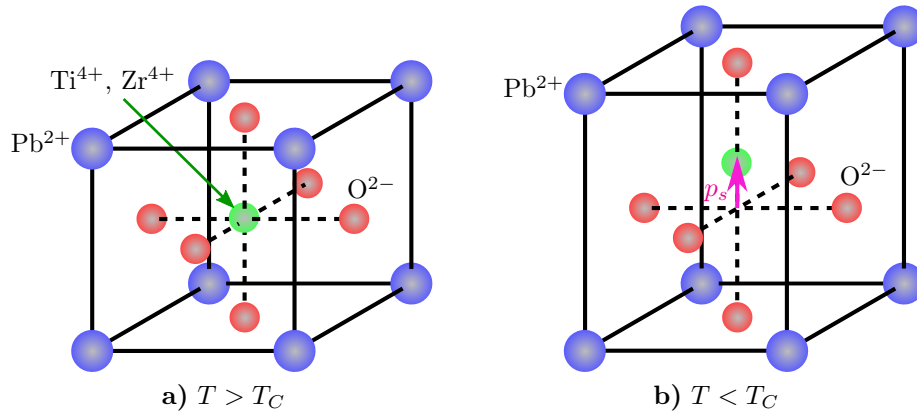


Figure 1.5: Crystal unit cell of PZT. (a) Above the Curie temperature T_C , the unit cell is cubic and non-ferroelectric. (b) Below the Curie temperature, the unit cell is tetragonal and ferroelectric.

switching occurs before electric breakdown. Common examples are lead zirconate titanate (PZT), which is widely used in industry and will be examined in experiments later, and barium titanate ($BaTiO_3$). Many other types of ferroelectric materials exist (see e.g. (Fatuzzo and Merz, 1967; Jona, 1962)) but are not of interest for the current investigation. As with ZnS, the PZT crystal has a polar axis, as shown in Fig. 1.5. In particular, Fig. 1.5(a) shows the high-temperature cubic phase, which is not ferroelectric and Fig. 1.5(b) shows the lower-temperature tetragonal phase, which exhibits ferroelectricity. The temperature at which a material transitions from a non-ferroelectric to a ferroelectric phase is called the Curie temperature T_C . Lead ions are on the corners of the unit cell with oxygen ions on the face-centered positions. Located in the center of the cubic phase is either a titanium or zirconium atom; different forms of PZT are obtained by using different fractions of titanium and zirconium. The ferroelectric effect can be seen by considering the charges of each of the atoms in the unit cell and by the fact that the cubic phase is centrosymmetric (the charges balance out), while the tetragonal phase is non-centrosymmetric and has a polar direction (the charges do not balance out and give rise to an electric polarization, p_s). One can intuitively see why domain switching is possible for PZT and not for ZnS by comparing the two crystal structures; in PZT, the charge imbalance is due to octahedra, which can more easily change orientation by the translation of the central atom while the charge imbalance in ZnS is due to tetrahedra where the central atom is more constrained.

1.1.3 Microstructure: Domains and domain walls

The spontaneous polarization in ferroelectrics gives rise to a complex microstructure. This is due to the different possible directions of the spontaneous polarization. For example, considering Fig. 1.5, if PZT forms a single-crystal at high temperature (i.e. in the cubic phase) during manufacturing (e.g. via sintering) but is then allowed to cool to room temperature, the crystal transforms to the tetragonal (ferroelectric) phase. Although Fig. 1.5 shows the spontaneous polarization pointing upwards, there is a total of six equivalent directions, as shown in Fig. 1.6. Switching between two states results in either so-called 90° or 180° domain switching depending on the rotation angle the polarization vector undergoes. Along with the changing polarization is a spontaneous strain associated with 90° domain switching due to the elongation of the unit cell. Materials tend to minimize the self-generated electric field (i.e. avoid having the entire crystal with the same orientation) as well as minimize the elastic energy (i.e. avoid 90° domain walls due to the strain mismatch). These two competing effects produce microstructure in sufficiently-large single-crystal ferroelectrics. Regions in the crystal with the same polarization orientation are called *domains* and the interfaces between those regions are called *domain walls*. If the relative orientation of polarization between two domains is 90° , the interface is referred to as a 90° domain wall. Similarly, 180° domain walls separate domains where their relative orientation of polarization is 180° .

The microstructure in ferroelectrics can be visualized using various approaches. On the largest scale (e.g. millimeters), optical methods such as polarized light microscopy (PLM) are commonly used. By passing polarized light through a ferroelectric single crystal, different domains with anisotropic indices of refraction alter the polarized light, which is recorded in a camera (different colors correspond to different domain orientations). The approach is limited to thin single-crystal specimens that are transparent (polycrystals would cause significant scattering). An example image of ferroelectric domains in single-crystal lead magnesium niobate-lead titanate (PMN-PT), which is a type of ferroelectric, is shown in Figs. 1.7(a) and (b). It can be seen that the microstructure tends to form a hierarchical lamination structure. Zooming in closer using piezo-force response microscopy (PFM), finer-scale domain laminates can be seen in Figs. 1.7(c) and (d). PFM is a type of scanning probe microscopy method similar to atomic force microscopy (AFM) where the cantilever tip is charged and thus experiences forces due to the electric polarization of the material. Typically, PFM is used to take images on the nano- to micron-scale. On the nanoscale, Fig. 1.8 shows an image of a domain lamination structure using transmission electron microscopy (TEM).

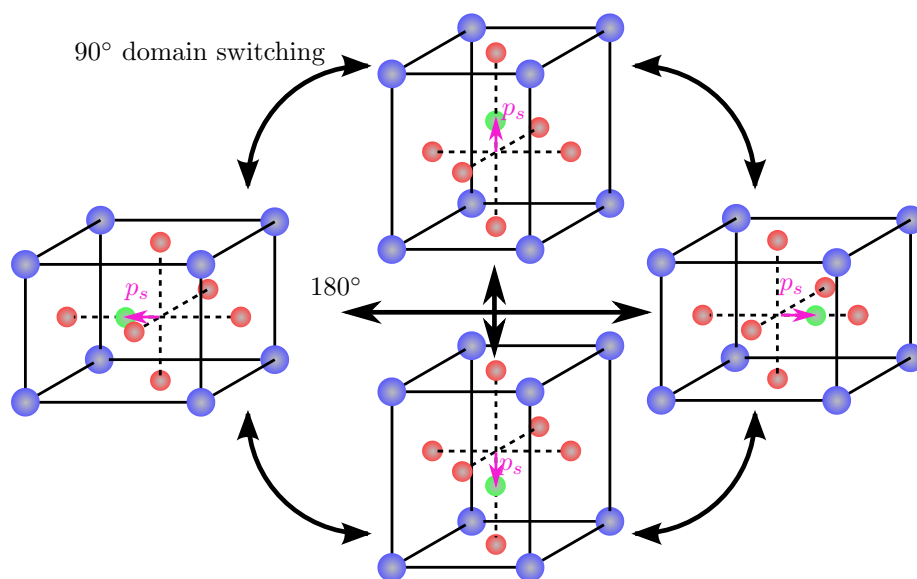


Figure 1.6: There are six equivalent directions of the spontaneous polarization in PZT: the four shown here as well as in and out of the page.

Manufacturing large single-crystal ferroelectrics is difficult and expensive. The largest sizes that are typically available have side lengths on the order of millimeters. Therefore, most structural applications of ferroelectrics utilize their polycrystalline form (i.e. ferroelectric ceramics). Ferroelectric ceramics are commonly manufactured using powder compaction and sintering processes. Thus, the original grain size of the powder governs the resulting grain size in the material. However, in addition to grains, the microstructure of ferroelectric ceramics still contains domains within individual grains. This can be seen in Fig. 1.9. One can see the granular structure formed through powder compaction and sintering in Fig. 1.9(a) using Scanning Electron Microscopy (SEM), while zooming in closer using AFM, one can see the domain lamination structure within individual grains in Fig. 1.9(b).

The microstructure is not necessarily constant. In particular, the domain structure can be altered by applying an external electric field. Applying a large electric field can cause domain switching (where the spontaneous polarization aligns with the external electric field). When multiple domains are present, domain switching usually occurs by increasing volume fractions of favorably-oriented domains and by a corresponding decrease of unfavorable domains through domain wall motion. In-situ observation using PLM has shown evolution of the domain structure upon appli-

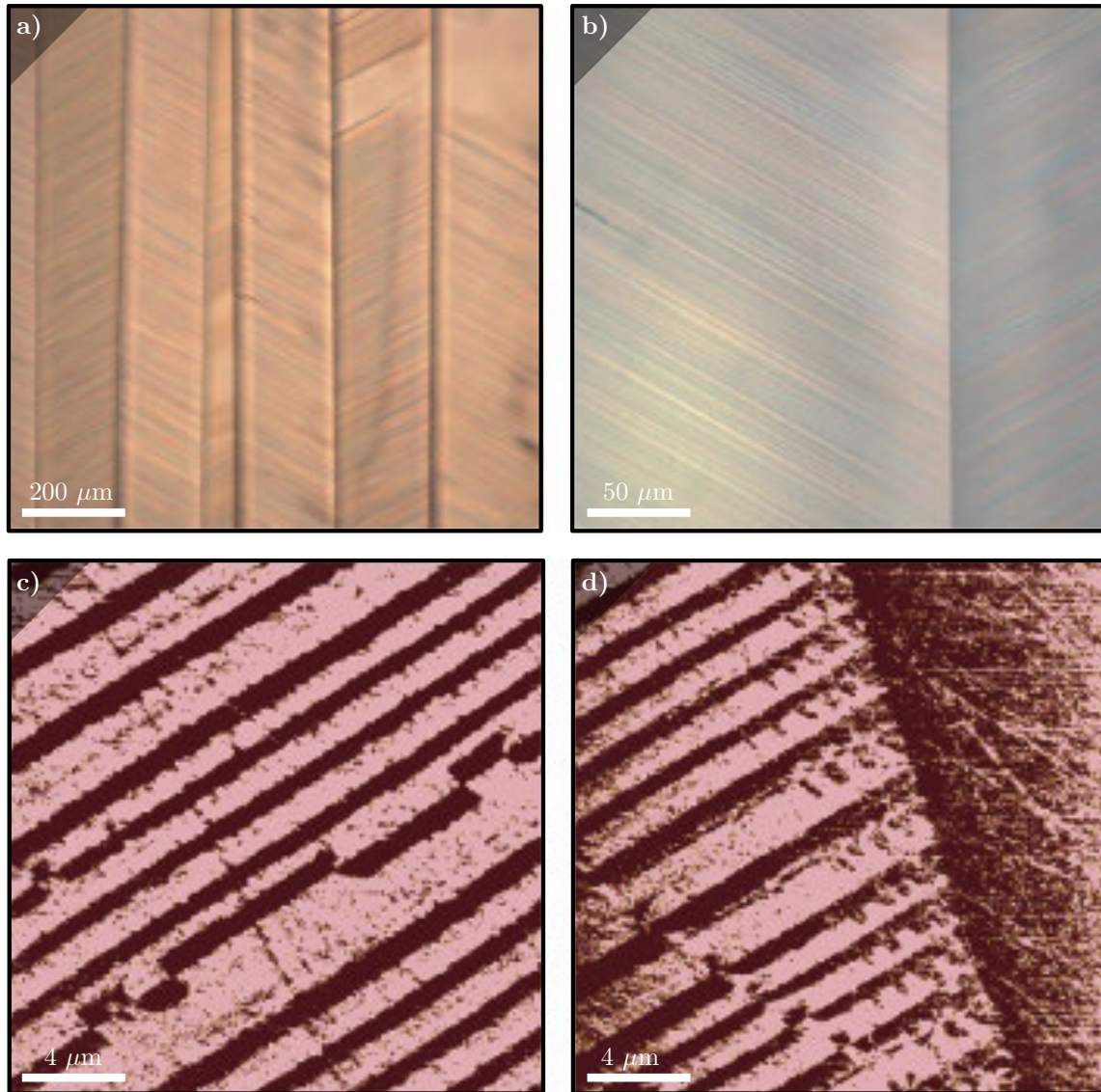


Figure 1.7: Images of the domain structure in PMN-PT at different length scales obtained from (a,b) PLM and (c,d) PFM. Images were adapted with permission from (Yao et al., 2011) © Wiley Materials. All rights reserved.

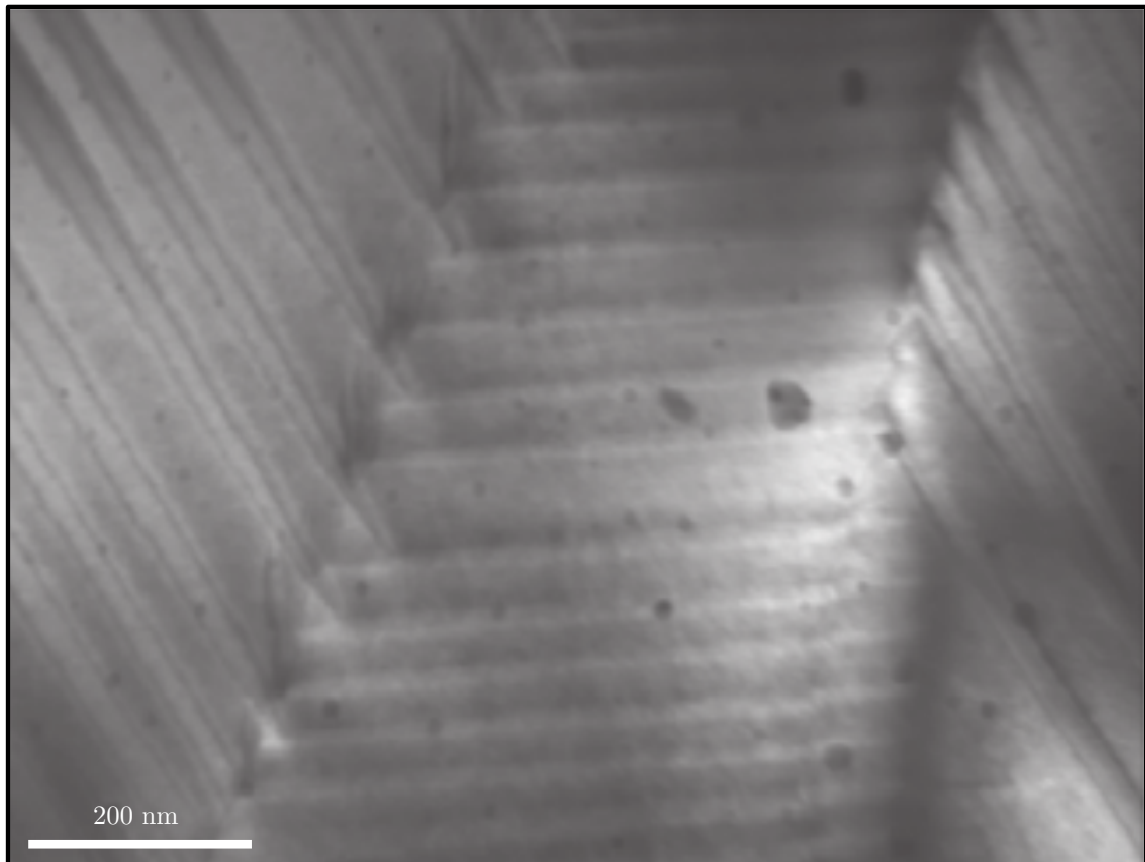


Figure 1.8: Images of the domain structure in PMN-PT obtained from TEM. Image was adapted with permission from (Yao et al., 2011) © Wiley Materials. All rights reserved.

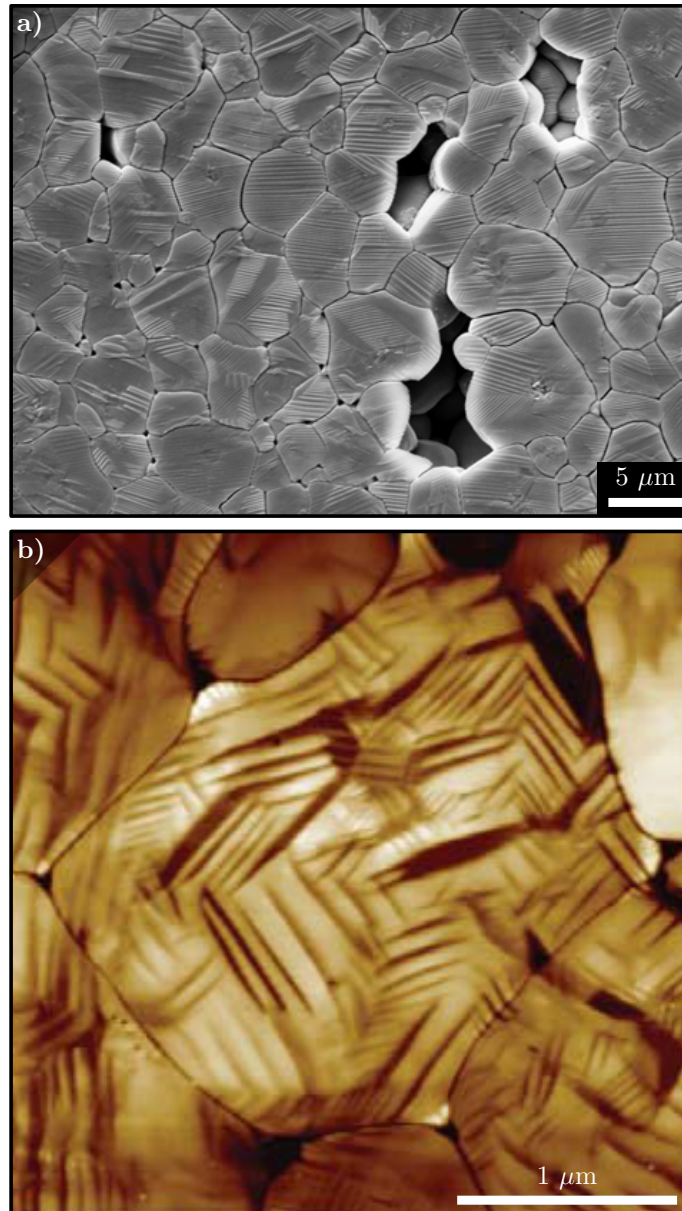


Figure 1.9: Images of polycrystalline PZT showing (a) granular structure via SEM and (b) domain structure within individual grains via AFM. Fig. (a) was adapted with permission from [King et al. \(2007\)](#) Materials Forum Vol 31 – © Institute of Materials Engineering Australasia Ltd. Fig. (b): [Wang et al. \(2003c\)](#). Atomic force microscope observations of domains in fine-grained bulk lead zirconate titanate ceramics. Smart Materials and Structures 12, 217. URL: <http://stacks.iop.org/0964-1726/12/i=2/a=309>. © IOP Publishing. Reproduced with permission. All rights reserved.

cation of an electric field as shown in Fig. 1.10. By applying an electric field, domains change orientation to align with the field, resulting in a larger domain that grows as the field is increased. Similar behavior is observed when applying mechanical stresses where domains realign to reduce elastic energy. The evolution of domain structure affects the macroscopic mechanical response. For example, the PZT unit cell exhibits anisotropic elastic constants, therefore, different volume fractions of differently-oriented domains change the effective elastic constants of the material. In addition, the domain switching process takes time and dissipates energy, which leads to a time-dependent mechanical response, which is of interest in this study.

1.1.4 Applications

Over the years, piezoelectrics and ferroelectrics have become widely used in many applications. The most common materials are the various forms of PZT and lead-free BaTiO₃, both of which are ceramic materials. Piezoelectricity and ferroelectricity can exist in non-ceramics such as polymers (e.g. piezoelectricity and ferroelectricity in polymers were first discovered by Japanese scientists in polyvinylidene fluoride (PVDF) (Kawai, 1969; Tamura et al., 1974)). The use of such polymer materials is attractive for light-weight applications in aerospace (Carvell and Cheng, 2010; Wegener, 2008) and in foams (Frioui et al., 2010; Iyer et al., 2014; Venkatesh and Challagulla, 2013). However, their extremely high coercive field (as high as 50 MV/m) makes them an undesirable material for exploring and potentially tapping their behavior during domain switching. Therefore, ferroelectric ceramics with lower coercive fields will be investigated.

Due to their electrical behavior, it is not surprising that piezoelectric and ferroelectric ceramics have been used in many electronic devices, such as computer memory, where polarization reversal can represent discrete states (Ramesh, 1997; Scott, 2000). An initial application of the piezoelectric effect was in quartz crystals used as resonators in radios. Today, piezoelectrics are commonly utilized in a myriad of transducers, actuators, and sensors (Crawley and Deluis, 1987) as well as more recently, in energy harvesters (De Marqui et al., 2011). However, the focus of this work is on the viscoelasticity of ferroelectrics during domain switching for structural applications, for which there has been little investigation in the literature.

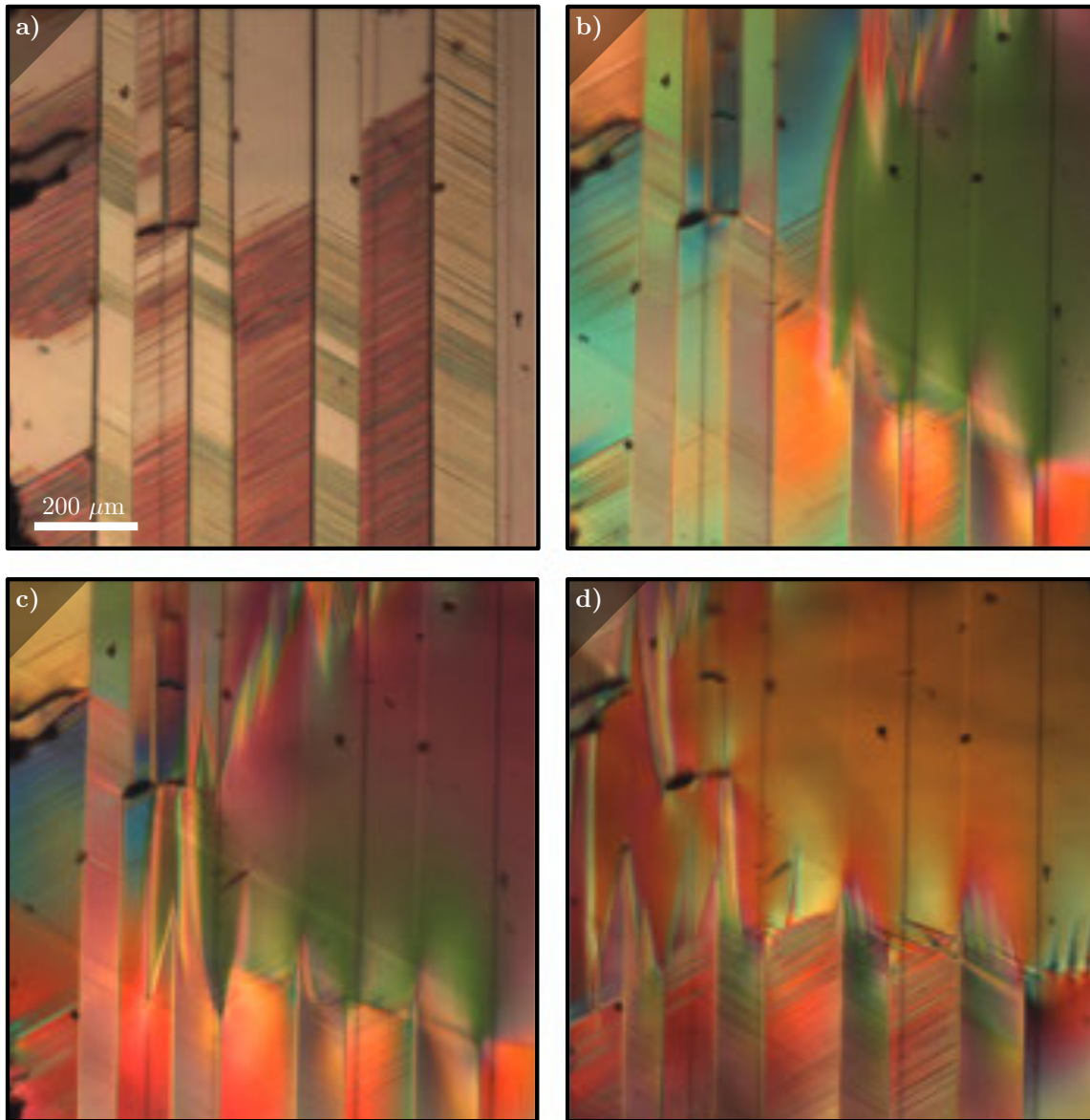


Figure 1.10: Images of the evolution of domain structure in PMN-PT upon application of an increasing electric field (a-d). Each image has the same scale. Snapshots were taken when the electric field was 0, 0.05, 0.067, and 0.083 MV/m in (a-d), respectively, in the horizontal direction. Images were obtained from PLM and adapted with permission from (Yao et al., 2011) © Wiley Materials. All rights reserved.

1.2 Concepts of linear viscoelasticity

Although the theory of viscoelasticity is often discussed in the context of polymers, it is nonetheless applicable to ferroelectric ceramics. As a fundamental property of a viscoelastic material, the mechanical response depends on the loading history and loading rate (the reader is referred to the texts on viscoelasticity by [Lakes \(1998\)](#) and [Christensen \(2003\)](#) for more details). Such a description applies to ferroelectrics; the evolution of the material's domain structure requires that the loading history of the material (electrical and mechanical) be known in order to predict how it will respond at a given point in time. With this in mind, the constitutive equation for a viscoelastic material is commonly postulated to be of the form

$$\boldsymbol{\sigma}(t) = \int_{-\infty}^t \mathcal{C}(t-t') \frac{d\boldsymbol{\varepsilon}(t')}{dt'} dt', \quad (1.3)$$

where $\boldsymbol{\sigma}$ is the Cauchy stress tensor, \mathcal{C} is the time-dependent modulus tensor, $\boldsymbol{\varepsilon}$ is the linearized strain tensor, and t is time. For current purposes, materials are assumed isotropic with time-dependent Young and shear moduli, $E(t)$ and $G(t)$, respectively. For the cases of uniaxial tension and simple shear, the relevant constitutive equations relate the longitudinal strain ε and shear strain γ to the longitudinal stress σ and shear stress τ , respectively, as

$$\sigma(t) = \int_{-\infty}^t E(t-t') \frac{d\varepsilon(t')}{dt'} dt', \quad \tau(t) = \int_{-\infty}^t G(t-t') \frac{d\gamma(t')}{dt'} dt'. \quad (1.4)$$

For the experiments performed in this work, harmonic motion is assumed and initial transient effects are assumed to be damped out quickly. Therefore, (1.4) can be rewritten by assuming harmonic forms for the stresses and strains:

$$\varepsilon(t) = \hat{\varepsilon} e^{i\omega t}, \quad \sigma(t) = \hat{\sigma} e^{i\omega t}, \quad \gamma(t) = \hat{\gamma} e^{i\omega t}, \quad \tau(t) = \hat{\tau} e^{i\omega t}, \quad (1.5)$$

where $(\hat{\cdot}) \in \mathbb{C}$ (hats) denote complex-valued amplitudes (which contain phase-information on the stresses and strains) and $\omega \in \mathbb{R}$ is the mechanical loading frequency. Substituting (1.5) into (1.4)

yields

$$\begin{aligned}\sigma(t) &= \left[-\omega \int_{-\infty}^t E(t-t') \sin \omega t' dt' + i\omega \int_{-\infty}^t E(t-t') \cos \omega t' dt' \right] \varepsilon(t), \\ \tau(t) &= \left[-\omega \int_{-\infty}^t G(t-t') \sin \omega t' dt' + i\omega \int_{-\infty}^t G(t-t') \cos \omega t' dt' \right] \gamma(t),\end{aligned}\tag{1.6}$$

where Euler's formula, $e^{i\omega t} = \cos \omega t + i \sin \omega t$ has been used. By inspection of (1.6), one can see that the terms in brackets are the apparent complex-valued Young and shear moduli E^* and G^* , respectively, i.e.

$$\sigma(t) = E^* \varepsilon(t), \quad \tau(t) = G^* \gamma(t).\tag{1.7}$$

In general, a complex number can be fully described by its magnitude and argument (i.e. $z = R e^{i\theta}$). Therefore, the measurements of the dynamic moduli, $|E^*|$ and $|G^*|$, and phase angles, δ_E and δ_G describe the complex Young and shear moduli, respectively. Mathematically, these quantities are,

$$\begin{aligned}|E^*| &= \sqrt{[\operatorname{Re}(E^*)]^2 + [\operatorname{Im}(E^*)]^2} = \frac{|\hat{\sigma}|}{|\hat{\varepsilon}|}, & \tan \delta_E &= \frac{\operatorname{Im}(E^*)}{\operatorname{Re}(E^*)} = \tan(\arg \varepsilon - \arg \sigma), \\ |G^*| &= \sqrt{[\operatorname{Re}(G^*)]^2 + [\operatorname{Im}(G^*)]^2} = \frac{|\hat{\tau}|}{|\hat{\gamma}|}, & \tan \delta_G &= \frac{\operatorname{Im}(G^*)}{\operatorname{Re}(G^*)} = \tan(\arg \gamma - \arg \tau),\end{aligned}\tag{1.8}$$

where $\tan \delta_E$ and $\tan \delta_G$ are the loss tangents corresponding to the Young and shear modulus, respectively. Thus, in experiments we measure the ratio of the amplitude of stress to strain to obtain the dynamic moduli and compute the tangent of the phase difference between stress and strain to obtain the loss tangent. As an example, the dynamic Young modulus and loss tangent can be measured via application of a time-varying sinusoidal uniaxial stress using Dynamic Mechanical Analysis (DMA) as shown in Fig. 1.11. The resulting strain lags behind the applied stress due to the viscoelasticity of the material. The phase angle between the stress and strain is δ , thus the loss tangent is $\tan \delta$. The dynamic Young modulus is the ratio of the amplitude of the stress to the strain: $|E^*| = \hat{\sigma}/\hat{\varepsilon}$. Plotting stress versus strain reveals a hysteresis loop. The area enclosed by the loops is related to the energy damped (absorbed) by the material. The higher the loss tangent, the greater the hysteresis and damping.

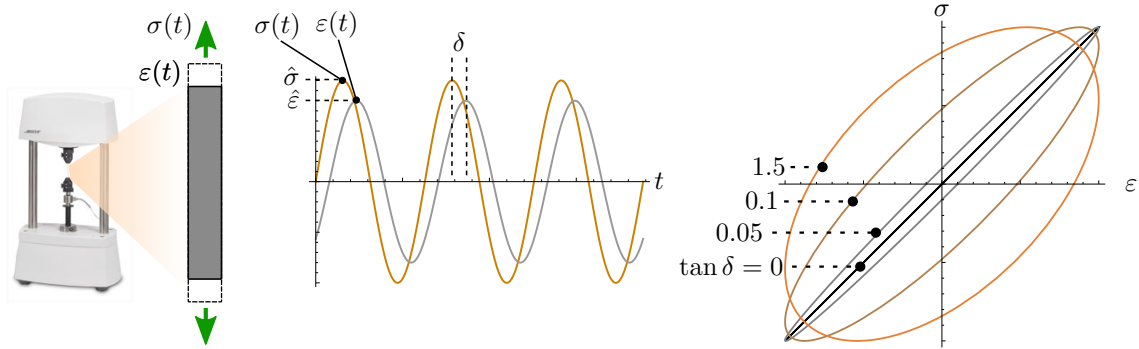


Figure 1.11: An example experiment to measure the viscoelastic properties of a material (i.e. the dynamic Young modulus and loss tangent) using harmonic loading in a DMA setup (an image of a Bose Electroforce is shown here).

1.3 Motivation

With the basic concepts of ferroelectricity and viscoelasticity reviewed, the motivation for studying the dynamic response of ferroelectrics is presented. The study of ferroelectric ceramics as energy absorbing materials (in particular for reducing vibrations in structures) has been ongoing for the past several decades. To this point, such applications can be separated into two categories, where the material is either passively or actively controlled in order to mitigate vibrations. Within these two categories are more specific methods to absorb energy. A typical method for creating passively-controlled energy absorbers is to short-circuit the ferroelectric material through a shunt resistor (Bachmann et al., 2012; Cross and Fleeter, 2002; Guyomar et al., 2008; Hagood and von Flotow, 1991); a strain-induced voltage on the surface of the ferroelectric specimen creates a current that dissipates energy through the resistor via heating. Similarly, others have investigated embedding ferroelectric inclusions in a conducting metal matrix, where current generated by a strain-induced voltage in the inclusion is dissipated in the metal matrix via Joule heating (Asare et al., 2012; Asare, 2004, 2007; Goff, 2003; Goff et al., 2004; Kampe et al., 2006; Poquette, 2005; Poquette et al., 2011). This type of material is difficult to manufacture due to depolarization of inclusions at high temperature. An alternative is to actively control the ferroelectric material via controlling an applied voltage to cancel out vibrations (Arafa and Baz, 2000; Bailey and Hubbard, 1985; Duffy et al., 2013; Fanson and Caughey, 1990; Forward, 1979; Hanagud et al., 1992; Sharma et al., 2013; Zheng et al., 2011) and other methods (Kumar and Singh, 2009; Li et al., 2008; Lin and

Table 1.1: Structural damping approaches and some of the typical loss tangents achieved.

passive	loss tangent
high-damping material layers in plates and beams (Capps and Beumel, 1990; Wetton, 1979)	> 1
tuned mass damper (Taranath, 1988)	–
piezoelectric damping via shunt resistor (Bachmann et al., 2012)	0.001 – 1.0
piezoelectric-metal matrix composites (Asare et al., 2012)	0.01
active	loss tangent
vibration canceling	–
piezoelectrics during temperature-induced phase changes (Cheng et al., 1996)	< 0.02
stress induced domain switching (Chaplya and Carman, 2002a)	< 0.1

Ermanni, 2004; Liu et al., 2010; Ngo et al., 2004; Richard et al., 1999; Tremaine, 2012; Trindade and Benjeddou, 2002). Additionally, the viscoelasticity of ferroelectrics has been studied but only under small electric fields (Budimir et al., 2004; Burianova et al., 2008) (i.e. when there is no microstructure evolution due to domain switching). As described in Section 1.2, a common metric for evaluating the ability of a material to absorb vibrational energy is to measure its loss tangent, $\tan \delta$. The higher the loss tangent, the more the material reduces vibrations. The problem with the passive methods is that they produce relatively small loss tangents (typically $\tan \delta < 0.01$) over most mechanical frequencies while only achieving significant damping near the resonance of the system (typically $\tan \delta = 1.0$). Furthermore, active methods add complexity and are limited by the strains and forces achievable by piezoelectricity, which makes their application in stiff, massive structures challenging. A summary of the mechanical damping reached by the aforementioned methods as well as others is shown in Tab. 1.1.

In order to achieve significant damping increase over many different frequencies, which is desirable in aircraft applications (Simpson and Schweiger, 1998), a different mechanism must be used. In addition, aircraft and spacecraft structures and other structural applications often require high-stiffness materials to rigidly support heavy loads. However, the combination of high stiffness and high damping is usually not present in common engineering materials, as shown in Fig. 1.12. Therefore, we seek to explore new damping mechanisms in materials, in particular, the kinetics of microstructure evolution in ferroelectrics ceramics (which already have a high stiffness). Previous methods have focused the piezoelectric effect (only small electric fields and small stresses/strains were applied). Instead, utilizing the full ferroelectric response of materials (i.e. including domain

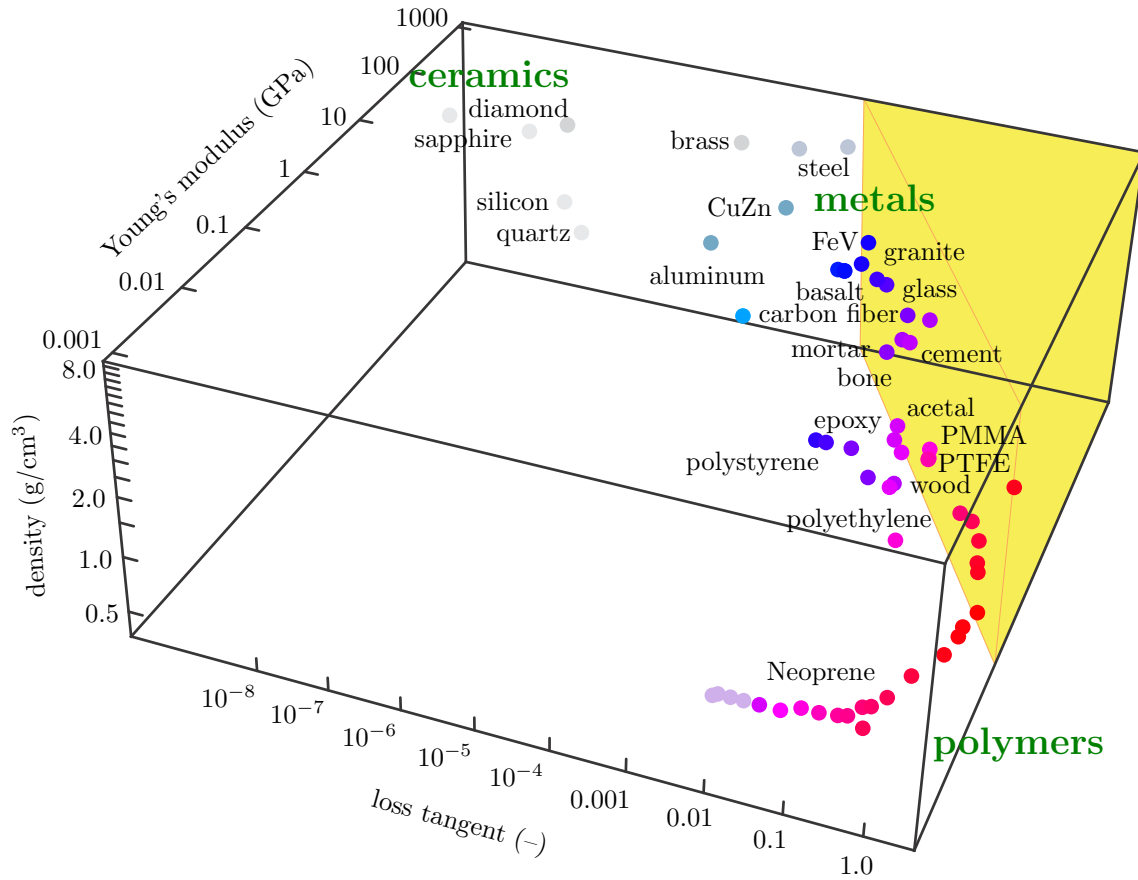


Figure 1.12: Plot of Young's modulus, loss tangent, and density of common engineering materials (including ceramics, metals, and polymers). Common engineering materials lack both a high Young modulus and high loss tangent (denoted by the shaded area). Values were obtained from (Callister and Rethwisch, 2009; Lakes, 1998).

switching) is studied. In particular we examine the viscoelastic response and compare with other methods for vibration control. This approach was first examined about a decade ago but little has been studied since then. In particular, [Chaplya and Carman \(2001a,b, 2002a,b\)](#) examined the dissipation in ferroelectrics due to stress-induced domain switching while [Jiménez and Vicente \(1998, 2000\)](#) investigated dissipation from electric field-induced domain switching.

Exploring the viscoelastic properties of electromechanically-coupled materials such as ferroelectrics may lead to new avenues of creating materials with controllable viscoelasticity. In a similar manner to metallic materials, for which damping is the macroscopic manifestation of the motion of point defects ([Snoek, 1941](#); [Zener, 1948](#)) or dislocations ([Eshelby, 1949](#); [Granato and Lücke, 2004](#)), of grain boundary activities ([Kê, 1947](#)), or of heterogeneous thermoelastic mechanisms ([Bishop and Kinra, 1995](#); [Zener, 1937, 1938](#)), additional damping can arise from domain wall motion in materials such as ferromagnets ([Burdett and Layng, 1968](#); [Gilbert, 2004](#); [Wuttig et al., 1998](#)) and ferroelectrics ([Abrahams et al., 1968](#); [Harrison and Redfern, 2002](#)). The motion and interaction of domain walls in ferroelectrics with defects ([Kontsos and Landis, 2009](#); [Schrade et al., 2007](#)) produce Debye peaks of dielectric losses ([Gentner et al., 1978](#); [Xu et al., 2001](#); [Zhou et al., 2001](#)) as well as increased mechanical damping ([Arlt and Dederichs, 1980](#); [Asare et al., 2012](#)) and hysteresis effects ([Cao and Evans, 1993](#); [Chen and Viehland, 2000](#); [Schmidt, 1981](#)). This effect becomes even more pronounced when the material is subjected to an electric field above the coercive field ([Merz, 1954](#); [Miller and Savage, 1958, 1960](#); [Tatara and Kohno, 2004](#); [Yin and Cao, 2001](#)). Thus, by carefully controlling an applied electric field, microstructure kinetics via domain wall motion and the resulting time-dependent response of ferroelectrics can be controlled. Therefore, the goal of the thesis research was to fully characterize the kinetics of domain switching in ferroelectrics (through experiments and modeling) for creating high stiffness, high damping structural materials and for new methods of actuation.

1.4 Outline

To better understand the influence of domain switching kinetics on the overall viscoelastic response of ferroelectrics, experiments are performed to measure the evolution of their viscoelastic stiffness and damping throughout the entire electric displacement hysteresis. In particular, the effect of different (multiaxial) mechanical and electrical loading rates on the kinetics of microstructural

changes, due to domain switching, are investigated. Furthermore, the influence of domain switching on the overall structural response of ferroelectric specimens (i.e. throughout the resonance spectrum) is determined, which is important for understanding their impact in structural applications. A continuum-mechanics model is also developed to capture experimental measurements and predict the behavior of new materials to optimize their viscoelastic response. With a better understanding of the viscoelastic properties of ferroelectrics, proof-of-concept experiments are performed to demonstrate potential applications of domain switching in set-and-hold actuators and for structural damping.

The following chapters first focus on experimental methods. As will become evident in the following chapter, the need for new experimental techniques motivated the development of Broadband Electromechanical Spectroscopy (BES), which will be presented in Chapter 2. Using this new method, the viscoelasticity of PZT under different electromechanical loading rates is presented and discussed in Chapter 3. With the aid of a newly-developed continuum model derived in Chapter 4, insight is gained on the material behavior and guidelines are provided for material design. In Chapter 5, domain switching kinetics are exploited in PZT-based actuators to demonstrate their set-and-hold actuation and structural damping capabilities. Finally, the main results of the thesis research are summarized in Chapter 6.

Chapter 2

Broadband Electromechanical Spectroscopy

The following sections follow from our previously published papers ¹ (le Graverend et al., 2015; Wojnar et al., 2014), however some additional details are provided. Understanding and ultimately technologically exploiting the electro-thermo-mechanically-coupled time-dependent properties of materials (e.g., of ferroelectric materials or of composites containing ferroelectric phases) requires currently-unavailable measurement capabilities. Indeed, most available experimental methods for characterizing viscoelastic materials are commonly performed by forced and free vibration testing (Zhou et al., 2005b) and are applicable over rather restricted portions of the time and frequency domains (Ferry, 1980).

Dynamic Mechanical Analysis (DMA) (Lakes, 2004), for instance, mechanically deforms samples by time-harmonic bending, torsion, or tension/compression. DMA apparatuses are versatile and experiments can be performed over wide ranges of ambient conditions; temperatures ranging from -150 to 600°C can be achieved in certain DMA setups (TA Instruments, 2015). However, the frequency range of DMA depends significantly on the sample and on the test apparatus used. For example, state-of-the-art DMA devices (Perkin Elmer, 2014) typically cover at most 0.001 to 600 Hz, and their use is also limited to a maximum specimen stiffness of less than 1 GPa, which

¹The method and experimental setup was described in le Graverend, J.B., Wojnar, C., Kochmann, D., 2015. Broadband Electromechanical Spectroscopy: Characterizing the dynamic mechanical response of viscoelastic materials under temperature and electric field control in a vacuum environment. *Journal of Materials Science* 50, 3656–3685. URL: <http://dx.doi.org/10.1007/s10853-015-8928-x>, doi: [10.1007/s10853-015-8928-x](https://doi.org/10.1007/s10853-015-8928-x). Additional experimental results and analysis are from Wojnar, C.S., le Graverend, J.B., Kochmann, D.M., 2014. Broadband control of the viscoelasticity of ferroelectrics via domain switching. *Applied Physics Letters* 105, 162912. URL: <http://scitation.aip.org/content/aip/journal/apl/105/16/10.1063/1.4899055>, doi: <http://dx.doi.org/10.1063/1.4899055>.

excludes testing of ceramics and metals in general. Usually, the inertia of the grips in contact with specimens in DMA limits the maximum driving frequency of the apparatus. Also, gripping or otherwise contacting stiff, brittle materials such as ferroelectrics (and ceramics) without damaging the specimen is difficult in practice, hence a contactless measurement approach is needed.

The Inverted Torsion Pendulum (ITP) is such a method that uses contactless techniques (Kê, 1947). However, the ITP is typically used for low-frequency experiments (10^{-5} to 10 Hz), which may be too slow for observing the influence of microstructural processes in ferroelectrics such as domain wall motion (Jiménez and Vicente, 2000; Miller and Savage, 1958). Like DMA, the ITP is also versatile and experiments have been performed over wide ranges of temperatures from cryogenic to elevated temperatures (-285°C to 1500°C) under vacuum (D’Anna and Benoit, 1990; Gadaud et al., 1990; Gribb and Cooper, 1998; Woigard et al., 1977). The ITP has mainly been used for characterizing metals and ceramics with Young moduli ranging from 10s to 100s of GPa. Its contactless approach of applying forces electromagnetically to specimens makes the ITP attractive for testing ceramics.

Although primarily used for measuring elastic moduli (Migliori et al., 1993), Resonant Ultrasound Spectroscopy (RUS) can determine the frequency-dependent viscoelastic moduli by scanning the specimen’s resonance spectrum in a double-transducer actuator-sensor setup (Lee et al., 2000). The frequency range of RUS instruments is larger than DMA as it does not require a mechanical driver but relies upon piezoelectric actuation. However, it is affected by the piezo-cells’ resonance frequencies and practical limitations. For typical specimen sizes, (Lee et al., 2000) and (Zadler et al., 2004) (for example) report RUS results from about 10 kHz to 10 MHz and from 5 kHz to 100 kHz, respectively. RUS has been performed under various ambient conditions such as temperatures ranging from -193 to 247°C (Kuokkala and Schwarz, 1992) and elevated pressures (Zhang et al., 1998), but not under vacuum, which is desirable for reducing spurious damping. In addition, the specific specimen geometry required by RUS makes applying uniform electric fields via surface electrodes difficult. Thus, electromechanical loading in RUS has not been attempted. A similar method called the Piezoelectric Ultrasonic Composite Oscillator Technique (PUCOT) (Daniels and Finlayson, 2006) tracks the specimen’s resonance spectrum in a forced-vibration cantilever configuration.

In a similar fashion to DMA, Broadband Viscoelastic Spectroscopy (BVS) performs bending and torsion but uses contactless techniques (Dong et al., 2008; Lakes and Quackenbusch, 1996; Lakes, 2004): moments are applied by electromagnetism and deformation is characterized by a laser-

Table 2.1: Comparison of the various viscoelastic characterization methods with BES. BES is the only method that allows for a wide range of viscoelastic materials to be tested in a contactless fashion and in a vacuum environment while simultaneously controlling the temperature and applying electric fields.

method	bandwidth	moduli	temp.	e-field	vac.	contactless
DMA	10^{-3} to 10^2 Hz	up to 1 GPa	-150 to 600°C	–	–	–
RUS	10^4 to 10^7 Hz	$\tan \delta < 10^{-2}$	-193 to 247°C	–	–	–
ITP	10^{-5} to 10 Hz	10 to 10^3 GPa	-268 to 1400°C	–	✓	✓
BVS	10^{-6} to 10^5	up to 10^4 GPa	up to 160°C	–	–	✓
BES	10 to 10^4 Hz	up to 10^4 GPa	up to 400°C	✓	✓	✓

detector setup. Thus, BVS offers higher sensitivity and finer resolution than DMA and is capable of scanning many decades of frequency (Brodt et al., 1995) with considerably lower compliance and less spurious damping. Moreover, the contactless testing prevents damaging of the specimens. BVS data has been reported for the range of roughly 10^{-6} to 10^5 Hz, i.e. covering approximately 11 decades of time and frequency (Lee et al., 2000). Of course, the exact frequency range depends on the test instrument, the electronic function generator, the laser detector used, and on the sample. Temperatures of up to 160°C have been reached in the BVS apparatus used in (Dong et al., 2011, 2008, 2010) using convection heating via air flow, which unfortunately can lead to spurious damping.

The capabilities of the aforementioned methods are summarized in Tab. 2.1. Despite all these techniques, *electric fields and mechanical loads over significant ranges of frequency have not been independently applied before*, which is necessary for fully-characterizing the thermo-electromechanical response of ferroelectrics. Thus, a different method and setup is needed.

A new technique called *Broadband Electromechanical Spectroscopy* (BES) has been developed, which measures the dynamic stiffness and damping of materials in a contactless fashion over a wide range of frequencies while simultaneously applying an electric field in a vacuum environment. The contactless testing allows for the characterization of brittle ceramics, the application of electric fields allows for the electromechanical response of ferroelectrics to be measured, the vacuum environment reduces spurious damping, and the apparatus allows for the temperature to be controlled. Thus, BES allows for the viscoelastic characterization of ferroelectrics and other electro-active materials, which was not possible with existing methods. The specific experimental setup used in the BES technique will be explained in detail. The capabilities of the specific BES apparatus presented are also given in Tab. 2.1 to compare with existing methods where it can be seen that BES can

test a wide range of viscoelastic materials under combined temperature and electric field control in a vacuum environment, while still having the capability to apply a wide range of mechanical frequencies as in BVS. A wide frequency range is important for characterizing the kinetics of domain switching as well as understanding its impact on structural resonance. We note that the BES method is more general than the specific apparatus presented here. In Chapter 3, using BES, the dynamic stiffness and damping in bending and torsion of a ferroelectric ceramic, viz. PZT, are measured during electric field-induced domain switching. Moreover, experiments performed in air and under vacuum are compared to quantify the influence of the surrounding air on the measured dynamic stiffness and damping.

2.1 Materials and methods used in Broadband Electromechanical Spectroscopy

To study a wide range of materials with thermo-electromechanically coupled properties from soft polymers such as PVDF (with a typical Young modulus of 3 GPa ([Tamura et al., 1974](#))) to stiff ferroelectric ceramics (which are studied here and have Young moduli on the order of 100 GPa) and composites containing ferroelectrics (whose dynamic moduli can be as high as 10^4 GPa ([Jaglinski et al., 2007](#))), the specimens are tested in bending and/or torsion, as opposed to uniaxial tests. Specimens with cantilevered beam geometry are gripped on one end and a bending and/or torsional moment is applied to their free end, as shown in a schematic of the apparatus in [Fig. 2.1](#). The cantilever beam setup is best suited for testing materials under time-varying temperatures and electric fields as both of which may cause eigenstrain in the material. The minimal grip contact with cantilever beams (compared to 3-point or 4-point bending setups) minimizes the amount of internal stresses arising from eigenstrain, which may influence the material response. In a similar manner to BVS ([Lakes, 2004](#)), bending and torsional moments are applied through Helmholtz coils via a permanent magnet attached to the specimen's free end. Specimen deflection/twist is captured via a laser-detector set-up as shown in [2.2\(a\)](#). Adding to the capabilities of BVS, an electric field is applied using surface electrodes on the specimen and electric displacements are measured via a Sawyer-Tower circuit connected to the grips ([Sawyer and Tower, 1930](#); [Sinha, 1965](#)). Furthermore, the BES apparatus comprises a vacuum chamber as shown in [Fig. 2.2\(a\)](#) to reduce the influence of spurious damping. The temperature inside the chamber can be controlled

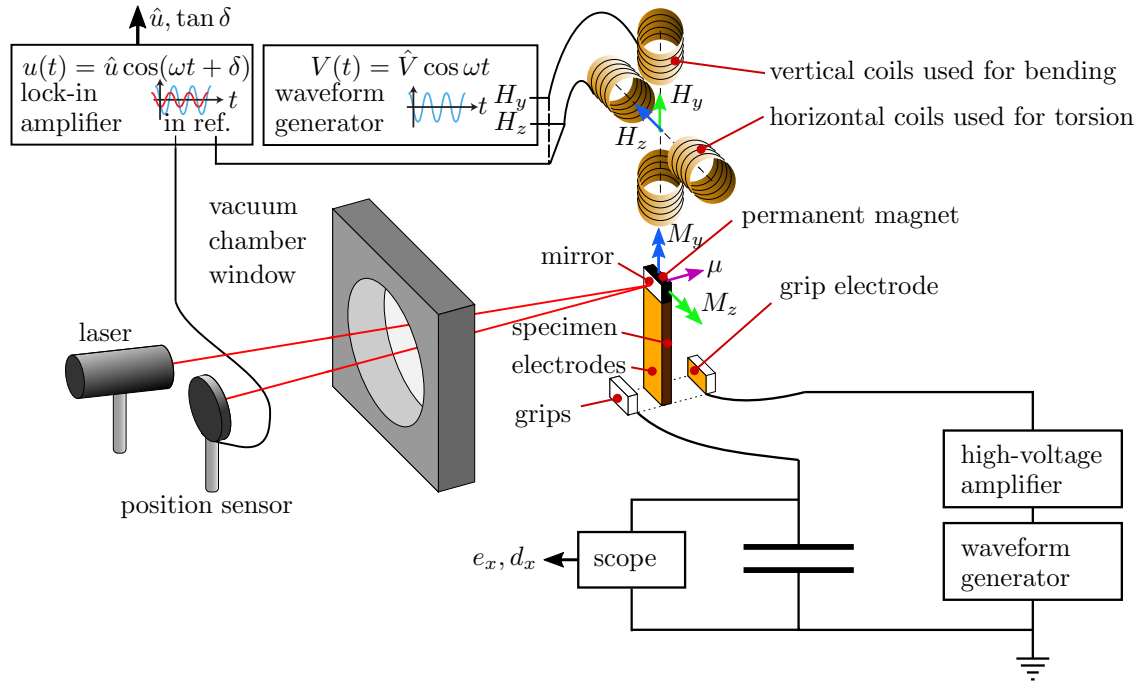


Figure 2.1: Schematic of the apparatus showing the specimen gripped in the center. Above the specimen are the two pairs of Helmholtz coils used for bending and torsion tests as in BVS. The coils are shown in their raised position allowing for the specimen to be positioned. Once the specimen is gripped in place, the coils are lowered over the specimen such that the magnet is located at the intersection of the two coil axes. The specimen and coils are placed inside a vacuum chamber with a window for the laser beam to enter and reflect back to the position sensor outside. In the top-left corner appears the lock-in amplifier set-up connected to the position sensor with the applied voltage to the coils used as the reference signal. The bottom-right corner shows the Sawyer-Tower circuit used.

via radiant heating (as opposed to convective heating used in previous BVS setups, which can effect damping measurements). However, experiments have so far all been performed at room temperature. Electromechanical characterization of PZT at different levels of temperature would nonetheless be a potential future direction of research. The overall size of the setup was designed for testing polycrystalline specimens on the millimeter scale, which is the size of ferroelectrics typically used in structural applications. The remainder of this section explains measurement techniques as well as data acquisition and post processing in more detail.

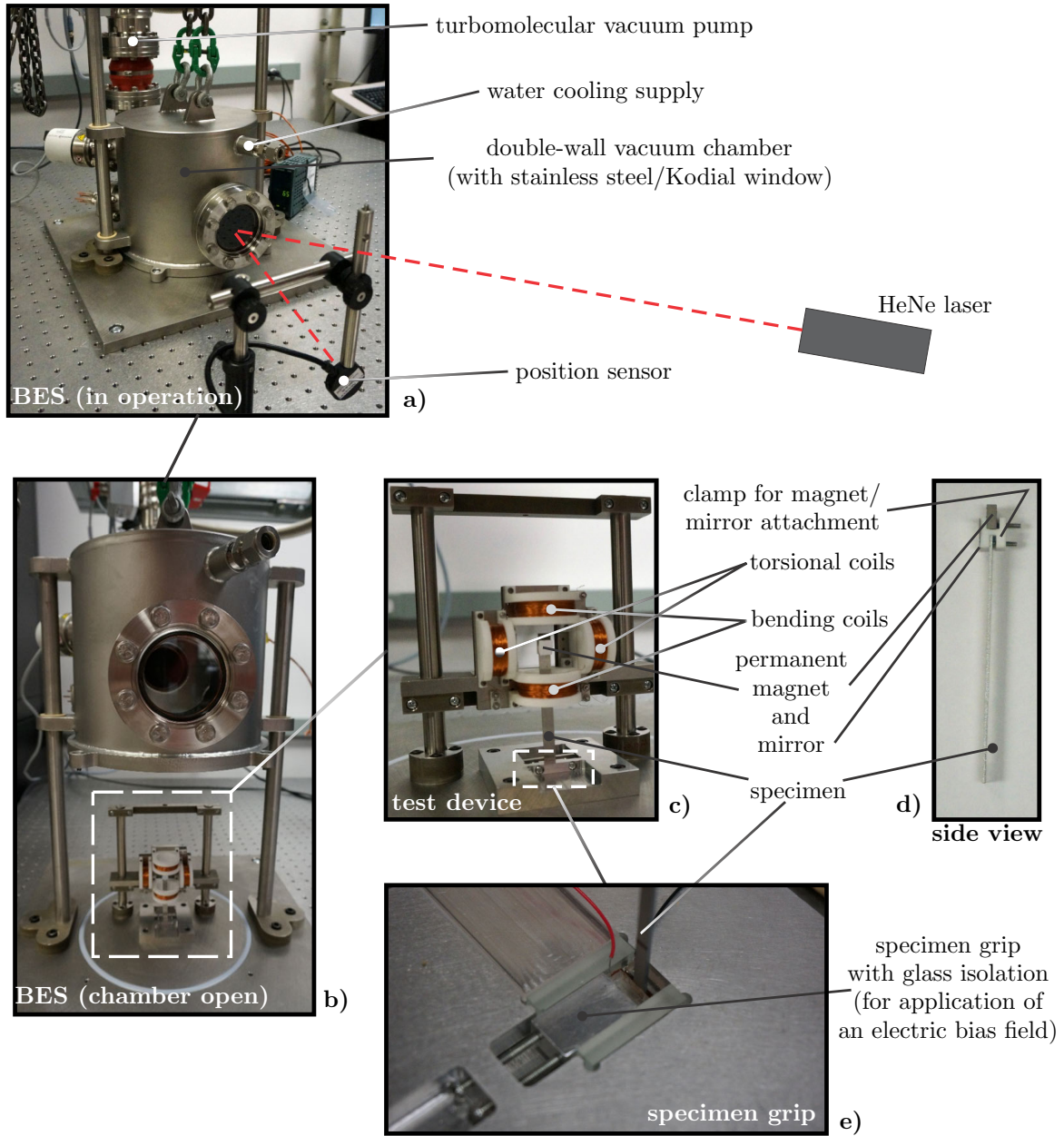


Figure 2.2: Pictures of the apparatus showing (a) the chamber in the operating position and how the laser enters the chamber, is reflected by the mirror, and is detected by the position sensor, (b) the chamber in the raised position, (c) the coils and their support structure, (d) the specimen and attached clamp holding the permanent magnet that applies the electromagnetic force generated by the coils to the specimen's free end, and a mirror used to reflect the incoming laser beam to measure specimen bending/twist, and (e) the specimen grip for the application of an electrical bias.

2.1.1 Force control

Due to the potentially large elastic moduli of the specimens to be tested, the compliance of the apparatus is reduced to a minimum by utilizing contactless techniques. To this end, the apparatus contains two pairs of Helmholtz coils (shown in Fig. 2.2(b,c)) for generating the driving magnetic fields that produce a torque on the specimen (via a neodymium-iron-boron permanent magnet with a maximum pull of 12 N attached to the specimen’s free end). These pairs of coils are used to apply bending (vertical coils) and/or torsional (horizontal coils) moments to the specimen, as shown in Fig. 2.1.

The coils are constructed by winding 32 AWG magnet wire around cylinders made of Macor (3 cm diameter, 8 mm long, 150 turns). The coils are approximately rigidly held in place by a supporting structure as shown in Fig. 2.2(b,c). The coils apply a moment to the magnet attached to the specimen using a clamp also manufactured from Macor. The clamp contains one slot on each side for attaching the specimen and magnet (Fig. 2.2(d)). For accurate thermo-electromechanical testing, the material used for the clamp and the core of the coils must be stable over a large range of temperatures (up to 1000 °C), electrically insulating so as to not short-circuit the specimen electrodes used to apply electric fields, non-magnetic so as to not interfere with the attached magnet and coils, and sufficiently stiff to effectively transfer the force from the magnet to the specimen and to minimize the compliance of the coil supports. Ceramic materials fulfill these criteria and Macor was chosen for the ease with which it can be machined.

Current is passed through the coils by applying a time-varying voltage $V(t)$ using a waveform generator to produce approximately uniform magnetic fields H_z and H_y between each pair of coils. The magnetic moment μ of the permanent magnet is oriented in such a way that the magnetic field from the vertical and horizontal coils applies a bending moment M_z , and a twisting moment M_y , respectively, to the magnet as shown in Fig. 2.1. Bending and/or torsional moments up to 10^{-4} Nm can be applied with the current setup up.

2.1.2 Measuring the deflection and twist of the specimen

The total deflection and/or twist of the specimen is also measured in a contactless way using a laser-detector setup: an incoming laser beam reflects off a mirror attached to the clamp and then returns to a position sensor as shown in Figs. 2.1 and 2.2(a). The laser source (5 mW 633 nm

helium-neon laser from Research Electro-Optics, Boulder, CO, USA) and detector (SpotOn Analog Positioning from Duma Optronics Ltd., Nesher, Israel) are placed outside the vacuum chamber. The laser detector has a resolution of $1\ \mu\text{m}$ and a response time of $60\ \mu\text{s}$. Thus, specimen deflection must be above the detection limit of the sensor and at frequencies well below 16 kHz. Testing at higher frequencies can be accomplished by a detector with faster response time. The chamber has a window made of Kodial (transmission factor above 92 % for the laser wavelength) to allow for the laser beam to be transmitted inside. Thus, the laser spot on the detector moves due to the thermo-electromechanical response of the specimen. In particular, bending and twisting cause the laser spot to move along the vertical and the horizontal axes of the sensor, respectively.

While applying the maximum bending or torsional moment, the maximum and minimum of the Young and shear moduli that can be measured with the current setup is shown in Fig. 2.3 for different specimen geometries. Fig. 2.3(a) shows the range in Young modulus (shaded region) that can be measured versus the specimen thickness for different specimen lengths (from Euler-Bernoulli beam theory). The maximum Young modulus that can be measured corresponds to the smallest resolvable deflection in the laser detector, $1\ \mu\text{m}$ (while applying the maximum bending moment and for the chosen distance between the specimen and detector, 0.4 m). The minimum Young modulus corresponds to the maximum deflection of the specimen for the same applied bending moment before the laser beam moves off the detector ($4500\ \mu\text{m}$). Similarly, the maximum and minimum shear moduli that can be measured are shown in Fig. 2.3(b) versus specimen thickness for different lengths.

2.1.3 Electric field control

To generate an electric field within the specimen, a voltage is applied across its thickness via surface electrodes deposited, for example, by sputtering. To avoid connecting wires directly to the specimen's electrodes, the grips that hold the specimen are covered with copper tape in order to apply a voltage, as shown in Figs. 2.1 and 2.2(e). This prevents the wires from affecting the mechanical response of the specimen and avoids mechanical degradation of the electrical connection when performing experiments over an extended period of time, e.g. during fatigue tests. In order to electrically isolate the grip from the apparatus, the portion of the grip in contact with the specimen that is covered with copper tape is fabricated from glass as shown in Fig. 2.2(e).

Under a large applied electric field, the ferroelectric materials of interest undergo microstructural

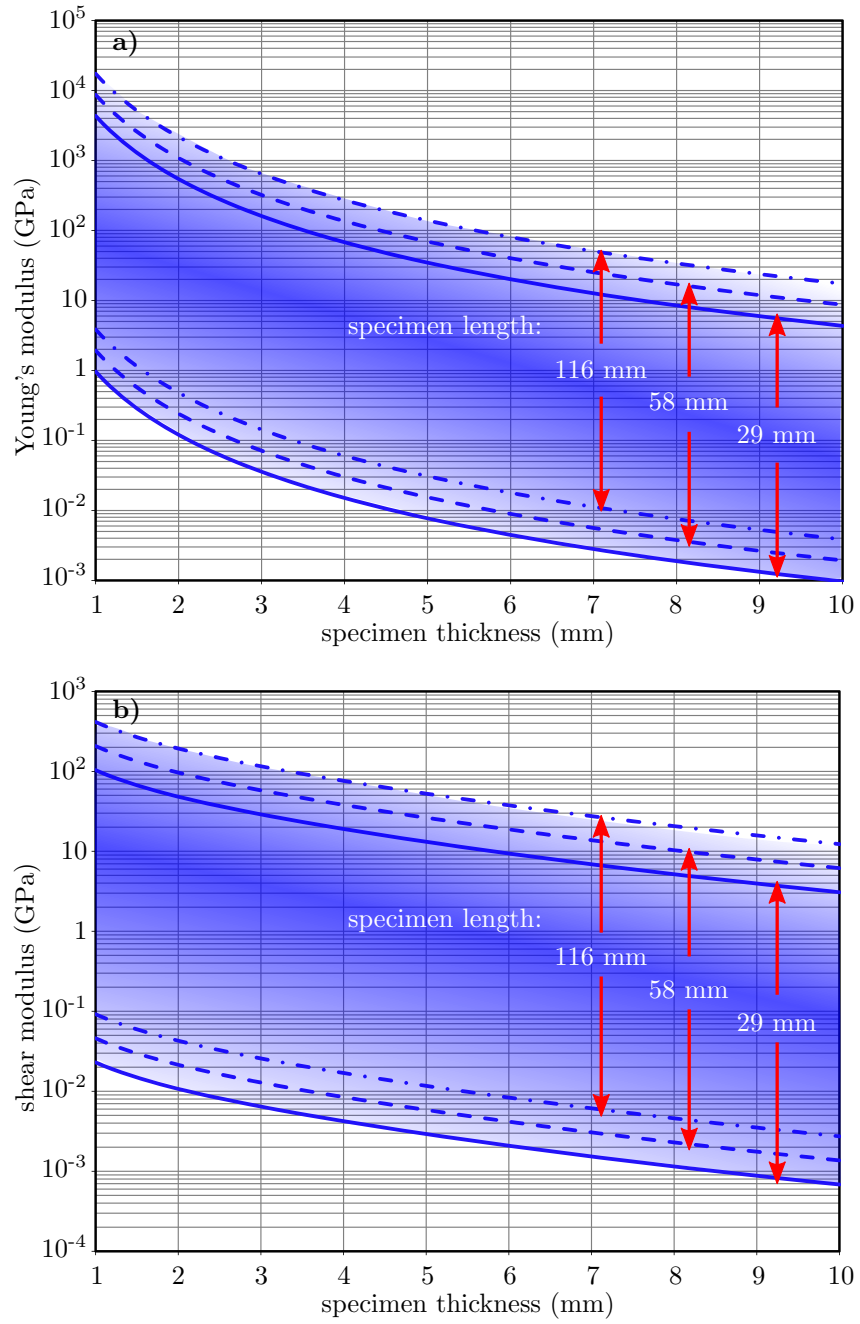


Figure 2.3: Ranges of specimen (a) Young modulus and (b) shear modulus that can be tested using the current BES setup (shaded region) versus specimen thickness. Several regions are shown for different lengths of the specimen.

evolution due to domain switching (i.e. reorientation of polarization through domain wall motion), which causes the non-linear behavior of the electric displacement (Cao and Evans, 1993; Chen and Viehland, 2000; Schmidt, 1981; Zhou et al., 2001). Changes in the macroscopic (average) electric displacement of the specimen are measured using a Sawyer-Tower circuit (Sawyer and Tower, 1930). In the circuit used, it was determined that a 100 μF reference capacitor was suitable for measuring the charge accumulation on the specimen. For the electric loading rates tested (i.e. to induce domain switching in the ferroelectric specimens, 0.01 to 1 Hz, triangle-wave voltages with amplitudes up to ± 2000 V were applied), the impedance of the measuring scope (1 M Ω) was sufficient to minimize charge leakage from the reference capacitor during experiments. An approximate calculation of the influence of the charge leakage on the measured electric displacement is shown in Appendix A. The high-voltage signal is provided by a waveform generator and amplified by a high-voltage amplifier (10/10B-HS from Trek, Lockport, NY, USA), which can apply 0 to ± 10 kV DC and supply 0 to ± 10 mA DC as shown in Fig. 2.4(a).

2.1.4 Vacuum chamber

The apparatus is enclosed by a massive chamber (see Fig. 2.2(a)) with a vacuum seal and wall-internal water cooling to allow for safe operation at high temperatures. The chamber also limits environmental noise such as mechanical and thermal oscillations caused by the surrounding air. In addition, the entire apparatus is placed upon Pneumatic Vibration Isolators (S-2000 series from Newport, Irvine, CA, USA) to reduce vibrations from the building. The overall size of the apparatus is determined by the specimen size to be tested ($1 \times 3 \times 38$ mm³), which itself is chosen so as to have a sufficiently high natural frequency (130 Hz in bending, and 1300 Hz in torsion). In this way, the mechanical loading of the specimen can be chosen well below the specimen's structural resonance frequency.

The vacuum is achieved after two stages of pumping: a primary pump (rotary vane pump from Pfeiffer Vacuum, Asslar, Germany) and a secondary pump (turbomolecular pump from Pfeiffer Vacuum, Asslar, Germany) as shown in Fig. 2.4(b-d). These pumps allow the apparatus to reach a final pressure of 1.9×10^{-6} mbar measured by a pressure gauge (active Pirani/cold cathode transmitter).

Controlling the pressure is essential when applying large voltages across the specimen. Indeed, Paschen's law gives the breakdown voltage between two parallel electrodes in a gas as a function of pressure and gap length (Hourdakis et al., 2006; Paschen, 1889). This is typically modeled using

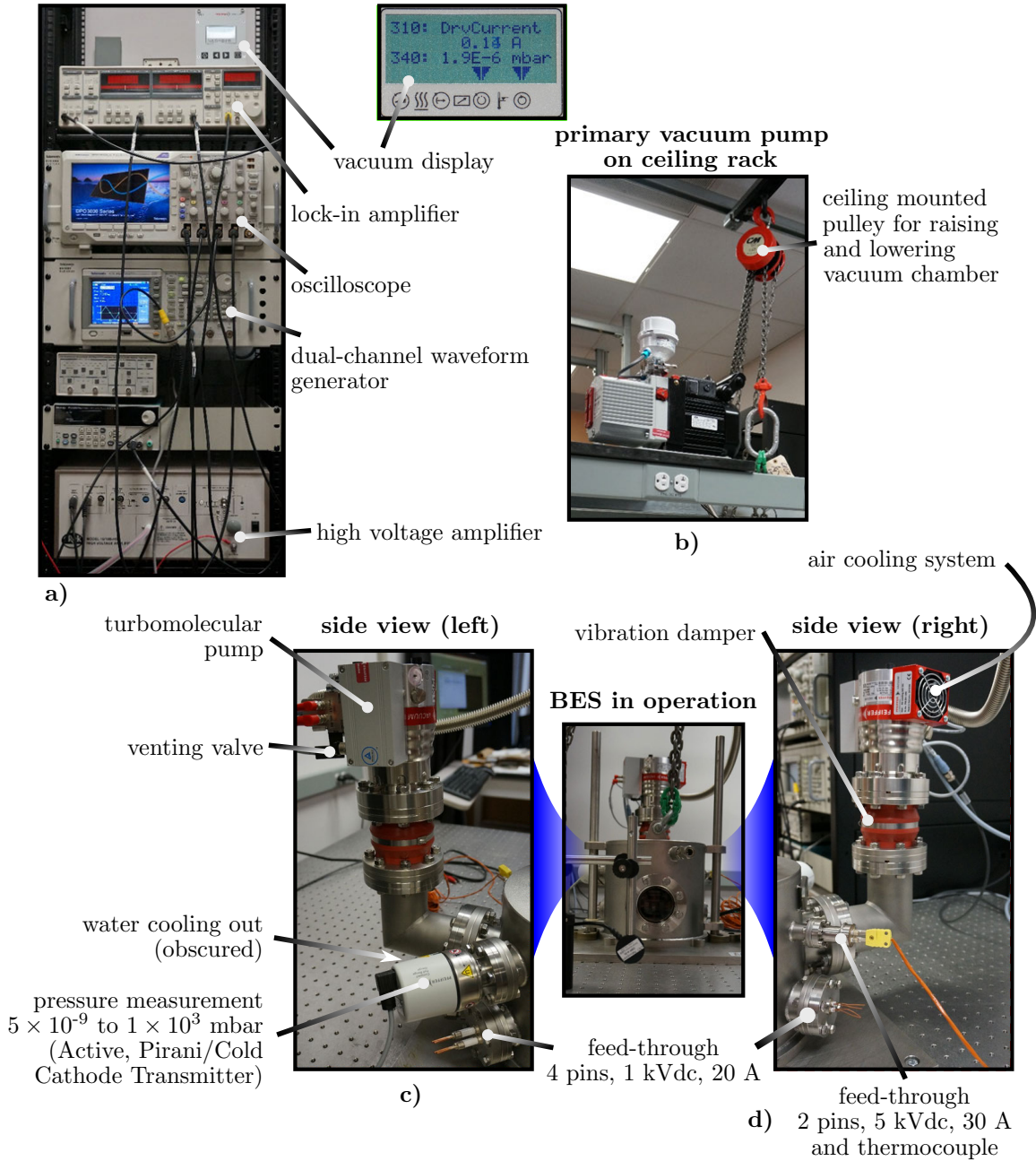


Figure 2.4: Additional pictures of the apparatus: (a) shows the electronics rack containing the various instruments used during an experiment, (b) shows the primary pump sitting above the apparatus on a ceiling rack that is connected to the chamber via a hose, (c) shows the chamber viewed from the left hand side, and (d) shows the chamber viewed from the right hand side.

the equation (see e.g. (Lieberman and Lichtenberg, 2005)),

$$V_B = \frac{A p d}{\ln(p d) + B}, \quad (2.1)$$

where p is the atmospheric pressure, d is the separation distance of the electrodes, and A and B are constants associated with the composition of the gas and the electrode material. This behavior has been extensively studied and characterized due to its importance for electronic packaging. See e.g. (Cobine, 1941) for more information on this phenomenon. Fig. 2.5 contains experimental data showing that the evolution of the breakdown voltage in air is not linear and highly depends on the product of the pressure and the separation distance of the electrodes (approximately 1 mm for the specimens tested). For atmospheric pressure, the voltage required for breakdown between electrodes separated by 1 mm is 3×10^3 V, and at first this decreases as the pressure decreases. However, the voltage required for breakdown starts to increase as the pressure continues to decrease below 7×10^{-3} bar. Thus, with decreasing pressure, the risk of electrical arcing increases (in particular at low voltages), unless the pressure is below the critical value (in which higher voltages are required for arcing). This behavior is due to two competing effects that determine the voltage required for electronic breakdown. On the one hand, decreasing the pressure reduces the likelihood an electron will be scattered by a gas molecule (and thus prevent a conduction path from forming). This gives rise to the breakdown voltage decreasing as the pressure is initially reduced from atmospheric pressure. However, on the other hand, reducing the pressure reduces the number of gas molecules available for ionization, which decreases the likelihood of electric breakdown. This effect dominates at low pressures, and eventually gives rise to an increase in breakdown voltage as the pressure is decreased further. For our purposes, voltages of up to ± 2 kV were used in the experiments. Therefore, from Fig. 2.5, a minimum vacuum pressure of 2×10^{-3} bar must be reached to prevent electrical arcing when using the vacuum chamber. In typical vacuum experiments, pressures of 10^{-4} mbar or less were used.

2.1.5 Temperature control

The vacuum chamber is also used to accurately control the temperature of the specimen. Temperatures of up to 400°C are achieved by radiant heaters placed inside of the chamber, a temperature controller, and a 2.6 kW power supply (0-50 V-DC/0-52 A-DC from Magna Power, Flemington,

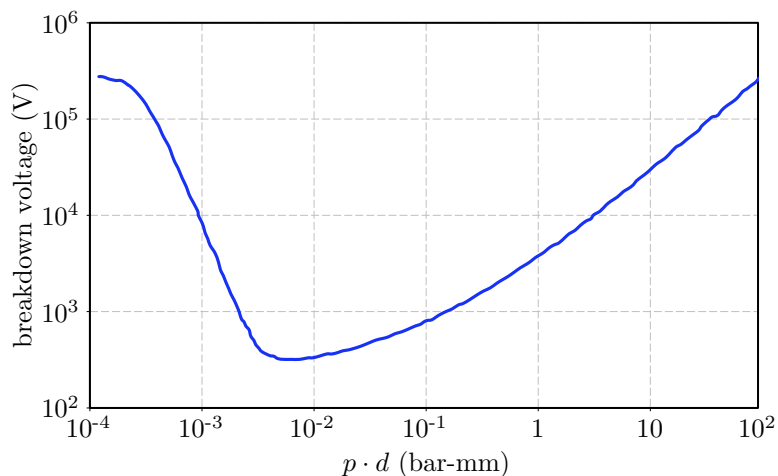


Figure 2.5: Evolution of the breakdown voltage in air as a function of the pressure p times the separation distance of the specimen electrodes d (Picot, 2000).

NJ, USA). The outer walls of the chamber can also be water cooled for safe operation at elevated temperatures.

The radiant heaters can draw a large current and generate a corresponding magnetic field which could give rise to undesired forces on the specimen magnet. Therefore, the chamber was designed to be large enough (0.2 m diameter) to ensure sufficient distance between radiant heaters and the specimen. As a simple check, Ampere’s law can be applied to a disk enclosing and with normal vector along the axis of the heaters (treated as a single infinitely long wire) as shown in Fig. 2.6. The radius of the disk extends from the chamber wall (where the heaters are) to the center of the chamber where the specimen is gripped; thus its radius is $d/2$ where d is the diameter of the chamber. Ampere’s law then gives the magnetic field at the center of the chamber, due to one of the heaters as

$$B_{\text{heat}} = \frac{\mu_0 I}{\pi d}, \quad (2.2)$$

where $I = P/V$ is the current through the heaters and μ_0 is the permeability of air. The maximum power and voltage of the power supply are $P = 2.6$ kW and $V = 50$ Vdc, respectively. The specimen is placed at the center of the chamber, which has a diameter of roughly $d = 0.207$ m. By inserting these values into (2.2) we obtain $B_{\text{heat}}/\mu_0 = 80$ A/m. The magnetic field generated by the Helmholtz coils (treated as ideal, infinitely long solenoids) is $B_{\text{coil}} = \mu_0 n i$. There are 150 turns of wire and the solenoid is 8 mm long, thus $n = 150/0.008$ m⁻¹. Typically, 7.2 V are applied

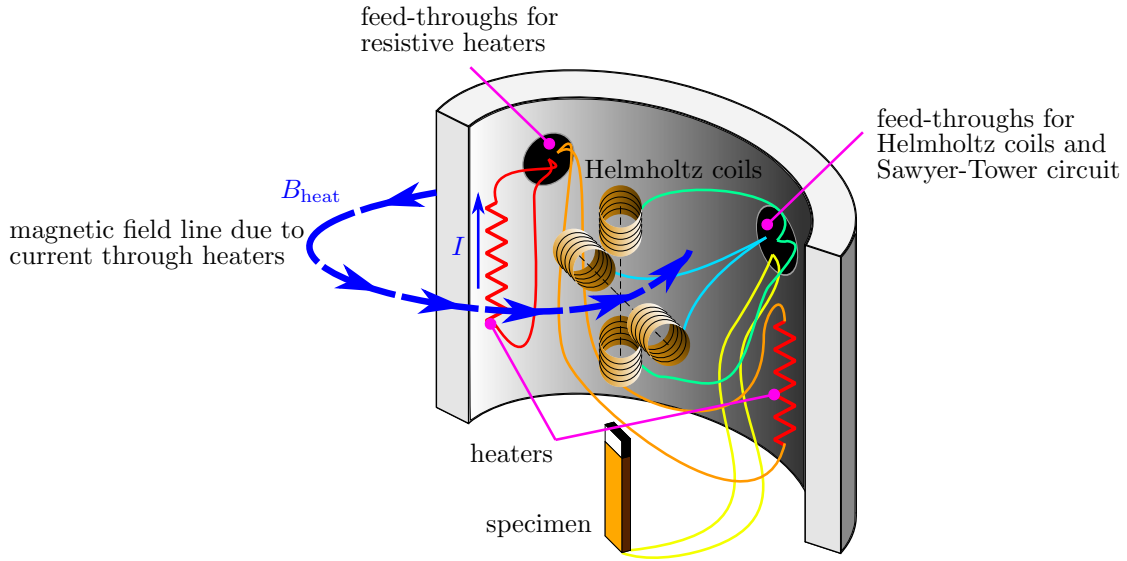


Figure 2.6: Drawing showing the approximate location of the two graphite resistive heaters on opposite sides of the inside wall of the vacuum chamber. Also shown are the approximate locations of cables for powering the Helmholtz coils, specimen surface electrodes, and heaters. It is important that the heater cables use a separate feed-through in the chamber wall on the opposite side to the feed-through for the coils and specimen electrodes to prevent electromagnetic interference due to the large heater current I creating a magnetic field B_{heat} .

and the resistance of the coils is roughly 30Ω , thus $i = 7.2/30 \text{ V}/\Omega$. Therefore, the magnetic field at the position of the specimen as generated by the coils is $B_{\text{coil}}/\mu_0 = 4500 \text{ A/m}$. We see the magnetic field at the specimen due to the Helmholtz coils is two orders of magnitude higher than the magnetic field at the specimen due to the heating elements (i.e. $B_{\text{coil}} \gg B_{\text{heat}}$). Therefore, this effect can indeed be neglected. Furthermore, feed-through cables in the chamber wall for the Helmholtz coils and Sawyer-Tower circuit are placed on the opposite side of those for the radiant heaters as shown in Fig. 2.6, thus reducing interference between electrical cables.

In summary, this method improves upon currently available BVS techniques by utilizing a radiative heating approach instead of heating by convection (which uses airflow). This enhances the measurement accuracy of the specimen's dynamic stiffness and damping by reducing measurement artifacts caused by the airflow, especially at high temperatures. The addition of the Sawyer-Tower circuit also adds the capability (beyond current devices) to apply electric fields and measure the electric displacement of the specimens – an important addition that can be used to fully characterize the thermo-electromechanical response of ferroelectrics and other materials whose properties can

be tuned by electric fields. BES can also test materials over a much larger range of mechanical loading frequencies than DMA; in the current configuration, frequencies ranging from 1 Hz to 4 kHz can be tested directly. In general, the main limitations on the maximum frequency are due to the waveform generator (max. 1 MHz), the lock-in amplifier bandwidth (max. 100 kHz), the laser detector (max. 16 kHz), and the impedance of the coils (max. 4 kHz). The latter can reduce the applied moment and decrease the signal-to-noise ratio at high frequencies. However, by using lower impedance coils or a laser detector with a faster response, higher-frequency experiments can be performed with this method. The lower limit on the frequency is due to temperature variations and low-frequency noise. The apparatus is placed on an air vibration isolation table, which reduces high-frequency noise but is susceptible to low frequency oscillations. For the current setup the most accurate measurements were obtained above 1 Hz. To perform low-frequency tests, the isolation table should be deflated or the apparatus placed on a more rigid support. However, all experimental results reported in this article were obtained from frequencies not less than 25 Hz, thus the influence of low-frequency noise was not significant.

2.2 Characterizing the material's response

The following section explains the details of using measurements obtained from the BES setup to compute the material properties. In particular, the data is used to infer the viscoelastic properties (i.e. dynamic Young and shear moduli and their associated loss tangents) as well as the ferroelectric properties (i.e. the electric displacement and thereby the state of polarization in a ferroelectric material).

2.2.1 Measuring viscoelastic properties

A voltage, $V(t) = \hat{V} \cos(\omega t)$ with frequency ω , is applied to the Helmholtz coils, which results in a current, $i(t) = \hat{i} \cos(\omega t + \phi)$. In a typical experiment, \hat{V} ranges from 2.0 to 7.2 Vpp (peak-to-peak voltage). The position of the laser beam in the detector, $u(t) = \hat{u} \cos(\omega t + \delta + \phi)$, is input to a lock-in amplifier (SR830 from Stanford Research Systems, Sunnyvale, CA, USA) using the applied voltage on the coils $V(t)$ as the reference signal as shown in Figs. 2.1 and 2.4(a). The lock-in amplifier gives a high-accuracy measurement of the laser spot movement at the same frequency as the reference signal, which has a total phase shift of $\delta + \phi$, where δ is due to the viscoelasticity of the specimen

and ϕ is the phase shift associated with the frequency response of the coils. Note that the vertical or horizontal position of the laser is selected when performing bending or torsion tests, respectively. Noise present in the signal at different frequencies is filtered out by the lock-in amplifier. The cutoff frequency f_{cutoff} for the low-pass filter applied to the output of the phase-sensitive detector in the lock-in amplifier was selected to be 5.3 Hz, which was determined to be sufficiently low to reduce noise in the measurements but sufficiently high so that the response of the lock-in is faster than any changes in the material response. Nominally, the cutoff frequency corresponded to a time constant τ setting of 30 ms on the lock-in amplifier, i.e. $\tau = 1/(2\pi f_{\text{cutoff}})$. See Appendix B for a more detailed analysis of the noise filtered by the lock-in amplifier. However, for different frequencies of the applied electric field, a different time constant was used (see discussion in Section 3.4.3).

For experiments performed away from structural resonance, the expression for static deflection/twist at the end of the bar still applies for the dynamic case and the correspondence principle can be applied with the elastic moduli replaced by their viscoelastic (complex-valued) ones (Lakes, 1998). When the mechanical frequencies approach the structural resonance frequencies, inertia effects become important and the static solution and the corresponding viscoelastic form obtained by the correspondence principle no longer apply. In this case the following formulation should instead be interpreted as the *structural* (i.e. geometry-dependent) response of the specimen. We proceed to utilize the static solutions for the Euler-Bernoulli beam and uniform torsion problems with the understanding that the solutions only give the material properties when experiments are performed away from resonance, otherwise they result in the structural response.

For small deformations, the deflection and total twist angles at the end of the specimen are

$$\theta_z = \frac{M_z L}{EI_z}, \quad \theta_y = \frac{M_y L}{GJ_y}, \quad (2.3)$$

respectively, where M_z is the bending moment, L is the length of the specimen, E is the static Young modulus, I_z is the bending moment of inertia along the z -axis with $I_z = bh^3/12$ (b is the width and h is the thickness) for rectangular cross sections, M_y is the torsional moment, G is the static shear modulus, and J_y is the torsional moment of inertia along the y -axis (for rectangular cross sections $J_y = bh(b^2 + h^2)/12$). Note that warping of the specimen's cross section during torsion is neglected. For a magnet with magnetic moment μ perpendicular to the axes of the coils, the total applied bending and torsional moments on the specimen are $M_z = \mu H_y$ and $M_y = \mu H_z$,

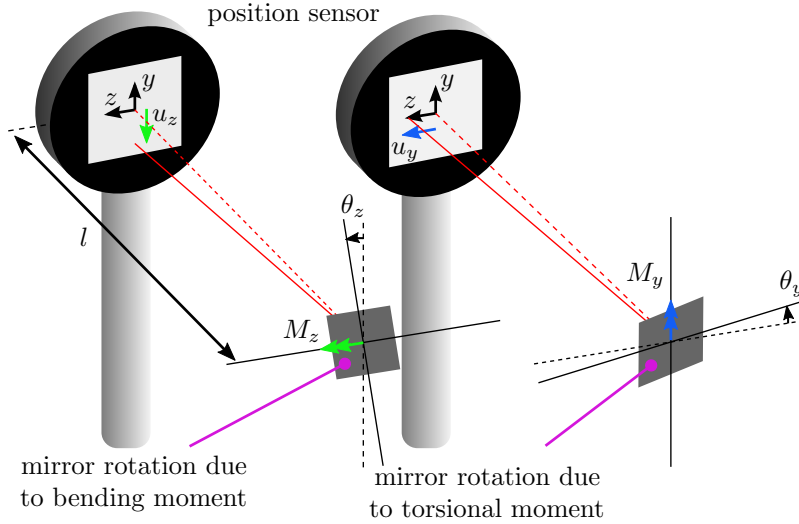


Figure 2.7: Illustration of the laser spot movement on the detector with components u_z and u_y due to applied bending and torsional moments M_z and M_y , respectively.

respectively, where H_y and H_z are the magnetic fields generated by the vertical and horizontal coils, respectively, as shown in Fig. 2.1. In a typical experiment, moments ranging from 10^{-5} to 10^{-4} Nm are applied. Assuming an ideal coil, the magnetic fields at the position of the magnet are $H_y = \alpha_z n_z i_z$ and $H_z = \alpha_y n_y i_y$, where n_i is the number of turns per unit length, i_i is the current, and α_i is a geometric factor for the deviation of the magnetic field from the idealized infinitely long solenoid and a subscript $i = z$ or $i = y$ corresponds to the respective values for the vertical and horizontal coils. Altogether, the total bending and torsional moments, respectively, can be expressed as

$$M_z = \mu \alpha_z n_z i_z, \quad M_y = \mu \alpha_y n_y i_y. \quad (2.4)$$

The deflection angle and twist θ_z and θ_y are related to the directional changes in position of the laser beam, u_z and u_y , in the detector by $\tan \theta_z = u_z/l$ and $\tan \theta_y = u_y/l$, respectively, where l is the distance between the specimen and the detector as shown in Fig. 2.7. For small deflections and twist angles, this is approximated by $\theta_i \approx u_i/l$. Combining this expression with (2.3) and (2.4) results in the specimen's Young and shear moduli,

$$E = \frac{\mu \alpha_z n_z i_z l}{u_z I_z} \equiv C_z \frac{i_z}{u_z}, \quad G = \frac{\mu \alpha_y n_y i_y l}{u_y J_y} \equiv C_y \frac{i_y}{u_y}, \quad (2.5)$$

respectively, where the constants C_z and C_y depend on parameters associated with the apparatus and geometry of the specimen, which were held constant for the experiments. For the dynamic case, we use the correspondence principle, so that (2.5) still applies but with the moduli replaced by their complex-valued counterparts, and the currents and displacements by their time-harmonic amplitudes, i.e.

$$E^* = C_z \frac{\hat{i}_z}{\hat{u}_z}, \quad G^* = C_y \frac{\hat{i}_y}{\hat{u}_y}. \quad (2.6)$$

Recall that the above relation holds for experiments performed away from resonance, and near resonance the moduli are the structural ones. For the experiments shown later, we choose to report the relative dynamic Young and shear moduli,

$$\frac{|E|}{|E^0|} = \frac{\hat{u}_z^0}{\hat{u}_z}, \quad \frac{|G|}{|G^0|} = \frac{\hat{u}_y^0}{\hat{u}_y}, \quad (2.7)$$

respectively, where superscript 0 refers to the case with no applied electric field, and \hat{u}_z and \hat{u}_y are the corresponding amplitudes of the laser spot motion on the position sensor (measured by the lock-in amplifier). The loss tangents of the complex Young and shear moduli follow from (2.6)

$$\tan \delta_E = \tan \left[\arg \left(\frac{\hat{i}_z}{\hat{u}_z} \right) \right], \quad \tan \delta_G = \tan \left[\arg \left(\frac{\hat{i}_y}{\hat{u}_y} \right) \right]. \quad (2.8)$$

In previous BVS setups, (2.8) is used where the applied current is measured as the voltage drop across a resistor in series with the coils (Lakes, 1998). As mentioned previously, in the BES setup the applied voltage to the coils is used as the reference signal for the lock-in amplifier instead of the current. In this way, a resistor in series with the coils is not needed, which allows for higher current through the coils (increasing the signal to noise ratio) and simplifies the electronic circuit. However, the phase shift ϕ introduced by the coils must be accounted for in post processing the phase signal output by the lock-in amplifier. Thus, when using the coil voltage as the reference signal, (2.8) becomes

$$\tan \delta_E = \tan \left[\arg \left(\frac{\hat{V}_z}{\hat{u}_z} \right) - \phi_z \right], \quad \tan \delta_G = \tan \left[\arg \left(\frac{\hat{V}_y}{\hat{u}_y} \right) - \phi_y \right], \quad (2.9)$$

where \hat{V}_z and \hat{V}_y are the amplitudes of the applied voltages to the vertical and horizontal coils, respectively, and ϕ_z and ϕ_y are the respective phase shifts between the voltage and resulting current.

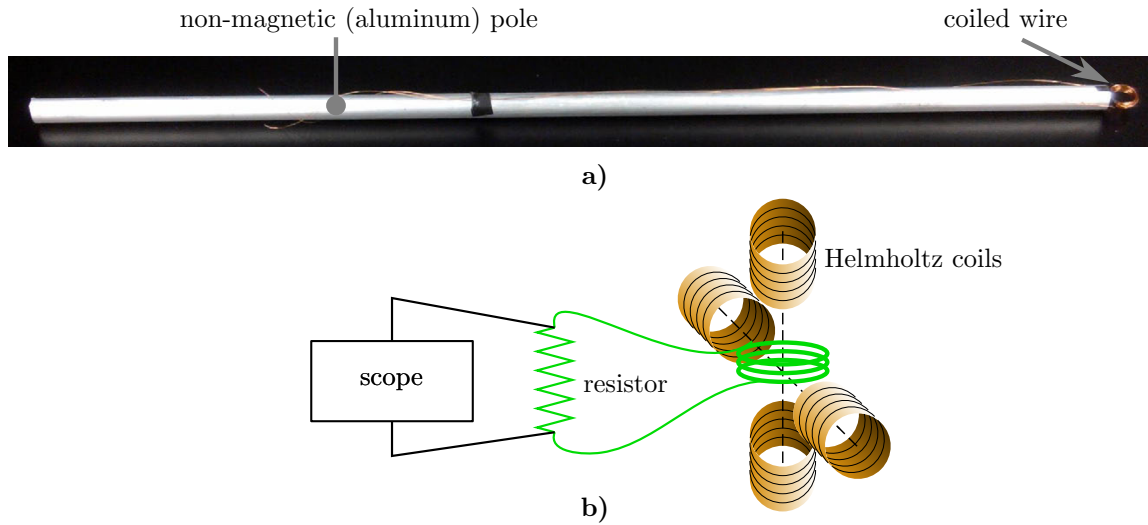


Figure 2.8: (a) Picture of the magnetometer made by coiling magnet wire and attaching it to the end of a pole so that it can be inserted between the Helmholtz coils. The diameter of the coiled wire was approximately 12 mm. (b) Illustrates how the magnetometer is placed in the Helmholtz coils and the current through it is measured via a resistor.

2.2.2 Frequency response of the Helmholtz coils

To determine the specimen's loss tangent from the lock-in amplifier output using (2.9), the phase shifts ϕ_z and ϕ_y introduced by the coils were measured a priori. This phase difference was measured by inserting a small solenoid (used as a magnetometer) collinear with either the horizontal or vertical coils, see Fig. 2.8. The induced current in the small solenoid, due to the coils, was measured via a resistor in series with the small solenoid. The frequency of the cyclically changing voltage in the coils is small compared to the speed of light, which means the phase of the measured current is the same as the magnetic field. Thus, the tangent of the phase difference between the applied voltage to the Helmholtz coils and the resulting current (in phase with the magnetic field) was measured for different frequencies and is shown in Fig. 2.9(a) for the vertical (bending) and horizontal (torsion) coils.

To quantify the frequency response of the coils, consider an electronic circuit consisting of a voltage source with frequency ω , coils modeled as an inductor with inductance L , and a resistor R to account for the wire resistance. This is an RL circuit where the tangent of the phase difference

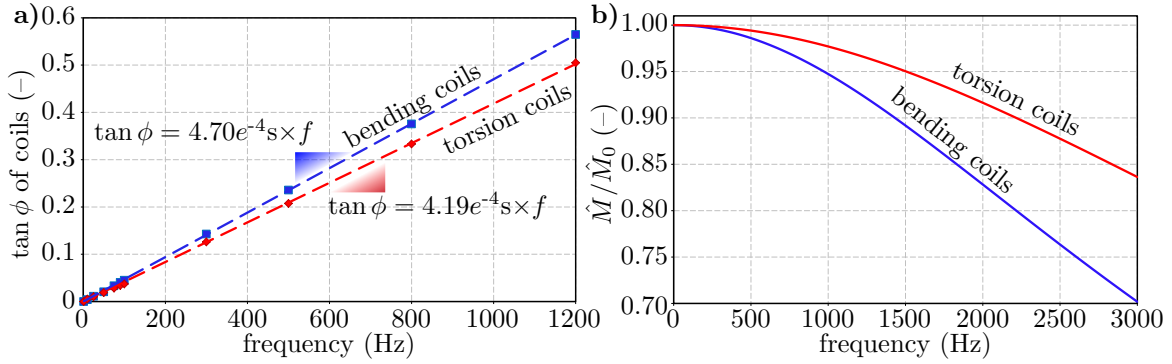


Figure 2.9: (a) Variation of the tangent of the phase between the applied voltage and magnetic field of the Helmholtz coils ($\tan \phi$) with the frequency of the applied voltage to the bending and torsion coils. (b) The change in the amplitude of the applied moment \hat{M} relative to the amplitude at 0 Hz (\hat{M}_0) versus the frequency of the applied voltage to the bending and torsion coils.

between the voltage and current and the impedance are given by

$$\tan \phi = \omega L/R, \quad Z = \sqrt{R^2 + (\omega L)^2}, \quad (2.10)$$

respectively, where the current amplitude through the coils is then given by $\hat{i} = \hat{V}/Z$. The resistance of the wires R for the bending and torsion coils was measured to be 25.8Ω and 22.4Ω , respectively. The inductance L can then be found from equating $\tan \phi$ in (2.10) to the slopes of the trend lines in Fig. 2.9(a). It was found that the inductances of the vertical and horizontal coils were 1.4 and 0.8 mH, respectively. Using the inductance obtained, ϕ can be computed for the frequency being used in the experiment. The measured inductances of the coils can also be compared to the theoretical result obtained by using the standard formula for a cylindrical air-core solenoid, $L = \mu_0 K n^2 A/l$, where $\mu_0 = 4\pi \times 10^{-7}$ H/m is the permeability of free space, the Nagaoka coefficient K (Nagaoka, 1909) is a correcting factor for the non-ideal geometry of the coils (typically 1 for slender solenoids), n is the number of turns, A is the cross-sectional area of each coil, and l is the length of each coil. For the coils used, this gives $K = 0.8821$ and $K = 0.9183$ for the vertical and horizontal coils, respectively. For the maximum frequency used in experiments (3 to 4 kHz) the phase difference of the coils can be as high as $\tan \phi = 1.57$. Thus, it is important to correct for this phase shift when using the coil voltage as the reference for the lock-in amplifier.

From (2.10), the impedance of the coils is also frequency dependent. The increase in the

impedance of the coils with increasing frequency causes the amplitude of the applied moment on the specimen to decrease with increasing frequency (for a constant amplitude voltage on the coils). As shown in (2.4), the applied moment is related to the current in the coils via $M = \mu \alpha n i$. Using the frequency-dependent impedance of the coils, this becomes, $\hat{M} = \mu \alpha n \hat{V} / Z(\omega)$, which is plotted in Fig. 2.9(b) after normalizing by \hat{M}_0 , the moment at 0 Hz. For the frequencies used, the applied moment decreases by up to 30 %. However, the applied moments are small such that the response of the material is in the linear viscoelastic regime. Thus, the variation of the applied moment does not effect the viscoelastic properties measured, a result which will be confirmed in Section 3.4.4.

Although results presented here were all from tests performed at room temperature, one must carefully correct for the phase shift due to the coil impedance when varying the temperature. Therefore, the coil impedance should be pre-determined for the temperature(s) of interest. For varying temperature, a more elegant and more accurate approach is to use the current in the coils as the reference for the lock-in as described in (Lakes, 1998) for BVS.

2.2.3 Approximate methods for extracting the material properties near resonance

The above methods yield the structural response of the specimen from measurements taken during an experiment. To find the material response, it is best to perform the experiment away from resonance so that inertial effects are small and the static solution for the beam deflection/twist and the viscoelastic form obtained by the correspondence principle apply. For the specimens tested, this applied for frequencies below 130 Hz in bending and 1300 Hz in torsion. When mechanical loading frequencies approach the resonance frequency, a different geometry specimen can be used with a different resonance frequency. As an alternative, an approximate correction can be applied to the structural measurements near resonance to obtain the material properties.

The bending problem can be approximated by a spring-mass-dashpot system subjected to an external force F as shown in Fig. 2.10, where the linear spring stiffness k and velocity proportional damping c represent the apparent stiffness and damping of the cantilever beam. The total mass of the attached magnet, mirror, and clamp corresponds to m . Force balance of the spring-mass-dashpot system in terms of the deflection w yields

$$k w + c \dot{w} + m \ddot{w} = F. \quad (2.11)$$

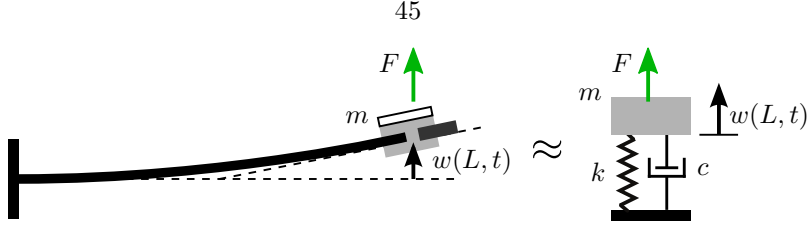


Figure 2.10: A cantilevered beam with tip deflection $w(L, t)$ due to an applied force F and with attached mass m is approximated by a spring-mass-dashpot system with stiffness k , mass m , and damping c .

Assuming a harmonic solution $w = \hat{w} e^{i\omega t}$ due to a time-varying force $F = \hat{F} e^{i\omega t}$, the complex modulus is

$$k^* = \hat{F}/\hat{w} = k - m\omega^2 + i\omega c. \quad (2.12)$$

Thus, taking the absolute value and tangent of the argument of (2.12) yields the structural dynamic stiffness and loss tangent as

$$|k^*| = k \sqrt{\left[1 - \left(\frac{\omega}{\omega_0}\right)^2\right]^2 + \left(\frac{\omega c}{k}\right)^2}, \quad \tan \delta_k = \frac{\omega c/k}{1 - (\omega/\omega_0)^2}, \quad (2.13)$$

where $\omega_0 = \sqrt{k/m}$ is the resonance frequency. The structural loss tangent ($\tan \delta_k$) becomes the material loss tangent ($\tan \delta$) when the frequency is well below the resonance frequency (i.e. $\omega/\omega_0 \ll 1$) and inertial effects are small, which yields $\tan \delta = \omega c/k$. Using this result, equations (2.13) can be solved for the material properties k and $\tan \delta$ in terms of the structural properties $|k^*|$ and $\tan \delta_k$, which gives

$$k = \frac{|k^*|}{[1 - (\omega/\omega_0)^2] \sqrt{1 + (\tan \delta_k)^2}}, \quad \tan \delta = \tan \delta_k [1 - (\omega/\omega_0)^2]. \quad (2.14)$$

Finally, the spring stiffness follows from the linear elastic beam solution (i.e. $k \propto E$), and normalization as in (2.7) yields:

$$\frac{E^0(\omega \rightarrow 0)}{E(\omega)} = \frac{|E^0|(\omega \rightarrow 0)}{|E|(\omega)} \sqrt{\frac{1 + [\tan \delta_E(\omega)]^2}{1 + [\tan \delta_E(\omega \rightarrow 0)]^2}} [1 - (\omega/\omega_0)^2], \quad (2.15)$$

where $|E^0|(\omega \rightarrow 0)$ and $\tan \delta_E(\omega \rightarrow 0)$ are taken at 25 Hz where inertial effects are small (i.e. $\omega/\omega_0 \ll 1$). The ratio $|E^0|(\omega \rightarrow 0)/|E|(\omega)$ is computed from (2.7). The material loss tangent is

then simply

$$\tan \delta_{E\text{mat}} = \tan \delta_E [1 - (\omega/\omega_0)^2]. \quad (2.16)$$

The same result for the torsion case can be derived where the problem is approximated by a torsional spring with damping and a mass with rotational inertia. Then, from linear elasticity, k is replaced by the torsional stiffness of the beam and normalized to obtain

$$\begin{aligned} \frac{G^0(\omega \rightarrow 0)}{G(\omega)} &= \frac{|G^0|(\omega \rightarrow 0)}{|G|(\omega)} \sqrt{\frac{1 + [\tan \delta_G(\omega)]^2}{1 + [\tan \delta_G(\omega \rightarrow 0)]^2}} [1 - (\omega/\omega_0)^2], \\ \tan \delta_{G\text{mat}} &= \tan \delta_G [1 - (\omega/\omega_0)^2]. \end{aligned} \quad (2.17)$$

In a similar manner to the bending case, $|G^0|(\omega \rightarrow 0)$ and $\tan \delta_G(\omega \rightarrow 0)$ are taken to be at 25 Hz where inertial effects are small, and $|G^0|(\omega \rightarrow 0)/|G|(\omega)$ is obtained from (2.7).

The accuracy of this approach can be seen by applying the corrections to the solution of a dynamic cantilevered Euler-Bernoulli beam (using expressions derived in Appendix C) with known constant compliance and loss tangent. The correction derived in equations (2.15) and (2.16) are applied to the predicted structural dynamic response of the Euler-Bernoulli beam given by (C.6). Both the structural and approximated material responses are shown together in Fig. 2.11. In addition, Fig. 2.11 shows the constant material (static) compliance and loss tangent. For both the compliance and loss tangent, Fig. 2.11 shows that while the structural response increases greatly near the first resonance, the approximate material response remains close to the constant static value. (Although the approximation increasingly deviates from the correct material response as the first resonance frequency is approached and surpassed.) Nonetheless, the approximated response still yields values for the compliance and loss tangent that are closer to the true material response up to the first resonance frequency. It should be noted that, in practice, pure bending or torsion is not achieved, due to small misalignments (as discussed in Section 3.4.2). Thus, when applying the corrections in bending or torsion, the approximation may not hold at particular frequencies due to resonance modes that are not accounted for by our analysis, which only considers the case of pure bending and pure torsion.

Another possible way to find the material response is to assume that the response of the specimen

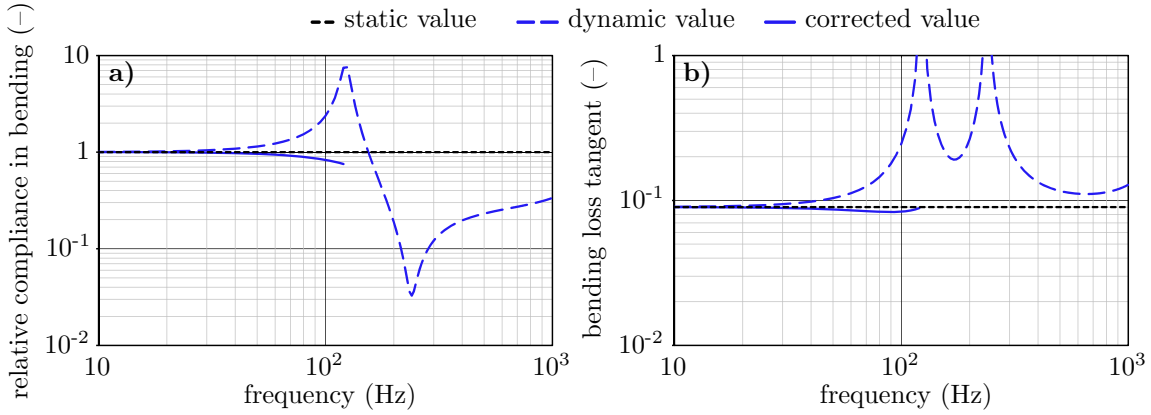


Figure 2.11: Comparison of the theoretical dynamic (a) compliance and (b) loss tangent (long dashed line) with their corrected response (solid line) using (2.15) and (2.16), respectively, for an Euler-Bernoulli beam. The parameters used are given in Tab. 3.2. The material compliance and loss tangent were taken to be constant and are shown by the short dashed line.

is the same as an Euler-Bernoulli beam with complex moduli, i.e. substituting

$$E \rightarrow E(1 + i \tan \delta_{E\text{mat}}), \quad G \rightarrow G(1 + i \tan \delta_{G\text{mat}}) \quad (2.18)$$

into the solutions derived in Appendix C for the dynamic Euler-Bernoulli beam and torsion problem. Thus, the dynamic Young modulus and loss tangent become

$$|E^*| = \left| \frac{\hat{M}_z}{\hat{\theta}_z} \right|, \quad \tan \delta_E = \frac{\text{Im} \left(\frac{\hat{M}_z}{\hat{\theta}_z} \right)}{\text{Re} \left(\frac{\hat{M}_z}{\hat{\theta}_z} \right)}. \quad (2.19)$$

Equating the left-hand-sides of (2.19) with the experimental measurements results in two equations for the two unknown material properties E and $\tan \delta_{E\text{mat}}$. Similarly for the torsion case, the dynamic shear modulus and loss tangent become,

$$|G^*| = \left| \frac{\hat{M}_y}{\hat{\theta}_y} \right|, \quad \tan \delta_G = \frac{\text{Im} \left(\frac{\hat{M}_y}{\hat{\theta}_y} \right)}{\text{Re} \left(\frac{\hat{M}_y}{\hat{\theta}_y} \right)}. \quad (2.20)$$

Comparing (2.20) with experimental measurements also yields two equations for the two unknown material properties G and $\tan \delta_{G\text{mat}}$. However the assumption that the material behaves like an Euler-Bernoulli beam may not be accurate, especially near higher resonances where the approxima-

tion of the clamp as a point mass is not exact. One could also, in principle, perform a finite element analysis, which better captures the geometry of the specimen, to find the appropriate material parameters that best reproduce the experimental measurements. In addition, resonance methods as described by Lakes (1998) can be used to obtain a material's loss tangent at resonance. However, such an approach is complicated by the fact that (as observed in the experiments of Chapter 3) the resonance frequency of the material changes due to the application of an electric field, which makes it difficult to define a resonance peak in the structural loss tangent.

2.2.4 Measuring electric displacement and electric field

The electrical response of the material is characterized by the specimen's macroscopic (average) electric displacement as shown in Fig. 2.12. The electric displacement is measured by a Sawyer-Tower circuit, as shown in Fig. 2.1. Changes in the electric displacement in the material (due to domain switching and electric field-dipole interaction) cause a charge Q to accumulate on the specimen's surface electrodes. The same charge Q accumulates on the reference capacitor and is reflected in its voltage $V_{\text{cap}} = Q/C$ (here an electrolytic capacitor was used with capacitance $C = 100 \mu\text{F}$). The macroscopic electric displacement through the specimen thickness d_x is then given by the total charge on the specimen divided by the surface area of the electrodes, i.e.

$$d_x = \frac{C V_{\text{cap}}}{b L}. \quad (2.21)$$

When applying cyclic electric fields, dielectric loss of the capacitor can lead to hysteresis in the electric displacement. However, for characterizing the electromechanical response of ferroelectrics, such capacitors are commonly used at frequencies of 1 Hz or less (Zhou et al., 2001) (which is the case here as well) and thus their dielectric loss is not significant (Zhou, 2003).

The high-voltage amplifier applies a known voltage V_{elec} to the surface electrodes of the specimen. The applied electric field e_x through the specimen thickness h is

$$e_x = \frac{V_{\text{elec}}}{h}. \quad (2.22)$$

The aspect ratio of the specimen's surface area to thickness is assumed to be sufficiently large so that variations in the electric field near the edges are negligible. Moreover, the capacitance of the

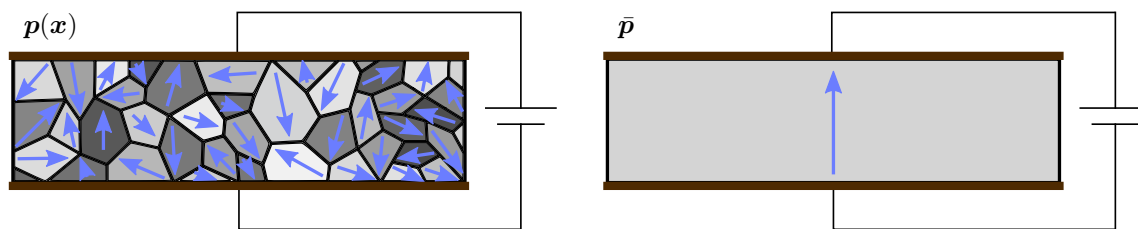


Figure 2.12: Illustration of how a polycrystalline specimen in a Sawyer-Tower circuit has spatially-varying polarization $\mathbf{p}(\mathbf{x})$ which gives rise to an average polarization $\bar{\mathbf{p}}$ that is reflected in the charge measured on the surface electrodes.

specimen is significantly smaller than the reference capacitor so that the voltage applied to the specimen is nearly the same as that applied by the high-voltage amplifier (i.e. the voltage drop across the reference capacitor is negligible). For a typical experiment, the high-voltage amplifier applied 2 kV while the voltage on the reference capacitor is 1 V. Therefore, the presence of the capacitor reduces the actual applied voltage to the specimen by 0.05 %.

2.3 Sources of error

Before performing experiments, various possible sources of error in the experimental setup were analyzed to ensure that their influence on the measurements were negligible (at least under the nominal conditions). In particular, the effects of laser misalignment, parasitic damping due to support loss, and electromagnetic coupling are explained and analyzed in the following sections.

2.3.1 Resolution of the laser detector

Due to the resolution of the sensor in the laser detector, there is an uncertainty in the position of the laser spot of $1 \mu\text{m}$. As the position of the laser spot is used in determining the specimen's Young and shear moduli, the resolution of the detector causes some uncertainty in their measurement. This uncertainty was quantified by measuring the deflection of a PZT specimen while applying the maximum static bending moment, 10^{-4} Nm . For a specimen with the same geometries tested (given in Tab. 3.2), the Young modulus was computed assuming an Euler-Bernoulli beam (i.e., using (2.3)) based on the laser beam position in the detector, which was $70 \mu\text{m}$ relative to its undeformed position. The Young modulus from the Euler-Bernoulli beam changed by 1 GPa upon

modifying the laser position by $1 \mu\text{m}$, the sensor resolution. Therefore, the uncertainty in the Young modulus measured for the PZT specimens is $\pm 1 \text{ GPa}$. The Young modulus (in the loading direction) reported by the supplier in Tab. 3.1 is 66 GPa . Thus, the uncertainty in the Young modulus is less than 2%. Using the same approach, the uncertainty for the shear modulus was also less than 2%.

2.3.2 Effect of laser misalignment

The strain due to polarization changes (which gives rise to the well-known butterfly curve as shown in e.g. (Zhou et al., 2001)) causes specimens to bend/twist one way or the other during a cycle of the electric field. That is, the laser spot on the detector oscillates about a mean value (due to the applied dynamic mechanical load), but this mean value changes slowly during the experiment due to the spontaneous strain in the material in response to the applied electric bias, whose frequency is much lower than the mechanical loading frequency. For the ferroelectrics tested, the spontaneous strain was never sufficient to cause the laser spot to leave the linear range of the detector. Nonetheless, it is important to verify that the slowly-changing mean position of the laser spot does not considerably affect the measurement of the dynamic moduli, which is related to the inverse of the amplitude of the laser spot movement via (2.7). For an illustration of this phenomenon, see Fig. 2.13 where it can be seen that changes in the laser position change the apparent amplitude of the laser motion. The problem will be analyzed in the case of bending. However, the same conclusions apply to the case of torsion. Under an applied mechanical loading, the deflection of the end of the specimen subtends an angle 2θ . The laser beam travels a distance l to the detector. Then, assume that the average specimen deflection changes (due to some eigenstrain) such that the laser now travels at an angle ϕ causing an average displacement Δ on the sensor. From the geometry, the two amplitudes can be written as

$$\hat{u}_y^0 = 2l \tan \theta, \quad \hat{u}_y = l [\tan(\phi + \theta) - \tan(\phi - \theta)]. \quad (2.23)$$

Using trigonometric identities and making the substitution $\tan \phi = \Delta/l$, the ratio of the two amplitudes can be written as

$$\frac{\hat{u}_y^0}{\hat{u}_y} = \frac{1 - (\Delta/l)^2 \tan^2 \theta}{1 + (\Delta/l)^2} \approx 1 - (1 + \tan^2 \theta)(\Delta/l)^2. \quad (2.24)$$

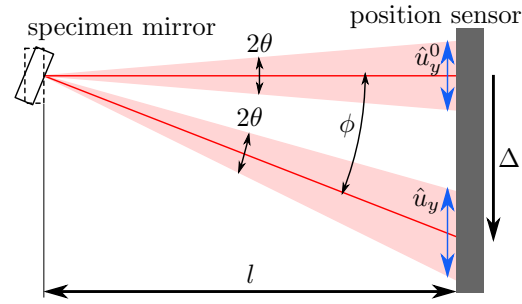


Figure 2.13: Illustration of the effect of the average laser position on the amplitude of the signal (not to scale).

For the stiff materials of interest, θ is small. Therefore, as long as Δ/l is small, the effects of eigenstrains in the material during testing can be considered small. For example, as a worst-case approximation, let Δ be the size of the detector (1 cm), let $\theta = \phi$, and take l to be 0.29 m (the actual distance in the apparatus), then $\hat{u}_y^0/\hat{u}_y = 0.999$, which is much smaller than the changes in the moduli measured (i.e. as much as 0.6 measured in the bending experiments of Section 3.2). The measured phase lag will be unaffected by the misalignment of the laser since the mechanical bending frequencies tested are many orders of magnitude slower than the speed of light of the laser beam, which would have to travel slightly farther due to misalignment.

2.3.3 Parasitic damping due to support loss

The specimen grip and surrounding vacuum chamber are designed to be stiff and massive to minimize the effect of the apparatus compliance on the specimen. However, the propagation of elastic waves into the grip and support structure can increase the measured damping of the specimen. This phenomenon has been analyzed in (Hao et al., 2003), where they compute the traction imparted by a vibrating cantilever (assumed to be of the same material as the grip for simplicity) attached to an elastic half-space as shown in Fig. 2.14. From the analysis in (Hao et al., 2003), the following closed-form expression was found for the apparent quality factor Q of a perfectly elastic specimen

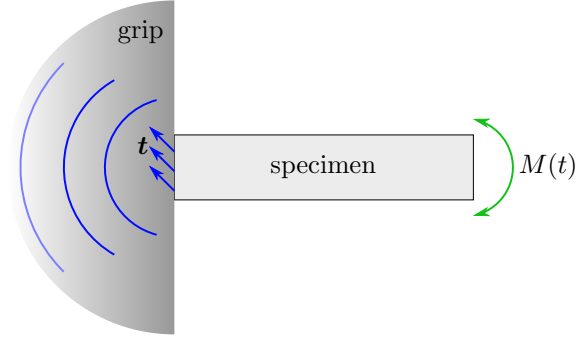


Figure 2.14: Illustration of a cantilevered beam specimen attached to a grip modeled as an elastic half-space. Harmonic bending of the specimen generates elastic waves that travel away through the grip and cause energy loss (or damping).

due to the energy loss through elastic waves,

$$Q = \frac{0.24(1-\nu)L^3}{\psi(1+\nu)(\beta_n\chi_n)^2h^3}, \quad (2.25)$$

$$\psi = \int_0^\infty \frac{\sqrt{\xi^2 - (c_L/c_T)^2}}{[2\xi^2 - (c_L/c_T)^2]^2 - 4\xi^2\sqrt{\xi^2 - (c_L/c_T)^2}\sqrt{\xi^2 - 1}} d\xi,$$

where ν is the Poisson ratio of the elastic support material, L is the length of the specimen, h is the specimen's thickness, and c_L and c_T are the longitudinal and shear wave speed of the support, respectively. The β_n and χ_n are shape factors for a particular resonance mode, e.g. for the first mode, they are 0.597 and -0.734, respectively (Hao et al., 2003). For a material such as steel Poisson's ratio is 0.28 and $\psi = 0.336$. Using the closed-form result for the estimation of the measured quality factor of the specimen $Q = (\tan \delta)^{-1}$, the loss tangent due to loss through the support structure is estimated to be 1.8×10^{-5} at the first resonance frequency (using the dimensions of the specimen in Tab. 3.2). The loss tangents measured in experiments were on the order 0.01 to 1.0 as shown later in Section 3.2; thus, the influence of support loss on the measured loss tangent is negligible.

2.3.4 Electromagnetic coupling

Although the ferroelectric materials of interest such as PZT are not magnetostrictive (i.e. stresses do not generate magnetic fields and vice versa), the application of large, time-varying electric fields

to the specimen while simultaneously applying time-varying magnetic fields via Helmholtz coils can lead to interference between the two fields. In addition, the metallic screws used to attach the magnet and clamp to the specimen may experience small forces due to applied magnetic fields. To measure the incremental stiffness and damping of materials under electric fields, it is necessary to use mechanical frequencies that are much higher than the electric field frequencies. As a result, it is expected that there is little interference between the two. Furthermore, the dielectric response of PZT causes electric charges to accumulate on surface electrodes, which partially shield the surrounding space outside of the specimen from the electric field generated by the applied voltage, which further reduces the electromagnetic coupling. Indeed, this coupling between electric and magnetic fields was found to be negligible in experiments. Experiments in bending and torsion were repeated after removing the attached magnet. The specimen deflection amplitudes were compared between tests with and without the permanent magnet (at 25 Hz, well below the first resonance frequency of the two specimens). In this case the amplitude of the signal from the laser position sensor (due to the specimen deflection) was measured to be at least 50 mV, with the attached magnet, for the bending experiments. Upon removing the magnet, the signal amplitude was near the resolution of the detector, 5 mV. Therefore, the effect of electromagnetic coupling in bending is small and can be neglected. A similar result was observed for the case of torsion. Near anti-resonance frequencies, when the deflection amplitude is near the detection limit, electromagnetic coupling may be important (along with noise in the system). Altogether, electromagnetic coupling in the setup does not affect the measured results. However, this effect may become important when testing comparable electric and magnetic field frequencies.

2.3.5 Noise measurements

To obtain an overall picture of the noise in the apparatus, the total noise floor was characterized by computing the power spectral density of the specimen deflection (in bending) under forced vibration at 75 Hz as shown in Fig. 2.15. The power spectral density was computed using the MATLAB function `pwelch()` on the laser position sensor output voltage. The amplitude of the signal at the driving frequency is much higher by at least four decades than noise occurring at other frequencies due to e.g. main voltage sources at 60 Hz and higher harmonics. As mentioned before, the current setup is susceptible to noise at low frequencies (i.e. below 1 Hz) as evident in Fig. 2.15 where the power spectral density increases significantly. However, such low frequencies were not currently of

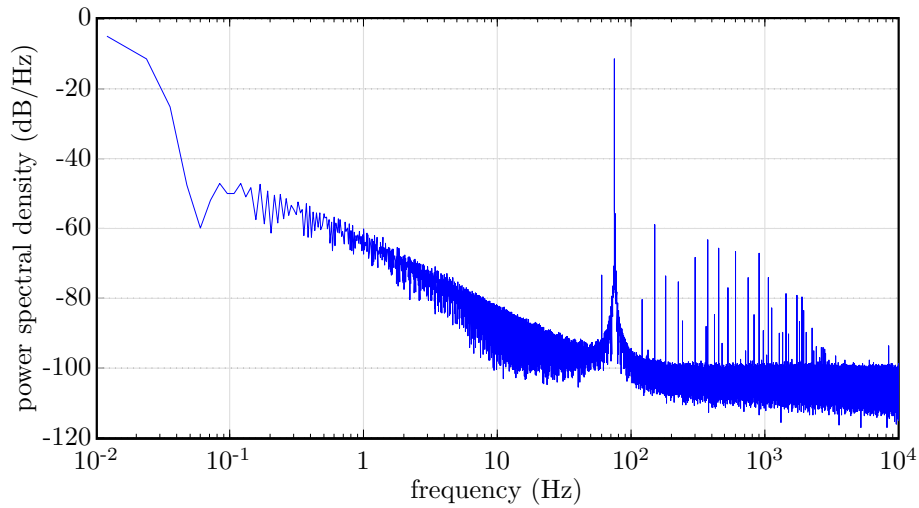


Figure 2.15: Power spectral density of the laser position sensor output when applying a mechanical bending frequency of 75 Hz and 7.2 Vpp amplitude. The signal power at 75 Hz, due to the applied moment, is much higher than noise occurring at other frequencies.

interest and thus experiments were not performed at those frequencies. To reduce noise at lower frequencies, the apparatus should be placed on a more rigid table or the isolation table should be deflated. However, by doing so, higher-frequency noise will be increased.

2.4 Validation

To demonstrate the accuracy of BES, experiments were performed to characterize already well-known behaviors of materials and compare them with results in the literature. The viscoelastic characterization capability of BES is shown through experiments performed on polymethyl methacrylate (PMMA), whose stiffness and damping have been well characterized ([Koppelman, 1958](#)), as well as aluminum. Second, the Sawyer-Tower circuit is used to characterize the evolution of the electric displacement of PZT, which has also been extensively studied in the literature ([Zhou et al., 2001](#)). In addition, comparison of the electric displacement evolution in air and under vacuum is discussed.

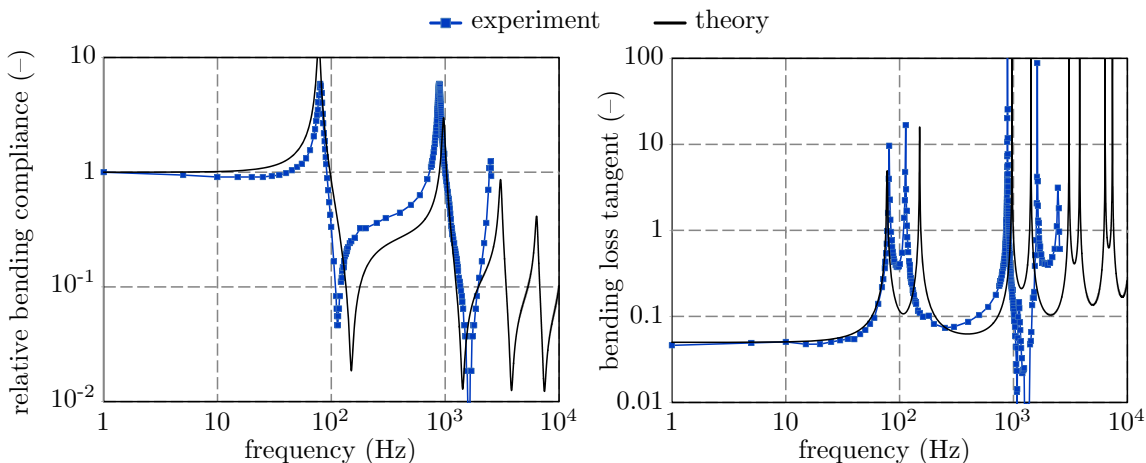


Figure 2.16: Viscoelastic response of a PMMA sample measured using BES with (a) showing the relative compliance and (b) showing the loss tangent in bending versus frequency. Blue points represent experimental data and solid black lines correspond to the dynamic Euler-Bernoulli solution using the parameters in Tab. 2.2.

2.4.1 Viscoelastic characterization of PMMA

A specimen of PMMA was cut to a size of $63.10 \times 5.44 \times 2.50 \text{ mm}^3$ and its dynamic compliance (inverse of Young's modulus) and loss tangent in bending were measured for frequencies from 25-2540 Hz as shown in Fig. 2.16. The compliance shows the typical resonance and anti-resonance behavior. That is, there is a large increase in the compliance (i.e. increase in the deflection amplitude) at a frequency of approximately 80 Hz, corresponding to the first resonance frequency. Then the compliance decreases significantly at 113 Hz, corresponding to the first anti-resonance frequency where the amplitude of the deflection becomes very small. This behavior is repeated for higher-frequency resonance modes. The behavior of the loss tangent also shows the typical large increase at resonance and anti-resonance frequencies. Note that to obtain positive loss tangents (physically admissible), the absolute value of the output of the lock-in amplifier phase angle is used.

To determine Young's modulus and loss tangent from the experiments, the solution of the dynamic Euler-Bernoulli beam in (C.6) is fit to the experimental data as shown in Fig. 2.16 by selecting the appropriate static Young modulus and loss tangent, which are assumed to be frequency independent (that is, by substituting $E \rightarrow E(1 + i \tan \delta_{Emat})$ and comparing $|E^*|$ and $\tan \delta_E$ to the experimental data). The parameters used in the Euler-Bernoulli beam model are shown in Tab. 2.2. The value of the static Young modulus and loss tangent that best match the experimental data

Table 2.2: Measured and fitted parameters of the PMMA specimen.

parameter	symbol	value
Young's modulus*	E	3 GPa
bending loss tangent*	$\tan \delta_E$	0.05
density	ρ	1180 kg/m ³
clamp mass	m	1.412 g
specimen free length	L	54.92 mm
specimen width	b	5.44 mm
specimen thickness	h	2.50 mm

* values obtained by fitting to experimental data

were 3 GPa and 0.05, respectively, which agree well with literature values. Young's modulus is reported to vary between 2.24 and 3.24 GPa (Callister and Rethwisch, 2009) and a loss tangent of 0.1 at 1.0 Hz is reported in (Koppelman, 1958). The discrepancy in the loss tangent is likely due to variations between specimens due to e.g. material processing and preparation. Therefore, the BES apparatus developed minimizes sources of error and results in accurate measurements of dynamic stiffness and damping.

2.4.2 Loss tangent of aluminum

To get an idea of the smallest loss tangents that can be resolved and measured with the current BES setup, the loss tangent of a low-loss (aluminum) specimen was measured. The specimen dimensions were $63.5 \times 6.5 \times 1.1$ mm³ cut from a sheet of aluminum 6061. A loss tangent of 0.005 was measured at a subresonance frequency of 10 Hz. A loss tangent of 0.001 was reported for aluminum in (Zener, 1948). Variations in material processing and cutting likely cause variations in the loss tangent between specimens that account for this discrepancy. Nonetheless, BES was able to resolve loss tangents on the order of 10^{-3} , which is well below the loss tangents that will be reported for PZT in Chapter 3, viz. near 0.1. Thus, in the worst case, the error in the loss tangent measured for PZT is no greater than 1%.

2.4.3 Electric displacement evolution in PZT

A triangle-wave electric field was applied to PZT specimens and the resulting macroscopic electric displacement was measured using the Sawyer-Tower circuit setup in BES. The electric displace-

ment was measured for different frequencies of applied bending/twisting moments as well as for different frequencies of the applied electric field. First, Fig. 2.17 shows the electric displacement versus electric field for different electric field frequencies ranging from 0.01 to 1.0 Hz while applying a bending moment at 75 Hz, which reveals the typical hysteresis curves obtained in numerous previous (static) studies, see e.g. (Hooker, 1998; Viehland and Chen, 2000; Zhou and Kamlah, 2006; Zhou et al., 2001). Similarly, Fig. 2.18 shows the electric displacement versus electric field for the same frequencies but while applying a torsional moment at 75 Hz. The important result is that the coercive field increases with electric field frequency, which is consistent with (Zhou et al., 2005a) for PZT and (Yin and Cao, 2002) for PZN-PT. There is asymmetry in the hysteresis curves with respect to the electric field. Such behavior has been observed for initially-poled PZT (the specimens tested here were also initially poled), see e.g. (Arlt and Neumann, 1988; Carl and Hardtl, 1977) for a discussion of this phenomenon. The asymmetry is due to an internal bias in the material formed during manufacturing when specimens are initially poled. The asymmetry has been shown to vanish after a large number of electric field cycles (Carl and Hardtl, 1977). The value of the coercive field (where the electric displacement crosses zero) in each direction is important for determining when domain switching occurs in order to explain the results obtained for the dynamic moduli and loss tangents shown in later experiments. In particular, domain switching occurs around the coercive field where there is highly non-linear behavior of the electric displacement corresponding to polarization reorientation in the material. Comparing the results obtained during bending and torsion in Figs. 2.17 and 2.18, respectively, shows slightly different coercive fields as well as spontaneous polarization (the value of the electric displacement at zero electric field). This difference is likely due to variation in the electrical properties of the two specimens tested.

For a fixed electric field frequency of 0.1 Hz, Fig. 2.19(a) shows the electric displacement versus electric field for various bending frequencies, which reveals similar hysteresis behavior as observed in Figs. 2.17 and 2.18. However, the individual curves for different mechanical bending frequencies coincide; the mechanical loading frequencies tested had no effect on the electric displacement hysteresis. That is, the stresses reached during mechanical loading had no influence on the evolution of the average polarization in the material. There is also asymmetry in the hysteresis curves. Specifically, the spontaneous polarization and coercive field for a positive electric field are 1.49 MV/m and 0.37 C/m², respectively, while for a negative electric field, they are -1.36 MV/m and -0.33 C/m², respectively. Similarly, Fig. 2.20(a) shows the electric displacement hysteresis for different torsional

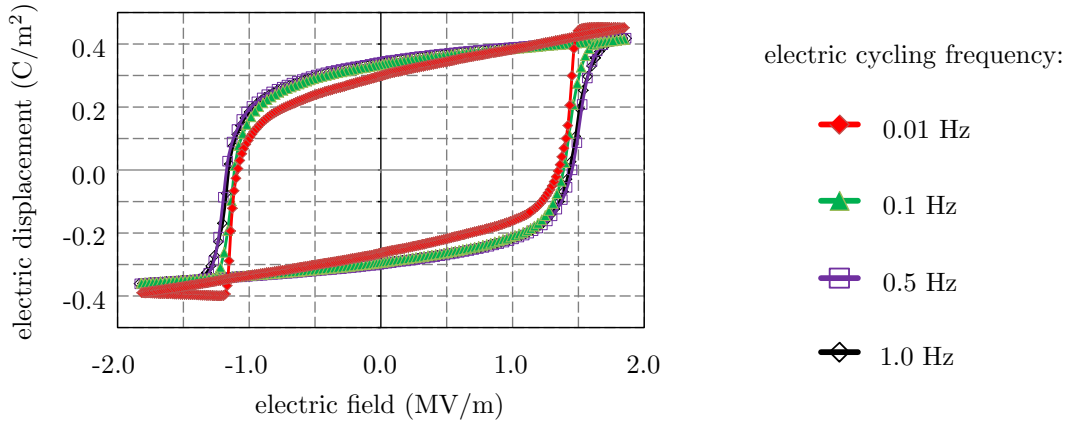


Figure 2.17: Variation of the electric displacement versus electric field for different triangle-wave electric field frequencies ranging from 0.01 to 1.0 Hz while applying a bending moment at 75 Hz.

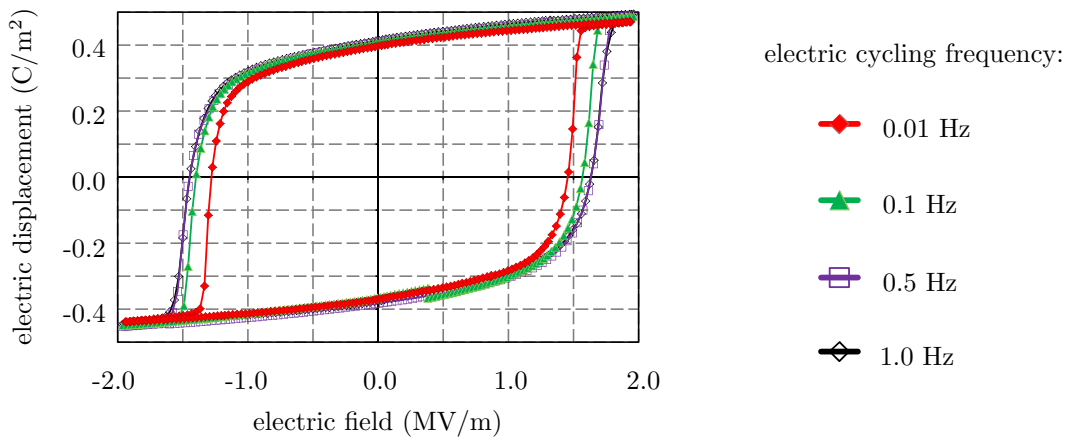


Figure 2.18: Variation of the electric displacement versus electric field for different triangle-wave electric field frequencies ranging from 0.01 to 1.0 Hz while applying a torsional moment at 75 Hz.

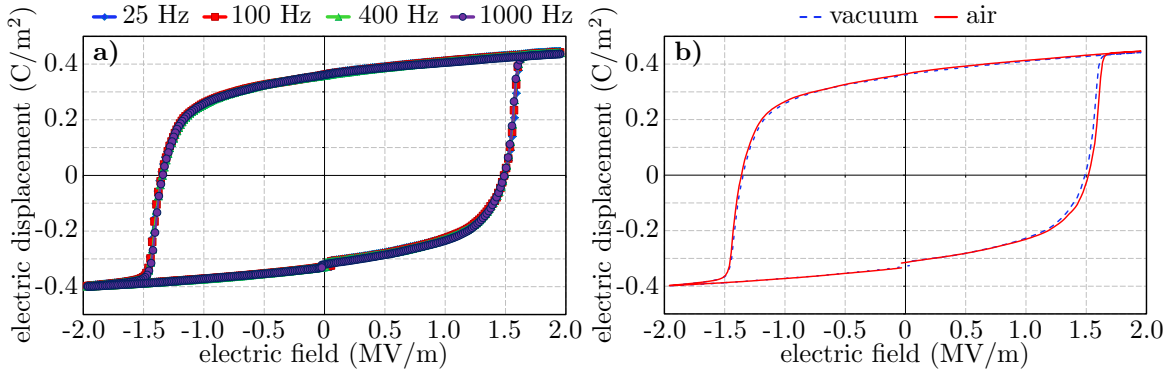


Figure 2.19: Electric displacement versus an applied cyclic electric field at 0.1 Hz: (a) effect of different mechanical bending frequencies (25-1000 Hz), (b) comparison between experiments performed in air and vacuum at a fixed mechanical frequency of 100 Hz.

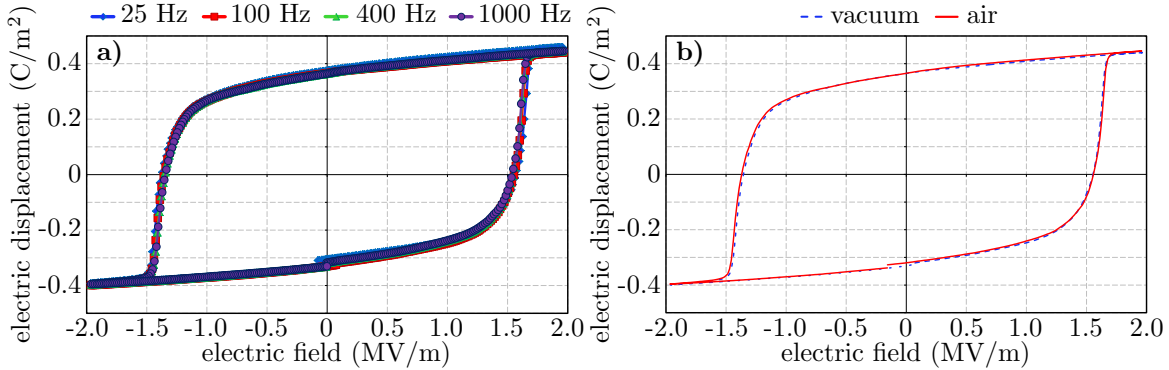


Figure 2.20: Electric displacement versus an applied cyclic electric field at 0.1 Hz: (a) effect of different torsion frequencies (25-1000 Hz), (b) comparison between experiments performed in air and under vacuum at a fixed mechanical frequency of 100 Hz.

frequencies. Again the curves coincide with each other (as was the case with the hysteresis curves obtained during bending). Thus, not only do the mechanical loading frequencies not affect the evolution of the macroscopic polarization, bending and torsional moments also do not have an impact on the evolution of the macroscopic polarization.

Comparing the electric displacement hysteresis in air and vacuum as shown in Figs. 2.19(b) and 2.20(b) for a mechanical bending or torsion frequency of 100 Hz reveals a slight decrease in the coercive field when performing cyclic electrical loading in vacuum compared to air. This effect may be due to the hydrostatic pressure applied by the surrounding air; hydrostatic pressure has been observed to affect the electric displacement hysteresis (Valadez et al., 2013).

2.5 Summarizing the capabilities of BES

The BES method and apparatus have been explained in detail in the previous sections. The relevant capabilities (i.e. bandwidth and amplitude/resolution) of the specific equipment used in the current BES setup are summarized in Tab. 2.3 along with explanations of some of their limitations. In particular, the equipment used in the setup for applying mechanical loads and measuring deformation, applying electric fields and measuring polarization, controlling temperature, and generating a vacuum are distinguished. The maximum range in mechanical loading frequencies that can be tested (due to the combined limitations of each piece of equipment) was reported previously in Tab. 2.1 for BES. Thus, Tab. 2.1 shows that a wide range of mechanical loading frequencies can be tested with the current apparatus (although slightly smaller than BVS) while controlling temperature and applying electric fields (necessary for characterizing the viscoelastic properties of ferroelectrics), which none of the other methods are capable of. It should also be stressed that the capabilities presented in Tab. 2.3 correspond to the specific equipment of the apparatus that was fabricated for testing ferroelectric ceramics. However, different equipment may be used to tailor the capabilities of the setup for testing other materials under different conditions.

Table 2.3: Amplitude of thermo-electromechanical loading and pressure that can be supplied by and the resolution of the material response that can be detected by the equipment used in the current BES apparatus and their associated bandwidths. Notes are provided that describe the particular limiting factor on the amplitude and/or bandwidth of some of the equipment.

equipment	bandwidth	amplitude/ resolution	notes
mechanical loading			
waveform generator	10^{-3} to 10^6 Hz	up to ± 10 V	
Helmholtz coils and magnet	up to 10^4 Hz	up to 10^{-4} Nm	limited by coil impedance noise at low frequencies from table
lock-in amplifier	10 to 10^5 Hz	10^{-9} to 1 V	
laser detector	up to 10^4 Hz	1 to ± 4500 μm	
electrical loading			
waveform generator	10^{-3} to 10^6 Hz	up to ± 10 V	
high-voltage amplifier	up to 10^5 Hz	up to $\pm 10^3$ V	frequency-dependent capacitance of electrolytic capacitor
Sawyer-Tower circuit	10^{-2} to 10^2 Hz	up to 100 μC	
oscilloscope	up to 10^6 Hz	10^{-3} to ± 20 V	
temperature			
power supply (4 kW)	quasistatic	up to 25 A dc at 160 V dc	
graphite resistors	quasistatic	r.t. to 400°C	
vacuum chamber			
vacuum pump	quasistatic	10^{-9} to 1 bar	vacuum depends on quality of o-rings

Chapter 3

Experiments on Polycrystalline Lead Zirconate Titanate

Using BES, the dynamic Young and shear moduli as well as the loss tangent in bending and torsion of a ferroelectric ceramic were measured while simultaneously applying a large, slowly-varying cyclic electric field at room temperature. With the present apparatus, dynamic tests are performed at previously unattainable mechanical and electric cycling frequencies. Furthermore, each test was performed in air at atmospheric pressure and under vacuum to demonstrate the improvement in accuracy of measurements by removing the effects of air. Some of the following experiments and discussions follow from our previous papers ¹ (le Graverend et al., 2015; Wojnar et al., 2014).

It should be noted that generally, the specimens tested are orthotropic and thus for our purposes, the Young modulus corresponds to the transverse one, E_{yy} , and the shear modulus corresponds to the out-of-plane one, G_{xy} , as shown in Fig. 3.1 (or, using typical naming conventions for transversely isotropic piezoactuators, E_1 and G_{13} , respectively, as used by the manufacturer). Only when the macroscopic polarization is zero (due to random orientations of the polarization within each grain), does the material display an approximately isotropic response. Thus, the Young modulus and shear modulus measured in the following sections follow from our naming convention.

¹The experiments performed at different mechanical frequencies were shown and discussed in le Graverend, J.B., Wojnar, C., Kochmann, D., 2015. Broadband Electromechanical Spectroscopy: Characterizing the dynamic mechanical response of viscoelastic materials under temperature and electric field control in a vacuum environment. *Journal of Materials Science* 50, 3656–3685. URL: <http://dx.doi.org/10.1007/s10853-015-8928-x>, doi: [10.1007/s10853-015-8928-x](https://doi.org/10.1007/s10853-015-8928-x). The effect of electrical loading frequency was presented for the bending case in Wojnar, C.S., le Graverend, J.B., Kochmann, D.M., 2014. Broadband control of the viscoelasticity of ferroelectrics via domain switching. *Applied Physics Letters* 105, 162912. URL: <http://scitation.aip.org/content/aip/journal/apl/105/16/10.1063/1.4899055>, doi: <http://dx.doi.org/10.1063/1.4899055>.

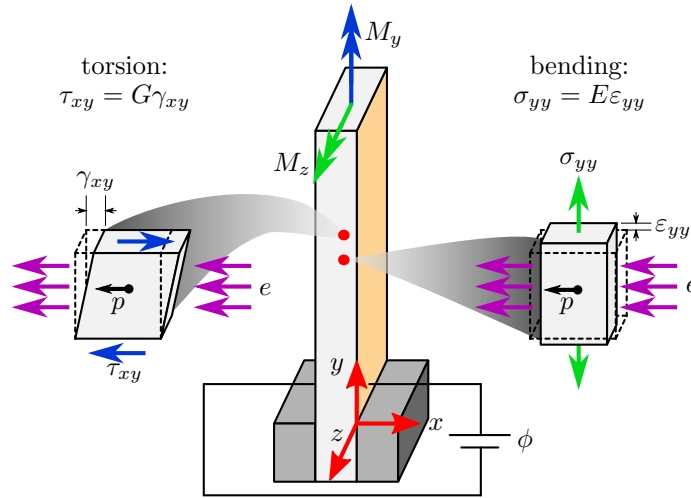


Figure 3.1: Drawing of the components of the imposed stresses and strains during bending and shearing, which are used to define the Young and shear moduli for the generally orthotropic material.

3.1 Materials

All measurements were performed using initially-poled Navy-type II lead zirconate titanate (PZT, PSI-5A4E from Piezo Systems Inc., Woburn, MA, USA), which is polycrystalline. This material is widely used in commercial applications, and thus is of interest in this study. The relevant material properties are listed in Tab. 3.1. The specimens were cut to $1 \times 3 \times 38 \text{ mm}^3$. The largest (top and bottom) surfaces of the specimens were coated with $10 \text{ }\mu\text{m}$ thick nickel electrodes by the supplier. Typical grain sizes in the specimens were $2 \text{ }\mu\text{m}$, as observed by Scanning Electron Microscopy (see Fig. 3.2).

3.2 Bending experiments

By activating the vertical coils in BES, bending moments are applied to the specimens and the resulting deflection angle is measured. Using the analysis in Section 2.2.1, the dynamic Young modulus and loss tangent are obtained. Various frequencies of the applied bending moment and of the applied electric field were tested to characterize the effect of mechanical and electrical loading rates.

Table 3.1: Physical properties of the PSI-5A4E soft PZT ceramic at room temperature (obtained from Piezo Systems Inc., Woburn, MA, USA).

material property	symbol	value
relative dielectric constant	ϵ_r	1800
Curie temperature	T_c	350°C
longitudinal strain-electric field coupling coefficient	d_{33}	390×10^{-12} m/V
transverse strain-electric field coupling coefficient	d_{31}	-190×10^{-12} m/V
longitudinal electric field-stress coupling coefficient	g_{33}	24×10^{-3} Vm/N
transverse electric field-stress coupling coefficient	g_{31}	-11.6×10^{-3} Vm/N
longitudinal electromechanical coupling coefficient	k_{33}	0.72
transverse electromechanical coupling coefficient	k_{31}	0.35
longitudinal Young modulus	E_3	66 GPa
transverse Young modulus	E_1	52 GPa
mechanical quality factor	$Q = (\tan \delta)^{-1}$	80

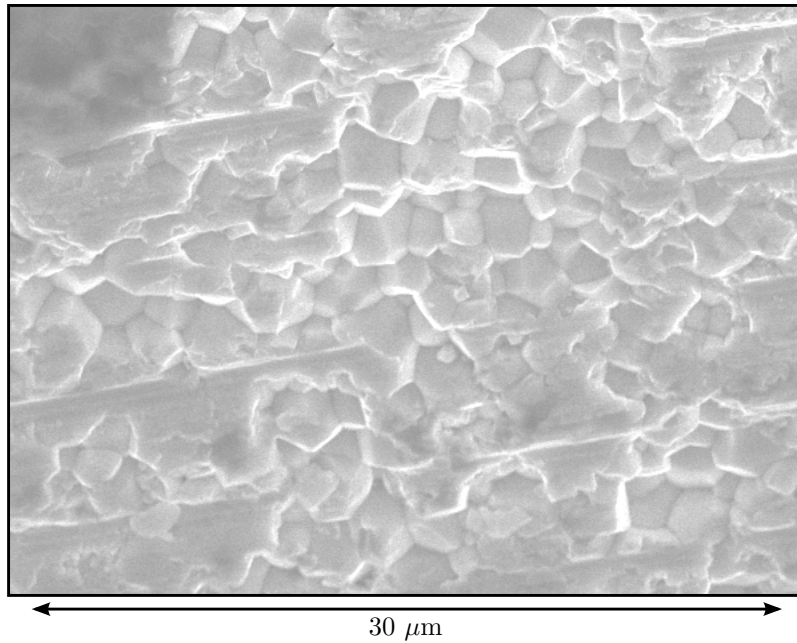


Figure 3.2: An image of a typical PZT specimen obtained from Scanning Electron Microscopy. Image is taken of the side of the specimen without the electrode (there was no surface preparation before imaging). Horizontal striations are due to the blade used by the manufacturer to cut specimens to size. Examining the surface reveals a granular structure with grains on the order of $2 \mu\text{m}$. The image was obtained under 20 kV with a working distance of 10.6 mm. The magnification is $2500\times$.

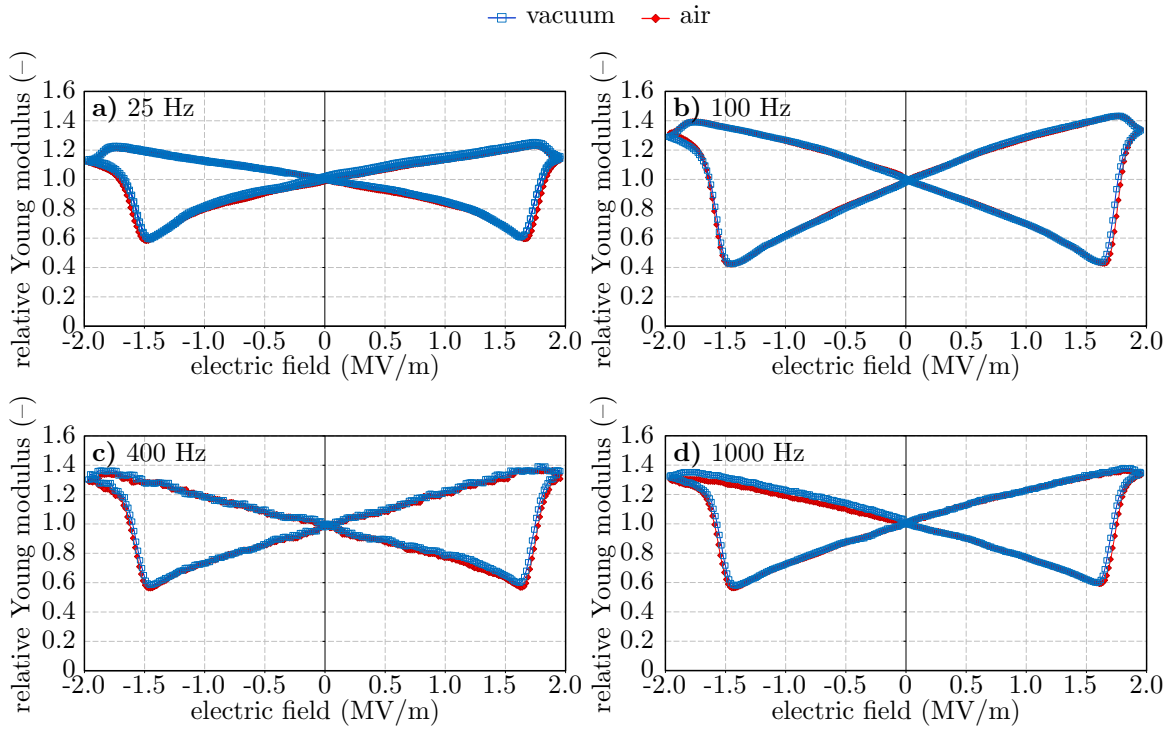


Figure 3.3: Relative Young modulus measured in air and under vacuum while applying a cyclic electric field at 0.1 Hz. Results for several mechanical frequencies are shown: (a) 25 Hz, (b) 100 Hz, (c) 400 Hz, and (d) 1000 Hz. The Young modulus during electrical cycling is normalized by the Young modulus when no electric field is applied, as presented in equation (2.7).

3.2.1 Different mechanical frequencies

Specimens were tested in bending to obtain the relative dynamic Young modulus and loss tangent for various mechanical loading frequencies. The relative dynamic Young modulus (normalized by the value at zero electric field) and the loss tangent are shown in Figs. 3.3 and 3.4, respectively, at bending frequencies of 25, 100, 400, and 1000 Hz. At each mechanical loading frequency a sinusoidal voltage was applied to the coils, with peak-to-peak amplitude $\hat{V} = 7.2$ V. The electric field cycling frequency was held constant at a 0.1 Hz triangle waveform with a 1.95 MV/m amplitude. Recall that the mechanical loading frequency did not affect the evolution of the macroscopic electric displacement, cf. Fig. 2.19(a).

Fig. 3.3 shows the relative dynamic Young modulus for different mechanical loading frequencies in air and under vacuum. For each mechanical frequency the modulus displays softening near

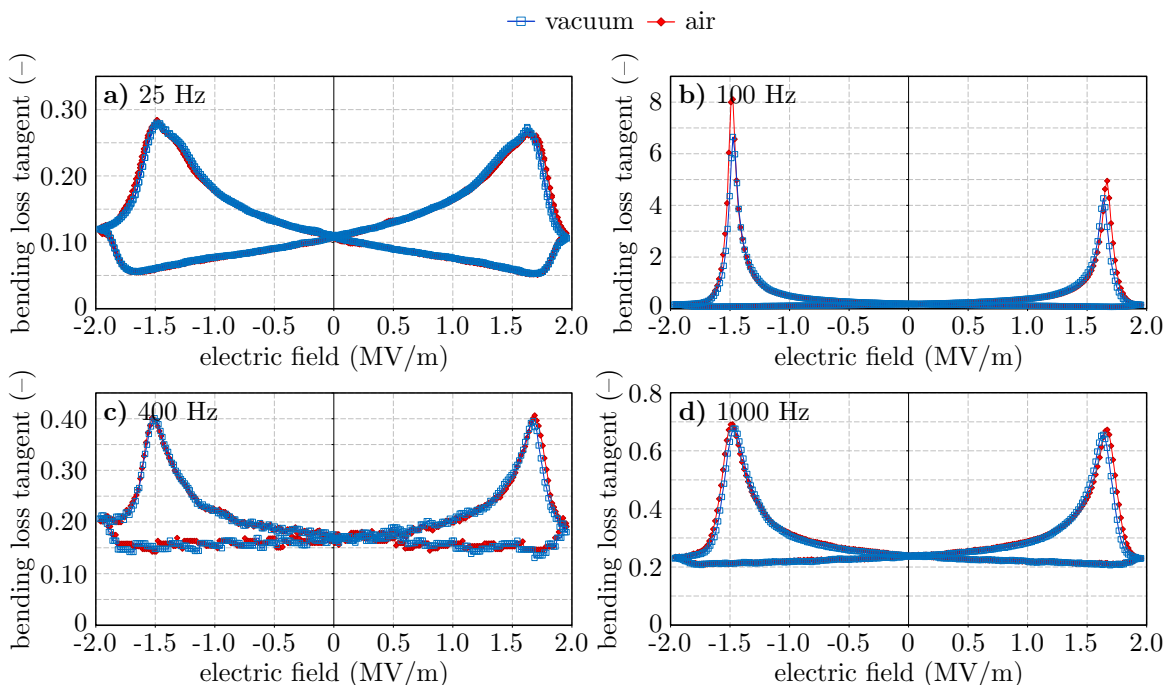


Figure 3.4: Loss tangent in bending measured in air and under vacuum while applying a cyclic electric field at 0.1 Hz. Several mechanical frequencies have been examined: (a) 25 Hz, (b) 100 Hz, (c) 400 Hz, and (d) 1000 Hz.

the coercive field. Away from the coercive field, the modulus varies linearly, which is due to the change of the elastic constants with applied electric field (Fu and Zhang, 2000a; Wang et al., 2003a) in addition to changing volume fractions of differently-polarized domains with anisotropic elastic constants (Burlage, 1965; Yin and Cao, 2001, 2002). Comparing the results obtained in air and under vacuum, there are only marginal effects on the measured modulus. However, consistent with observations made of the electric displacement (slightly higher coercive fields in air), the minimum Young modulus appears at slightly higher electric fields when experiments are performed in air compared to under vacuum, which is when domain switching occurs.

The effect of the mechanical loading frequency on the loss tangent is shown in Fig. 3.4. For each case, the loss tangent increases substantially near the coercive field, indicating additional dissipation caused by domain wall motion. Linear variations away from domain switching can be attributed to the electric field dependence of the complex elastic constants, which has been measured before in (Wang et al., 2003b). For the case of 25 Hz in Fig. 3.4(a), the loss tangent is 0.11 at zero

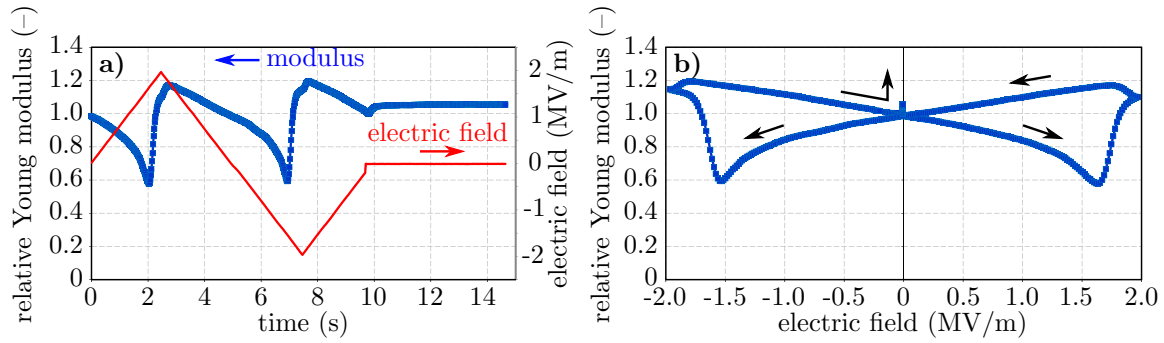


Figure 3.5: Transient behavior of the relative Young modulus at 25 Hz (a) versus time (along with the electric field) and (b) versus electric field (arrows indicate increasing time). Upon switching off the electric field, the relative dynamic Young modulus decays to a different steady-state value than that observed at zero electric field during electric field cycling.

electric field and becomes as large as 0.28 near the coercive field – an increase by more than 250%. It is important to point out that the loss tangent at 0 MV/m shown here is noticeably higher than typical values reported in the literature (e.g., 0.01 to 0.015 in (Jiménez and Vicente, 2000), and 0.0125 reported by the supplier). This is attributed to domain wall motion as follows. Even though the electric field passes through 0 MV/m, this does not imply that all domain walls are in equilibrium. The plots shown in Figs. 3.3 and 3.4 are obtained after at least one cycle of the electric field where the measured response reaches a steady behavior. However, upon switching off the electric field permanently, as shown in Figs. 3.5(a) and 3.6(a), there is a transient time of about 1 s during which the stiffness and loss tangent change before reaching their steady-state equilibrium values. This can also be seen in the corresponding plots of relative Young modulus and loss tangent vs. electric field in Figs. 3.5(b) and 3.6(b), respectively, where the modulus increases and the damping decreases at zero electric field. In this final steady state, the relative modulus increases by 5% and the loss tangent in bending reaches approximately 0.02, which is close to the reported literature values. A similar behavior was observed in (Jiménez and Vicente, 2000), where a completely different DMA-type setup was used. Therefore, this behavior is not an artifact of the experimental setup. The phenomenon is observed across different mechanical loading frequencies. This behavior is also observed in torsion experiments and when testing different electric cycling frequencies, and will be discussed in Sections 3.3 and 3.2.2, respectively.

The effect of air on the measured loss tangent – in particular on the maximum damping reached –

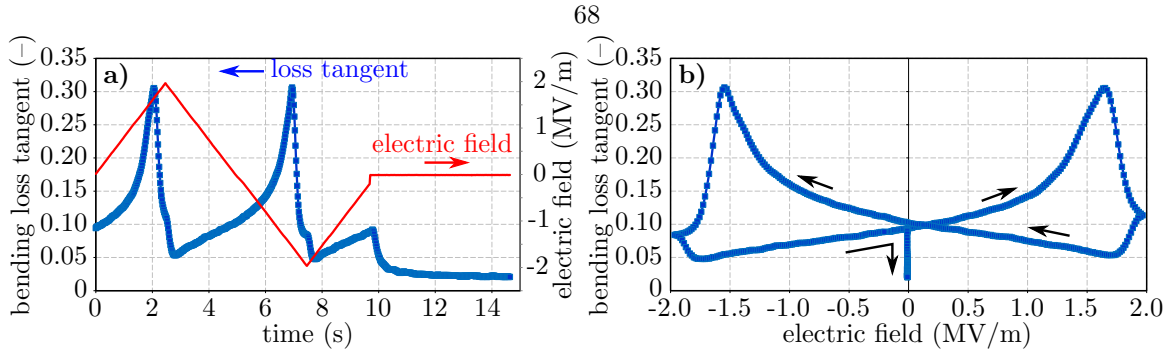


Figure 3.6: Transient behavior of the loss tangent in bending at 25 Hz (a) versus time (along with the electric field) and (b) versus electric field (arrows indicate increasing time). Upon switching off the electric field, the loss tangent decays to a different steady-state value than that observed at zero electric field during cyclic electric fields.

is more significant than the impact on the Young modulus. This is most pronounced near resonance, when the bending amplitude is highest (as observed in (Anderson et al., 1996)), which can be attributed to the generation of acoustic waves in the surrounding air and will be examined more closely in Section 3.4.2. Moreover, the damping peaks for the vacuum appear for lower electric field values for all mechanical frequencies studied here, which is again consistent with the small changes in the coercive field between air and vacuum.

Additional mechanical frequencies beyond those shown in Figs. 3.3 and 3.4 were also tested, up to 5 kHz. For conciseness and to more easily see their trends with mechanical bending frequency, the variations of the compliance (inverse of Young's modulus) and the loss tangent with mechanical frequency are shown in Fig. 3.7 with the compliance normalized by the static value (taken at 25 Hz) and zero electric field. Experimental data points illustrate the compliance at zero electric field ($e_x = 0$) and the maximum compliance occurring near the coercive field ($e_x = e_c$). The compliance shows the structural response, increasing up to the first resonance frequency at approximately 120 Hz and then decreasing significantly up to the first anti-resonance frequency at approximately 250 Hz. The behavior is repeated for the second resonance and anti-resonance frequencies occurring at approximately 1200 Hz and 3000 Hz, respectively. The curve of the compliance near the coercive field exhibits the same behavior but is shifted to lower frequencies. This is due to the softening in the modulus seen in Fig. 3.3, near the coercive field, which causes a decrease in each (anti-)resonance frequency. The loss tangent in Fig. 3.7(b) also shows the structural response, viz. increased damping near resonance and anti-resonance frequencies. In addition, the damping measurements at the

coercive field are higher than at zero electric field due to the increase in domain wall motion near the coercive field.

For frequencies below resonance, both the measured dynamic Young modulus and the loss tangent showed small variations with mechanical frequency, in particular their respective minimum and maximum values achieved during domain switching, as shown by the red curve in Fig. 3.7 (or in Fig. 4.3). Damping increases slightly with frequency and at high mechanical frequencies it is ultimately assisted by the structural resonance of the specimen (occurring at 147 Hz under no electric field and decreasing during switching due to reduction in the elastic modulus (Wang et al., 2003b)). Previous experiments showed a damping decrease with increasing frequency (Jiménez and Vicente, 2000); however, those experiments were performed at elevated temperatures, which is expected to decrease the relaxation time associated with domain switching (Savage and Miller, 1960). Experiments at ultrasonic frequencies (10 MHz) also revealed significant damping in single crystals (Yin and Cao, 2001); yet, those primarily exploited the elastic anisotropy, to be controlled by electric fields that affect the volume fractions of differently-polarized domains. Here, the kinetics of the domain switching process itself produces remarkable variations in stiffness and damping.

Fig. 3.7 compares the solution of the dynamic Euler-Bernoulli beam with an attached end mass (representing the clamp), as derived in Appendix C, to the experimental results. The two curves were obtained by using the material's static Young modulus and 65% of the static Young modulus (which corresponds to the softened value near the coercive field). Also, the loss tangents were selected to be 0.09 and 0.28 (three times higher) for the two cases (assumed to be constant with frequency). The Young modulus was also assumed to be frequency independent and was fit to the experimental results, which resulted in the specimen parameters of Tab. 3.2. The fitted Young modulus was less than the modulus reported by the supplier in Tab. 3.1. This discrepancy may be due to variation of material properties between particular specimens as well as approximations of the Euler-Bernoulli model and clamp. A more sophisticated model will be developed in Chapter 4. Nonetheless, one can see that the Euler-Bernoulli solution agrees well with the behavior around the first (anti-)resonance frequency, but starts to deviate at higher frequencies likely due to the approximation of the clamp as a point mass. In particular, by decreasing Young's modulus in the Euler-Bernoulli solution, the resonance behavior shifts to lower frequencies, as observed in the experiments.

Near resonance frequencies, the experimental results presented correspond to the structural

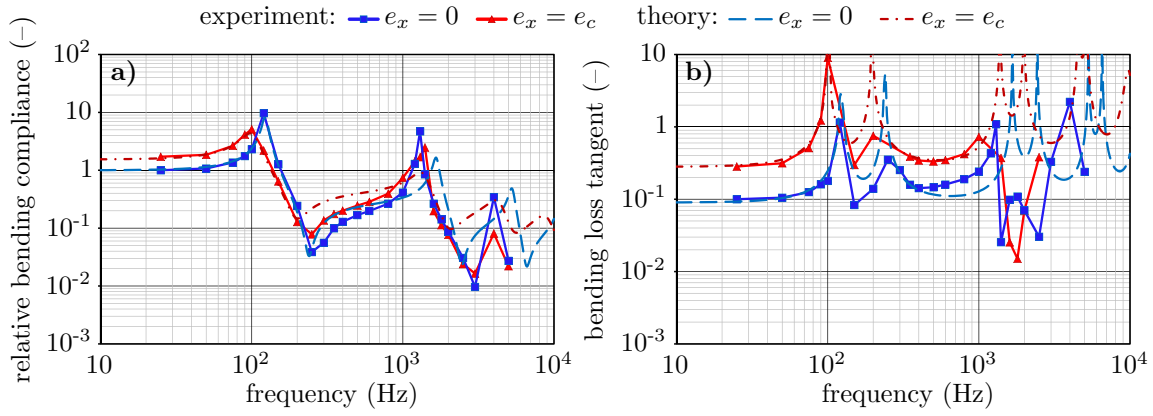


Figure 3.7: The compliance (a) and the loss tangent (b) in bending are shown vs. mechanical frequency for two different values of the applied electric field (red and blue points) and are compared to the theoretical Euler-Bernoulli solution (red and blue dashed lines).

Table 3.2: Measured and fitted parameters of the specimen.

parameter	symbol	value
Young's modulus*	E	35 GPa
shear modulus*	G	10 GPa
bending loss tangent*	$\tan \delta_E$	0.09
torsion loss tangent*	$\tan \delta_G$	0.1
density	ρ	6776 kg/m ³
clamp mass	m	1.594 g
clamp moment of inertia	I_m	2.14×10^{-8} kg m ⁴
specimen free length	L	30.46 mm
specimen width	b	3.62 mm
specimen thickness	h	1.04 mm
applied moment	M	6×10^{-5} Nm

* values obtained by fitting to experimental data

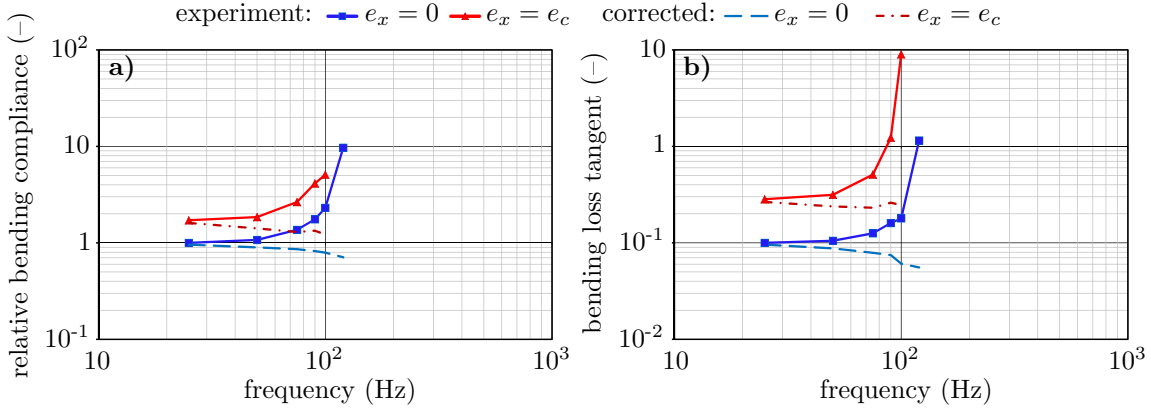


Figure 3.8: Summary of the results from Fig. 3.7 after applying the corrections in (2.15) and (2.16) to obtain the material response up to the first resonance frequency.

Young modulus and loss tangent. To obtain the material properties near resonance, the corrections derived in (2.15) and (2.16) were applied to the results in Fig. 3.7 to obtain the approximate material response shown in Fig. 3.8. In particular, the first resonance frequencies, ω_0 , for the bending case used in (2.15) were 123 and 101 Hz for the measurements at zero electric field and at the coercive field, respectively. There are much smaller variations in the material compliance and loss tangent compared to the structural one (i.e. they do not increase sharply close to the first resonance frequency). Thus, the approximate method for finding the material response gives a more accurate value than when using the structural response.

3.2.2 Effect of electrical loading frequency

Fig. 3.9 illustrates the variations of stiffness and damping for electric field cycling frequencies of 0.01, 0.1, 0.5, and 1 Hz at a constant mechanical bending frequency of 75 Hz and amplitude of 7.2 Vpp. Recall that the corresponding electric displacement measurements were already shown in Fig. 2.17, which in particular shows how the coercive field increases with electric field frequency. After the onset of domain switching (near the coercive field when the polarization is changing the most), the dynamic Young modulus softens significantly, to below 70% of its original value without electric fields, see Fig. 3.9(b). The faster the electric field cycling, the greater the softening effect. As observed in single-crystalline PZN-PT (Yin and Cao, 2001), the modulus variation is partly due to elastic anisotropy: 90°-switched domains, observed in polycrystals under cyclic electric

fields (Tsurumi et al., 1997), reduce the apparent modulus in the loading direction. This effect is more gradual in polycrystals (Burlage, 1965) due to the distributed grain orientations. Linear variation of the modulus with electric field before and after switching was also observed in PZT polycrystals in (Wang et al., 2003b).

The loss tangent shown in Fig. 3.9(c) exhibits peaks during domain switching, which become more pronounced with increasing electric field frequency. Like the dynamic Young modulus, the loss tangent varies linearly with the electric field before and after domain switching (as observed previously (Wang et al., 2003b)). The remarkable damping seen during domain switching with $\tan \delta > 0.4$ is commonly found in polymers, rarely in ceramics. Its physical origin is similar to that found in single crystals (Yin and Cao, 2001) but the polycrystalline orientation distribution leads to a more gradual evolution of the macroscopic viscoelastic properties.

The rate-dependent stiffness and damping variations have been attributed to 90°-domain switching (Arlt and Dederichs, 1980; Chaplya and Carman, 2002a). For higher electric field frequencies, the domain wall velocity increases (Merz, 1956; Miller, 1958; Miller and Savage, 1958, 1959a,b, 1960, 1961; Tataru and Kohno, 2004), which leads to an accelerated repoling process, see Fig. 3.9(a). This in turn results in larger spontaneous longitudinal strains during each mechanical cycle, thereby decreasing the apparent modulus. Also, the increases in domain wall velocity and apparent coercive field (which increases the domain-wall driving force) together increase the dissipated energy. Owing to the analogous thermodynamic driving force (or *energy momentum tensor*) arising from surfaces of discontinuities (Abeyaratne and Knowles, 1990; Eshelby, 1975), similar phenomena can be expected from domain wall motion in ferromagnetic materials (James, 2002; Wuttig et al., 1998).

3.3 Torsion experiments

The previous tests in bending generally gave rise to states of uniaxial stress and strain for small amplitudes, which allowed for the apparent Young modulus to be measured. BES also has the capability to apply torsional moments in order to measure the specimen's response in shear and characterize the apparent shear modulus. Here, similar experiments to those in bending are performed where the torsional frequency and electric field frequency are varied independently.

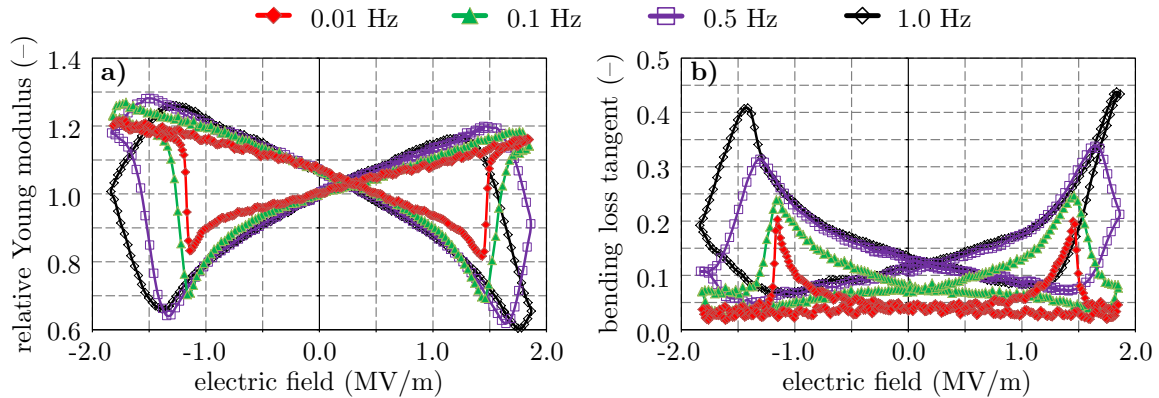


Figure 3.9: Experimental data of (a) relative Young modulus (normalized by the modulus without electric bias) and (b) loss tangent in bending vs. electric field for triangle-wave electric field (1.8 MV/m amplitude) frequencies of 0.01, 0.1, 0.5, and 1.0 Hz, and constant bending vibration at 75 Hz.

3.3.1 Different mechanical frequencies

Specimens were characterized in torsion with the same experimental conditions as in bending. The effect of torsional mechanical frequencies of 25, 100, 400, and 1000 Hz on the relative dynamic shear modulus (normalized by the value at zero electric field) and loss tangent were measured in air and under vacuum as shown in Figs. 3.10 and 3.11, respectively. The torsional moment was generated by applying a sinusoidal voltage, with peak-to-peak amplitude $\hat{V} = 6.0$ V, to the coils. Recall that the different torsional frequencies did not affect the evolution of the macroscopic electric displacement as shown in Fig. 2.20.

The qualitative nature of the curves for the normalized dynamic shear modulus (Fig. 3.10) are similar to those observed in bending; the modulus changes linearly away from the coercive field (due to the change of the elastic constants with electric field and anisotropy of changing volume fractions of differently-polarized domains) but exhibits less softening at the coercive field during domain switching than in bending for all the mechanical frequencies tested. For example, at 25 Hz during bending, Young's modulus decreases to approximately 60% of its value at zero electric field, while the shear modulus only decreases to approximately 70% of its value at zero electric field (and it should be noted that experiments for determining the effect of mechanical loading frequencies in bending and torsion were all performed using the same PZT specimen). This seems to indicate that domain reorientation has more of an effect on the Young modulus than the shear modulus. This is

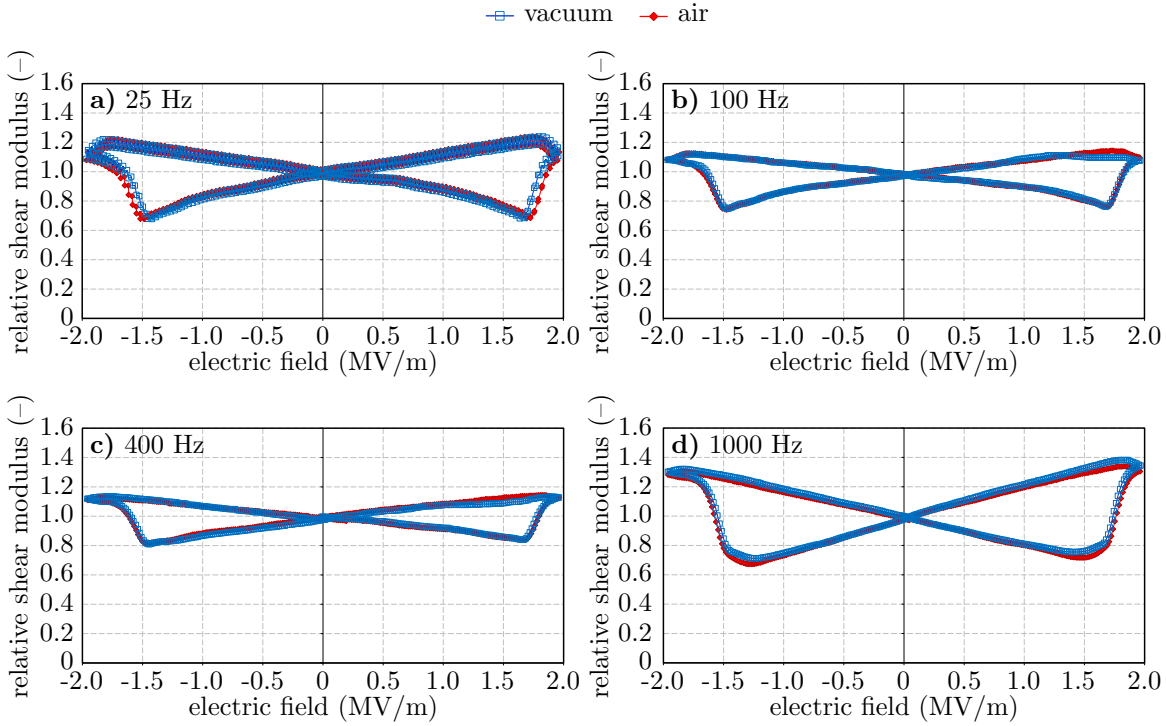


Figure 3.10: Relative shear modulus measured in air and under vacuum in torsion while applying a cyclic electric field at 0.1 Hz. Several mechanical frequencies are shown: (a) 25 Hz, (b) 100 Hz, (c) 400 Hz, and (d) 1000 Hz. The shear modulus during electrical cycling is normalized by the shear modulus when no electric field is applied, as presented in (2.7).

theorized to stem from the effect of changing volume fractions of anisotropic phases on the Young modulus is larger than on the shear modulus (which involves volume-preserving deformations). The loss tangent in torsion for different mechanical frequencies is shown in Fig. 3.11. As in bending, there is a large increase in damping near the coercive field due to domain switching (an increase by nearly a factor of three) and a linear variation away from the coercive field due to the electric field dependence and anisotropy of the complex elastic constants. As was the case in bending, the measured loss tangent at 0 MV/m is noticeably higher than typical values of PZT without applied electric fields (e.g. up to 0.02 in (Mason, 2013)), which can, again, be attributed to domain wall motion. That is, similar behavior to that seen in Figs. 3.5 and 3.6 was obtained in torsion experiments.

In addition, by comparing the response at 25 Hz in Figs. 3.4(a) and 3.11(a), respectively, we find similar values for the loss tangents in bending and torsion (0.11 and 0.12 at 0 MV/m, and 0.27

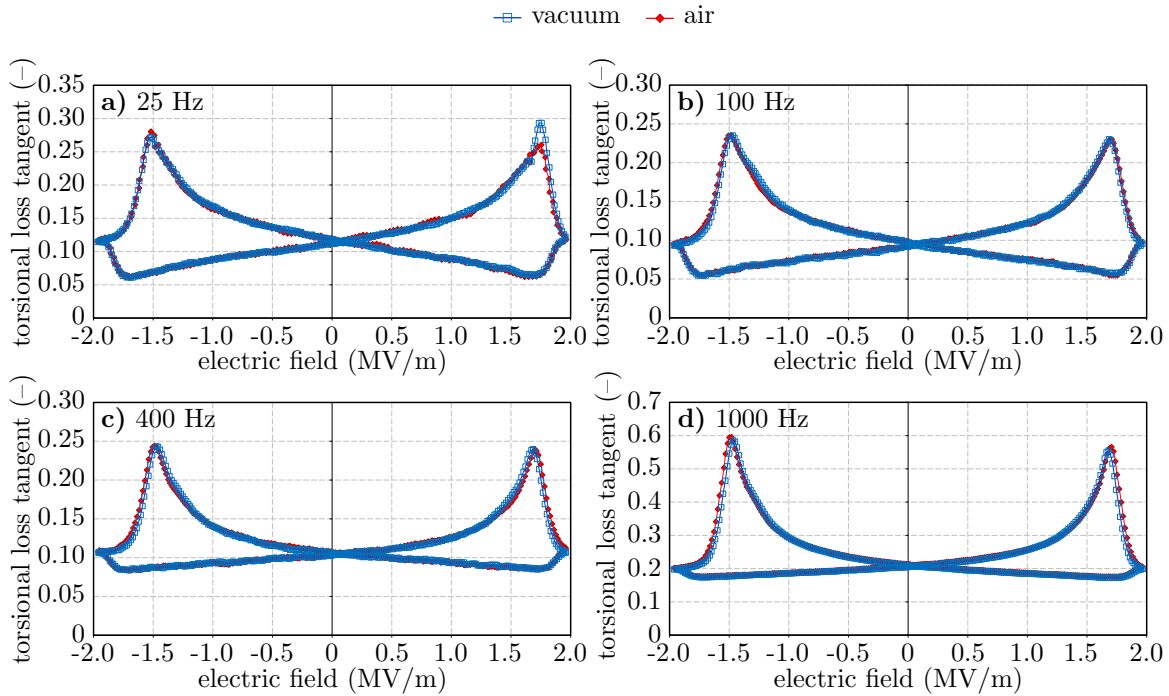


Figure 3.11: Loss tangent in torsion measured in air and under vacuum while applying a cyclic electric field at 0.1 Hz. Several mechanical frequencies are shown: (a) 25 Hz, (b) 100 Hz, (c) 400 Hz, and (d) 1000 Hz.

and 0.28 at the coercive field, both in bending and torsion, respectively). These values give rise to similar fitted loss tangents obtained using an Euler-Bernoulli model and torsion model as shown in Tab. 3.2, and they suggest viscoelastic isotropy. Viscoelastic isotropy was also shown for another ferroelectric perovskite, viz. barium titanate (Dong et al., 2008) (there, loss tangents in bending and torsion were both approximately 0.025).

The effect of the air on the measured dynamic shear modulus is small (similar to bending). However, dissimilar to bending, the effect of the air on the loss tangent is also small, even when approaching the torsional resonance frequency as shown in Fig. 3.11(d). This can be expected since the displacements of the specimen in torsion are significantly smaller than in bending, which decreases the amplitude of acoustic waves produced and thus causes less dissipation. Recall that the specimens, as well as the clamp and magnet, are of rectangular cross section such that torsion results in air movement due to specimen rotation.

The compliance and loss tangent of the specimen under torsional moments have been tested

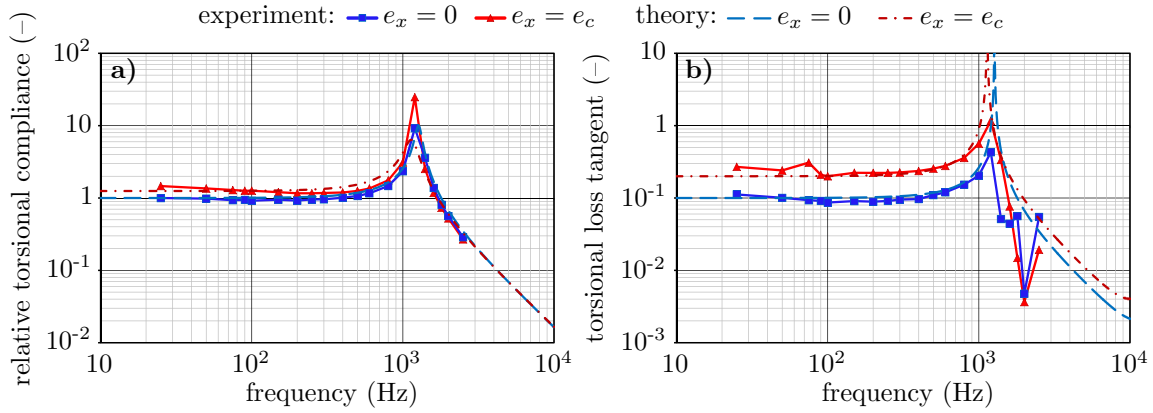


Figure 3.12: The compliance (a) and the loss tangent (b) in torsion are shown vs. mechanical frequency with and without an applied electric field (red and blue points) and are compared to the theoretical prediction (red and blue dashed lines).

at many additional frequencies beyond those shown in Figs. 3.10 and 3.11. Compliance and loss tangent for torsional frequencies up to 2.5 kHz are shown in Fig. 3.12. The first resonance of the specimen in torsion occurred at a much higher frequency (approximately 1300 Hz) than in bending (approximately 130 Hz). The first resonance frequency in torsion is close to the second resonance frequency in bending. This can be seen by the large increase in the torsional compliance and damping at 1300 Hz in Fig. 3.12, which is analogous to Fig. 3.7. As with the bending case, the modulus decreases near the coercive field and thereby also decreases the resonance frequency. The solution to the dynamic torsion response (as derived in Appendix C and in e.g. (Gottenberg and Christensen, 1964)) is included in Fig. 3.12 using the parameters in Tab. 3.2 for the data at $e_x = 0$, and using 80% of the static shear modulus and a loss tangent of 0.2 for the data at $e_x = e_c$. The softening in shear during domain switching becomes less pronounced at low frequencies; the gap between the two curves in Fig. 3.12 decreases from 25 Hz to approximately 300 Hz (where structural effects begin to cause the compliance to increase). This decrease can be attributed to Debye peak behavior associated with the relaxation time of polarization switching. As the mechanical frequency increases, the polarization configuration has less time to change during one mechanical cycle, which leads to reduced softening in the dynamic shear modulus.

Since the first resonance frequency in torsion is much higher than in bending, there is a larger range of frequencies where the effects of inertia are small and the measured structural response can be interpreted as the material response. Nonetheless, as with the bending experiments, we can apply

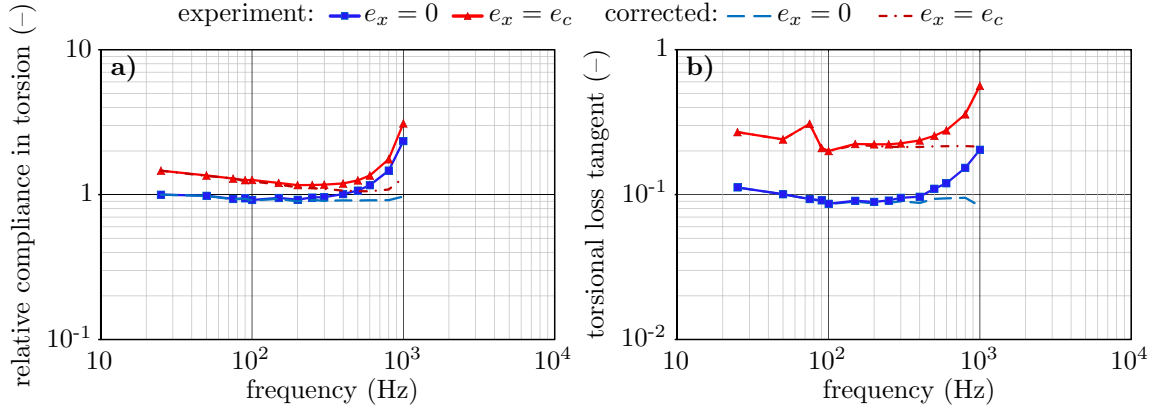


Figure 3.13: Results from Fig. 3.12 after applying the correction in (2.17) to obtain the material response.

the correction derived in (2.17) to the measured response in Fig. 3.12 to obtain an approximation for the material properties, which are shown in Fig. 3.13. The approximation was computed by taking ω_0 in (2.17) as 1300 Hz and 1270 Hz at zero electric field and at the coercive field, respectively. As was the case in bending, the approximated material response is more accurate than the structural response since the compliance and loss tangent do not increase sharply near resonance.

3.3.2 Effect of electrical loading frequency

The electric displacement hysteresis for different electric field frequencies while applying torsional moments was shown previously in Fig. 2.18. There, it was observed that the coercive field increases with electric field frequency (similar to bending) while the mechanical loading frequency did not have an effect. With these results in mind, Fig. 3.14(a) and (b) shows the effect of electric field frequencies of 0.01, 0.1, 0.5, and 1.0 Hz on the relative shear modulus and loss tangent in torsion, respectively. The amplitude of the electric field was 2 MV/m while the mechanical bending was fixed by applying 6.0 V_{pp} to the horizontal Helmholtz coils at a frequency of 75 Hz. The behavior of the shear modulus and torsional loss tangent are the same as in bending. The softening in the shear modulus during domain switching (around the coercive field) becomes more pronounced for increasing electric field frequency while away from domain switching, the shear modulus varies linearly with the electric field. The increased loss tangent during domain switching also becomes more pronounced with increasing electric field frequency while varying linearly with electric field

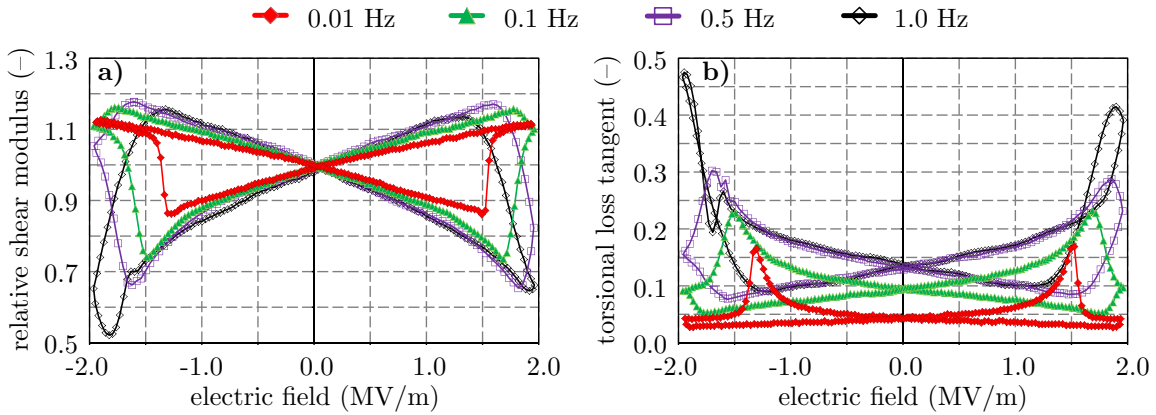


Figure 3.14: Experimental data of (a) relative shear modulus (normalized by the modulus without electric bias) and (b) loss tangent in torsion vs. electric field for triangle-wave electric field (2.0 MV/m amplitude) frequencies of 0.01, 0.1, 0.5, and 1.0 Hz and constant torsional vibration at 75 Hz.

away from domain switching. Although the behavior of the incremental complex shear modulus during domain switching has not been reported in the literature, the mechanisms giving rise to variations in the moduli and loss tangents are likely the same since the behavior is the same. Therefore, the softening in shear modulus can be attributed to domain wall motion (which increases for higher electric field cycling frequencies) as well as different overall elastic moduli due to changing volume fractions of differently-polarized domains. Likewise, the increased damping during domain switching can be attributed to the dissipation caused by domain wall motion. Increasing the electric field frequency increases the velocity and driving force on domain walls, which increases dissipation. The linear behavior in both the shear modulus and loss tangent can be attributed to the electric field dependence of the the elastic constants.

Comparing the effect of electrical frequency in bending and torsion (in Figs. 3.9 and 3.14) quantitatively, the relative Young modulus varies from 0.6 to 1.2 and the relative shear modulus varies from 0.5 to 1.2 for an electric field frequency of 1.0 Hz. The loss tangent in bending is as high as 0.45 and the loss tangent in torsion is as high as 0.47. Thus, the difference in the response of PZT in bending and torsion for different electric field frequencies is not large and likely only due to variation in material properties between specimens – Figs. 3.9 and 3.14 were obtained from different specimens from the same supplier. This also explains why the softening in the shear modulus and the increased loss tangent in torsion appear at higher electric fields than the corresponding values

in bending; the coercive field shown in Fig. 2.18 for the specimen tested in torsion was higher than that seen in Fig. 2.17 for the specimen tested in bending. The average coercive field was 1.3 MV/m for the bending specimen and 1.5 MV/m for the torsion specimen.

3.4 Discussion

The new capabilities brought by BES allowed for the determination of the dynamic Young and shear moduli and their associated loss tangents of PZT. Such experiments give insight into how the kinetics of domain switching affect the material’s viscoelastic response. Also, improved accuracy was observed when performing experiments in vacuum compared to air (current methods such as BVS have only tested materials in air), especially for the loss tangent near resonance. This will be confirmed by examining the energy dissipation by acoustic waves. Possible sources of error including the frequency response of the coils will be quantified.

3.4.1 Viscoelasticity of ferroelectrics

Damping in ferroelectric ceramics due to domain switching was previously investigated in the sub resonance, low-frequency regime (Chaplya and Carman, 2001b, 2002a,b; Jiménez and Vicente, 2000). For example, the damping of PZT at frequencies up to 40 Hz was studied by DMA (Jiménez and Vicente, 2000) while quasistatically varying the electric bias (at approximately 2 mHz). The combination of mechanical compression and electric fields also led to increased damping and variations of the effective Young modulus (Chaplya and Carman, 2002a), yet these effects were far less pronounced than those in (Jiménez and Vicente, 2000). Indeed, applying compressive stresses (on the order of 1-100 MPa) can align domains (Chaplya and Carman, 2001a) and thereby yield significant damping by promoting non-180° domain wall motion, as observed in (Asare et al., 2012; Carman and McKnight, 2002) for PZT. Our results show that the observed damping and softening occur across wide ranges of mechanical frequencies and alter the specimen’s (anti-)resonance frequencies.

The variations of the viscoelastic properties can be attributed to domain wall motion and, more specifically, their interactions with lattice defects. These interactions dissipate energy (Kontsos and Landis, 2009; Schrade et al., 2007) and offer stress relaxation mechanisms through microstructural domain reconfiguration (Ahluwalia and Cao, 2001; Arlt and Sasko, 1980; Cheng et al., 1996; Little,

1955; Merz, 1954). As shown for single-crystalline PZN-PT (Yin and Cao, 2001), the modulus variations are partly due to elastic anisotropy, since 90° -switched domains reduce the apparent modulus in the loading direction. The distributed grain orientations in the investigated polycrystals lead to more gradual moduli and damping changes (Burlage, 1965).

The methods presented here allow for mechanical testing over a significantly wider frequency range in bending and torsion compared to previous studies (Chaplya and Carman, 2001b, 2002a,b; Jiménez and Vicente, 2000), as shown in Figs. 3.7 and 3.12. Our results show that stiffness and damping in bending and torsion vary in a highly-nonlinear fashion during domain switching near the coercive field, resulting in considerable dynamic moduli softening and large increases of the loss tangent over the full range of frequencies investigated. In contrast to the equilibrium viscoelastic properties at low electric field frequencies (Yin and Cao, 2002), our results at higher frequencies display a clear dependence on the rate of the electric field, as shown in Figs. 3.9 and 3.14, for both bending and torsion experiments, respectively. The viscoelastic relaxation mechanisms become more pronounced (i.e., they result in larger damping) when the electric field frequency increases. In addition, by comparing results in bending and shearing, the relative changes in moduli and their associated loss tangents are comparable, which indicates viscoelastic isotropy. Going beyond all previous studies, we have shown that these effects persist throughout the full structural resonance spectrum of the specimen with maximal damping increases close to resonance, which hints at new opportunities for ferroelectric active damping technologies.

3.4.2 Parasitic damping due to surrounding air

Figs. 3.4 and 3.11 show that the damping is slightly higher in air than under vacuum (becoming more noticeable near resonance), as shown previously for quartz tuning forks at 32 kHz (Christen, 1983) and for various geometries of vibrating plates in (Stephens and Scavullo, 1965). Moreover, the difference between air and vacuum is higher for bending tests due to the larger deflection amplitude of the specimen (the amplitude dependence of parasitic air damping has also been observed previously (Adams and Bacon, 1973; Stephens and Scavullo, 1965)). For the frequencies tested and the small amplitude deflection of the specimen (viz. at high Reynolds number), it is assumed that the viscous effects of the air are small and, instead, the generation of acoustic waves due to specimen motion is the primary damping mechanism. Thus, the specimen, in bending, transmits more energy into the environment by acoustic waves, causing a larger discrepancy between the damping

measured in air and under vacuum as illustrated in Fig. 3.15. The loss tangent is a measure of the apparent energy dissipated by the specimen: the more energy carried away by acoustic waves, the higher the loss tangent measured. Fig. 3.16 summarizes this result by plotting the relative error between the average maximum damping (during one cycle of the electric field) obtained in air and vacuum for both the loss tangent in bending and in torsion versus the mechanical loading frequency. From Figs. 3.4 and 3.11, as well as from results from further experiments, the average maximum damping values were obtained by computing the average of the two damping peaks (between the negative and positive electric field peaks). The electric cycling frequency was constant at 0.1 Hz. As seen in Fig. 3.16(a), the error increases substantially close to certain frequencies: approximately 130 Hz and 1200 Hz. These frequencies correspond to the resonance frequencies of the specimen, leading to large vibration amplitudes which in turn dissipate more energy by acoustic waves. Although the first resonance in torsion is at 1300 Hz, there is still an increase in the torsional loss tangent error around 130 Hz due to the resonance in bending as seen in Fig. 3.16(b); in practice pure bending or torsion is not achieved. Thus, small misalignments between the magnet clamp and coils can lead to bending motion when attempting to apply torsional moments and vice versa. Since the second bending resonance frequency is near the first torsional resonance frequency, the loss tangent error in bending and torsion both start to increase at 1200 Hz. One can quantitatively compare Figs. 3.16(a) and 3.16(b) to see that the loss tangent error in bending is approximately an order of magnitude larger than that of the torsional loss tangent.

The results given in Fig. 3.16 are also consistent with the following results, obtained by fixing the mechanical frequency at 75 Hz and by only modifying the electric field frequency from 0.01 Hz to 1.5 Hz, as shown in Fig. 3.17. In both bending and torsion, the higher the electric field frequency is, the higher the error is. The value of the error may rise up to 129% and 48% for the bending and torsion experiments, respectively. The reason for this growing difference is due to the increased softening in the elastic moduli for higher electric field frequencies and resulting polarization evolution, as shown in Figs. 3.9(a) and 3.14(a). The higher the softening, the larger the deflection amplitude, which increases the dissipation by acoustic waves. Furthermore, for a fixed mechanical bending frequency, a decrease in the modulus due to domain switching brings the specimen slightly closer to resonance, which also causes an increase in the deflection amplitude.

The parasitic damping of air has been documented e.g. in (Adams and Bacon, 1973; Stephens and Scavullo, 1965) and is oftentimes modeled by the introduction of a velocity-dependent damping

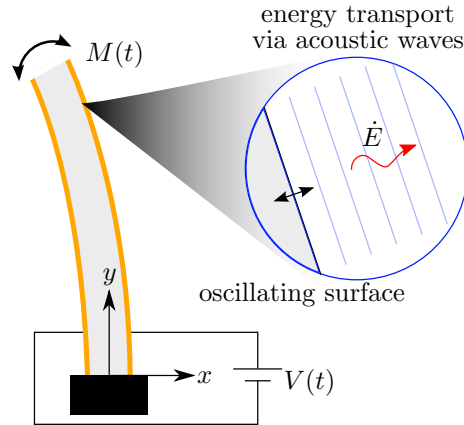


Figure 3.15: Illustration of how the bending vibration of the specimen generates acoustic waves at the surface that propagate and thus transmit energy into the surrounding air causing parasitic damping. 1D acoustic wave theory is applied to quantify this effect using the geometry shown; each point on the surface of the specimen approximately oscillates in the x -direction giving rise to acoustic waves propagating in the same direction. The surface also oscillates in the normal direction during torsion due to the rectangular cross section of the specimens. Energy dissipated due to the generation of vortices from the edges of the specimen is neglected.

force into the governing equation for beam bending or torsion (Hosaka et al., 1995; Meirovitch, 1997). Typically (see e.g. (Anderson et al., 1996)), that damping force is taken to be linear or quadratic in velocity, and parameters are obtained by fitting to experimental data. Here, instead of assuming a particular form of the damping force due to the surrounding air, the increased energy dissipation seen in experiments can be quantified by considering 1D inviscid acoustic wave theory (e.g. see (Liepmann and Roshko, 1957)) applied to the problem illustrated in Fig. 3.15, since specimen deflections are small (and neglecting energy dissipation due to vortex generation on the edges of the specimen). The governing wave equations for the density perturbation and velocity are, respectively,

$$\frac{\partial^2 \rho'}{\partial t^2} - a^2 \frac{\partial^2 \rho'}{\partial x^2} = 0, \quad \frac{\partial^2 v}{\partial t^2} - a^2 \frac{\partial^2 v}{\partial x^2} = 0, \quad (3.1)$$

where ρ' denotes the relative perturbation of the density, ρ_0 is the ambient density, a is the wave speed, x stands for the 1D spatial coordinate, and t denotes time. Considering only the forward propagating wave generated by the moving specimen surface, the general solution for the velocity is $v(x, t) = f(x/a - t)$ for a function f that satisfies the boundary conditions. The beam deflection is of the form $w(t) = \hat{w} \sin \omega t$, so that the velocity boundary condition is $v(0, t) = \dot{w}(t) = \hat{w} \omega \cos \omega t$.

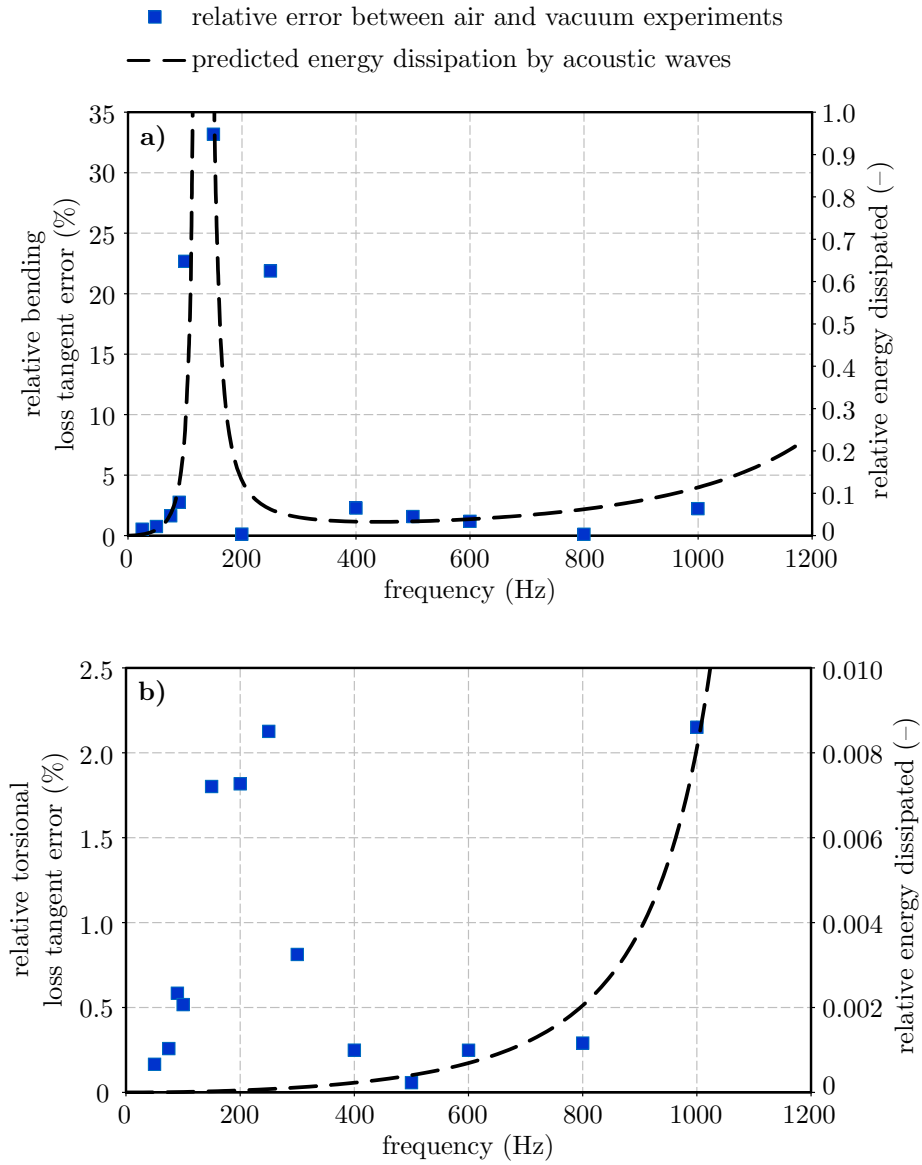


Figure 3.16: Relative damping error of the average maximum loss tangent in air compared to under vacuum as a function of the mechanical loading frequency of (a) bending and (b) torsion tests performed under cyclic electric fields with a frequency of 0.1 Hz. The theoretical relative error in bending and torsion is given by $D_{\text{bending}}/D_{\text{bending}}^0$ and $D_{\text{torsion}}/D_{\text{torsion}}^0$, respectively.

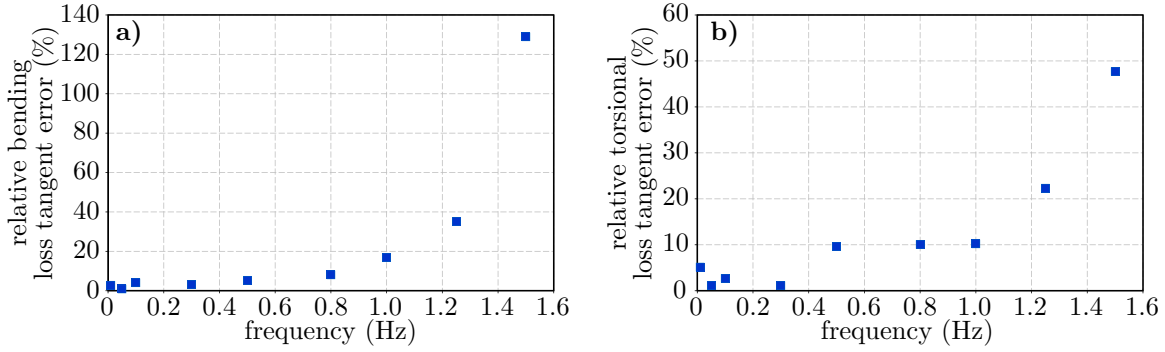


Figure 3.17: Relative damping error of the average maximum loss tangent in air compared to under vacuum as a function of the applied electric field frequency for (a) bending and (b) torsion tests performed with a mechanical loading at 75 Hz.

Therefore, the solution for the velocity can be found and substituted into the continuity equation $\partial\rho'/\partial t = -\partial v/\partial x$ to obtain the density perturbation, which yields

$$\begin{aligned}\rho'(x, t) &= (\hat{w} \omega/a) \cos(\omega(x/a - t)), \\ v(x, t) &= \hat{w} \omega \cos(\omega(x/a - t)).\end{aligned}\tag{3.2}$$

Finally, the pressure distribution p about the ambient pressure p_0 is related to the density change by an isentropic process $p/p_0 = (\rho/\rho_0)^\gamma$, where $\rho = \rho_0(1 + \rho')$ is the total density distribution and γ is the ratio of specific heats. The pressure for small density perturbations is then

$$p = p_0 (1 + \rho')^\gamma \approx p_0(1 + \gamma\rho').\tag{3.3}$$

The energy flux \dot{E} of the acoustic waves is the product of the velocity and the pressure shown in (3.2) and (3.3), respectively (Rayleigh, 1945). The dissipation of the acoustic waves per unit area is related to the root mean square (RMS) value of the energy flux, viz.

$$\dot{E}_{\text{RMS}} = (\omega/2\pi) \int_0^{2\pi/\omega} p(x, t)v(x, t) dt = \frac{p_0\gamma\hat{w}^2\omega^2}{2a}.\tag{3.4}$$

To compute the total dissipation from acoustic waves in the experiment, we solve for the deflection of the specimen, assuming a dynamic Euler-Bernoulli beam whose amplitude of deflection $\hat{w}(y)$ is derived in Appendix C. Using this expression, the total dissipation in bending, D_{bending} , is found

Table 3.3: Numerical values for STP air (Liepmann and Roshko, 1957).

parameter	symbol	value
ambient pressure	p_0	100 kPa
speed of sound	a	348 m/s
ratio of specific heats	γ	1.4

by integration of \dot{E}_{RMS} over the two opposite faces of the specimen S ,

$$D_{\text{bending}} = 2 \int_S \dot{E}_{\text{RMS}} \, ds = \frac{p_0 \gamma b \omega^2}{a} \int_0^L \hat{w}(y)^2 \, dy. \quad (3.5)$$

To gain a better qualitative impression of (3.5), examine the case of small $\omega \ll \sqrt{EI/(\rho AL^4)}$ (i.e., for mechanical frequencies well below the first resonance frequency), then (3.5) reduces to

$$D_{\text{bending}} = \frac{36 L^5 \hat{M}^2 p \gamma}{5 a b h^6 E^2} \omega^2 + O(\omega^4), \quad (3.6)$$

where \hat{M} is the amplitude of the applied moment. This result agrees with the damping error in bending for different mechanical frequencies (shown in Fig. 3.16(a)) where below the first resonance frequency, the error has a square dependence on ω . Looking at the entire range of frequencies, equation (3.5) is plotted in Fig. 3.16(a) using the specimen's physical parameters in Tab. 3.2 and the parameters for air at standard temperature and pressure (STP) given in Tab. 3.3. The dissipation plotted is normalized by the reference value

$$D_{\text{bending}}^0 = \frac{p \gamma \hat{M}^2 L}{a h \rho E I_z}. \quad (3.7)$$

The dissipation by acoustic waves shows the same behavior as observed in experiments: the air dissipation increases as the mechanical bending frequency increases, and it increases greatly near the specimen's resonance frequencies (where the specimen deflection is largest). The observation that the damping error increases with increasing electric cycling frequency, shown in Fig. 3.17(a), can also be seen by examining (3.6), which shows that the dissipation increases as the Young modulus E decreases (causing larger deflections). This is consistent with experiments of varying electric cycling frequency, where the corresponding Young modulus at maximum damping decreases with increasing electric field frequency due to increased domain wall motion as described previously.

The same expression in (3.5) can be used to compute the dissipation due to air in the torsional case,

$$\begin{aligned} D_{\text{torsion}} &= 2 \int_S \dot{E}_{\text{RMS}} \, ds = \frac{p_0 \gamma \omega^2}{a} \int_0^L \int_{-b/2}^{b/2} (\hat{\alpha}(y)z)^2 \, dz \, dy \\ &= \frac{p_0 \gamma b^3 \omega^2}{12 a} \int_0^L \hat{\alpha}(y)^2 \, dy, \end{aligned} \quad (3.8)$$

where the deflection of the specimen in torsion is due to the twisting angle along the length of the specimen $\hat{w}(y, z) = \hat{\alpha}(y)z$. The twisting angle per unit length is given in Appendix C. The predicted dissipation from (3.8) is also plotted in Fig. 3.16(b) using parameters in Tabs. 3.2 and 3.3 and is normalized by the reference value

$$D_{\text{torsion}}^0 = \frac{2p_0 \gamma b^3 L \hat{M}^2}{3a J_y^2 G \rho}. \quad (3.9)$$

The solution in torsion shows a similar result to the bending case where the dissipation caused by the air increases near resonance (1200 Hz in the torsional case). However, the solution fails to capture the increase in damping near 130 Hz in Fig. 3.16(b). Indeed, the torsion solution assumes pure twisting and thus does not account for the actual multiaxial response of the specimen near the bending resonance frequency at 130 Hz. Well below resonance, i.e. $\omega \ll \sqrt{G/\rho}/L$, (3.8) reduces to

$$D_{\text{torsion}} = \frac{6 b L^3 \hat{M}^2 p_0 \gamma}{a h^2 (b^2 + h^2)^2 G^2} \omega^2 + O(\omega^4). \quad (3.10)$$

Thus, as in bending, due to the increased softening in the modulus as the frequency of the applied electric field on the specimen increases, the damping due to the generation of acoustic waves increases quadratically, as seen in Fig. 3.17(b).

By accounting for the energy flux due to acoustic waves generated by the vibrating specimen, the overall behavior of the damping error for varying mechanical and electrical loading frequencies was well described. Therefore, it can be concluded that the difference in damping measured in air and under vacuum is due to the generation of acoustic waves. This error is small (e.g. at 50 Hz in bending, the difference is 0.5 % compared to vacuum measurements) for low cyclic electric field frequencies and mechanical frequencies away from resonance. Instead, the use of the vacuum chamber is essential for taking high-accuracy measurements of the specimen's damping near resonance and

for soft materials (either low static moduli or moduli that are reduced by e.g. an applied electric field), which both increase the deflection amplitude of the specimen.

3.4.3 Selecting the time constant of the lock-in amplifier

The lock-in amplifier time constant setting was nominally chosen to be 30 ms since it minimized noise in the measured output and allowed the lock-in to respond sufficiently fast to capture changes in the specimen's response. To demonstrate this behavior, the effect of the time constant setting on the measured viscoelastic properties in bending at 50 Hz and an electric field frequency of 0.1 Hz is shown in Fig. 3.18 (the same result holds for the torsion case but is not shown for brevity). Decreasing the time constant to 10 ms (which results in a faster response of the lock-in) only caused small variations, as shown in Fig. 3.18. However, this gave rise to increased noise in the output at 25 Hz. Increasing the time constant to 100 ms (also shown in Fig. 3.18) caused significant smearing of the measured response. Thus, it was concluded that a time constant of 30 ms was ideal for minimizing the effect of the lock-in amplifier on the results obtained for an applied electric field frequency of 0.1 Hz. However, for higher electric field frequencies of 0.5 and 1.0 Hz, which were used to obtain Figs. 3.9 and 3.14, a time constant setting of 30 ms caused smearing of the lock-in output. Therefore, the time constant was decreased to 10 ms for experiments with electric field frequencies of 0.5 and 1.0 Hz. A mechanical frequency of 75 Hz was sufficiently high to allow low-frequency noise to be filtered by the lock-in amplifier (as opposed to e.g. 25 Hz mentioned previously, which resulted in noisy measurements). However, there may still be some smearing of the lock-in output for 1.0 Hz electric field frequencies even with a time constant of 10 ms. Unfortunately, further reduction of the time constant to 3 ms gave rise to a significant amount of noise. Generally, measuring the dynamic stiffness and loss tangent using a lock-in amplifier is difficult in the current setup (or any other setup) when mechanical and electrical frequencies are comparable (i.e. mechanical frequencies below 25 Hz and electrical frequencies above 1.0 Hz). Besides, in this situation, the dynamic moduli and loss tangents would no longer correspond to the *incremental* response and would need to be interpreted differently. Therefore, the case of comparable mechanical and electrical frequencies goes beyond our scope but may be of interest in future work.

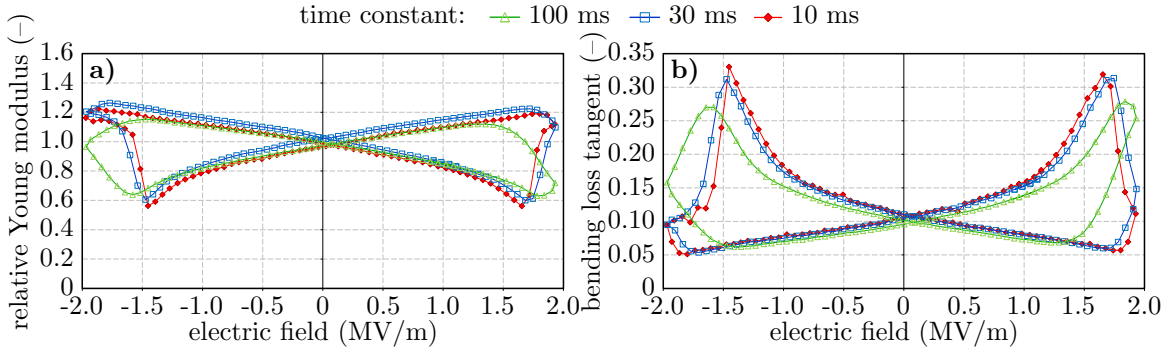


Figure 3.18: The effect of different lock-in amplifier time constants (10, 30, and 100 ms) on the measured viscoelastic stiffness (a) and damping (b). Results are shown for a bending frequency of 50 Hz and a cyclic electric field frequency of 0.1 Hz.

3.4.4 Frequency response of the Helmholtz coils

To compute the loss tangent using (2.9), the phase shift of the coils was measured a priori and subtracted from the lock-in output. To check the accuracy of this correction, experiments were performed using the current as the reference signal for the lock-in using the circuit described in (Lakes, 1998) for BVS (with a 3Ω resistor in series with the coils). Fig. 3.19 shows the loss tangent computed using (2.8) with the current as the reference, the loss tangent measured using the voltage as the reference before removing the phase shift due to the coils, and after correcting for the phase shift using (2.9). The correction collapses the measured data using the voltage reference onto the data taken using the current as a reference (i.e. the loss tangent difference between the two is solely due to the phase shift of the coils and can be measured a priori). Thus, using either (2.8) or (2.9) yields the same result.

When measuring the dynamic moduli, it was assumed previously that the specimen's viscoelastic response was linear. In this way, the reduction in the applied moment amplitude due to the frequency-dependent impedance of the coils in (2.10) does not affect the measured moduli and loss tangents. To check this assumption, both dynamic moduli and their associated loss tangents were measured for different amplitudes of the applied voltage on the coils (and thus different moment amplitudes) and for different frequencies. The effect of a voltage amplitude varying from 2.0 to 7.2 Vpp on the dynamic Young modulus and on the loss tangent is shown in Figs. 3.20(a,b) and 3.20(c,d), respectively. An amplitude of 7.2 Vpp was used in the previous experiments. Similarly, the effect of different amplitudes of the applied voltage to the torsion coils (2.0 to 6.0 Vpp)

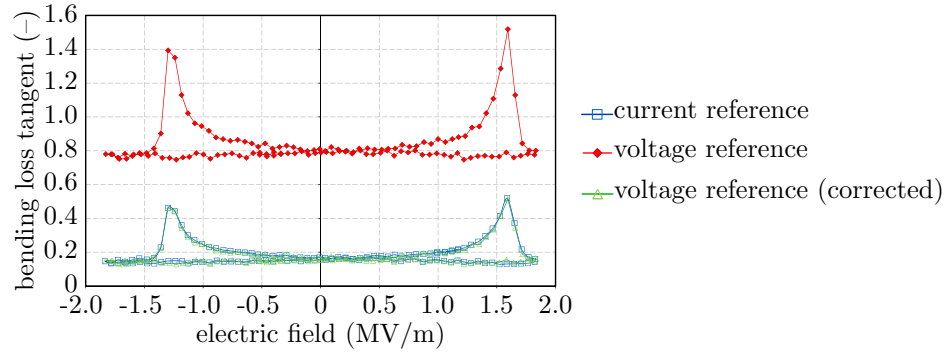


Figure 3.19: Comparison between the loss tangent in bending obtained using the applied voltage to the Helmholtz coils and the resulting current as the reference for the lock-in amplifier. By applying the phase correction measured beforehand, the results collapse.

on the dynamic shear modulus and on the loss tangent is shown in Figs. 3.21(a,b) and 3.21(c,d), respectively, where 6.0 V_{pp} was used in the previous experiments. For both the bending and torsion experiments, for each frequency, the variation of both the moduli and damping with electric field are mainly unchanged for different voltage amplitudes. However, for low applied voltage amplitudes, the deflection/twist of the specimen becomes smaller (decreasing the signal to noise ratio) thereby causing oscillations in the measurements (e.g. for 2.0 V_{pp} and 25 Hz in the torsional case shown in Fig. 3.21(a,c)). Since there were only small variations in the moduli and damping between different applied voltage amplitudes, the deformation of the material is indeed in the linear viscoelastic regime and the measured quantities are unaffected by variations in the amplitude of the applied moment arising from the frequency response of the Helmholtz coils.

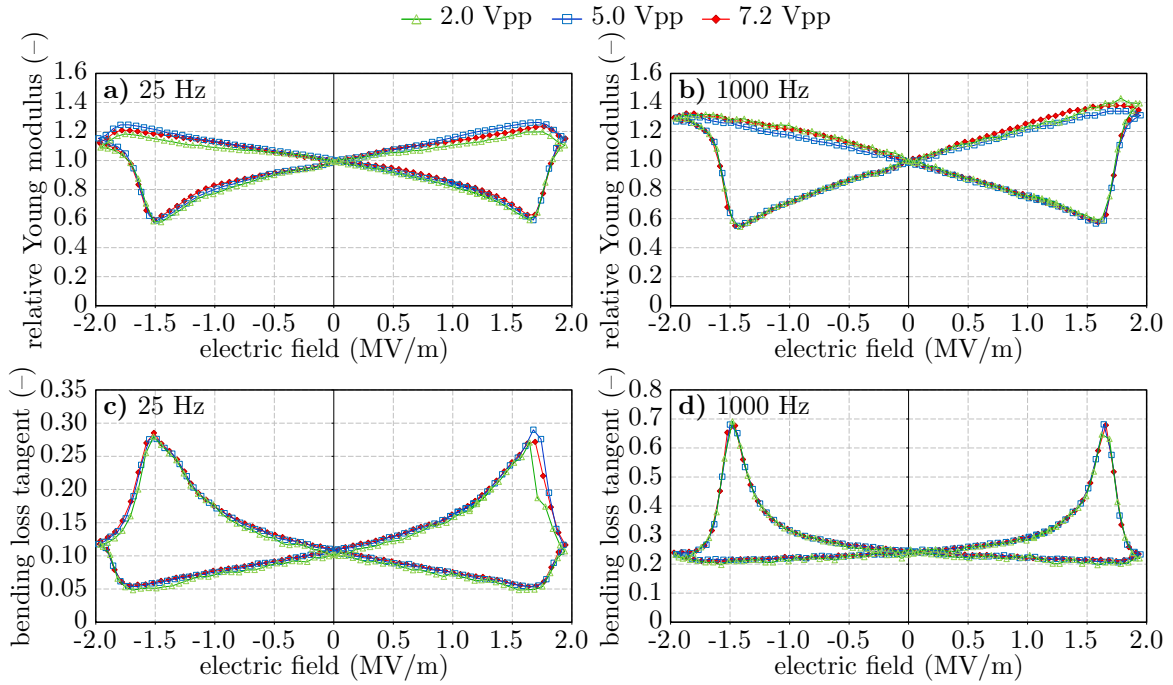


Figure 3.20: Effect of different amplitudes of the applied voltage to the (bending) Helmholtz coils on the measured viscoelastic response. (a) and (b) show the relative Young modulus for mechanical frequencies of 25 and 1000 Hz, respectively. (c) and (d) show the bending loss tangent for mechanical frequencies of 25 and 1000 Hz, respectively. Each experiment was performed for a fixed electric field cycling frequency of 0.1 Hz.

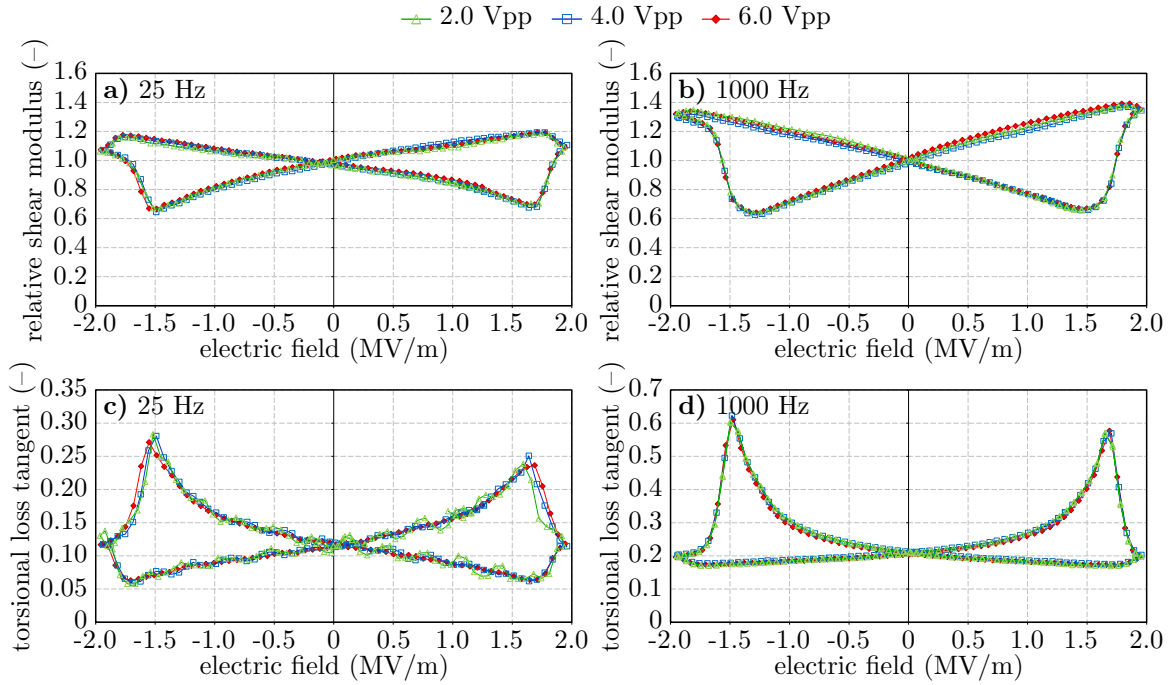


Figure 3.21: Effect of different amplitudes of the applied voltage to the (torsion) Helmholtz coils on the measured viscoelastic response. (a) and (b) show the relative shear modulus for mechanical frequencies of 25 and 1000 Hz, respectively. (c) and (d) show the torsional loss tangent for mechanical frequencies of 25 and 1000 Hz, respectively. Each experiment was performed for a fixed electric field cycling frequency of 0.1 Hz.

Chapter 4

A Continuum Model of the Viscoelasticity of Ferroelectrics

The BES method has allowed, for the first time, the viscoelastic response of ferroelectrics to be measured throughout the entire electric displacement hysteresis loop. Moreover, the influence of both electric field and mechanical cycling frequencies was characterized. Based upon current understanding of domain walls, the measured increase in damping and decrease in stiffness near the coercive field were attributed to domain switching. Using guidance from experiments, a model was developed to predict the viscoelastic response. By incorporating various material properties into the model and simulating their influence on the viscoelastic response, guidelines for creating new materials with optimal properties (such as large damping increases during domain switching) were determined.

4.1 Background and motivation

The equilibrium response of ferroelectrics has been extensively studied, beginning with the theories of [Landau \(1937\)](#) and [Devonshire \(1949, 1951\)](#). They postulated a multi-well energy landscape for ferroelectric materials with different local minima corresponding to different possible orientations of spontaneous polarization. The various temperature-dependent parameters of the energy landscape can be appropriately chosen for different materials to predict experimentally-observed phase transformations (i.e. ferroelectric to non-ferroelectric phases) as well as different types of experimentally-observed transformations including first-order or second-order transitions ([Fatuzzo](#)

and Merz, 1967). However, in those examples the proposed energy landscape was mainly used to gain insight into the behavior of single-domain single crystals. Alternatively, starting from an atomistic point of view, the dielectric properties of piezoelectrics and ferroelectrics at different temperatures have been predicted by Cochran (1959, 1961) and Takashige et al. (1982) through analyzing crystal lattice dynamics and as well by Chen (2011) and Zhang (2004) using atomistic simulations. More recently, predicting full-field behavior in ferroelectric polydomain single-crystals has been accomplished using microscopic phase field models (Su and Landis, 2007; Xu et al., 2010; Zhang and Bhattacharya, 2005a,b), which typically utilize a Landau Devonshire-type energy but allow for microstructure evolution through a kinetic relation. Finally, on the continuum level, the relaxation-based approaches of (Kinderlehrer, 1987; Shu and Bhattacharya, 2001) compute the influence of ferroelectric domains through the effective behavior of lamination-type microstructure. These methods have been applied in numerous previous studies (Arockiarajan and Sansour, 2008; Chen and Lynch, 1998; Elhadrouz et al., 2005; Huber, 2005; Huber and Fleck, 2001; Hwang et al., 1995; Iwata et al., 2007; Xu et al., 2010). For polycrystalline materials, there are many existing phenomenological models (Arlt, 1996; Cocks and McMeeking, 1999; Landis, 2002; Ooi et al., 2007; Pasco and Berry, 2004; Yu et al., 2002) and thermodynamics-based models (Arockiarajan et al., 2006; Bassiouny et al., 1988a,b; Bassiouny and Maugin, 1989; Hwang et al., 1998; Kim, 2011; Miehe and Rosato, 2011). For an overview of such methods, the reader may refer to the review papers by Kamlah (2001) and Landis (2004). These various modeling approaches have been able to show how the electrical hysteresis depends on material microstructure (Ahluwalia and Cao, 2001; Arlt and Sasko, 1980; Cheng et al., 1996; Little, 1955; Merz, 1954) and on free charges (Kanata et al., 1987; Setter et al., 2006; Takeuchi et al., 1994, 1997), which both give rise to size effects (Gaynutdinov et al., 2013; Lee and Aksay, 2001; Lu et al., 2000; Merz, 1956; Miller and Savage, 1960; Ng et al., 2009; Shih et al., 1994; Tura et al., 1997).

While many models have been developed to predict the time-dependent dielectric response of ferroelectrics (in particular for applications in electronics), the development of models to predict their viscoelastic response is more limited, in particular during domain switching. Predicting the viscoelastic response under low electric fields (below the coercive field in the linear regime) is typically accomplished by introducing complex elastic and piezoelectric constants (Herbiet et al., 1989; Holland, 1967; Robels et al., 1989). In addition, the variation of other mechanical properties such as strength with applied electric fields have been modeled by Fu and Zhang (2000b). For large

electric fields it has been shown experimentally that the piezoelectric constants change (Kamiya et al., 1997; Yang et al., 2000) and that during domain switching, the elastic constants change (Burlage, 1965). Therefore, it becomes difficult to capture the nonlinear behavior of the viscoelastic response through electric field-, stress-, and temperature-dependent complex elastic and piezoelectric constants. Alternatively, incorporating microstructural evolution into the elastic moduli enables a more physics-based approach.

As the viscoelastic response of ferroelectrics during domain switching observed in experiments has been attributed to microstructural processes such as domain switching and domain wall motion, we seek to create a model that incorporates such phenomena. There exist many approaches to describing the properties and kinetics of domain walls (Genenko et al., 2013; Ishibashi, 1989, 1990; Ishibashi and Salje, 2004; Kliem and Kuehn, 2011; Kruger, 1976; Schmidt, 1981; Song and Yang, 2009; Viehland and Chen, 2000) such as domain wall size, domain wall energy, and driving force, which are used to predict the macroscopic electric displacement hysteresis. Incorporating domain wall motion (due to thermal oscillations) to predict viscoelastic properties was explored by Arlt et al. (1987) and Gridnev (2007). Modeling the viscoelastic properties during domain switching has only been of interest in (Jiménez and Vicente, 2000), where the analysis was mainly qualitative and only applied during domain switching. Nonetheless, predicting the viscoelastic response of ferroelectrics throughout the entire electric displacement hysteresis for arbitrary electrical and mechanical loading histories is still an open challenge. A thermodynamics-based continuum model that incorporates microstructure evolution along with a method for extracting the viscoelastic response of the material is presented.

4.2 Review of electrostatics in a continuum

Before developing a model of ferroelectricity, the basic equations of electrostatics in polarizable materials are reviewed (see e.g. (Grindlay and Haar, 2013; Landau et al., 1984) for more details). First, Maxwell’s equation is

$$\operatorname{div} \mathbf{e} = \frac{q}{\epsilon_0}, \quad (4.1)$$

where $\mathbf{e} = -\operatorname{grad} \phi$ is the electric field (and ϕ is the electric potential), q is the total charge, and $\epsilon_0 = 8.854 \times 10^{-12}$ F/m is the vacuum permittivity. The total charge is due to so-called “free” and “bound” charges corresponding to macroscopically-applied charges (due to e.g. electrodes) and

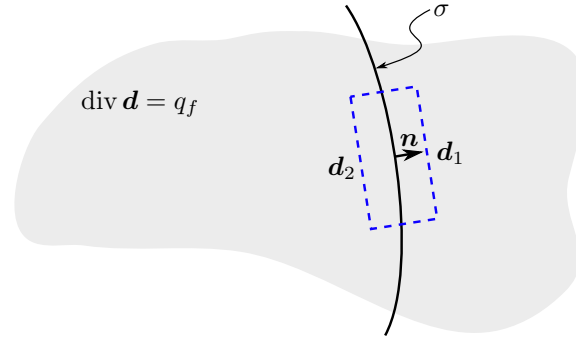


Figure 4.1: Illustration of a volume enclosing an interface with charge per unit area σ and unit normal \mathbf{n} pointing from side 2 to side 1 with electric displacements \mathbf{d}_2 and \mathbf{d}_1 , respectively.

microscopic charges (e.g. due to ions), respectively. On the macroscale, instead of resolving the microscopic charges, only the apparent electric dipole per unit volume formed by those charges is important. This apparent electric dipole is characterized by the material's polarization \mathbf{p} , such that $q_b = -\text{div } \mathbf{p}$ is the bound charge. Then, the total charge is $q = q_f + q_b$, where q_f are the free charges. Consequently, (4.1) becomes

$$\text{div}(\epsilon_0 \mathbf{e} + \mathbf{p}) \equiv \text{div } \mathbf{d} = q_f, \quad (4.2)$$

where we define the electric displacement $\mathbf{d} = \epsilon_0 \mathbf{e} + \mathbf{p}$. It will be useful later to find the form of (4.2) applied to a boundary, which can be found by considering (4.2) inside a volume enclosing an interface with surface charge density σ as shown in Fig. 4.1. Using the divergence theorem and taking the limit as the volume shrinks to zero about the interface gives the condition

$$\sigma = \llbracket \mathbf{d} \rrbracket \cdot \mathbf{n} = (\mathbf{d}_1 - \mathbf{d}_2) \cdot \mathbf{n}. \quad (4.3)$$

A collection of free charges can be placed into an electric field and arranged by an external mechanism that performs work on the charges. The force on a charge q is $\mathbf{F} = -q \text{grad } \phi$. The work required to move a charge to a position \mathbf{x} in an electric field from infinity is

$$\begin{aligned} W_q(\mathbf{x}) &= \lim_{|\mathbf{x}_0| \rightarrow \infty} \int_{\mathbf{x}_0}^{\mathbf{x}} \mathbf{F} d\mathbf{x}' = \lim_{|\mathbf{x}_0| \rightarrow \infty} \int_{\mathbf{x}_0}^{\mathbf{x}} -q \text{grad } \phi d\mathbf{x}' = \lim_{|\mathbf{x}_0| \rightarrow \infty} -q [\phi(\mathbf{x}) - \phi(\mathbf{x}_0)] \\ &= -q\phi(\mathbf{x}), \end{aligned} \quad (4.4)$$

where we assume the potential decays to zero at infinity. A useful quantity that will appear later is the power expended (or the rate of work done on the charge) due to a changing electric field,

$$\mathcal{P}_q = \dot{W}_q = -q\dot{\phi}. \quad (4.5)$$

The minus sign is due to the convention that positive charges are attracted by negative electric potentials and vice versa. Thus moving a positive charge from infinity to a position with positive potential will do negative work since the charge is being moved in the direction of the force on it from the electric field.

4.3 Constitutive equations

We begin developing a model of ferroelectricity by considering the constitutive equations. In particular, we choose the primal variables to be the stress $\boldsymbol{\sigma}$ and electric field \mathbf{e} with dual variables of strain $\boldsymbol{\varepsilon}$ and electric displacement \mathbf{d} , respectively. It is noted that for the ferroelectric ceramics studied in experiments, the mechanical deformations are assumed to be small due to the large stiffness of the materials. Therefore, the deformation of the material is assumed to be characterized by the small-strain tensor $\boldsymbol{\varepsilon} = \text{sym}(\text{grad } \mathbf{u})$, where \mathbf{u} is the displacement field.

First, the general equations of piezoelectricity for the electric displacement and strain are given by (Uchino, 1997)

$$\begin{aligned} \mathbf{d} &= \boldsymbol{\varepsilon}\mathbf{e} + \mathbf{h}\boldsymbol{\sigma}, & \boldsymbol{\varepsilon} &= \mathbb{S}\boldsymbol{\sigma} + \mathbf{h}^\top\mathbf{e}, \\ d_i &= \varepsilon e_i + h_{ijk}\sigma_{jk}, & \varepsilon_{jk} &= \mathbb{S}_{jklm}\sigma_{lm} + h_{jki}e_i, \end{aligned} \quad (4.6)$$

respectively, where \mathbf{h} is the third-order piezoelectric tensor and \mathbb{S} is the fourth-order compliance tensor. In piezoelectricity, the total polarization in the material is the dielectric and piezoelectric response such that $\mathbf{p} = \varepsilon_0\chi\mathbf{e} + \mathbf{h}\boldsymbol{\sigma}$ in equation (4.2) and $\varepsilon = \varepsilon_0(1 + \chi)$ is the permittivity, where χ is the relative permittivity. In ferroelectricity, the material exhibits a spontaneous (average) polarization \mathbf{p}_s and corresponding eigenstrain $\boldsymbol{\varepsilon}^r(\mathbf{p}_s)$ (in the following, we drop the subscript s for brevity such that $\mathbf{p}_s \rightarrow \mathbf{p}$). Then, the equations of piezoelectricity in (4.6) are extended to

ferroelectrics, where we have

$$\mathbf{d} = \epsilon \mathbf{e} + \mathbf{h}(\mathbf{p})\boldsymbol{\sigma} + \mathbf{p} + \mathbf{d}^e(\mathbb{S}, \boldsymbol{\sigma}), \quad \boldsymbol{\varepsilon} = \mathbb{S}(\mathbf{e}, \mathbf{p})\boldsymbol{\sigma} + \mathbf{h}(\mathbf{p})^\top \mathbf{e} + \boldsymbol{\varepsilon}^r(\mathbf{p}). \quad (4.7)$$

Note that in general, \mathbf{h} depends on the spontaneous polarization. Moreover, using guidance from experiments, we let the compliance tensor depend on electric field and spontaneous polarization. Note that the last term \mathbf{d}^e needs to be introduced since we allow the compliance to depend on the electric field and we must satisfy the Maxwell relations (shown later in (4.13)). This term can be thought of as a contribution from electrostriction. To find the expression for \mathbf{d}^e , we assume the constitutive equations are derived from an energy function $\psi(\boldsymbol{\sigma}, \mathbf{e}, \mathbf{p})$ such that

$$\mathbf{d} \equiv \frac{\partial \psi}{\partial \mathbf{e}}, \quad \boldsymbol{\varepsilon} \equiv \frac{\partial \psi}{\partial \boldsymbol{\sigma}}. \quad (4.8)$$

Integrating the constitutive equation for strain results in

$$\psi(\boldsymbol{\sigma}, \mathbf{e}, \mathbf{p}) = \frac{1}{2} \boldsymbol{\sigma} \cdot \mathbb{S}(\mathbf{e}, \mathbf{p})\boldsymbol{\sigma} + \boldsymbol{\sigma} \cdot \mathbf{h}(\mathbf{p})^\top \mathbf{e} + \boldsymbol{\sigma} \cdot \boldsymbol{\varepsilon}^r(\mathbf{p}) + f(\mathbf{e}, \mathbf{p}). \quad (4.9)$$

Then, computing the electric displacement from the potential yields

$$\mathbf{d} = \frac{\partial \psi}{\partial \mathbf{e}} = \frac{1}{2} \boldsymbol{\sigma} \cdot \frac{\partial \mathbb{S}(\mathbf{e}, \mathbf{p})}{\partial \mathbf{e}} \boldsymbol{\sigma} + \boldsymbol{\sigma} \cdot \mathbf{h}(\mathbf{p})^\top + \frac{\partial f(\mathbf{e}, \mathbf{p})}{\partial \mathbf{e}}. \quad (4.10)$$

Comparing with the desired form of the electric displacement in (4.7) with (4.10), it can be seen that

$$\begin{aligned} \epsilon \mathbf{e} + \mathbf{p} + \mathbf{d}^e(\mathbb{S}, \boldsymbol{\sigma}) &= \frac{1}{2} \boldsymbol{\sigma} \cdot \frac{\partial \mathbb{S}(\mathbf{e}, \mathbf{p})}{\partial \mathbf{e}} \boldsymbol{\sigma} + \frac{\partial f(\mathbf{e}, \mathbf{p})}{\partial \mathbf{e}} \\ \Rightarrow \mathbf{d}^e(\mathbb{S}, \boldsymbol{\sigma}) &= \frac{1}{2} \boldsymbol{\sigma} \cdot \frac{\partial \mathbb{S}(\mathbf{e}, \mathbf{p})}{\partial \mathbf{e}} \boldsymbol{\sigma}, \quad f(\mathbf{e}, \mathbf{p}) = \frac{1}{2} \epsilon \mathbf{e} \cdot \mathbf{e} + \mathbf{e} \cdot \mathbf{p}. \end{aligned} \quad (4.11)$$

Therefore, putting everything together, the energy is given by

$$\psi(\boldsymbol{\sigma}, \mathbf{e}, \mathbf{p}) = \frac{1}{2} \boldsymbol{\sigma} \cdot \mathbb{S}(\mathbf{e}, \mathbf{p})\boldsymbol{\sigma} + \boldsymbol{\sigma} \cdot \mathbf{h}(\mathbf{p})^\top \mathbf{e} + \boldsymbol{\sigma} \cdot \boldsymbol{\varepsilon}^r(\mathbf{p}) + \frac{1}{2} \epsilon \mathbf{e} \cdot \mathbf{e} + \mathbf{e} \cdot \mathbf{p}, \quad (4.12)$$

which can be shown to satisfy the Maxwell relation

$$\frac{\partial^2 \psi}{\partial \boldsymbol{\sigma} \partial \mathbf{e}} = \frac{\partial^2 \psi}{\partial \mathbf{e} \partial \boldsymbol{\sigma}} \quad \Rightarrow \quad \frac{\partial \boldsymbol{\varepsilon}}{\partial \mathbf{e}} = \frac{\partial \mathbf{d}}{\partial \boldsymbol{\sigma}}. \quad (4.13)$$

In general, to satisfy material frame indifference, the dependencies of the compliance and piezoelectric tensor on electric field and spontaneous polarization should be of the form

$$\mathbb{S}(\mathbf{e}, \mathbf{p}) \rightarrow \mathbb{S}(|\mathbf{e}|, |\mathbf{p}|, \mathbf{e} \cdot \mathbf{p}, \dots), \quad \mathbf{h}(\mathbf{p}) \rightarrow \mathbf{h}(|\mathbf{p}|, \dots). \quad (4.14)$$

However, based on experiments, we only consider the $|\mathbf{p}|$ and $\mathbf{e} \cdot \mathbf{p}$ terms for the compliance and the $|\mathbf{p}|$ term for the piezoelectric tensor. As a result, the energy satisfies material frame indifference. That is, considering an arbitrary rotation matrix \mathbf{R} ,

$$\psi(\mathbf{R} \cdot \boldsymbol{\sigma} \mathbf{R}, \mathbf{R} \mathbf{e}, \mathbf{R} \mathbf{p}) = \psi(\boldsymbol{\sigma}, \mathbf{e}, \mathbf{p}), \quad \forall \quad \mathbf{R} \in SO(3). \quad (4.15)$$

To follow the general framework of solving problems in solid mechanics, we transform the energy into a function of strain, $\psi(\boldsymbol{\sigma}, \mathbf{e}, \mathbf{p}) \rightarrow \psi^*(\boldsymbol{\varepsilon}, \mathbf{e}, \mathbf{p})$. Therefore, we perform a Legendre transform (we rewrite the function $\psi(\boldsymbol{\sigma}, \mathbf{e}, \mathbf{p})$ in terms of its slope, $\boldsymbol{\varepsilon} = \partial \psi / \partial \boldsymbol{\sigma}$),

$$\psi^*(\boldsymbol{\varepsilon}, \mathbf{e}, \mathbf{p}) = \sup_{\boldsymbol{\sigma}} [\boldsymbol{\varepsilon} \cdot \boldsymbol{\sigma} - \psi(\boldsymbol{\sigma}, \mathbf{e}, \mathbf{p})], \quad (4.16)$$

which yields a unique transform since $\psi(\boldsymbol{\sigma}, \mathbf{e}, \mathbf{p})$ is a convex function in $\boldsymbol{\sigma}$. Solving for the maximizer $\boldsymbol{\sigma}^*$,

$$\begin{aligned} \boldsymbol{\varepsilon} &= \frac{\partial \psi}{\partial \boldsymbol{\sigma}}(\boldsymbol{\sigma}^*, \mathbf{e}, \mathbf{p}) = \mathbb{S}(\mathbf{e}, \mathbf{p}) \boldsymbol{\sigma}^* + \mathbf{h}(\mathbf{p})^\top \mathbf{e} + \boldsymbol{\varepsilon}^r(\mathbf{p}) \\ \Rightarrow \quad \boldsymbol{\sigma}^* &= \mathbb{S}(\mathbf{e}, \mathbf{p})^{-1} [\boldsymbol{\varepsilon} - \mathbf{h}(\mathbf{p})^\top \mathbf{e} - \boldsymbol{\varepsilon}^r(\mathbf{p})] \equiv \mathbb{S}(\mathbf{e}, \mathbf{p})^{-1} \boldsymbol{\varepsilon}^e, \end{aligned} \quad (4.17)$$

where we define the elastic strain: $\boldsymbol{\varepsilon}^e \equiv \boldsymbol{\varepsilon} - \mathbf{h}^\top \mathbf{e} - \boldsymbol{\varepsilon}^r$ (for brevity, here and in the following we do not write the explicit dependence of \mathbb{S} and \mathbf{h} on \mathbf{e} and \mathbf{p}). Substituting the minimizer of (4.17)

into (4.16) yields the transformed energy function,

$$\begin{aligned}
\psi^*(\boldsymbol{\varepsilon}, \mathbf{e}, \mathbf{p}) &= \boldsymbol{\varepsilon} \cdot \mathbb{S}^{-1} \boldsymbol{\varepsilon}^e - \frac{1}{2} (\mathbb{S}^{-1} \boldsymbol{\varepsilon}^e) \cdot \mathbb{S} \mathbb{S}^{-1} \boldsymbol{\varepsilon}^e - (\mathbb{S}^{-1} \boldsymbol{\varepsilon}^e) \cdot \mathbf{h}^\top \mathbf{e} - \mathbb{S}^{-1} \boldsymbol{\varepsilon}^e \cdot \boldsymbol{\varepsilon}^r - \frac{1}{2} \boldsymbol{\varepsilon}^e \cdot \mathbf{e} - \mathbf{e} \cdot \mathbf{p} \\
&= [\boldsymbol{\varepsilon} - \mathbf{h}^\top \mathbf{e} - \boldsymbol{\varepsilon}^r] \cdot \mathbb{S}^{-1} \boldsymbol{\varepsilon}^e - \frac{1}{2} (\mathbb{S}^{-1} \boldsymbol{\varepsilon}^e) \cdot \boldsymbol{\varepsilon}^e - \frac{1}{2} \boldsymbol{\varepsilon}^e \cdot \mathbf{e} - \mathbf{e} \cdot \mathbf{p} \\
&= \frac{1}{2} \boldsymbol{\varepsilon}^e \cdot \mathbb{S}^{-1} \boldsymbol{\varepsilon}^e - \frac{1}{2} \boldsymbol{\varepsilon}^e \cdot \mathbf{e} - \mathbf{e} \cdot \mathbf{p} \\
&= \frac{1}{2} \boldsymbol{\varepsilon}^e \cdot \mathbb{C} \boldsymbol{\varepsilon}^e - \frac{1}{2} \boldsymbol{\varepsilon}^e \cdot \mathbf{e} - \mathbf{e} \cdot \mathbf{p},
\end{aligned} \tag{4.18}$$

where the elasticity tensor is the inverse of the compliance tensor, $\mathbb{S}^{-1} = \mathbb{C}$. The dual variables are computed from the transformed energy function as

$$\frac{\partial \psi^*}{\partial \mathbf{e}} = \boldsymbol{\varepsilon} \cdot \frac{\partial \boldsymbol{\sigma}^*}{\partial \mathbf{e}} - \frac{\partial \psi}{\partial \mathbf{e}} - \frac{\partial \psi}{\partial \boldsymbol{\sigma}^*} \cdot \frac{\partial \boldsymbol{\sigma}^*}{\partial \mathbf{e}}, \quad \frac{\partial \psi^*}{\partial \boldsymbol{\varepsilon}} = \boldsymbol{\sigma}^* + \boldsymbol{\varepsilon} \cdot \frac{\partial \boldsymbol{\sigma}^*}{\partial \boldsymbol{\varepsilon}} - \frac{\partial \psi}{\partial \boldsymbol{\sigma}^*} \cdot \frac{\partial \boldsymbol{\sigma}^*}{\partial \boldsymbol{\varepsilon}}. \tag{4.19}$$

Using the fact that $\boldsymbol{\varepsilon} = \partial \psi / \partial \boldsymbol{\sigma}$ and $\mathbf{d} = \partial \psi / \partial \mathbf{e}$, the derivatives of the transformed energy become

$$\mathbf{d} = -\frac{\partial \psi^*}{\partial \mathbf{e}}, \quad \boldsymbol{\sigma} = \frac{\partial \psi^*}{\partial \boldsymbol{\varepsilon}}. \tag{4.20}$$

Thus, the constitutive equations in terms of the transformed energy are given by (4.20).

To enforce admissible values of the spontaneous polarization, we introduce an energy penalty term $\psi^r(\mathbf{p})$, which will be referred to as the remnant energy, such that $|\mathbf{p}| \leq p_s$. Usually ψ^r can be thought of as the relaxation of the Landau-Devonshire theory for the energy of ferroelectrics. Thus the total energy is

$$\Psi(\boldsymbol{\varepsilon}, \mathbf{e}, \mathbf{p}) = \frac{1}{2} \boldsymbol{\varepsilon}^e(\mathbf{e}, \mathbf{p}) \cdot \mathbb{C}(\mathbf{e}, \mathbf{p}) \boldsymbol{\varepsilon}^e(\mathbf{e}, \mathbf{p}) - \frac{1}{2} \boldsymbol{\varepsilon}^e \cdot \mathbf{e} - \mathbf{e} \cdot \mathbf{p} + \psi^r(\mathbf{p}). \tag{4.21}$$

Since $\psi^r(\mathbf{p})$ does not depend on strain or electric field, it does not affect the expressions for their dual variables, which are simply

$$\mathbf{d} = -\frac{\partial \Psi}{\partial \mathbf{e}}, \quad \boldsymbol{\sigma} = \frac{\partial \Psi}{\partial \boldsymbol{\varepsilon}}. \tag{4.22}$$

4.4 Kinetic relation

We treat the spontaneous polarization as an internal variable and thus, to close the system, we need to specify a kinetic relation for its evolution. Following the ideas of Coleman and Noll (1963),

we postulate that the above energy is the internal energy density of a thermodynamic system (consisting of the space Ω occupied by the material) such that the total internal energy is

$$\mathcal{U} = \int_{\Omega} \Psi(\boldsymbol{\varepsilon}, \mathbf{e}, \mathbf{p}) \, d\mathbf{x}, \quad (4.23)$$

where \mathbf{x} is the spatial coordinate. For a particular thermodynamic process, power can be supplied to the system by the rate of work done by external forces and electric fields, viz.

$$\mathcal{P} = \int_{\Omega} [\rho \mathbf{b} \cdot \dot{\mathbf{u}} - q_f \dot{\phi}] \, d\mathbf{x} + \int_{\partial\Omega} [\mathbf{t} \cdot \dot{\mathbf{u}} - \sigma \dot{\phi}] \, ds, \quad (4.24)$$

consisting of the typical mechanical work components as well the work done on distributed free internal charges q_f and surface charges σ (cf. (4.5)). In addition, the total kinetic energy is

$$\mathcal{T} = \int_{\Omega} \frac{1}{2} \rho \dot{\mathbf{u}} \cdot \dot{\mathbf{u}} \, d\mathbf{x}. \quad (4.25)$$

Then, the Clausius-Duhem inequality requires the total dissipation \mathcal{D} to be greater than or equal to zero for any process. That is,

$$\mathcal{D} = \mathcal{P} - \frac{d}{dt} [\mathcal{T} + \mathcal{U}] \geq 0 \quad \forall \text{ processes.} \quad (4.26)$$

Using the divergence theorem on the power and the fact that $\mathbf{t} = \boldsymbol{\sigma} \mathbf{n}$ and $\sigma = -\mathbf{d} \cdot \mathbf{n}$ where \mathbf{n} is the outward pointing normal vector from the body (in the region Ω),

$$\mathcal{P} = \int_{\Omega} [(\operatorname{div} \boldsymbol{\sigma} + \rho \mathbf{b}) \cdot \dot{\mathbf{u}} + \boldsymbol{\sigma} \cdot \operatorname{grad} \dot{\mathbf{u}} + (\operatorname{div} \mathbf{d} - q_f) \dot{\phi} + \mathbf{d} \cdot \operatorname{grad} \dot{\phi}] \, d\mathbf{x}. \quad (4.27)$$

Recall that $\sigma = -\mathbf{d} \cdot \mathbf{n}$ comes from (4.3) where we assume the electric displacement outside the specimen is zero. Taking the time derivative of the sum of (4.25) and (4.23) yields

$$\frac{d}{dt} (\mathcal{T} + \mathcal{U}) = \int_{\Omega} \left[\rho \ddot{\mathbf{u}} \cdot \dot{\mathbf{u}} + \frac{\partial \Psi}{\partial \boldsymbol{\varepsilon}} \cdot \dot{\boldsymbol{\varepsilon}} + \frac{\partial \Psi}{\partial \mathbf{e}} \cdot \dot{\mathbf{e}} + \frac{\partial \Psi}{\partial \mathbf{p}} \cdot \dot{\mathbf{p}} \right] \, d\mathbf{x}. \quad (4.28)$$

Then, substituting (4.27) and (4.28) into (4.26), the total dissipation becomes

$$\mathcal{D} = \int_{\Omega} \left[\left(\boldsymbol{\sigma} - \frac{\partial \Psi}{\partial \boldsymbol{\varepsilon}} \right) \cdot \dot{\boldsymbol{\varepsilon}} - \left(\mathbf{d} + \frac{\partial \Psi}{\partial \mathbf{e}} \right) \cdot \dot{\mathbf{e}} - \frac{\partial \Psi}{\partial \mathbf{p}} \cdot \dot{\mathbf{p}} \right] \, d\mathbf{x} \geq 0 \quad \forall \text{ processes,} \quad (4.29)$$

where we have substituted the balance of linear momentum and Maxwell's equation (4.2). In addition, we substituted $\boldsymbol{\varepsilon} = \text{sym}(\text{grad } \mathbf{u})$ and $\mathbf{e} = -\text{grad } \phi$. The inequality is satisfied due to our definitions in (4.22) so long as $\mathbf{y} \cdot \dot{\mathbf{p}} \geq 0$, where the driving force on the polarization is defined as $\mathbf{y} = -\partial\Psi/\partial\mathbf{p}$. A common form for the kinetic relation (cf. (Miehe and Rosato, 2011)), which will be used here, is a power law,

$$\dot{\mathbf{p}} = \frac{1}{\eta} \left\langle \frac{|\mathbf{y}|}{e_c} - 1 \right\rangle^m \frac{\mathbf{y}}{|\mathbf{y}|}, \quad (4.30)$$

where the angular brackets are Macaulay brackets. That is, the bracketed term is zero when the quantity inside is negative and is equal to the value inside when it is positive, i.e. $\langle \cdot \rangle \equiv [(\cdot) + |\cdot|]/2$. The variables η , m , and e_c denote material parameters. It can be verified that equation (4.30) is thermodynamically admissible as $\mathbf{y} \cdot \dot{\mathbf{p}} \geq 0$ for any $\dot{\mathbf{p}}$.

4.5 Variational principle

Although current applications of the developed model can be reduced to material point calculations due to the simple geometry of the experiments, a useful form that can be used in Finite Element implementations is derived. The stationarity conditions are shown to satisfy the governing equations and stability conditions are derived for the material parameters.

4.5.1 Potential energy of the electromechanical system

When deriving the constitutive equations from an energy, it is useful to cast the energy function back in terms of stresses and apply balance of linear momentum. To this end we write in integral form

$$\int_{\Omega} \psi(\boldsymbol{\sigma}, \mathbf{e}, \mathbf{p}) \, d\mathbf{x} = \sup_{\mathbf{u}} \left[\int_{\Omega} \boldsymbol{\sigma} \cdot \boldsymbol{\varepsilon} \, d\mathbf{x} - \int_{\Omega} \Psi(\boldsymbol{\varepsilon}, \mathbf{e}, \mathbf{p}) \, d\mathbf{x} \right]. \quad (4.31)$$

Applying the divergence theorem and changing the problem to minimization yields

$$\int_{\Omega} \psi(\boldsymbol{\sigma}, \mathbf{e}, \mathbf{p}) \, d\mathbf{x} = -\inf_{\mathbf{u}} \left[\int_{\Omega} \Psi(\boldsymbol{\varepsilon}, \mathbf{e}, \mathbf{p}) \, d\mathbf{x} + \int_{\Omega} (\text{div } \boldsymbol{\sigma}) \cdot \mathbf{u} \, d\mathbf{x} - \int_{\partial\Omega} (\boldsymbol{\sigma}\mathbf{n}) \cdot \mathbf{u} \, ds \right]. \quad (4.32)$$

When solving solid mechanics problems, we usually know the body force \mathbf{b} being applied, as well as the surface traction \mathbf{t} . Therefore, in equilibrium, $\text{div } \boldsymbol{\sigma} = -\rho\mathbf{b}$ and $\boldsymbol{\sigma}\mathbf{n} = \mathbf{t}$. This stress state in

equilibrium is denoted as $\boldsymbol{\sigma}^*$. Then (4.32) can be written in the form

$$\int_{\Omega} \psi(\boldsymbol{\sigma}^*, \mathbf{e}, \mathbf{p}) \, d\mathbf{x} = - \inf_{\mathbf{u}} \left[\int_{\Omega} \Psi(\boldsymbol{\varepsilon}, \mathbf{e}, \mathbf{p}) \, d\mathbf{x} - \int_{\Omega} \rho \mathbf{b} \cdot \mathbf{u} \, d\mathbf{x} - \int_{\partial\Omega} \mathbf{t} \cdot \mathbf{u} \, ds \right], \quad (4.33)$$

where the right-hand-side corresponds to applying the Principle of Minimum Potential Energy (for the mechanical problem), which is commonly used in the Finite Element Method. That is, when performing the Legendre transform to stresses and imposing the balance of linear momentum, the minimizer \mathbf{u}^* corresponds to the equilibrium displacement field. In this case the potential energy is the quantity being minimized,

$$I_{\text{mech}}[\mathbf{u}, \mathbf{e}, \mathbf{p}] = \int_{\Omega} \Psi(\boldsymbol{\varepsilon}, \mathbf{e}, \mathbf{p}) \, d\mathbf{x} - \int_{\Omega} \rho \mathbf{b} \cdot \mathbf{u} \, d\mathbf{x} - \int_{\partial\Omega} \mathbf{t} \cdot \mathbf{u} \, ds. \quad (4.34)$$

Then, the displacement field that satisfies equilibrium and the boundary conditions is the one satisfying stationarity of the potential energy, i.e. $\delta_{\mathbf{u}} I_{\text{mech}}[\mathbf{u}, \mathbf{e}, \mathbf{p}] = 0$. The same procedure can be applied for the electrical quantities. Since in experiments we normally know the charge distribution, it is convenient to perform a Legendre transform from electric fields to electric displacements,

$$\begin{aligned} \int_{\Omega} \psi^{**}(\boldsymbol{\sigma}, \mathbf{d}, \mathbf{p}) \, d\mathbf{x} &= \sup_{\phi} \left[\int_{\Omega} \mathbf{d} \cdot \mathbf{e} \, ds - \int_{\Omega} \psi(\boldsymbol{\sigma}, \mathbf{e}, \mathbf{p}) \, d\mathbf{x} \right] \\ &= \sup_{\phi} \left[\int_{\Omega} (\text{div } \mathbf{d}) \phi \, d\mathbf{x} - \int_{\partial\Omega} \mathbf{d} \cdot \mathbf{n} \phi \, ds - \int_{\Omega} \psi(\boldsymbol{\sigma}, \mathbf{e}, \mathbf{p}) \, d\mathbf{x} \right], \end{aligned} \quad (4.35)$$

where the divergence theorem was applied. Then, from experiments, we can typically apply the distributed charges and surface charges such that $\text{div } \mathbf{d} = q_f$ and $-\mathbf{d} \cdot \mathbf{n} = \sigma$. The electric displacement field corresponding to the equilibrium state is denoted \mathbf{d}^* . Plugging these conditions into (4.35) gives

$$\int_{\Omega} \psi^{**}(\boldsymbol{\sigma}^*, \mathbf{d}^*, \mathbf{p}) \, d\mathbf{x} = \sup_{\phi} \left[\int_{\Omega} q_f \phi \, d\mathbf{x} + \int_{\partial\Omega} \sigma \phi - \int_{\Omega} \psi(\boldsymbol{\sigma}^*, \mathbf{e}, \mathbf{p}) \, d\mathbf{x} \right]. \quad (4.36)$$

Substituting the Legendre transform of $\psi(\boldsymbol{\sigma}^*, \mathbf{e}, \mathbf{p})$ in (4.33) into (4.36) yields

$$\begin{aligned} \int_{\Omega} \psi^{**}(\boldsymbol{\sigma}^*, \mathbf{d}^*, \mathbf{p}) \, d\mathbf{x} &= \sup_{\phi} \left[\int_{\Omega} q_f \phi \, d\mathbf{x} + \int_{\partial\Omega} \sigma \phi \, ds \right. \\ &\quad \left. + \inf_{\mathbf{u}} \left(\int_{\Omega} \Psi(\boldsymbol{\varepsilon}, \mathbf{e}, \mathbf{p}) \, d\mathbf{x} - \int_{\Omega} \rho \mathbf{b} \cdot \mathbf{u} \, d\mathbf{x} - \int_{\partial\Omega} \mathbf{t} \cdot \mathbf{u} \, ds \right) \right]. \end{aligned} \quad (4.37)$$

Factoring out the minimization part (since the external forces applied do not depend on ϕ), the previous expression can be written as

$$\int_{\Omega} \psi^{**} d\mathbf{x} = \sup_{\phi} \inf_{\mathbf{u}} \left[\int_{\Omega} \Psi(\boldsymbol{\varepsilon}, \mathbf{e}, \mathbf{p}) d\mathbf{x} - \int_{\Omega} \rho \mathbf{b} \cdot \mathbf{u} d\mathbf{x} - \int_{\partial\Omega} \mathbf{t} \cdot \mathbf{u} ds + \int_{\Omega} q_f \phi d\mathbf{x} + \int_{\partial\Omega} \sigma \phi ds \right], \quad (4.38)$$

where the potential energy functional is

$$I[\mathbf{u}, \phi, \mathbf{p}] = \int_{\Omega} \Psi(\boldsymbol{\varepsilon}, \mathbf{e}, \mathbf{p}) d\mathbf{x} - \int_{\Omega} \rho \mathbf{b} \cdot \mathbf{u} d\mathbf{x} - \int_{\partial\Omega} \mathbf{t} \cdot \mathbf{u} ds + \int_{\Omega} q_f \phi d\mathbf{x} + \int_{\partial\Omega} \sigma \phi ds. \quad (4.39)$$

This is consistent with the general idea of the potential energy being of the form $I = \mathcal{U} - \mathcal{V}$ where \mathcal{U} is the internal energy and \mathcal{V} is the work done by external forces (i.e. with (4.23) and (4.24)), which in this case are,

$$\begin{aligned} \mathcal{U} &= \int_{\Omega} \Psi d\mathbf{x}, \\ \mathcal{V} &= \int_{\Omega} \rho \mathbf{b} \cdot \mathbf{u} d\mathbf{x} + \int_{\partial\Omega} \mathbf{t} \cdot \mathbf{u} ds - \int_{\Omega} q_f \phi d\mathbf{x} - \int_{\partial\Omega} \sigma \phi ds. \end{aligned} \quad (4.40)$$

In summary, solving the Euler-Lagrange equations of I corresponds to finding the equilibrium solutions of \mathbf{u} and ϕ , i.e. solving $\delta_{\mathbf{u}} I = 0$ and $\delta_{\phi} I = 0$ for \mathbf{u} and ϕ .

4.5.2 Euler-Lagrange equation

We can verify that equilibrium is satisfied by minimizing the potential energy in (4.39). The first variation with respect to displacements is

$$\begin{aligned} \delta_{\mathbf{u}} I &= \int_{\Omega} \left[\frac{\partial \Psi}{\partial \boldsymbol{\varepsilon}} \cdot \text{grad } \delta \mathbf{u} - \rho \mathbf{b} \cdot \delta \mathbf{u} \right] d\mathbf{x} - \int_{\partial\Omega} \mathbf{t} \cdot \delta \mathbf{u} ds \\ &= - \int_{\Omega} [\text{div } \boldsymbol{\sigma} + \rho \mathbf{b}] \cdot \delta \mathbf{u} d\mathbf{x} + \int_{\partial\Omega} [\boldsymbol{\sigma} \mathbf{n} - \mathbf{t}] \cdot \delta \mathbf{u} ds = 0 \quad \forall \delta \mathbf{u}, \\ &\Rightarrow \text{div } \boldsymbol{\sigma} + \rho \mathbf{b} = \mathbf{0} \quad \text{in } \Omega, \quad \boldsymbol{\sigma} \mathbf{n} = \mathbf{t} \quad \text{on } \partial\Omega. \end{aligned} \quad (4.41)$$

Similarly, the first variation with respect to the electric potential is,

$$\begin{aligned}
\delta_\phi I &= \int_\Omega \left[-\frac{\partial \Psi}{\partial \mathbf{e}} \cdot \text{grad } \delta\phi + q_f \delta\phi \right] d\mathbf{x} + \int_{\partial\Omega} \sigma \delta\phi ds \\
&= \int_\Omega [-\text{div } \mathbf{d} + q_f] \delta\phi d\mathbf{x} + \int_{\partial\Omega} [\mathbf{d} \cdot \mathbf{n} + \sigma] \delta\phi ds = 0 \quad \forall \delta\phi, \\
&\Rightarrow \quad \text{div } \mathbf{d} = q_f \quad \text{in } \Omega, \quad -\mathbf{d} \cdot \mathbf{n} = \sigma \quad \text{on } \partial\Omega.
\end{aligned} \tag{4.42}$$

Therefore, by minimizing the potential energy, we solve the balance of linear momentum and Maxwell's equation in the domain, subject to the traction and charge boundary conditions.

4.5.3 Uniqueness

The second variations of the potential energy can be computed to find conditions for the stability and uniqueness of solutions. Taking the second variation of the potential energy in (4.39) with respect to displacement gives

$$\delta_{uu}^2 I = \int_\Omega \text{grad } \delta\mathbf{u} \cdot \frac{\partial^2 \Psi}{\partial \boldsymbol{\varepsilon}^2} \text{grad } \delta\mathbf{u} d\mathbf{x} \geq 0 \quad \forall \text{grad } \delta\mathbf{u}, \tag{4.43}$$

which is satisfied by requiring $\partial^2 \Psi / \partial \boldsymbol{\varepsilon}^2 = \mathbb{C}$ to be positive definite (i.e. for isotropic materials, the bulk and shear moduli must be positive for a unique solution). Similarly for the electric potential,

$$\delta_{\phi\phi}^2 I = \int_\Omega \text{grad } \delta\phi \cdot \frac{\partial^2 \Psi}{\partial \phi^2} \text{grad } \delta\phi d\mathbf{x} \leq 0 \quad \forall \text{grad } \delta\phi, \tag{4.44}$$

which is satisfied by requiring $\partial^2 \Psi / \partial \phi^2 = -\epsilon$ to be negative, or that $\epsilon \geq 0$ for a unique solution. Recall that the solution for ϕ is the one that maximizes the potential energy in (4.38), hence the requirement of negative-definiteness of $\partial^2 \Psi / \partial \phi^2$.

4.6 Incremental complex moduli

Although the material model presented above is based upon previous thermodynamic models of ferroelectricity, a new approach is presented that allows for the viscoelastic properties to be determined from the material model. Our method for extracting the incremental complex moduli (i.e. dynamic stiffness and damping in bending or torsion) follows from linearization. In particular,

we assume that the applied electric field is uniform through the specimen. However, the stress, strain, and polarization are decomposed into a quasistatic value, plus a small perturbation due to the mechanical loading (e.g. bending or torsional moments). That is, their quasistatic values evolve slowly due to the slowly-varying electric field, while the small perturbations occur much faster due to the mechanical loading frequency being much greater than the applied electric field frequency. In addition, it is assumed that the resulting deformation is in the linear regime (which was demonstrated experimentally) such that the linearization is accurate. Thus, we write

$$\boldsymbol{\sigma} = \bar{\boldsymbol{\sigma}} + \Delta\boldsymbol{\sigma}, \quad \boldsymbol{\varepsilon} = \bar{\boldsymbol{\varepsilon}} + \Delta\boldsymbol{\varepsilon}, \quad \boldsymbol{p} = \bar{\boldsymbol{p}} + \Delta\boldsymbol{p}, \quad (4.45)$$

where the overbar denotes the quasistatic value and the delta denotes the perturbation due to the mechanical loading. Expanding to first order the increment in stress yields

$$\Delta\boldsymbol{\sigma} = \boldsymbol{\sigma}(\bar{\boldsymbol{\varepsilon}} + \Delta\boldsymbol{\varepsilon}, \boldsymbol{e}, \bar{\boldsymbol{p}} + \Delta\boldsymbol{p}) - \bar{\boldsymbol{\sigma}} = \frac{\partial\boldsymbol{\sigma}}{\partial\boldsymbol{\varepsilon}}(\bar{\cdot})\Delta\boldsymbol{\varepsilon} + \frac{\partial\boldsymbol{\sigma}}{\partial\boldsymbol{p}}(\bar{\cdot})\Delta\boldsymbol{p}, \quad (4.46)$$

where $(\bar{\cdot}) = (\bar{\boldsymbol{\varepsilon}}, \boldsymbol{e}, \bar{\boldsymbol{p}})$ denotes that the quantity is evaluated at the quasistatic state. Similarly, the kinetic relation is linearized as

$$\Delta(\dot{\boldsymbol{p}}) = \dot{\boldsymbol{p}}(\bar{\boldsymbol{\varepsilon}} + \Delta\boldsymbol{\varepsilon}, \boldsymbol{e}, \bar{\boldsymbol{p}} + \Delta\boldsymbol{p}) - \bar{\dot{\boldsymbol{p}}} = \frac{\partial\dot{\boldsymbol{p}}}{\partial\boldsymbol{\varepsilon}}(\bar{\cdot})\Delta\boldsymbol{\varepsilon} + \frac{\partial\dot{\boldsymbol{p}}}{\partial\boldsymbol{p}}(\bar{\cdot})\Delta\boldsymbol{p}. \quad (4.47)$$

Assuming harmonic motion, the polarization increment can be written as $\Delta\boldsymbol{p} \sim \exp(i\omega t)$, where ω is the frequency of the mechanical loading. Then, (4.47) can be written as

$$i\omega\Delta\boldsymbol{p} = \frac{\partial\dot{\boldsymbol{p}}}{\partial\boldsymbol{\varepsilon}}(\bar{\cdot})\Delta\boldsymbol{\varepsilon} + \frac{\partial\dot{\boldsymbol{p}}}{\partial\boldsymbol{p}}(\bar{\cdot})\Delta\boldsymbol{p}, \quad \Rightarrow \quad \Delta\boldsymbol{p} = \left[i\omega\boldsymbol{I} - \frac{\partial\dot{\boldsymbol{p}}}{\partial\boldsymbol{p}}(\bar{\cdot}) \right]^{-1} \frac{\partial\dot{\boldsymbol{p}}}{\partial\boldsymbol{\varepsilon}}(\bar{\cdot})\Delta\boldsymbol{\varepsilon}, \quad (4.48)$$

where \boldsymbol{I} is the identity matrix. Now substituting (4.48) into (4.46) yields

$$\begin{aligned} \Delta\boldsymbol{\sigma} &= \frac{\partial\boldsymbol{\sigma}}{\partial\boldsymbol{\varepsilon}}(\bar{\cdot})\Delta\boldsymbol{\varepsilon} + \frac{\partial\boldsymbol{\sigma}}{\partial\boldsymbol{p}}(\bar{\cdot}) \left[i\omega\boldsymbol{I} - \frac{\partial\dot{\boldsymbol{p}}}{\partial\boldsymbol{p}}(\bar{\cdot}) \right]^{-1} \frac{\partial\dot{\boldsymbol{p}}}{\partial\boldsymbol{\varepsilon}}(\bar{\cdot})\Delta\boldsymbol{\varepsilon} \\ &= \mathbb{C}^* \Delta\boldsymbol{\varepsilon}, \end{aligned} \quad (4.49)$$

where the incremental complex modulus is defined as

$$\mathbb{C}^*(\bar{\cdot}) \equiv \frac{\partial \boldsymbol{\sigma}}{\partial \boldsymbol{\varepsilon}}(\bar{\cdot}) + \frac{\partial \boldsymbol{\sigma}}{\partial \mathbf{p}}(\bar{\cdot}) \left[i\omega \mathbf{I} - \frac{\partial \dot{\mathbf{p}}}{\partial \mathbf{p}}(\bar{\cdot}) \right]^{-1} \frac{\partial \dot{\mathbf{p}}}{\partial \boldsymbol{\varepsilon}}(\bar{\cdot}). \quad (4.50)$$

By using the constitutive equations, the incremental modulus can be rewritten as

$$\mathbb{C}^*(\bar{\cdot}) = \mathbb{C}_0 - \frac{\partial \mathbf{y}}{\partial \boldsymbol{\varepsilon}}(\bar{\cdot}) \left[i\omega \mathbf{I} - \frac{\partial \dot{\mathbf{p}}}{\partial \mathbf{p}}(\bar{\cdot}) \right]^{-1} \frac{\partial \dot{\mathbf{p}}}{\partial \mathbf{y}}(\bar{\cdot}) \frac{\partial \mathbf{y}}{\partial \boldsymbol{\varepsilon}}(\bar{\cdot}), \quad (4.51)$$

where the static incremental stiffness is defined as $\partial^2 \Psi / \partial \boldsymbol{\varepsilon}^2 \equiv \mathbb{C}_0$ and we assume that the kinetic relation is purely a function of the driving force, $\dot{\mathbf{p}} = \dot{\mathbf{p}}(\mathbf{y})$. Then, the dynamic stiffness of each elastic constant and its associated loss tangent are given by

$$|\mathbb{C}_{ijkl}^*| = \sqrt{[\text{Re}(\mathbb{C}_{ijkl}^*)]^2 + [\text{Im}(\mathbb{C}_{ijkl}^*)]^2}, \quad \tan \delta_{ijkl} = \frac{\text{Im}(\mathbb{C}_{ijkl}^*)}{\text{Re}(\mathbb{C}_{ijkl}^*)} \quad \text{no sum.} \quad (4.52)$$

Thus, for a given state of stress, electric field, and polarization, the instantaneous dynamic elastic constants and their loss tangents (in response to a mechanical loading at frequency ω) can be computed via (4.52).

4.7 Material model

The potential energy of (4.39) can be used to solve general problems using Finite Element Analysis and has been implemented based on the parameters of (Miehe and Rosato, 2011). However, due to the simplicity of the geometry in experiments, the general 3D model can be reduced to a 1D material point calculation, which is presented in the following section. In particular, the bending model presented next corresponds to the model proposed in our previous paper ¹ (Wojnar et al., 2014).

4.7.1 Pure bending

From the experiments, the electromechanical problem becomes 1D and each material point can be approximated as being subjected to a uniaxial tension/compression stress σ , which results in a

¹Wojnar, C.S., le Graverend, J.B., Kochmann, D.M., 2014. Broadband control of the viscoelasticity of ferroelectrics via domain switching. Applied Physics Letters 105, 162912. URL: <http://scitation.aip.org/content/aip/journal/apl/105/16/10.1063/1.4899055>, doi: <http://dx.doi.org/10.1063/1.4899055>.

uniaxial strain ε . In addition, in experiments, the average polarization and electric field have one non-zero component through the thickness, p , and e , respectively, as shown in Fig. 4.2. Therefore, we write the elastic energy in quadratic form using the longitudinal Young modulus E and transverse elastic strain ε^e and the electric field energy terms together as

$$\Psi^{1D}(\varepsilon, e, p) = \frac{E(e, p)}{2} (\varepsilon^e)^2 - \frac{\epsilon}{2} e^2 - e p + \psi^r(p). \quad (4.53)$$

Then the constitutive equations follow as,

$$\sigma = \frac{\partial \Psi^{1D}}{\partial \varepsilon}, \quad d = -\frac{\partial \Psi^{1D}}{\partial e}. \quad (4.54)$$

For the 1D case, the elastic strain can be simplified from the 3D version as,

$$\varepsilon^e = \varepsilon - d_{31}(p)e - (\varepsilon_s/p_s)|p|, \quad (4.55)$$

where d_{31} is the corresponding coefficient of the \mathbf{h} -tensor, and we assume the longitudinal strain due to the polarization is linear and varies from zero to ε_s (the longitudinal spontaneous strain) as the polarization varies from zero to p_s (the spontaneous polarization). Both terms are negative as the transverse electric field and polarization tend to cause longitudinal shrinkage (due to the Poisson effect and geometry of the crystal unit cell). Regarding the electric field- and polarization-dependent Young modulus, we assume a form that satisfies material frame indifference,

$$\begin{aligned} E(e, p) &= E'(e, p)[1 + i \tan \delta_E(e, p)], \quad \text{where} \\ E'(e, p) &= E^0 \left[1 + c_1 \frac{ep}{e_c p_s} + c_2 \frac{|p|}{p_s} \right] \quad \text{and} \\ \tan \delta_E(e, p) &= \tan \delta^0 + c_3 \frac{ep}{e_c p_s} + c_4 \omega \left[1 - \left(\frac{|p|}{p_s} \right)^2 \right]^2. \end{aligned} \quad (4.56)$$

Furthermore, we use a logarithmic form of the remnant energy term along the lines of (Miehe and Rosato, 2011),

$$\psi^r(p) = -h \left[\log \left(1 - \frac{|p|}{p_s} \right) + \frac{|p|}{p_s} \right]. \quad (4.57)$$

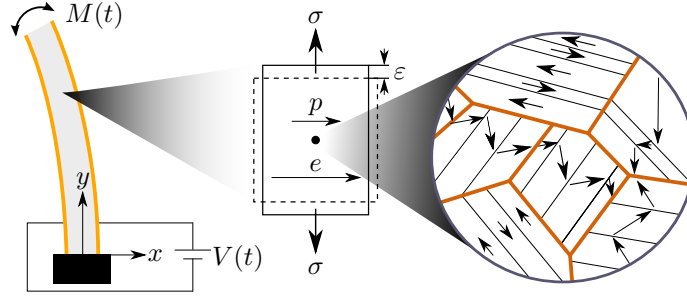


Figure 4.2: Longitudinal stress σ (arising from an applied moment M) and transverse electric field e give rise to changes in the transverse component of the macroscopic polarization p and strain ε .

Constant c_1 characterizes the approximately linear variation of the Young modulus with electric field and constant c_2 the polarization dependence (due to anisotropy). The loss tangent depends linearly on the electric bias through c_3 and on the mechanical frequency through c_4 ; the latter dependence peaks during domain switching (experimentally observed near $\bar{p} = 0$). E_0 and $\tan \delta_0$ are, respectively, the Young modulus and loss tangent without an applied electric field. Experiments show no variation in the electric displacement with ω . Thus, the increasing loss tangent with mechanical frequency seen in experiments in the subresonance regime (cf. Fig. 4.3) is included in the complex modulus instead of the kinetic relation (microscale oscillations of domain walls are not captured in the evolution of the macroscopic polarization). The 1D form of the kinetic relation in (4.30) is

$$\dot{p} = \frac{1}{\eta} \left\langle \frac{|y|}{e_c} - 1 \right\rangle^m \text{sign}(y), \quad (4.58)$$

where $y = -\partial\Psi^{1D}/\partial p$ and e_c is a parameter corresponding to the coercive field (the magnitude of the electric field required for domain switching). That is, from (4.58) the polarization does not begin evolving until the driving force on the polarization exceeds the coercive field.

By assuming pure bending, the problem is reduced to a material point calculation, where in the quasistatic state, the electric field is a known triangle wave and the material is in a stress-free state (i.e. the total strain is found by enforcing $\sigma = 0$). The kinetic relation was integrated in time using a forward-Euler time-stepping scheme with a time step Δt that varied from 0.2 to 0.002 s for electric field frequencies increasing from 0.01 Hz to 1.0 Hz, respectively. The forward-Euler method was used for simplicity. However, one may use an implicit variational constitutive update along the lines of (Miehe and Rosato, 2011; Ortiz and Stainier, 1999). Material parameters (unless

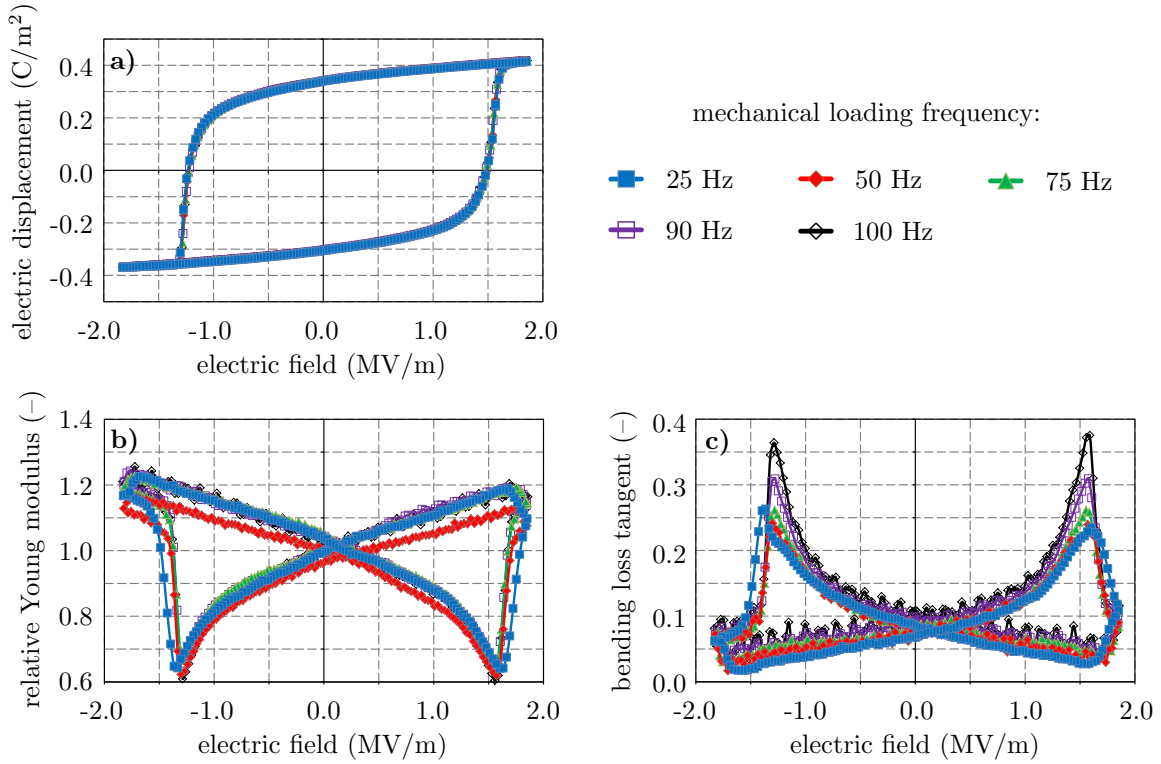


Figure 4.3: Results of bending experiments showing (a) the evolution of the electric displacement, (b) relative Young modulus, and (c) loss tangent versus applied electric field for different mechanical bending frequencies from 25-100 Hz and a fixed electric field frequency of 0.1 Hz.

Table 4.1: Material parameters for polycrystalline PZT.

parameter	known value	parameter	fitted value
E_0	66 GPa	η	0.002 m ² s/C
$\tan \delta_0$	0.08	m	2
ϵ	41×10^{-9} J/(mV ²)	c_1	0.25
p_s	0.37 C/m ²	c_2	0.5
ϵ_s	0.001	c_3	-0.03
e_c	1.2 MV/m	c_4	4.2×10^{-4} s
d_{31}	assumed 0	h	3×10^4 J/m ³

known from the supplier) were obtained by fitting to experimental data (see Tab. 4.1). Note that for simplicity, the piezoelectric contribution to the strain is neglected (i.e. $d_{31} = 0$).

The model predictions shown in Fig. 4.4 agree well with the experimental data in Figs. 3.9, 2.17, and 4.3. We see qualitatively the same behavior: linear variations of stiffness and damping with electric field away from domain switching as well as pronounced softening and damping during domain switching that increase with electric field frequency. The model also captures an increase of the damping peaks during domain switching with increasing mechanical frequency. Decreasing the viscosity η , increasing the spontaneous strain ε_s , or increasing the modulus E_0 were observed to promote higher damping and stronger softening during switching.

4.7.2 Qualitative interpretation of stiffness and damping during domain switching

To gain qualitative insight into the behavior of the viscoelastic response of ferroelectrics during domain switching, we can apply a few assumptions to the form of the complex modulus in (4.51). For the 1D bending problem, (4.51) becomes

$$E^* = E - \frac{\partial \dot{p}}{\partial y} \left(\frac{\partial y}{\partial \varepsilon} \right)^2 \left/ \left[i\omega + \frac{\partial \dot{p}}{\partial y} \frac{\partial^2 \Psi^{1D}}{\partial p^2} \right] \right., \quad (4.59)$$

using the fact that $\partial \dot{p} / \partial p = (\partial \dot{p} / \partial y)(\partial y / \partial p) = -(\partial \dot{p} / \partial y)(\partial^2 \Psi^{1D} / \partial p^2)$. Next, we can consider several further simplifications of the 1D bending model. In particular if we assume the static Young modulus is real-valued (i.e. neglecting intrinsic nominal damping), is independent of electric field and polarization, and if we let the local curvature of the remnant energy $\psi^r(p)$ be κ , the curvature of the total energy is

$$\frac{\partial^2 \Psi^{1D}}{\partial p^2} = \left(\frac{\varepsilon_s}{p_s} \right)^2 E + \kappa \quad (4.60)$$

and

$$\frac{\partial y}{\partial \varepsilon} = -\frac{\varepsilon_s}{p_s} E \operatorname{sign} p. \quad (4.61)$$

Furthermore, we let $\dot{p} = y/\eta$ (e.g. equation (4.58) with $m = 1$ after the onset of domain switching ($|y| > e_c$)) such that $\partial \dot{p} / \partial y = 1/\eta$. Then, substituting (4.60) and (4.61) into (4.59), the expression

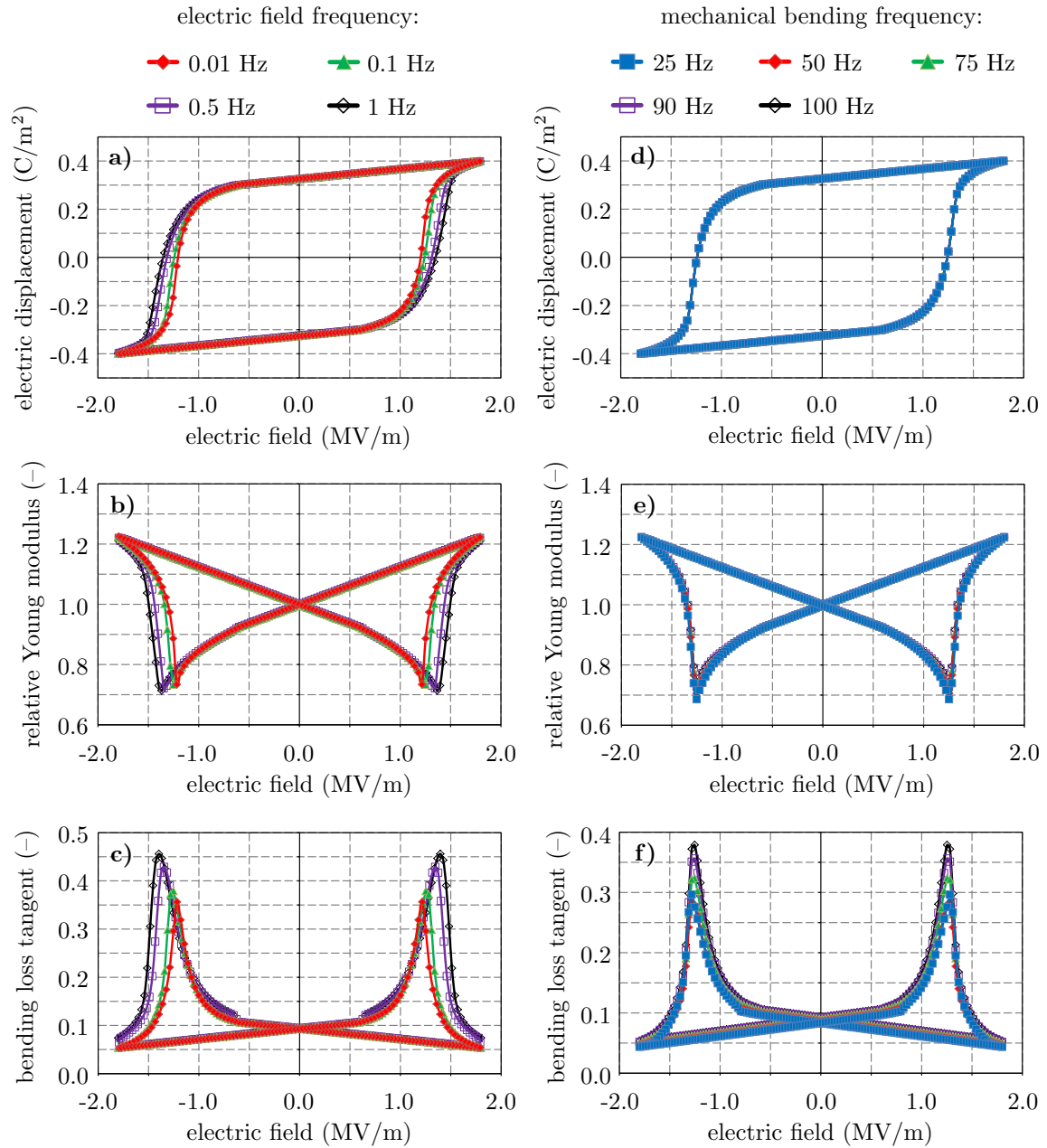


Figure 4.4: Results of bending simulations showing the evolution of the electric displacement, relative Young modulus, and loss tangent versus applied electric field. The effect of different triangle-wave electric field frequencies from 0.01-1.0 Hz is shown in (a-c) while the effect of different mechanical bending frequencies from 25-100 Hz is shown in (d-f).

for the complex Young modulus becomes

$$E^* = E - \frac{\xi E^2/\eta}{i\omega + (\xi E + \kappa)/\eta}, \quad \xi \equiv \sqrt{\frac{\varepsilon_s}{p_s}}. \quad (4.62)$$

The dynamic stiffness and loss tangent can be computed as

$$|E^*| = E \sqrt{\frac{1 + [\omega\eta/\kappa]^2}{[1 + E\xi/\kappa]^2 + [\omega\eta/\kappa]^2}}, \quad \tan \delta = \frac{(E\xi/\kappa)[\omega\eta/\kappa]}{1 + E\xi/\kappa + [\omega\eta/\kappa]^2}. \quad (4.63)$$

In general, we see that at low frequencies, the loss tangent decays to zero while the dynamic stiffness approaches a value less than the static Young modulus. At very high frequencies, the loss tangent again decays to zero and the dynamic stiffness approaches the static Young modulus. We can compute the frequency of maximum loss tangent (and its value) as,

$$\omega_0 = (\kappa/\eta)\sqrt{1 + E\xi/\kappa}, \quad \tan \delta_{\max} = \frac{E\xi/\kappa}{2\sqrt{1 + E\xi/\kappa}}. \quad (4.64)$$

By examining (4.64), we can qualitatively see that the frequency at which maximum damping occurs increases as the viscosity decreases, as the local curvature of the remnant energy increases, or as the product $E\xi$ increases, which corresponds to increasing the static Young modulus, increasing the spontaneous strain, and decreasing the spontaneous polarization. Also, the maximum value of the loss tangent increases as the product $E\xi/\kappa$ increases. For small values of this term, the loss tangent increases linearly with a slope of one half. For large values, it increases with a square-root dependence. A similar analysis of the dynamic Young modulus shows that its minimum value occurs at $\omega = 0$, and corresponds to $|E^*| = E/(1 + E\xi/\kappa)$.

To observe these trends, the variation of the dynamic Young modulus and loss tangent for the simplified 1D case given in (4.63) (for different material parameters that result in easily-noticeable trends) are plotted versus mechanical bending frequency $\omega = 2\pi f$ in Figs. 4.5 and 4.6, respectively. Each figure shows the influence of various material parameters. This serves as a starting point for identifying optimized ferroelectric materials by experimentally fine-tuning material properties (e.g. composition and microstructure). Possible future directions will be to examine the effect of these parameters experimentally. That is, performing experiments with different materials and observing the resulting change in behavior of the dynamic stiffness and loss tangent.

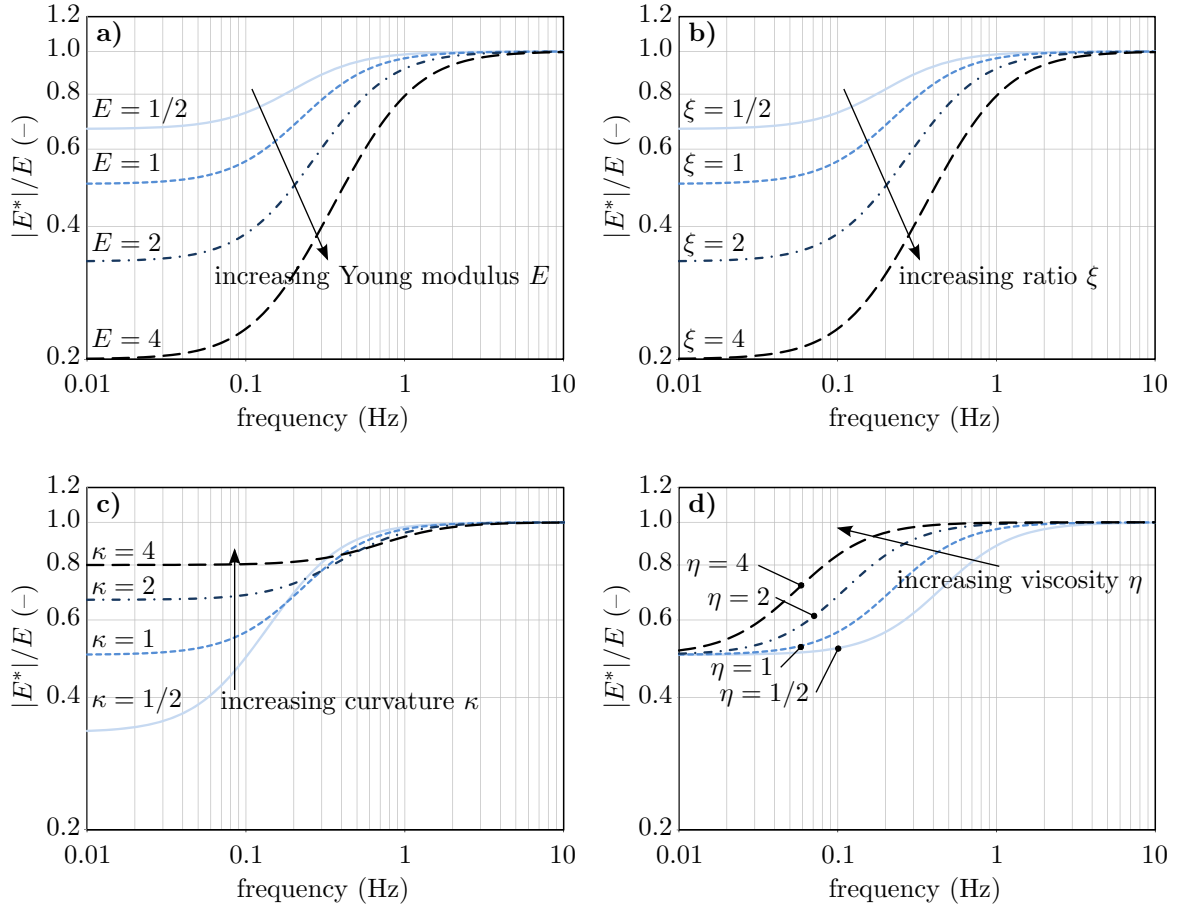


Figure 4.5: Relative dynamic Young modulus during domain switching versus mechanical frequency showing the affect of (a) increasing static Young modulus, (b) increasing ratio $\xi = \varepsilon_s/p_s$, (c) increasing parameter κ , and (d) increasing viscosity parameter η . Unless specified in the figure, the parameters used were $\eta = 1$, $\xi = 1$, $E = 1$, and $\kappa = 1$.

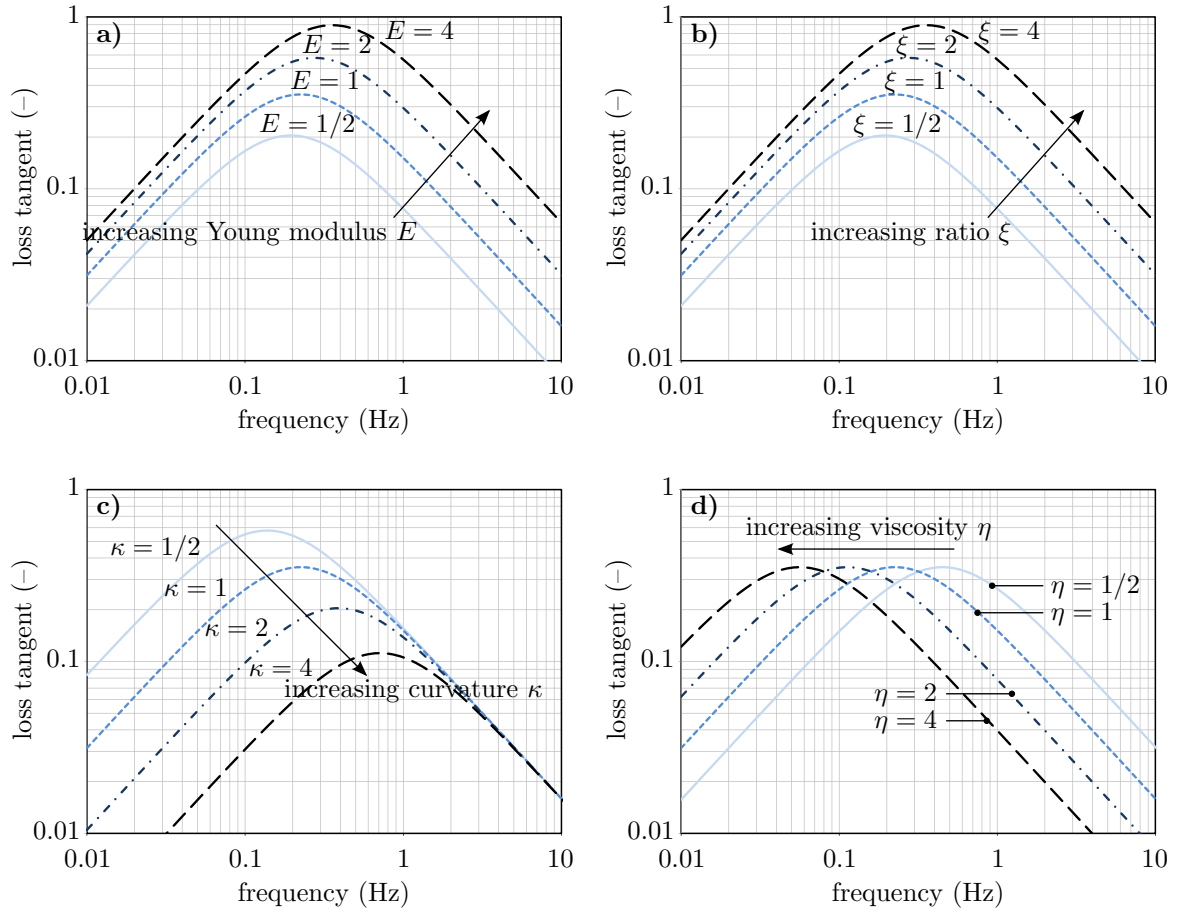


Figure 4.6: Loss tangent in bending during domain switching versus mechanical frequency showing the affect of (a) increasing static Young modulus, (b) increasing ratio $\xi = \varepsilon_s/p_s$, (c) increasing parameter κ , and (d) increasing viscosity parameter η . Unless specified in the figure, the parameters used were $\eta = 1$, $\xi = 1$, $E = 1$, and $\kappa = 1$.

Chapter 5

Set-and-Hold Actuation and Structural Damping via Domain Switching

The previous experiments on PZT coupled with the model that was developed provided insight into how the time-dependent mechanical response of ferroelectrics is affected by the kinetics of domain switching. Using this new understanding, domain switching kinetics are taken advantage of in two particular structural applications. First, utilizing the microstructural changes associated with domain switching is demonstrated as a means of creating set-and-hold actuators. Then, motivated by experiments on PZT where the loss tangent (or damping) was observed to increase during domain switching, ferroelectric actuators attached to structures are shown to increase the damping of the entire structure when domain switching is controlled in the attached actuators.

5.1 Motivation

The piezoelectric effect in materials is commonly used in sensors and actuators ([Uchino, 1997](#); [Xu, 2013](#)). In ferroelectric materials, this behavior is restricted to small electric fields well below the coercive field before the onset of domain switching, which occurs at approximately 1.2 MV/m for PZT. The maximum strain that can typically be achieved from piezoelectricity is on the order of 0.1 % ([Park and Shrout, 1997](#)). The fast response of piezoelectricity makes the approach desirable for ultrasonics and precise displacement control. In addition, ferroelectric ceramics such as PZT do not exhibit as much creep as, for example, ferroelectric polymers ([Vinogradov and Holloway, 2000](#)).

However, using piezoelectricity in applications requiring larger actuation requires larger specimens, which increases cost. To bypass this limitation, piezoelectrics have been used to activate control surfaces in structures to achieve larger displacements (e.g. by beam or plate bending). Furthermore, carefully designed systems can amplify strains, examples include stack actuators (Pasco and Berry, 2004), rainbow actuators (Chandran et al., 1996; Haertling, 1999), and hierarchically designed structures (Conway et al., 2007; Newnham et al., 1993; Seffen and Toews, 2004; Ueda et al., 2008, 2010; Wood et al., 2005). However many of these examples have the drawback of reducing the force applied by the actuator when connected to a structural member, which reduces the achievable maximum strain. Taking a different approach, new materials have been manufactured that give rise to higher maximum strain. For example, materials utilizing (anti-)ferroelectric phase transitions can reach strains of 0.2-0.9 % (Pan et al., 1989). Lead magnesium niobate-lead titanate (PMN-PT) and lead zinc niobate-lead titanate (PZN-PT) materials have been developed that generate up to 1.7 % strain (Luo et al., 2006; Park and Shrout, 1997). As shown in Fig. 5.1, higher strains for the same electric field are reached by the specially-designed compositions of PMN-PT and PZN-PT. In addition, large strains can be reached by ferroelectric polymer actuators albeit with lower force, which makes their application in stiff or massive structures difficult.

A new method of generating large strains using stress and electric field-induced domain switching was demonstrated using single-crystal barium titanate by Burcsu and coworkers (2000; 2004). Maximum strains of 1.1% were achieved. Larger strains of 5% were predicted by Shu and Bhattacharya (2001) for other materials. This method and other approaches for large strain actuation are described in (Bhattacharya and Ravichandran, 2003). However, the approach of Burcsu et al. utilized single-crystal ferroelectrics and required a large compressive stress to induce 90° domain switching, which gave rise to large actuation strain. As an alternative, domain switching in polycrystalline materials, which already have an abundance of 90° domain walls, can be controlled solely via electric fields. Besides, the goal of Burcsu et al. was to generate large, reversible electrostriction instead of permanent deformation for set-and-hold actuators, which would be useful in e.g. deformable mirrors for space telescopes (see the work by Patterson (2014) for details on this concept). In particular, set-and-hold actuators would not require a continuous power supply to maintain their deformed shape, which is advantageous in space applications. Therefore, our demonstration of domain switching as a means of controlling set-and-hold actuators will utilize a ferroelectric ceramic. In particular, to apply the large electric fields required for domain switching

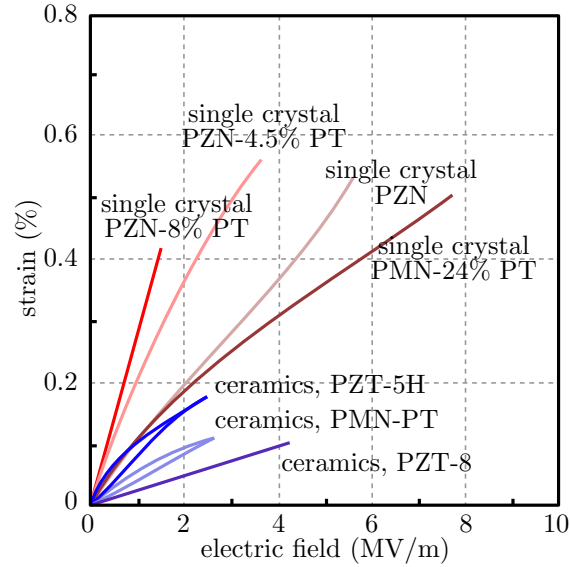


Figure 5.1: Piezoelectric strain versus applied electric field shown for common piezoelectric ceramics (PZT and PMN-PT) as well as various single crystal compositions of PZN-PT demonstrating increased actuation. Experimental data was adapted from (Park and ShROUT, 1997).

using smaller, more practical voltages, a type of stack actuator will be used as an example, namely the Macro Fiber Composite (MFC) actuator.

Furthermore, the viability of using such MFC actuators in structures for vibration damping will be investigated. Although large increases in loss tangent were observed in previous experiments on pure PZT cantilevers and gave insight into domain switching kinetics, structures constructed solely from PZT are not practical in many applications due to their brittleness. Alternatively, it is more feasible to attach MFC actuators (or other types of piezoelectric actuators) to existing structures. Therefore, the influence of domain switching in MFC actuators attached to cantilevers on the overall structural loss tangent will be characterized.

5.2 Materials

Due to its use in the aerospace industry, the MFC actuator was chosen to demonstrate the concept of set-and-hold actuation via domain switching. MFC actuators were originally developed by NASA (Wilkie et al., 2003) and are currently manufactured by Smart Material Corp. FL, USA,

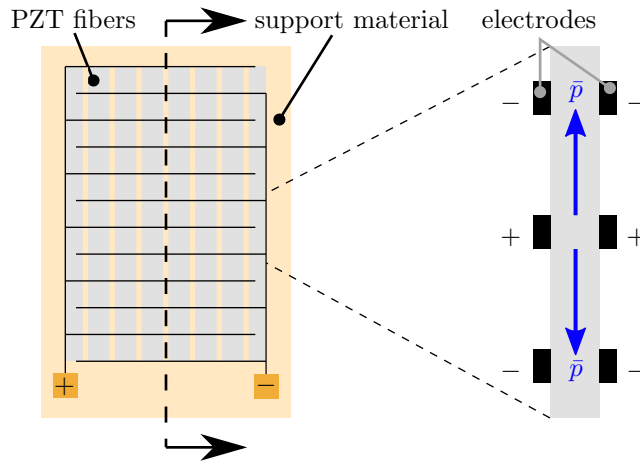


Figure 5.2: Illustration of the design of a MFC actuator. Planar view is shown on the left where the PZT fibers are covered by alternating positive and negative electrodes. A zoomed-in cross-sectional view is shown on the right revealing the electrodes on the reverse side. The electric field between positive and negative electrodes is nominally in the direction of the macroscopic polarization \bar{p} .

which is where the actuators being used were obtained from. In particular, the MFC P1 type specimens were tested, which are used for longitudinal actuation. Their size is $37 \times 20 \text{ mm}^2$.

MFC actuators are manufactured from individual piezoceramic fibers. The fibers form a single layer and are aligned in the longitudinal direction. The fibers are embedded in an epoxy matrix and electrodes are applied to the surface. One of the major advantages of MFC actuators over normal piezoceramics is that the fiber construction and epoxy matrix makes MFC actuators flexible and damage resistant (against mechanical and electrical loading) so they can easily be used in a myriad of structural applications. The ceramic fibers for the longitudinal actuators are poled in the longitudinal direction (and alternating) as shown in Fig. 5.2. Therefore, applying a small voltage across the positive and negative terminals gives rise to a longitudinal strain via the piezoelectric effect. The behavior of MFC actuators in various applications has been studied extensively by [Sodano \(2003\)](#). However, their nonlinear behavior during electric field-induced domain switching has not been characterized nor has the nonlinear response been utilized for set-and-hold actuation or for mechanical damping. In the following sections, experiments are performed that demonstrate the set-and-hold actuation and mechanical damping capabilities of MFC actuators.

5.3 Quasistatic electromechanical testing

Large cyclic voltages (exceeding the manufacturer-specified operational range) at different frequencies were applied to the MFC actuators. The resulting longitudinal strain and polarization were measured for various frequencies of the applied voltage. Then, by applying a particular domain switching-inducing voltage history to an MFC actuator attached to a cantilever, permanent deflection (i.e. set-and-hold actuation) of the cantilever was observed.

5.3.1 Experimental methods

The electric field was applied and the resulting polarization of the actuator was measured using the same Sawyer-Tower circuit constructed for the BES apparatus (cf. Section 2.1.3). In particular, the same 100 μF electrolytic capacitor was used to measure the charge accumulation on the specimen. As the geometry of the electrodes and PZT material in the actuators is complex, it cannot be approximated as 1D, where the average electric displacement is given by the total charge divided by the surface area of the electrodes. Thus, (2.21) cannot be applied. Instead, the total charge is reported. Nonetheless, measuring the charge reveals a hysteresis loop similar to the electric displacement due to domain switching. However, the charge is scaled depending on the size and geometry of the actuator, which was held constant in the following experiments.

The longitudinal strain of the actuator was measured simultaneously using Digital Image Correlation (DIC), which is an optical method of tracking 2D displacements of a surface (DIC was first used in experimental mechanics by [Chu et al. \(1985\)](#) and [Peters and Ranson \(1982\)](#)). The resulting displacement field is used to compute the strain. By recording images of the specimen's surface while applying a voltage, the evolution of longitudinal strain was determined by DIC using the commercial software, VIC-2D (Correlated Solutions, Inc. SC, USA). The basic experimental setup will be described below; however, the VIC-2D program is treated as a black box and the reader is referred to e.g. ([Sutton et al., 2009](#)) for an introduction to the mathematical analysis used by commercial programs such as VIC-2D.

To track the deformation of the actuator optically, speckle patterns were applied to the MFC actuator surface using spray paint. First, Kapton tape was used to cover the electrode terminals during painting. Then, Krylon flat white paint was applied uniformly and allowed to dry. The white spray paint was applied by aiming the paint jet at the specimen while holding the spray can

approximately 12 cm from the surface. Moving the can side to side while spraying was determined to give a smooth and uniform coating. Finally, Krylon flat black paint was applied to create the speckles. To obtain a fine speckle pattern, the spray paint jet was aimed over the specimen while holding the spray can approximately 0.6 m away from the surface and moving the can side to side. This approach allowed for smaller and fewer paint particles to fall down onto the specimen, which generated the speckle pattern. Speckles were continuously applied until the surface appeared to have equal areas of white and black paint. Spray painting was performed in a fume hood for ventilation. After the paint dried, the Kapton tape was removed and wires were soldered to the electrode terminals, which were then connected to the Sawyer-Tower circuit.

To hold the MFC actuators in place during the experiment, specimens were gripped at the bottom (at the lower edge of the actuator illustrated in Fig. 5.2) below the electrical terminals. To record images for DIC, a camera (EO-1312M 1/2" CMOS Monochrome USB Camera – stock No. 59-365 – Edmund Optics Inc. NJ, USA) was mounted to the table in front of the specimen. Images were recorded at 10 fps while applying a cyclic voltage to the actuator. The same oscilloscope used for the BES setup was used to record the applied voltage and the charge from the Sawyer-Tower circuit. The sampling rate of the scope was also held constant at 10 samples/s. Since the frame rate of the camera was limited to 5-15 fps, the maximum frequency of the applied voltage was limited to 0.1 Hz. Therefore, strain measurements were only measured for voltage frequencies of 0.1 and 0.01 Hz. The charge hysteresis curves were obtained at the same frequencies as well as at the higher frequencies of 1 and 10 Hz.

An example image recorded by the camera during an experiment is shown in Fig. 5.3 with the displacement field computed from VIC-2D overlaid upon it. A lens was attached to the camera such that its field of view captured the entire width of the actuator's surface. The resolution of the camera (1280×1024 pixels²) resulted in a scaling of 62 pixels/mm and typical speckle diameters of 10 pixels. While the entire width of the specimen was visible, the area of interest used for DIC was taken only over the PZT part of the actuator (i.e. not the surrounding support material) as shown in Figs. 5.2 and 5.3. The subset size and spacing used in VIC-2D were 21 and 5 pixels, respectively. The strain of the actuator was expected to be uniform (within the resolution of the camera), which can be seen in the displacement field data of Fig. 5.3; contour lines in the displacement field are nearly straight. Therefore, the strain of the actuator was computed by spatially averaging the strain field computed by VIC-2D, which reduces noise. Also, before computing the strain field,

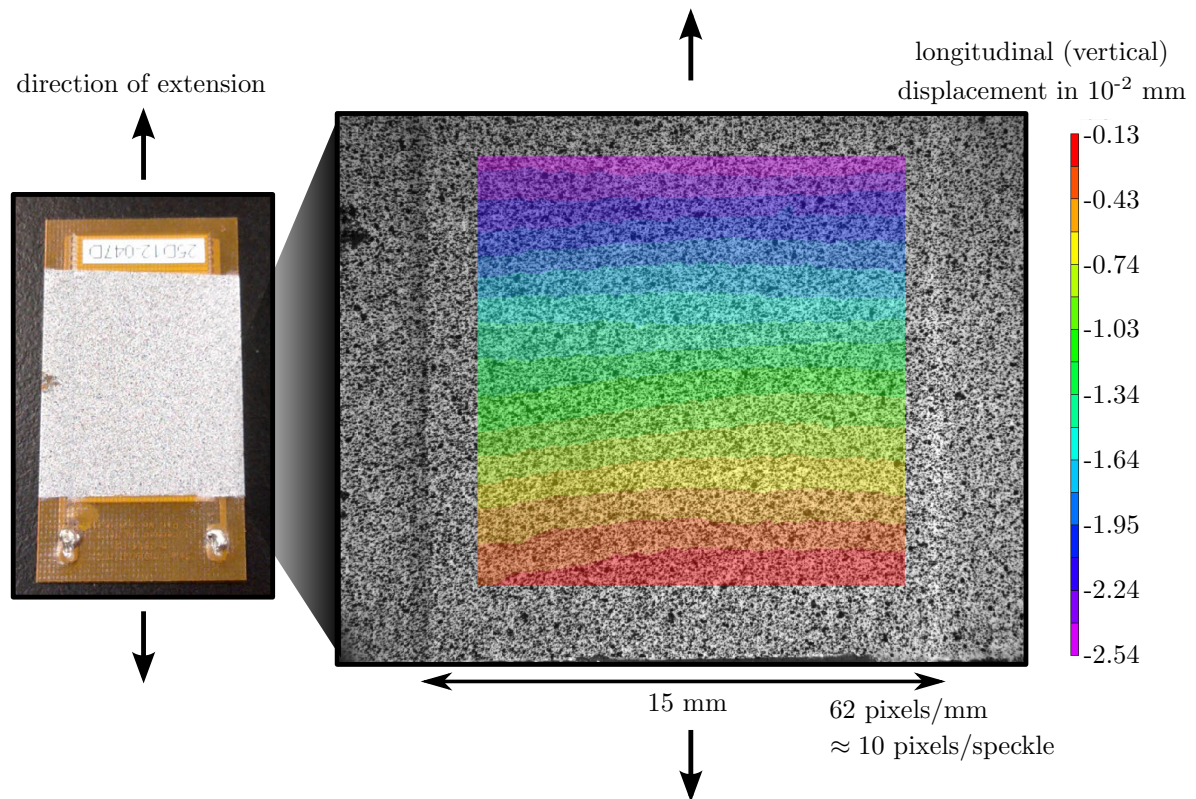


Figure 5.3: Images showing (left) an MFC actuator with an applied speckle pattern and (right) full-field displacement measurements obtained from VIC-2D overlaid on the corresponding image taken by the camera. The dark and light vertical bands appearing in the camera image correspond to the slight protrusion of the PZT layer in the MFC actuator. The PZT layer was used as the area of interest for DIC.

the displacement field was sent through a low-pass filter in the VIC-2D software (using the default settings), which also reduced noise.

5.3.2 Measuring longitudinal strain and charge

The average longitudinal strain versus an applied triangle-wave voltage is shown in Fig. 5.4 for different voltage frequencies and amplitudes. The strain is measured relative to its minimum value achieved during domain switching near the coercive field. For large voltage amplitudes (5 kVpp), the strain hysteresis partially resembles that of pure PZT ceramics (see e.g. (Zhou et al., 2001)). There are, however, noticeable differences. For example, the residual strain (the strain at zero electric

field) in (Zhou et al., 2001) was 0.25%, while for the actuators, the residual strain was lower and the hysteresis was highly asymmetric. Depending on the poling direction, residual strains of 0.04% or 0.11% can be seen in Fig. 5.4. The discrepancy is possibly due to different material compositions and poling directions as well as the influence of the actuator's support material. That is, the support material causes internal compressive stresses as the actuator elongates during electrical loading, which does not occur when the PZT material is free-standing as in (Zhou et al., 2001). Also, the MFC actuators are thin (0.25 mm), therefore the spray paint layer may be of comparable thickness and have the same influence as the support material. A similar effect of compressive stress on the strain hysteresis was observed for PLZT by Lynch (1996). Another explanation is that the geometry of the actuators reduces the electric field in certain parts of the PZT layer (i.e. between the top and bottom electrodes of the same sign as shown in Fig. 5.2). Therefore, domain switching may not occur throughout the entire material, which reduces the total strain achievable. However, comparing Fig. 5.4 with the results in (Zhou et al., 2001), similar trends can be seen with increasing electric field (or voltage) frequency. As the voltage cycling frequency increases, the area of the strain hysteresis increases, which is due to the inherent time required for domain switching. Also shown in Fig. 5.4 is the evolution of the longitudinal strain while applying a lower amplitude cyclic voltage of 1 kVpp – within the manufacturer specifications where there is no significant domain switching. The variation of strain is nearly linear since domain switching is not occurring. In many applications of MFC actuators, domain switching is not desirable as it alters (and can reduce) the piezoelectric constants. In summary, the longitudinal strain hysteresis due to electric field-induced domain switching indicates that permanent strains and thereby set-and-hold actuators can be realized by using MFC actuators.

The charge accumulation on the MFC actuators was also measured for different electric field frequencies and different voltage amplitudes as shown in Fig. 5.5, which reveals the typical hysteresis loops as seen by Zhou et al. (2001). The coercive field and spontaneous polarization vary significantly for different frequencies of the applied voltage. The coercive voltage increases from 1.00 kV to 1.22 kV for positive voltages and from 0.77 kV to 1.24 kV for negative voltages as the frequency increases from 0.01 to 10 Hz. The spontaneous charge decreases from 44 to 28 μC (when poled in the positive direction) and decreases from 40 to 25 μC (when poled in the negative direction) as the frequency increases from 0.01 to 10 Hz. In a manner similar to the PZT experiments in Fig. 2.17, the hysteresis asymmetry is due to an internal bias in the material formed during

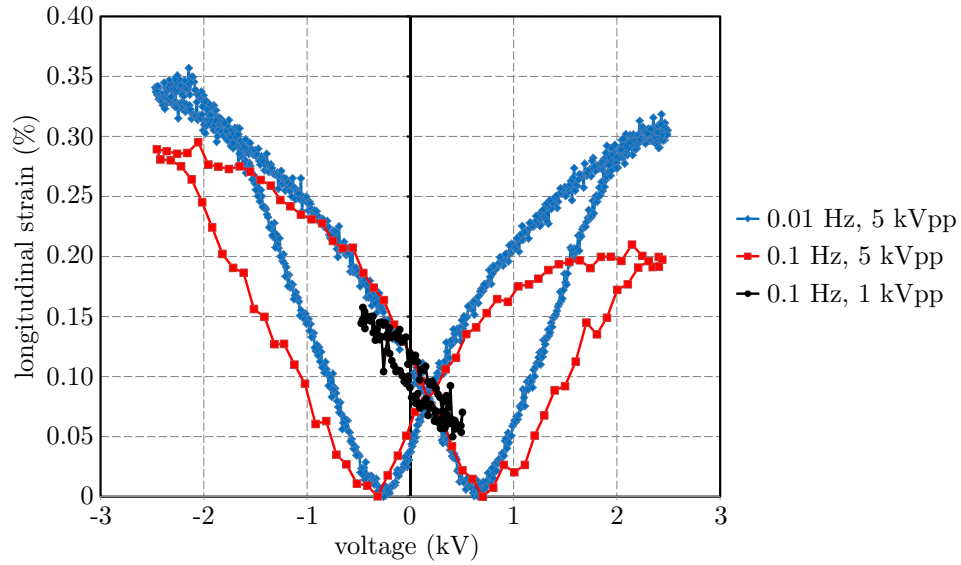


Figure 5.4: Average longitudinal strain measured using DIC versus applied voltage. Different frequencies of 0.01 and 0.1 Hz as well as different peak-to-peak amplitudes of the applied voltage are shown.

manufacturing. Indeed, the maximum voltages specified by the manufacturer are not symmetric since the onset of domain switching occurs at different voltages depending on the sign. For a smaller voltage amplitude of 1 kVpp at 0.1 Hz, which is within the manufacturer specifications, there is only a small hysteresis seen in Fig. 5.5 because there is no significant domain switching in the material. Comparing the strain measured in Fig. 5.4 with the charge measured in Fig. 5.5, the minimum strain does not occur at the coercive field. This is because of internal stresses arising from the support material and spray paint; at the coercive field when the average polarization is zero, which is normally taken as the zero strain datum, the strain will not be a minimum due to stretching induced by the support material and spray paint. This behavior is important to characterize if one seeks to control the permanent strain of the MFC actuator as the response differs from pure PZT. In addition, bonding the actuator to a structure will similarly affect the evolution of strain.

An additional experiment was performed to observe any effect of the spray paint on the strain and charge evolution. On a different MFC actuator, the white paint used for the initial coating was applied similarly to the black paint by spraying the jet over the specimen while holding the can approximately 0.6 m away. In this way, paint particles fell more gently and did not bond as well to the MFC surface as before (while more paint was sprayed in order to fully coat the surface).

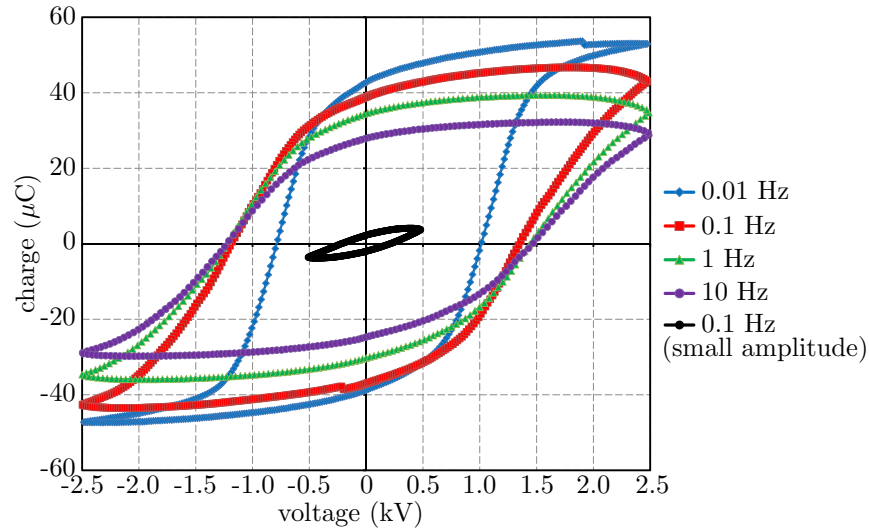


Figure 5.5: Total charge accumulation on an MFC actuator versus an applied triangle-wave voltage with frequencies ranging from 0.01 to 10 Hz. To demonstrate the difference in response when operating the actuator within the manufacturer specifications and when going beyond the specifications, different voltage amplitudes of 1 kVpp and 5 kVpp, respectively, were applied.

Therefore, stretching of the paint due to the actuator does not generate as much stress as before. A 4 kVpp amplitude triangle-wave voltage was applied at 0.1 Hz and the resulting charge and strain were measured as shown in Fig. 5.6. The charge hysteresis is different from that shown in Fig. 5.5 where a higher coercive voltage of 1.2 kV was observed for the specimen with well-bonded paint, as compared to the 1.0 kV coercive voltage observed for the specimen with weakly-bonded paint. This points to domain switching occurring at lower voltages because of reduced internal stresses from the paint. Thus, as shown in Fig. 5.6, the minimum strain reached by the specimen with weakly-bonded paint occurs closer to the coercive field, which is closer to the behavior of pure PZT. Furthermore, the residual strain is higher for the specimen with weakly-bonded paint, which is also because of reduced internal stress. Therefore, it is important to characterize the strain behavior of the actuators as they vary significantly from that of pure PZT specimens.

It should be noted that small misalignment between the specimen surface and camera may arise when gripping two different specimens, which can contribute to the differences in strain between Figs. 5.4 and 5.6. In particular, both in-plane and out-of-plane misalignment can affect the measured displacement fields. However, perfectly aligning the specimens and camera is difficult with the current setup. To quantify the error due to misalignment, images obtained of the specimen before

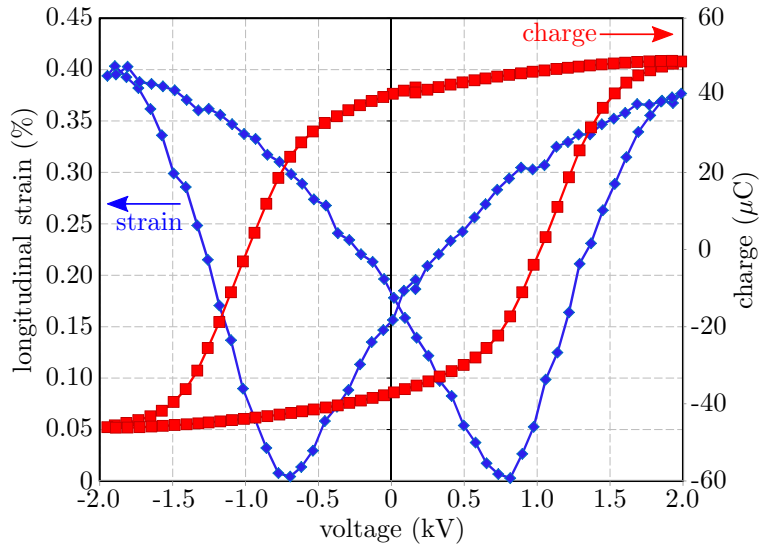


Figure 5.6: Average longitudinal strain and total charge versus an applied triangle-wave voltage with a frequency of 0.1 Hz for a specimen with weakly-bonded paint. The specimens used in Figs. 5.4 and 5.5 had well-bonded paint.

and after rigidly translating the camera were correlated. With perfect alignment, the displacement fields are constant. However, with the current setup, variations in displacement on the order of 2 pixels were observed. For typical experiments, the maximum displacements observed were also on the order of 2 pixels. This discrepancy may also be because the camera was moved by hand, which likely did not result in perfectly in-plane translation. Therefore, a more sophisticated setup should be used in the future where the camera alignment and position can be carefully controlled.

5.3.3 Demonstration of a set-and-hold actuator

To demonstrate the set-and-hold capability of MFC actuators via electric field-induced domain switching, an MFC actuator was bonded to a substrate material; longitudinal extension of the actuator results in curvature of the substrate. A $25 \times 93 \text{ mm}^2$, 1.5 mm thick piece of plexiglass was used as the substrate shown in Fig. 5.7(a) with an MFC actuator adhered to the surface. The particular geometry shown in Fig. 5.7(a) was chosen such that the specimen fits within the BES apparatus, which will be used in later experiments. To demonstrate a set-and-hold actuator, the specimen was gripped (on the end closest to the actuator) using a vise. The experimental setup is shown in Fig. 5.7(b) and (c). In particular, Fig. 5.7(b) shows the entire setup where the specimen

is gripped in the center of the image and the MFC actuator electrode terminals are connected to the high-voltage amplifier. To observe the deflection of the specimen, a camera views the specimen from the side as shown in Fig. 5.7(b); deflection of the specimen is viewed as sideways motion in the camera's field of view. A lamp shines on the plexiglass specimen and scatters such that the normally-transparent material can be seen by the camera. Behind the specimen (from the point of view of the camera) is grid paper (3 mm spacing), which allows for the specimen's deflection to be quantified. Fig. 5.7(c) shows a close-up of the specimen gripped in the vise.

The deflection of the specimen was recorded using the camera while applying 0.1 Hz triangle-wave voltages at different amplitudes. Applying a 1 kVpp voltage resulted in a maximum tip deflection of approximately 1 mm. Upon turning off the applied voltage, the specimen returned to its initial position, which is the piezoelectric response. Applying 5 kVpp and thereby going beyond the linear response showed maximum deflections of up to 3 mm. Most importantly, turning off the applied voltage upon reaching 1.8 kV resulted in a permanent deflection of approximately 1 mm as shown in Fig. 5.8. Applying large, domain switching-inducing voltages resulted in a permanent deformation that was on the order of the maximum reversible deformation reached under small voltages. This not only demonstrates the possible use of domain switching in set-and-hold actuators, but also shows that the achievable permanent deformations are on the order of those achieved via piezoelectricity for the specimen tested. Furthermore, additional adjustments can be made by applying small voltages on top of the permanent deformation to fine-tune the deflection.

From the strain hysteresis curves, measured using DIC, that were shown in Figs. 5.4 and 5.6, it is apparent that the achievable permanent strain is highly dependent on the voltage applied (both magnitude and rate) due to the kinetics of domain switching. Therefore, additional experiments should be performed to measure how the permanent strain reached depends on the voltage loading history. In addition, further experiments can test specimens where the actuator is attached in different locations to find the optimal overall design of the structure. Various MFC actuator geometries are also expected to exhibit a different strain hysteresis due to different internal stresses arising from the support material. Therefore, understanding the influence of residual stress and electrical loading history on domain switching for each MFC configuration is required before creating different designs of set-and-hold actuators. Future work is also needed to study the stability of set-and-hold actuators. In particular, large, cyclic electric fields applied to ferroelectric ceramics can lead to electrical fatigue, which is a poorly-understood phenomenon (Lupascu, 2004).

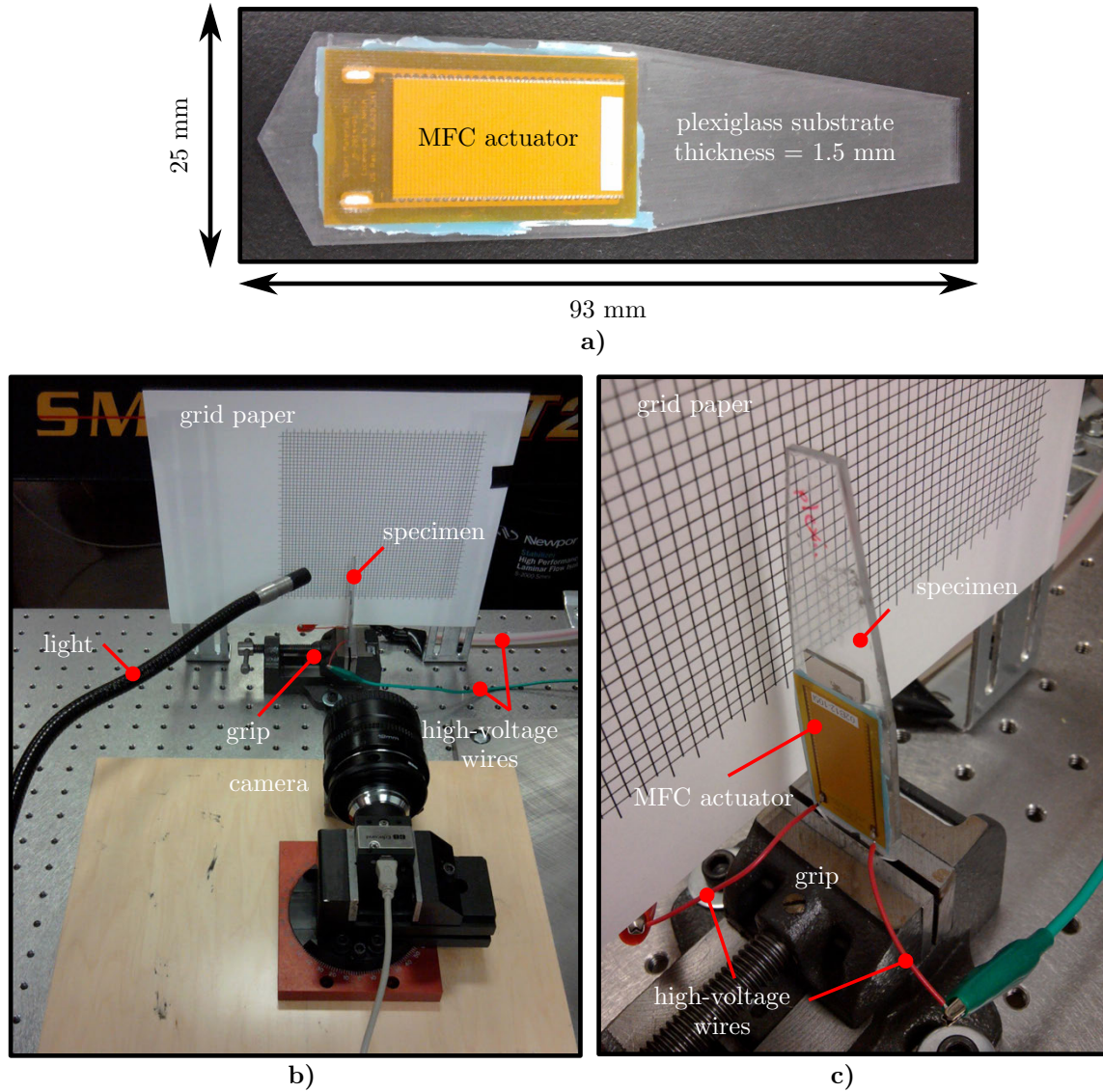


Figure 5.7: Experimental setup used for demonstrating a set-and-hold actuator. An MFC actuator is adhered to a plexiglass substrate (a) and a voltage is applied causing the plexiglass to bend, which is observed by a camera (b). The plexiglass is held in place using a vise (c).

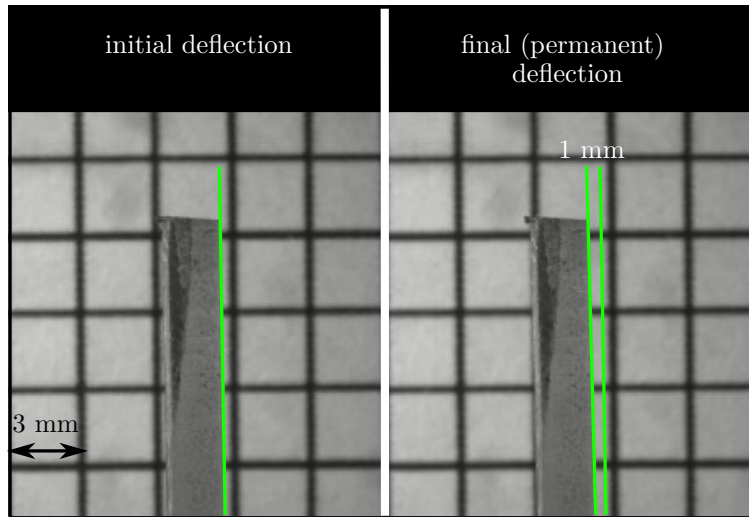


Figure 5.8: Before (left) and after (right) image of the free end of the specimen shown in Fig. 5.7(a) after applying a large voltage exceeding the normal operational range (i.e. ramping to 1800 V) and suddenly turning off the voltage. Applying a large voltage results in domain switching in the MFC actuator, which causes a permanent deflection of the specimen of 1 mm.

5.4 Dynamic electromechanical testing

A substantial increase in the loss tangent of PZT during electric field-induced domain switching was observed in the experiments of Chapter 3. To understand this phenomenon in structural applications, the overall loss tangent of a cantilever, with an attached PZT actuator undergoing domain switching, was characterized. In particular, the overall loss tangent in bending was measured using BES on specimens similar to that shown in Fig. 5.7(a) (i.e. a plexiglass substrate with an attached MFC actuator). However, a second MFC actuator was attached to the reverse side of the plexiglass substrate (opposite the first MFC actuator). In this way, the extension of the actuators is symmetric, which reduces the overall deflection of the specimen. This was necessary because the deflection of the specimens used to demonstrate set-and-hold actuators was sufficiently large to cause the reflected laser ray in the BES setup to move out of the position sensor.

A cyclic, triangle-wave voltage was applied to both MFC actuators simultaneously (and symmetrically) at different frequencies with an amplitude of 5 kVpp. A mechanical bending moment was applied at 25 Hz with an amplitude of 7.2 Vpp. The loss tangent in bending and charge accumulation were measured throughout the electric hysteresis for each frequency as shown in Fig. 5.9.

First, Fig. 5.9(a) shows the charge hysteresis. One can see that the spontaneous charge is approximately twice that seen in the experiments performed on specimens with a single MFC actuator as shown in Fig. 5.5 for comparable frequencies. This is because of the contribution to the total charge from both MFC actuators, which are connected in parallel. The coercive voltages for the specimens with two MFC actuators are approximately the same as those with one actuator.

The bending loss tangent versus applied voltage is shown in Fig. 5.9(b) for electric field frequencies of 0.01 and 1 Hz. The bending loss tangent of the MFC actuator specimen is both qualitatively and quantitatively different than that observed in the experiments on PZT shown in Fig. 3.9(b). For the case of 0.01 Hz, the loss tangent variation is substantially reduced from that seen in Fig. 3.9(b), where the loss tangent increases from 0.048 at zero electric field to only 0.054 during domain switching. However, there is still a rate dependence as the damping variation is more substantial for 1 Hz, where the loss tangent increases from 0.054 at zero electric field to as much as 0.081 during domain switching. Unlike PZT, two peaks appear in the loss tangent (for the 1 Hz case) as the electric field increases from zero and passes through the coercive field and as the voltage decreases back to zero (the former is more pronounced than the latter). This could be attributed to domain wall motion occurring while the electric field is being reduced. Since internal stresses are present in the actuators, domains may “un-switch” to reduce stress, which does not occur in free-standing PZT. Finally, the magnitudes of the loss tangent during domain switching for the MFC actuators is much smaller than that of pure PZT. This is due to the geometry of the actuators. For the specimens tested, which are similar to the one shown in Fig. 5.7, the mechanical bending applies a tensile/compressive stress along the poling direction of the attached actuators. Therefore, 90° domain switching caused by the mechanical loading is significantly reduced compared to the experiments shown in Fig. 3.9(b) where the mechanical loading was applied transverse to the poling direction; mechanically induced strains along the poling direction can be accommodated through 180° domain switching, which results in less dissipation than 90° domain switching.

These experiments demonstrated that electric field-induced domain switching in attached actuators can increase damping in structures. However, the increased loss tangent is only marginally higher than the base loss tangent of the plexiglass substrate, which is approximately 0.05. The greatest increase was observed when applying a 1 Hz cyclic voltage where the loss tangent increased by 50 % (compared to nearly 500% for pure PZT from Fig. 3.9). Therefore, further studies should investigate potential ways of increasing the damping in the actuator, for example, by test-

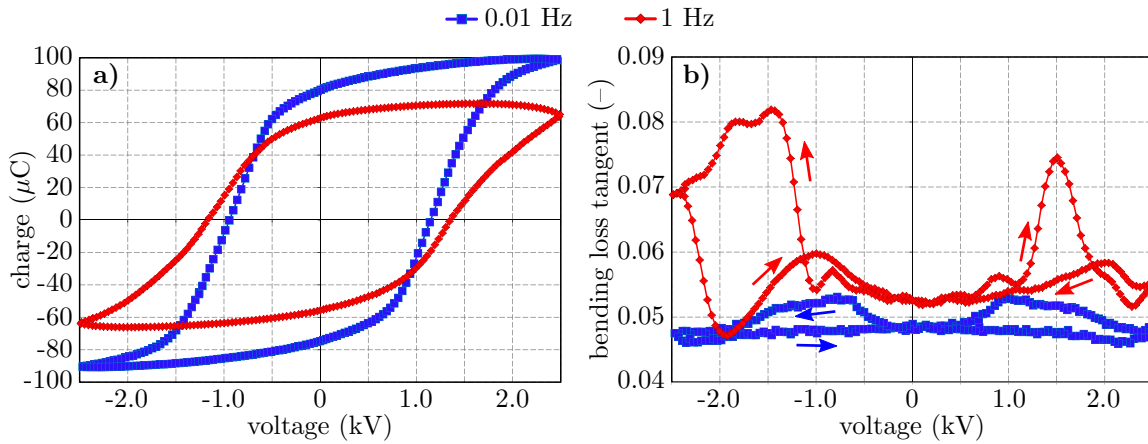


Figure 5.9: Evolution of the (a) charge accumulation and (b) bending loss tangent versus applied voltage for the double-sided actuator specimen. Different triangle-wave voltage frequencies of 0.01 Hz and 1 Hz were tested. The mechanical bending frequency was held constant at 25 Hz. Arrows indicate increasing time.

ing specimens with differently oriented MFC actuators such that mechanical stresses are applied transverse to their poling direction and cause more 90° domain switching. In addition, different types of MFC actuators, or other actuators in general, should be tested for their damping capacity. Characterization of the influence of domain switching in attached actuators on the full resonance spectrum of structures is also needed. Finally, different types of substrate material should be tested to see, for example, how the damping changes for stiffer or softer substrates.

Chapter 6

Conclusions

The goal of the research in this thesis was to gain a better understanding of the kinetics of domain switching in ferroelectric ceramics and how it influences their dynamic mechanical response. To this end, the experimental method and setup of BES was designed and built to characterize the dynamic mechanical response of ferroelectrics during electric field-induced domain switching. Using BES, the viscoelastic response of polycrystalline PZT was characterized and a model was developed that accurately predicts experimentally-observed behavior. The experiments and model gave insight into the kinetics of domain switching, which was then applied to demonstrate potential applications in set-and-hold actuators and structural damping. The main results from each of these thesis components are summarized below and are followed by recommendations for future work.

6.1 Broadband Electromechanical Spectroscopy

Previous research into domain switching effects on the mechanical response of ferroelectrics was rather limited. This was mainly because of a lack of experimental methodology. Therefore, to characterize the dynamic electromechanical response of ferroelectrics (and electro-active materials in general), an apparatus and method called Broadband Electromechanical Spectroscopy (BES) was developed. Using BES, the dynamic stiffness and damping of PZT were measured throughout the electric displacement hysteresis for a wide range of cyclic mechanical and electrical loading frequencies (beyond the capabilities of experimental setups used by, e.g., [Chaplya and Carman \(2002a\)](#) and [Jiménez and Vicente \(2000\)](#)). Going beyond all previous studies, the electromechanical response under torsional loading was also characterized for the first time using BES. The contactless

methods used to apply forces and measure deformation reduce the potential for damaging the brittle specimens. Moreover, the vacuum chamber in BES allowed for high-accuracy measurements of the specimen's loss tangent, which become strongly influenced by surrounding air when testing mechanical frequencies near resonance and for high electric field frequencies when the specimen deflection increases significantly. Error analysis and validation experiments of well-characterized materials showed that, indeed, high-accuracy measurements are obtained using BES. The main take-away points on BES as shown in this thesis are:

- BES allows for previously-unattainable combinations of electrical and multi-axial mechanical loading frequencies to be applied simultaneously to a wide range of materials,
- the vacuum chamber allows for high-accuracy damping measurements,
- the BES apparatus design incorporates features for future high-temperature experiments.

6.2 Viscoelastic characterization and modeling of PZT

Using BES, the dynamic stiffness and loss tangent in bending and torsion of a particular ferroelectric, polycrystalline lead zirconate titanate (PZT), were measured. In particular, the effect of different cyclic mechanical and electric field frequencies was characterized. Substantial softening in the stiffness and a corresponding large increase in the loss tangent were measured during electric field-induced domain switching. Particular experiments showed a decrease in the dynamic shear modulus of one-half and an increase in the loss tangent by almost an order of magnitude (i.e. increasing from 0.05 when no electric field was applied to almost 0.5 during domain switching). The remarkable loss tangent of 0.5 is typically observed in polymer materials and not ceramics and was attributed to 90° domain wall motion along the lines of (Arlt and Dederichs, 1980; Chaplya and Carman, 2002a). The dynamic stiffness and loss tangent during domain switching was highly-dependent on the frequency of the applied electric field. For higher frequencies, the increase in compliance and loss tangent during domain switching became more pronounced. The behavior of the dynamic stiffness and damping throughout the electric displacement hysteresis was also characterized throughout the full resonance spectrum of the specimen. The increased compliance and loss tangent during domain switching occurred for a wide range of mechanical frequencies and also resulted in a decrease in the specimen's (anti-)resonance frequencies. Therefore, domain switching not only results in temporary

large, broadband increases in damping, but also changes the resonance spectrum of the specimen, which is useful in structural applications for reducing vibrations.

Predicting the viscoelastic response of ferroelectrics during domain switching promises the design of materials and structures that yield the optimal dynamic mechanical response. Therefore, a continuum model similar to that of (Miehe and Rosato, 2011) was developed. A new linearization approach was used to extract the incremental complex moduli and compute the dynamic stiffness and loss tangent (as opposed to directly simulating the dynamic response due to oscillating mechanical loads using a time-stepping scheme). Excellent agreement between the model and experiments was achieved by selecting the appropriate parameters of the kinetic relation. In addition, the influence of the various static material properties and domain switching parameters (through the kinetic relation) was determined. Thus, guidelines were obtained on various ways of selecting or designing materials to obtain optimal viscoelastic performance. The main take-away points of the new physical understanding gained on domain switching kinetics are:

- the model predictions of the evolution of electric displacement, dynamic stiffness, and loss tangent agreed with experimental measurements for a wide range of mechanical and electric field cycling frequencies,
- domain switching decreases the incremental stiffness and increases the loss tangent,
- the influence of domain switching is more pronounced as the electrical loading rate increases,
- the effect of domain switching on viscoelastic properties occurs over a wide range of mechanical loading frequencies and shifts the specimen's (anti-)resonance to lower frequencies,
- using the newly-developed model, various material properties are predicted to increase the damping during domain switching: increasing static moduli, increasing spontaneous strain, decreasing spontaneous polarization, and increasing domain-wall mobility.

6.3 Structural applications

Towards taking advantage of the new understanding gained on the kinetics of domain switching, a proof-of-concept set-and-hold actuator was demonstrated. By controlling the evolution of the microstructure through electric field-induced domain switching, the macroscopic deformation of

ferroelectrics can be permanently altered and was measured using Digital Image Correlation (DIC). As an example, Macro Fiber Composite (MFC) actuators were attached to cantilevers such that their overall deflection was controlled by applying a voltage to the actuators. While applying small-amplitude voltages, the piezoelectric response of the actuators resulted in small, reversible deflections. However, going beyond piezoelectricity by applying large cyclic voltages resulted in larger amplitude deflections. In particular, turning off the applied voltage in the middle of domain switching resulted in a permanent deflection of the cantilever. This set-and-hold capability arising from domain switching has many applications where continuously applying a voltage to maintain a particular deformation is undesirable. For example, using active, deformable mirrors for telescopes in space normally requires continuous powering of piezoelectric actuators to alter the mirror's surface and correct for any errors. Alternatively, a larger voltage applied over a short period of time could be used to permanently deform the actuators, thus reducing the power requirements of the spacecraft. If power consumption is not a problem, additional small electric fields can be applied on top of the permanent deformed configuration to fine-tune the deformed shape.

In addition, the increased damping during domain switching in ferroelectrics was shown to control the overall damping in structures. Again, MFC actuators were attached to cantilevers and the overall damping of the specimen was characterized using BES while applying large, cyclic voltages. As in the experiments on free-standing PZT, increases in loss tangent were observed for the cantilevers when domain switching was occurring in the attached actuators. However, the effect was much less pronounced than in free-standing PZT due to internal stresses present in the actuators as well as the different orientation of the poling direction in the MFC actuators. Nonetheless, the increased damping of the cantilever during domain switching is useful for controlling the vibration of structures. The main results obtained from the structural application experiments are:

- permanent deflection and overall damping of cantilevers can be controlled via electric field-induced domain switching in attached MFC actuators,
- permanent deflections are on the order of the reversible deflections reached via piezoelectricity in the specimens tested,
- the increased overall damping of cantilevers was less pronounced than that observed in free-standing ferroelectrics due to coupling between the structure and actuator as well as the particular orientation of the actuators used.

6.4 Future work

Although new understanding was gained on how domain switching kinetics affects the time-dependent mechanical response of ferroelectrics, there remain many unexplored effects, the study of which presents possible directions of future work. The various topics of potential future studies are described below.

1. So far, the temperature-control capabilities of BES have not been utilized. Nonetheless, the effect of temperature on the kinetics of domain switching and domain wall motion is significant ([Savage and Miller, 1960](#)). Therefore, it is expected that the viscoelastic properties of ferroelectrics during domain switching are temperature dependent. Studying the fully-coupled thermo-electromechanical response is necessary for potential applications such as the set-and-hold actuators presented in Section [5.3.3](#). In particular, when controlling deformable mirrors in space applications, the material will be subjected to wide ranges of temperature. Although the current setup allows for increased temperature (above room temperature), adding the capability to lower the temperature would also be beneficial; ferroelectric materials can transition to different ferroelectric phases at reduced temperature, which changes their viscoelastic response. For example, PZT with zirconium levels above the morphotropic phase boundary can transform from a high-temperature rhombohedral form to a low-temperature form near 0°C – the exact temperature depends on composition ([Jaffe et al., 1971](#)).
2. PZT was investigated due to its wide use in industry. However, similar experiments should be performed on different ferroelectric ceramics such as (lead-free) barium titanate (BaTiO_3), which exhibits different spontaneous strains and will therefore exhibit a different viscoelastic response during domain switching. Also, the effect of different microstructures (e.g. grain and domain size and orientation) that can arise from different manufacturing processes needs further study. Testing composites of ferroelectric materials may lead to interesting behavior due to unstable phases, where large increases in dynamic stiffness and damping have been predicted ([Fritzen and Kochmann, 2014](#); [Lakes et al., 2001](#); [Wojnar and Kochmann, 2014a,b](#)); temperature-induced phase-transforming inclusions in composites were observed by [Jaglinski et al. \(2007\)](#) to cause large increases in stiffness and damping. A similar behavior is expected for electric field-induced eigenstrain in composites with ferroelectric inclusions.

3. To characterize the viscoelastic Young and shear moduli, separate bending and torsional moments were applied to PZT specimens. However, possible coupling between bending and torsional moments may be studied by applying different combinations of bending and torsional moments simultaneously, resulting in complex, multiaxial loading.
4. Incremental viscoelastic properties were determined by applying mechanical loads at frequencies much higher than the cyclic electric field frequency. Nonetheless, potential structural applications may be subjected comparable mechanical and electrical loading frequencies, which should be investigated.
5. To further expand on ways of controlling domain switching kinetics, different electrical loading histories, such as set-and-hold and ramp-and-hold histories, should be investigated. That is, in order to answer the question: to reach a certain permanent strain from a certain initial state, what voltage history should be applied?
6. For long-term applications of domain switching in e.g. set-and-hold actuators, the mechanical and electric fatigue behavior of ferroelectrics and actuators must be characterized. This can be done using BES by applying long-duration mechanical and electrical loading, and initial studies have been conducted in our group showing interesting long-term characteristics with a Hill-type fatigue evolution.
7. Further investigation of domain switching kinetics in different types of actuators and structures is needed to be able to select the optimal type of actuator for a given application.
8. Although not reported here, the continuum-mechanics model presented in Chapter 4 has been implemented in a Finite Element framework where it can be beneficially exploited to simulate structures with attached ferroelectric actuators (e.g. for the set-and-hold actuator concept or for structural damping). A detailed validation and verification study is required to assess the accuracy of the constitutive model and make it available for structural applications.
9. Exploring domain wall kinetics on the micro level and how it affects macroscopic viscoelasticity is warranted. For example, performing experiments where the evolution of domains is observed in-situ under dynamic electromechanical loading would give insight into the mobility of domain walls. In addition, the development of microstructure-sensitive models can reveal ways of controlling microstructure to give the optimal viscoelastic response.

Appendix A

Estimating Current Leakage

A schematic of the Sawyer-Tower circuit used in BES experiments is shown in Fig. A.1. Due to the time-dependent response of the circuit, accurate measurements can only be taken for certain triangle-wave voltage $V(t)$ frequencies, f , applied to the specimen. We assume that the response time of the circuit is much faster than the applied voltage frequencies. Indeed, the response of the specimen limits the maximum applied voltage frequency to below 10 Hz, which is much slower than the response of the circuit. However, the well-known problem of charge leakage off the reference capacitor C_0 through the scope (with finite impedance R_s) limits the minimum frequency that can be used. For slow frequencies, there is more time for charge to leak off the capacitor during one cycle, which alters the inferred electric displacement of the specimen. Different circuit elements can be chosen to reduce this effect. In this section, a lower bound on the frequency for a given set-up is derived to determine appropriate circuit components.

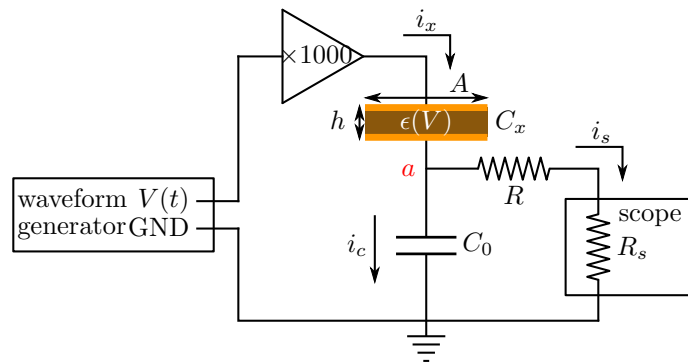


Figure A.1: Sawyer-Tower circuit.

First, apply Kirchhoff's current law at point a in Fig. A.1,

$$i_x = i_c + i_s = C_0 \frac{dV_a}{dt} + \frac{V_a}{R + R_s}. \quad (\text{A.1})$$

In order to assume the charge on the two capacitors is nearly the same, which is done when inferring the electric displacement on the specimen, the leakage current (at any given time) should be a small fraction of the total current going onto the capacitor, that is

$$i_c \gg i_s \Rightarrow C_0 \frac{dV_a}{dt} \gg \frac{V_a}{R + R_s}. \quad (\text{A.2})$$

The electric displacement of the specimen through the thickness is $d = \epsilon e + p$. The charge on the surface of the specimen is the electric displacement times the area,

$$Q = Ad = A\epsilon e + Ap = A\epsilon V/h + Ap, \quad (\text{A.3})$$

where the electric field is given by $e = V/h$ (neglecting the voltage drop across the reference capacitor). The current through the specimen is

$$i_x = \frac{dQ}{dt} = \frac{A\epsilon}{h} \frac{dV}{dt} + A \frac{dp}{dt} = \frac{A\epsilon}{h} \left(\frac{dV}{dt} - \frac{dV_a}{dt} \right) + A \frac{dp}{dt}. \quad (\text{A.4})$$

Inserting (A.4) into (A.1) yields

$$\begin{aligned} \frac{A\epsilon}{h} \left(\frac{dV}{dt} - \frac{dV_a}{dt} \right) + A \frac{dp}{dt} &= C_0 \frac{dV_a}{dt} + \frac{V_a}{R + R_s}, \\ \Rightarrow \frac{dV_a}{dt} &= \left(A \frac{dp}{dt} + \frac{A\epsilon}{h} \frac{dV}{dt} - \frac{V_a}{R + R_s} \right) / (C_0 + A\epsilon/h). \end{aligned} \quad (\text{A.5})$$

Now the system is solved so we can substitute (A.5) into the condition in (A.2),

$$\begin{aligned} \frac{C_0}{C_0 + A\epsilon/h} \left(A \frac{dp}{dt} + \frac{A\epsilon}{h} \frac{dV}{dt} - \frac{V_a}{R + R_s} \right) &\gg \frac{V_a}{R + R_s}, \\ \Rightarrow \frac{C_0}{C_0 + A\epsilon/h} \left(A \frac{dp}{dt} + \frac{A\epsilon}{h} \frac{dV}{dt} \right) &\gg \frac{V_a}{R + R_s} \left(1 + \frac{C_0}{C_0 + A\epsilon/h} \right). \end{aligned} \quad (\text{A.6})$$

The dp/dt and dV/dt terms have the same sign since the polarization changes in the same direction as the changing electric field. Then the left hand side of (A.6) can be bounded from below by

Table A.1: Approximate properties of circuit components used and voltages applied in experiments.

parameter	symbol	value
voltage measured by oscilloscope	V_s	1 V
voltage amplitude applied to specimens	V_0	10^3 V
impedance of oscilloscope	R_s	10^6 Ω
linear capacitance of specimen	C_x	5×10^{-8} C/V

neglecting the dp/dt term,

$$\begin{aligned} \frac{C_0 A \epsilon / h}{C_0 + A \epsilon / h} \frac{dV}{dt} &\gg \frac{V_a}{R + R_s} \left(1 + \frac{C_0}{C_0 + A \epsilon / h} \right) \\ \frac{C_0 (C_x / C_0)}{2 + C_x / C_0} \frac{dV}{dt} &\gg \frac{V_a}{R + R_s}, \end{aligned} \quad (\text{A.7})$$

where the linear capacitance of the specimen is $C_x = A \epsilon / d$. The voltage across the capacitor should be much less than that across the specimen, i.e. $C_x / C_0 \ll 1$. Thus, (A.7) becomes

$$\frac{C_x}{2} \frac{dV}{dt} \gg \frac{V_a}{R + R_s}. \quad (\text{A.8})$$

For a triangle-wave input $|dV/dt| = 4V_0 f$, where V_0 is the amplitude of the applied voltage $V(t)$. Also, V_a can be written in terms of V_s so that

$$2C_x V_0 f \gg V_s / R_s \quad \Rightarrow \quad f \gg \frac{V_s / V_0}{2R_s C_x}. \quad (\text{A.9})$$

Using comparable order of magnitudes for the components and applied voltages used in experiments (shown in Tab. A.1) results in the condition: $f \gg 10^{-2}$ Hz. Thus, for the circuit used, the frequency of the applied electric field should be higher than 0.01 Hz, which is the case in most of the experiments performed. However, when testing the effect of electric fields at 0.01 Hz, the Sawyer-Tower circuit had to be modified by adding a 48 M Ω resistance between the reference capacitor and the scope to reduce the charge leakage (effectively increasing R_s). By doing so, the voltage on the reference capacitor is not what is measured by the oscilloscope as the additional resistor acts as a voltage divider. Thus the voltage on the capacitor must be computed.

Appendix B

Selecting the Time Constant of the Lock-In Amplifier

The purpose of the lock-in amplifier is to extract the amplitude and phase of the laser position due to the deflection/twist of the specimen during the experiment. The driving voltage on the coils is used as the reference signal:

$$V_{\text{ref}}(t) = \hat{V}_{\text{ref}} \sin(\omega_{\text{ref}}t + \phi_{\text{ref}}), \quad (\text{B.1})$$

where \hat{V}_{ref} , ω_{ref} , and ϕ_{ref} are its amplitude, frequency, and phase shift, respectively. The response of the specimen causes the laser position to move in the detector resulting in a voltage signal that is used as the input to the lock-in amplifier,

$$V_{\text{in}}(t) = \hat{V}_{\text{sig}} \sin(\omega_{\text{sig}}t + \phi_{\text{sig}}) + \hat{V}_{\text{noise}} \sin(\omega_{\text{noise}}t + \phi_{\text{noise}}), \quad (\text{B.2})$$

where quantities with subscript “sig” refer to the material response of the specimen and subscript “noise” refers to any noise components of the signal. Since we are interested in the response of the specimen, we use the lock-in amplifier to extract its contribution from the overall signal. First, the lock-in amplifier multiplies the reference and input signals resulting in a signal

$$\begin{aligned} V_{\text{psd}}(t) &= V_{\text{in}}(t)V_{\text{ref}}(t) = V_{\text{ref}} \sin(\omega_{\text{ref}}t + \phi_{\text{ref}}) [V_{\text{sig}} \sin(\omega_{\text{sig}}t + \phi_{\text{sig}}) + V_{\text{noise}} \sin(\omega_{\text{noise}}t + \phi_{\text{noise}})] \\ &= \frac{1}{2} V_{\text{ref}} V_{\text{sig}} [\cos((\omega_{\text{sig}} - \omega_{\text{ref}})t + \phi_{\text{sig}} - \phi_{\text{ref}}) + \cos((\omega_{\text{sig}} + \omega_{\text{ref}})t + \phi_{\text{sig}} + \phi_{\text{ref}})] \\ &\quad + \frac{1}{2} V_{\text{ref}} V_{\text{noise}} [\cos((\omega_{\text{noise}} - \omega_{\text{ref}})t + \phi_{\text{noise}} - \phi_{\text{ref}}) + \cos((\omega_{\text{noise}} + \omega_{\text{ref}})t + \phi_{\text{noise}} + \phi_{\text{ref}})], \end{aligned}$$

where trigonometric identities have been used. Next, $V_{\text{psd}}(t)$ is input to a low-pass filter. Ideally, the low-pass filter removes any time-varying component of the signal. At steady-state, the response of the specimen is at the driving frequency (i.e. $\omega_{\text{sig}} - \omega_{\text{ref}} = 0$), which gives rise to a DC component of the signal,

$$X(t) = \frac{1}{2}V_{\text{ref}}V_{\text{sig}} \cos(\phi_{\text{sig}} - \phi_{\text{ref}}) \quad (\text{B.3})$$

assuming the noise is different from the driving frequency. Then, the process is repeated where the lock-in multiplies the input signal with the reference signal phase shifted by 90° , i.e. replacing $\phi_{\text{ref}} \rightarrow \phi_{\text{ref}} + 90^\circ$. The low-pass filter then produces the second signal

$$Y(t) = \frac{1}{2}V_{\text{ref}}V_{\text{sig}} \cos(\phi_{\text{sig}} - \phi_{\text{ref}} - 90^\circ) = \frac{1}{2}V_{\text{ref}}V_{\text{sig}} \sin(\phi_{\text{sig}} - \phi_{\text{ref}}). \quad (\text{B.4})$$

Finally, taking the magnitude of (B.3) and (B.4) (denoted by R) results in a signal proportional to the signal amplitude \hat{V}_{sig} , i.e.

$$R = \sqrt{X^2 + Y^2} = \frac{1}{2}V_{\text{ref}}V_{\text{sig}}. \quad (\text{B.5})$$

In addition, the tangent of the phase difference between the driving signal and response signal is found by

$$\frac{Y}{X} = \frac{\sin(\phi_{\text{sig}} - \phi_{\text{ref}})}{\cos(\phi_{\text{sig}} - \phi_{\text{ref}})} = \tan \delta, \quad (\text{B.6})$$

where $\delta \equiv \phi_{\text{sig}} - \phi_{\text{ref}}$ is the phase shift. Normally, $\tan \delta$ is the loss tangent (damping) of the material. In addition, the results in Chapter 3 report the relative moduli (or ratio of deflection/twist amplitude to a reference value). Thus, for the same reference signal, V_{ref} is constant and drops out upon taking the ratio of R for e.g. different frequencies or applied electric fields, which was used in (2.7).

The above analysis applies for an ideal filter and no noise. To account for and mitigate these effects, it is important to select an appropriate time constant setting for the lock-in amplifier. The roll-off behavior or slope of the cutoff can also be selected on the lock-in amplifier, however, the greatest slope (of -24 dB/dec) was always used. The time constant setting $\tau \equiv 2\pi/f_{\text{cutoff}}$ controls the cutoff frequency f_{cutoff} for the low-pass filter applied to V_{psd} . A typical Bode magnitude plot is shown in Fig. B.1. The cutoff frequency is defined as the frequency where the output signal is reduced by 3 dB (or approximately half of the input amplitude). Recall that the signal being filtered, $V_{\text{psd}}(t)$, contains four time-varying components due to the $\omega_{\text{sig}} \pm \omega_{\text{ref}}$ and $\omega_{\text{noise}} \pm \omega_{\text{ref}}$ terms. As before, $\omega_{\text{sig}} - \omega_{\text{ref}} = 0$. Therefore, the low-pass filter should remove the other three terms. Since

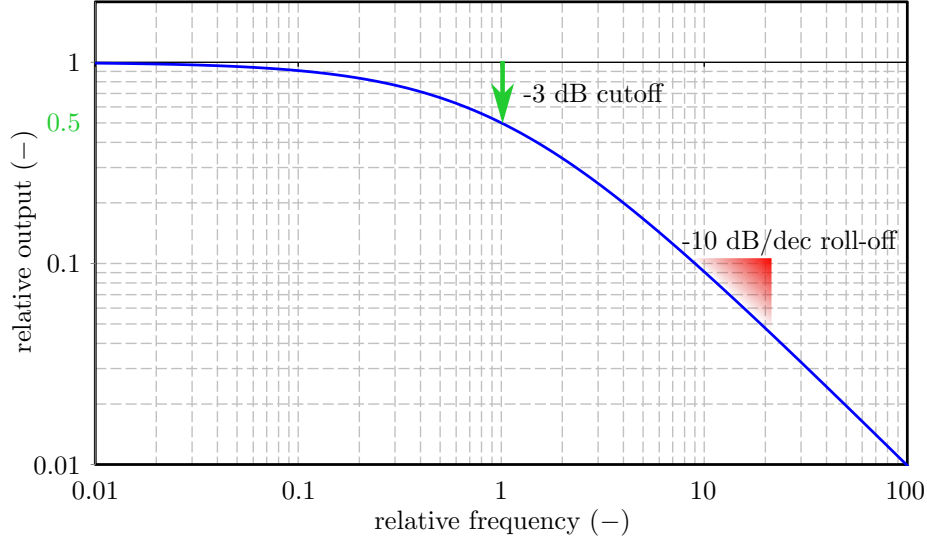


Figure B.1: Example Bode magnitude plot of a (first order) low-pass filter. The relative magnitude of the output to the input is plotted versus the relative frequency (relative to the cutoff frequency).

$|\omega_{\text{noise}} - \omega_{\text{ref}}| < \omega_{\text{noise}} + \omega_{\text{ref}}$, we only need consider the former; if the $\omega_{\text{noise}} - \omega_{\text{ref}}$ term is filtered out, then so will be the $\omega_{\text{noise}} + \omega_{\text{ref}}$ term. Furthermore, we know that $\omega_{\text{sig}} + \omega_{\text{ref}} = 2\omega_{\text{ref}}$. Thus, to remove the two terms in $V_{\text{psd}}(t)$ with $\omega_{\text{noise}} - \omega_{\text{ref}}$ and $2\omega_{\text{ref}}$, we should choose

$$f_{\text{cutoff}} < \min\{2f_{\text{ref}}, |f_{\text{noise}} - f_{\text{ref}}|\}, \quad (\text{B.7})$$

where f_{ref} and f_{noise} are the respective frequencies in Hertz of the angular frequencies ω_{ref} and ω_{noise} . Alternatively, the condition on the time constant is

$$\tau > 2\pi \max\left\{\frac{1}{2f_{\text{ref}}}, \frac{1}{|f_{\text{noise}} - f_{\text{ref}}|}\right\}. \quad (\text{B.8})$$

Thus, to obtain a pure DC output from the lock-in amplifier (if noise is not significant), the time constant should be greater than 0.13 s for the minimum frequency tested in experiments (i.e. 25 Hz). However, a 30 ms time constant was required to reduce smearing of the output due to its variation with the applied electric field. Therefore, for low frequencies such as 25 Hz, the lock-in output was more noisy compared to higher frequencies that were used. For frequencies above 100 Hz, the condition of (B.8) was satisfied.

Appendix C

Bending and Torsion Problems

The experiments of Chapter 3 were modeled using the dynamic Euler-Bernoulli beam as well as the dynamic torsion of a bar. The solutions to the two cases are give in the following sections. In particular, the effect of the specimen clamp, which holds the magnet, is accounted for in the boundary-value problem.

C.1 Solution of the dynamic Euler-Bernoulli beam

For bending experiments, the beam deflection $w(y, t)$ can be approximated by a dynamic Euler-Bernoulli beam with the governing equation

$$EI_z \frac{\partial^4 w}{\partial y^4}(y, t) = -\rho A \ddot{w}(y, t) \quad (\text{C.1})$$

and boundary conditions

$$\begin{aligned} w(0, t) = 0, \quad \frac{\partial w}{\partial y}(0, t) = 0, \quad EI_z \frac{\partial^3 w}{\partial y^3}(L, t) = m \ddot{w}(L, t), \\ EI_z \frac{\partial^2 w}{\partial y^2}(L, t) = M_z(t), \end{aligned} \quad (\text{C.2})$$

where E is Young's modulus, I_z is the bending moment of inertia, ρ is the mass density, A denotes the cross-sectional area, m represents the end mass due to the clamped magnet, $M_z(t)$ is the applied moment, and L is the free length of the specimen. Assuming harmonic motion of the beam at steady-state (i.e. $w(y, t) = \hat{w}(y)e^{i\omega t}$ and $M_z(t) = \hat{M}_z e^{i\omega t}$) with frequency ω , (C.1) and (C.2)

become

$$EI_z \frac{\partial^4 \hat{w}}{\partial y^4}(y) = \rho \omega^2 A \hat{w}(y) \quad (\text{C.3})$$

and

$$\begin{aligned} \hat{w}(0) = 0, \quad \frac{\partial \hat{w}}{\partial y}(0) = 0, \quad EI_z \frac{\partial^3 \hat{w}}{\partial y^3}(L) = -m \omega^2 \hat{w}(L), \\ EI_z \frac{\partial^2 \hat{w}}{\partial y^2}(L) = \hat{M}_z, \end{aligned} \quad (\text{C.4})$$

respectively. The solution of (C.3) with boundary conditions (C.4) yields the amplitude of the beam deflection as

$$\begin{aligned} \hat{w}(y) = \frac{\hat{M}_z}{2EI_z \lambda^2} & [\cosh(\xi(1-y')) + r\xi \sinh(\xi(1-y')) \\ & + \cosh(y'\xi)(\cos \xi - r\xi \sin \xi) \\ & + \sinh(y'\xi)(\sin \xi + r\xi \cos \xi) \\ & - \cos(y'\xi)(\cos \xi + \cosh \xi - r\xi(\sin \xi - \sinh \xi)) \\ & - \sin(y'\xi)(\sin \xi - \sinh \xi + r\xi(\cos \xi - \cosh \xi))] \\ & / [1 + \cos \xi \cosh \xi + r\xi(\cos \xi \sinh \xi - \sin \xi \cosh \xi)], \end{aligned} \quad (\text{C.5})$$

where $\lambda^4 = \rho A \omega^2 / (EI_z)$, $y' = y/L$, $\xi = \lambda L$, and $r = m / (\rho AL)$. Using this result, the angle at the end of the beam $\hat{\theta}_z = (\partial \hat{w} / \partial y)(L)$ is,

$$\hat{\theta}_z = \frac{\hat{M}_z [\cosh \xi (r\xi \cos \xi + \sin \xi) + \cos \xi \sinh \xi - r\xi]}{EI_z \lambda [\cosh \xi (\cos \xi - r\xi \sin \xi) + r\xi \cos \xi \sinh \xi + 1]}. \quad (\text{C.6})$$

C.2 Solution of the dynamic torsion of a bar

The derivation for the solution of the dynamic torsion of a bar with an attached end mass with rotational inertia I_m is given in (Gottenberg and Christensen, 1964) and is repeated here for convenience. The governing equation for the twisting angle $\alpha(y, t)$ along the bar is

$$G \frac{\partial^2 \alpha}{\partial y^2}(y, t) = -\rho \ddot{\alpha}(y, t) \quad (\text{C.7})$$

with boundary conditions

$$\alpha(0, t) = 0, \quad GJ_y \frac{\partial \alpha}{\partial y}(L, t) = M_y(t) - I_m \ddot{\alpha}(L, t). \quad (\text{C.8})$$

Assuming harmonic motion at steady-state ($\alpha(y, t) = \hat{\alpha}(y)e^{i\omega t}$ and $M_y(t) = \hat{M}_y e^{i\omega t}$), the governing equation and boundary conditions become

$$G \frac{\partial^2 \hat{\alpha}}{\partial y^2}(y) = \rho \omega^2 \hat{\alpha}(y) \quad (\text{C.9})$$

and

$$\hat{\alpha}(0) = 0, \quad GJ_y \frac{\partial \hat{\alpha}}{\partial y}(L) = \hat{M}_y + I_m \omega^2 \hat{\alpha}(L), \quad (\text{C.10})$$

respectively. Solving equation (C.9) with boundary conditions (C.10) gives the twisting angle

$$\hat{\alpha}(y) = \frac{\hat{M}_y \sin(\Lambda y)}{GJ_y \Lambda \cos(\Lambda L) - I_m \omega^2 \sin(\Lambda L)}. \quad (\text{C.11})$$

Finally, evaluating (C.11) at the free end yields the twisting angle $\hat{\theta}_y = \hat{\alpha}(L)$ to be

$$\hat{\theta}_y = \frac{\hat{M}_y}{GJ_y \Lambda [\cot(\Lambda L) - (I_m/J_y)\Lambda/\rho]}, \quad (\text{C.12})$$

where $\Lambda = \omega/\sqrt{G/\rho}$.

Bibliography

- Abeyaratne, R., Knowles, J.K., 1990. On the driving traction acting on a surface of strain discontinuity in a continuum. *Journal of the Mechanics and Physics of Solids* 38, 345–360. URL: <http://www.sciencedirect.com/science/article/pii/002250969090003M>, doi:[http://dx.doi.org/10.1016/0022-5096\(90\)90003-M](http://dx.doi.org/10.1016/0022-5096(90)90003-M).
- Abrahams, S.C., Kurtz, S.K., Jamieson, P.B., 1968. Atomic displacement relationship to Curie temperature and spontaneous polarization in displacive ferroelectrics. *Physical Review* 172, 551–553. URL: <http://link.aps.org/doi/10.1103/PhysRev.172.551>, doi:[10.1103/PhysRev.172.551](https://doi.org/10.1103/PhysRev.172.551).
- Adams, R.D., Bacon, D.G.C., 1973. Measurement of the flexural damping capacity and dynamic Young's modulus of metals and reinforced plastics. *Journal of Physics D: Applied Physics* 6, 27. URL: <http://stacks.iop.org/0022-3727/6/i=1/a=308>.
- Ahluwalia, R., Cao, W., 2001. Computer simulations of domain pattern formation in ferroelectrics. *AIP Conference Proceedings* 582, 185–190. URL: <http://link.aip.org/link/?APC/582/185/1>, doi:<http://dx.doi.org/10.1063/1.1399703>.
- Alexopoulos, N.D., Migklis, E., Stylianos, A., Myriounis, D.P., 2013. Fatigue behavior of the aeronautical alclii (2198) aluminum alloy under constant amplitude loading. *International Journal of Fatigue* 56, 95–105. URL: <http://www.sciencedirect.com/science/article/pii/S0142112313002016>, doi:<http://dx.doi.org/10.1016/j.ijfatigue.2013.07.009>.
- Anderson, T.J., Nayfeh, A.H., Balachandran, B., 1996. Experimental verification of the importance of the nonlinear curvature in the response of a cantilever beam. *Journal of Vibration and Acoustics* 118, 21–27. URL: <http://vibrationacoustics.asmedigitalcollection.asme.org/article.aspx?articleid=1469701>, doi:[10.1115/1.2889630](https://doi.org/10.1115/1.2889630).

- Arafa, M., Baz, A., 2000. Dynamics of active piezoelectric damping composites. *Composites Part B-Engineering* 31, 255–264. doi:[10.1016/S1359-8368\(00\)00020-2](https://doi.org/10.1016/S1359-8368(00)00020-2).
- Arlt, G., 1996. A physical model for hysteresis curves of ferroelectric ceramics. *Ferroelectrics* 189, 103–119. URL: <http://dx.doi.org/10.1080/00150199608213410>, doi:[10.1080/00150199608213410](https://doi.org/10.1080/00150199608213410).
- Arlt, G., Dederichs, H., 1980. Complex elastic, dielectric and piezoelectric constants by domain wall damping in ferroelectric ceramics. *Ferroelectrics* 29, 47–50. URL: <http://www.tandfonline.com/doi/abs/10.1080/00150198008009006>, doi:[10.1080/00150198008009006](https://doi.org/10.1080/00150198008009006).
- Arlt, G., Dederichs, H., Herbiet, R., 1987. 90°-domain wall relaxation in tetragonally distorted ferroelectric ceramics. *Ferroelectrics* 74, 37–53. URL: <http://dx.doi.org/10.1080/00150198708014493>, doi:[10.1080/00150198708014493](https://doi.org/10.1080/00150198708014493).
- Arlt, G., Neumann, H., 1988. Internal bias in ferroelectric ceramics: Origin and time dependence. *Ferroelectrics* 87, 109–120. URL: <http://dx.doi.org/10.1080/00150198808201374>, doi:[10.1080/00150198808201374](https://doi.org/10.1080/00150198808201374).
- Arlt, G., Sasko, P., 1980. Domain configuration and equilibrium size of domains in BaTiO₃ ceramics. *Journal of Applied Physics* 51, 4956–4960. URL: <http://link.aip.org/link/?JAP/51/4956/1>, doi:<http://dx.doi.org/10.1063/1.328372>.
- Arockiarajan, A., Menzel, A., Delibas, B., Seemann, W., 2006. Computational modeling of rate-dependent domain switching in piezoelectric materials. *European Journal of Mechanics - A/Solids* 25, 950–964. URL: <http://www.sciencedirect.com/science/article/pii/S0997753806000076>, doi:<http://dx.doi.org/10.1016/j.euromechsol.2006.01.006>.
- Arockiarajan, A., Sansour, C., 2008. Micromechanical modeling and simulation of rate-dependent effects in ferroelectric polycrystals. *Computational Materials Science* 43, 842–854. URL: <http://www.sciencedirect.com/science/article/pii/S0927025608000888>, doi:<http://dx.doi.org/10.1016/j.commatsci.2008.01.073>.
- Asare, T., Poquette, B., Schultz, J., Kampe, S., 2012. Investigating the vibration damping behavior of barium titanate (BaTiO₃) ceramics for use as a high damping reinforcement in metal matrix

- composites. *Journal of Materials Science* 47, 2573–2582. URL: <http://dx.doi.org/10.1007/s10853-011-6080-9>, doi:10.1007/s10853-011-6080-9.
- Asare, T.A., 2004. Fabrication and Damping Behavior of Particulate BaTiO₃ Ceramic Reinforced Copper Matrix Composites. Master's thesis. Virginia Polytechnic Institute and State University. URL: <http://scholar.lib.vt.edu/theses/available/etd-12032004-141136/unrestricted/Thesisetd.pdf>.
- Asare, T.A., 2007. Investigating Ferroelastic and Piezoelectric Vibration Damping Behavior in Nickel-Barium Titanate and Nickel-PZT Composites. Ph.D. thesis. Virginia Polytechnic Institute and State University. URL: <http://scholar.lib.vt.edu/theses/available/etd-10062007-151616/unrestricted/ETD-FINAL.pdf>.
- Bachmann, F., de Oliveira, R., Sigg, A., Schnyder, V., Delpero, T., Jaehne, R., Bergamini, A., Michaud, V., Ermanni, P., 2012. Passive damping of composite blades using embedded piezoelectric modules or shape memory alloy wires: A comparative study. *Smart Materials and Structures* 21, 075027. URL: <http://stacks.iop.org/0964-1726/21/i=7/a=075027>.
- Bailey, T., Hubbard, J.E., 1985. Distributed piezoelectric-polymer active vibration control of a cantilever beam. *Journal of Guidance Control and Dynamics* 8, 605–611. doi:10.2514/3.20029.
- Bassiouny, E., Ghaleb, A.F., Maugin, G.A., 1988a. Thermodynamical formulation for coupled electromechanical hysteresis effects - I. Basic equations. *International Journal of Engineering Science* 26, 1279–1295. URL: <http://www.sciencedirect.com/science/article/pii/002072258890047X>, doi:[http://dx.doi.org/10.1016/0020-7225\(88\)90047-X](http://dx.doi.org/10.1016/0020-7225(88)90047-X).
- Bassiouny, E., Ghaleb, A.F., Maugin, G.A., 1988b. Thermodynamical formulation for coupled electromechanical hysteresis effects - II. Poling of ceramics. *International Journal of Engineering Science* 26, 1297–1306. URL: <http://www.sciencedirect.com/science/article/pii/0020722588900481>, doi:[http://dx.doi.org/10.1016/0020-7225\(88\)90048-1](http://dx.doi.org/10.1016/0020-7225(88)90048-1).
- Bassiouny, E., Maugin, G.A., 1989. Thermodynamical formulation for coupled electromechanical hysteresis effects - IV. Combined electromechanical loading. *International Journal of Engineering Science* 27, 989–1000. URL: <http://www.sciencedirect.com/science/article/pii/0020722589900396>, doi:[http://dx.doi.org/10.1016/0020-7225\(89\)90039-6](http://dx.doi.org/10.1016/0020-7225(89)90039-6).

- Bhattacharya, K., Ravichandran, G., 2003. Ferroelectric perovskites for electromechanical actuation. *Acta Materialia* 51, 5941–5960. URL: <http://www.sciencedirect.com/science/article/pii/S1359645403004671>, doi:<http://dx.doi.org/10.1016/j.actamat.2003.08.001>. the Golden Jubilee Issue. Selected topics in Materials Science and Engineering: Past, Present and Future.
- Bishop, J.E., Kinra, V.K., 1995. Analysis of elastothermodynamic damping in particle-reinforced metal-matrix composites. *Metallurgical and Materials Transactions A* 26, 2773–2783. URL: <http://dx.doi.org/10.1007/BF02669635>, doi:[10.1007/BF02669635](http://dx.doi.org/10.1007/BF02669635).
- Brodtt, M., Cook, L.S., Lakes, R.S., 1995. Apparatus for measuring viscoelastic properties over ten decades: Refinements. *Review of Scientific Instruments* 66, 5292–5297. URL: <http://link.aip.org/link/?RSI/66/5292/1>, doi:[10.1063/1.1146101](http://dx.doi.org/10.1063/1.1146101).
- Budimir, M., Damjanovic, D., Setter, N., 2004. Large enhancement of the piezoelectric response in perovskite crystals by electric bias field antiparallel to polarization. *Applied Physics Letters* 85, 2890–2892. URL: <http://link.aip.org/link/?APL/85/2890/1>, doi:[10.1063/1.1799231](http://dx.doi.org/10.1063/1.1799231).
- Burcsu, E., 2001. Investigation of large strain actuation in barium titanate. Ph.D. thesis. California Institute of Technology. URL: <http://resolver.caltech.edu/CaltechETD:etd-10232001-192042>.
- Burcsu, E., Ravichandran, G., Bhattacharya, K., 2000. Large strain electrostrictive actuation in barium titanate. *Applied Physics Letters* 77, 1698–1700. URL: <http://scitation.aip.org/content/aip/journal/apl/77/11/10.1063/1.1308533>, doi:<http://dx.doi.org/10.1063/1.1308533>.
- Burcsu, E., Ravichandran, G., Bhattacharya, K., 2004. Large electrostrictive actuation of barium titanate single crystals. *Journal of the Mechanics and Physics of Solids* 52, 823–846. URL: <http://www.sciencedirect.com/science/article/pii/S0022509603001315>, doi:<http://dx.doi.org/10.1016/j.jmps.2003.08.001>.
- Burdett, C.F., Layng, R.B., 1968. Magnetic damping in terbium. *Journal of Physics D: Applied Physics* 1, 1005. URL: <http://stacks.iop.org/0022-3727/1/i=8/a=307>.

- Burianova, L., Panos, S., Hana, P., Nosek, J., 2008. The influence of DC electric field on piezoelectric coefficients of PZT ceramics. *Ferroelectrics* 367, 45–54. URL: <http://www.tandfonline.com/doi/abs/10.1080/00150190802365681>, doi:10.1080/00150190802365681.
- Burlage, S., 1965. The dependence of elastic constants on polarization in a ferroelectric ceramic. *Sonics and Ultrasonics, IEEE Transactions on* 12, 5–8. doi:10.1109/T-SU.1965.29349.
- Callister, W., Rethwisch, D., 2009. *Fundamentals of materials science and engineering: An integrated approach*. John Wiley & Sons.
- Cao, H., Evans, A.G., 1993. Nonlinear deformation of ferroelectric ceramics. *Journal of the American Ceramic Society* 76, 890–896. URL: <http://dx.doi.org/10.1111/j.1151-2916.1993.tb05312.x>, doi:10.1111/j.1151-2916.1993.tb05312.x.
- Capps, R.N., Beumel, L.L., 1990. *Dynamic Mechanical Testing*. chapter 5. pp. 63–78. URL: <http://pubs.acs.org/doi/abs/10.1021/bk-1990-0424.ch004>, doi:10.1021/bk-1990-0424.ch004.
- Carl, K., Hardtl, K.H., 1977. Electrical after-effects in $\text{Pb}(\text{Ti,Zr})\text{O}_3$ ceramics. *Ferroelectrics* 17, 473–486. URL: <http://dx.doi.org/10.1080/00150197808236770>, doi:10.1080/00150197808236770.
- Carman, G.P., McKnight, G., 2002. Damping in composite materials through domain wall motion. URL: <http://appft1.uspto.gov/netacgi/nph-Parser?Sect1=PTO1&Sect2=HITOFF&d=PGO1&p=1&u=/netahtml/PTO/srchnum.html&r=1&f=G&l=50&s1=20020004543.PGNR..> Patent.
- Carvell, J., Cheng, R., 2010. Study of electrical polarization hysteresis in ferroelectric polyvinylidene fluoride films. *Materials Letters* 64, 1992–1995. URL: <http://www.sciencedirect.com/science/article/pii/S0167577X10004829>, doi:http://dx.doi.org/10.1016/j.matlet.2010.06.030.
- Chandran, S., Kugel, V.D., Cross, L., 1996. Characterization of the linear and non-linear dynamic performance of rainbow actuator, in: *Applications of Ferroelectrics, 1996. ISAF '96.*, Proceedings of the Tenth IEEE International Symposium on, pp. 743–746. doi:10.1109/ISAF.1996.598131.
- Chaplya, P.M., Carman, G.P., 2001a. Dielectric and piezoelectric response of lead zirconate–lead titanate at high electric and mechanical loads in terms of non-180° domain wall motion. *Journal*

- of Applied Physics 90, 5278–5286. URL: <http://link.aip.org/link/?JAP/90/5278/1>, doi:10.1063/1.1410330.
- Chaplya, P.M., Carman, G.P., 2001b. Investigation of energy absorption capabilities of piezoelectric ceramic. Proceedings of SPIE 4333, 214–220. URL: <http://dx.doi.org/10.1117/12.432759>, doi:10.1117/12.432759.
- Chaplya, P.M., Carman, G.P., 2002a. Compression of piezoelectric ceramic at constant electric field: Energy absorption through non-180° domain-wall motion. Journal of Applied Physics 92, 1504–1510. URL: <http://link.aip.org/link/?JAP/92/1504/1>, doi:10.1063/1.1489498.
- Chaplya, P.M., Carman, G.P., 2002b. Compression of PZT-5H piezoelectric ceramic at constant electric field: Investigation of energy absorption mechanism. Proceedings of SPIE 4699, 124–132. URL: <http://dx.doi.org/10.1117/12.474967>, doi:10.1117/12.474967.
- Chen, J., 2011. Atomistic field theory of nano energy harvesting. Journal of Computational and Theoretical Nanoscience 8, 722–728. URL: <http://www.ingentaconnect.com/content/asp/jctn/2011/00000008/00000004/art00028>, doi:doi:10.1166/jctn.2011.1744.
- Chen, W., Lynch, C.S., 1998. A micro-electro-mechanical model for polarization switching of ferroelectric materials. Acta Materialia 46, 5303–5311. URL: <http://www.sciencedirect.com/science/article/pii/S1359645498002079>, doi:[http://dx.doi.org/10.1016/S1359-6454\(98\)00207-9](http://dx.doi.org/10.1016/S1359-6454(98)00207-9).
- Chen, Y.H., Viehland, D., 2000. Relaxational polarization dynamics in soft ferroelectrics. Applied Physics Letters 77, 133–135. doi:10.1063/1.126900.
- Cheng, B., L., Gabbay, M., Maglione, M., Jorand, Y., Fantozzi, G., 1996. Domain walls motions in barium titanate ceramics. Journal de Physique IV France 06, C8–647–C8–650. URL: <http://dx.doi.org/10.1051/jp4:19968139>.
- Christen, M., 1983. Air and gas damping of quartz tuning forks. Sensors and Actuators 4, 555–564. URL: <http://www.sciencedirect.com/science/article/pii/0250687483850677>, doi:[http://dx.doi.org/10.1016/0250-6874\(83\)85067-7](http://dx.doi.org/10.1016/0250-6874(83)85067-7).
- Christensen, R., 2003. Theory of Viscoelasticity: Second Edition. Dover Civil and Mechanical Engineering, Dover Publications. URL: <https://books.google.com/books?id=h7TDAGAAQBAJ>.

- Chu, T., Ranson, W., Sutton, M., 1985. Applications of digital-image-correlation techniques to experimental mechanics. *Experimental Mechanics* 25, 232–244. URL: <http://dx.doi.org/10.1007/BF02325092>, doi:10.1007/BF02325092.
- Cobine, J., 1941. *Gaseous Conductors: Theory and Engineering Applications*. Electrical engineering texts, McGraw-Hill book Company, Incorporated. URL: <http://books.google.com/books?id=zuwgAAAAMAAJ>.
- Cochran, W., 1959. Crystal stability and the theory of ferroelectricity. *Physical Review Letters* 3, 412–414. URL: <http://link.aps.org/doi/10.1103/PhysRevLett.3.412>, doi:10.1103/PhysRevLett.3.412.
- Cochran, W., 1961. Crystal stability and the theory of ferroelectricity part ii. Piezoelectric crystals. *Advances in Physics* 10, 401–420. URL: <http://dx.doi.org/10.1080/00018736100101321>, doi:10.1080/00018736100101321.
- Cocks, A.C.F., McMeeking, R.M., 1999. A phenomenological constitutive law for the behaviour of ferroelectric ceramics. *Ferroelectrics* 228, 219–228. URL: <http://dx.doi.org/10.1080/00150199908226136>, doi:10.1080/00150199908226136.
- Coleman, B., Noll, W., 1963. The thermodynamics of elastic materials with heat conduction and viscosity. *Archive for Rational Mechanics and Analysis* 13, 167–178. URL: <http://dx.doi.org/10.1007/BF01262690>, doi:10.1007/BF01262690.
- Conway, N.J., Traina, Z.J., Kim, S.G., 2007. A strain amplifying piezoelectric MEMS actuator. *Journal of Micromechanics and Microengineering* 17, 781. URL: <http://stacks.iop.org/0960-1317/17/i=4/a=015>.
- Crawley, E.F., Deluis, J., 1987. Use of piezoelectric actuators as elements of intelligent structures. *AIAA Journal* 25, 1373–1385. doi:10.2514/3.9792.
- Cross, C.J., Fleeter, S., 2002. Shunted piezoelectrics for passive control of turbomachine blading flow-induced vibrations. *Smart Materials and Structures* 11, 239. URL: <http://stacks.iop.org/0964-1726/11/i=2/a=307>.
- Curie, J., Curie, P., 1880a. Développement, par pression, de l'électricité polaire dans les cristaux hémihédres à faces inclinées. *Comptes Rendus de l'Académie des Sciences* 91, 294–295.

- Curie, J., Curie, P., 1880b. Sur l'électricité polaire dans les cristaux hémihédres à faces inclinées. *Comptes Rendus de l'Académie des Sciences* 91, 838–386.
- Daniels, J.E., Finlayson, T.R., 2006. Automated apparatus for dynamic mechanical analysis using the piezoelectric ultrasonic composite oscillator technique. *Journal of Physics D: Applied Physics* 39, 5290. URL: <http://stacks.iop.org/0022-3727/39/i=24/a=028>.
- D'Anna, G., Benoit, W., 1990. Apparatus for dynamic and static measurements of mechanical properties of solids and of flux-lattice in type-II superconductors at low frequency (10^{-5} –10 Hz) and temperature (4.7–500 K). *Review of Scientific Instruments* 61, 3821–3826. URL: <http://scitation.aip.org/content/aip/journal/rsi/61/12/10.1063/1.1141507>, doi:<http://dx.doi.org/10.1063/1.1141507>.
- De Marqui, Jr., C., Vieira, W.G.R., Erturk, A., Inman, D.J., 2011. Modeling and analysis of piezoelectric energy harvesting from aeroelastic vibrations using the doublet-lattice method. *Journal of Vibration and Acoustics-Transactions of the ASME* 133. doi:[10.1115/1.4002785](https://doi.org/10.1115/1.4002785).
- Devonshire, A.F., 1949. XCVI. Theory of barium titanate. *Philosophical Magazine Series 7* 40, 1040–1063. URL: <http://www.tandfonline.com/doi/abs/10.1080/14786444908561372>, doi:[10.1080/14786444908561372](https://doi.org/10.1080/14786444908561372).
- Devonshire, A.F., 1951. CIX. Theory of barium titanate: Part ii. *Philosophical Magazine Series 7* 42, 1065–1079. URL: <http://www.tandfonline.com/doi/abs/10.1080/14786445108561354>, doi:[10.1080/14786445108561354](https://doi.org/10.1080/14786445108561354).
- Dong, L., Stone, D., Lakes, R., 2011. Giant anelastic responses in (BaZrO₃-ZnO)-BaTiO₃ composite materials. *Europhysics Letters* 93, 66003. URL: <http://stacks.iop.org/0295-5075/93/i=6/a=66003>.
- Dong, L., Stone, D.S., Lakes, R.S., 2008. Broadband viscoelastic spectroscopy measurement of mechanical loss and modulus of polycrystalline BaTiO₃ vs. temperature and frequency. *Physica Status Solidi (b)* 245, 2422–2432. URL: <http://dx.doi.org/10.1002/pssb.200880270>, doi:[10.1002/pssb.200880270](https://doi.org/10.1002/pssb.200880270).
- Dong, L., Stone, D.S., Lakes, R.S., 2010. Softening of bulk modulus and negative Poisson ratio in

- barium titanate ceramic near the Curie point. *Philosophical Magazine Letters* 90, 23–33. URL: <http://dx.doi.org/10.1080/09500830903344907>, doi:10.1080/09500830903344907.
- Duffy, K.P., Choi, B.B., Provenza, A.J., Min, J.B., Kray, N., 2013. Active piezoelectric vibration control of subscale composite fan blades. *Journal of Engineering for Gas Turbines and Power-Transactions of the ASME* 135. doi:10.1115/1.4007720.
- Elhadrouz, M., Ben Zineb, T., Patoor, E., 2005. Constitutive law for ferroelectric and ferroelastic single crystals: A micromechanical approach. *Computational Materials Science* 32, 355–359. URL: <http://www.sciencedirect.com/science/article/pii/S0927025604002149>, doi:<http://dx.doi.org/10.1016/j.commatsci.2004.09.032>.
- Eshelby, J., 1975. The elastic energy-momentum tensor. *Journal of Elasticity* 5, 321–335. URL: <http://dx.doi.org/10.1007/BF00126994>, doi:10.1007/BF00126994.
- Eshelby, J.D., 1949. Dislocations as a cause of mechanical damping in metals. *Proceedings of the Royal Society A* 197, 396–416. doi:10.1098/rspa.1949.0072.
- Fanson, J.L., Caughey, T.K., 1990. Positive position feedback-control for large space structures. *AIAA Journal* 28, 717–724. doi:10.2514/3.10451.
- Fatuzzo, E., Merz, W., 1967. *Ferroelectricity. Series of Monographs on Selected Topics in Solid State Physics*, North-Holland Pub. Co. URL: <https://books.google.com/books?id=JitRAAAAMAAJ>.
- Ferry, J., 1980. *Viscoelastic Properties of Polymers*. Wiley. URL: <https://books.google.com/books?id=9dqQY3Ujxs4C>.
- Forward, R.L., 1979. Electronic damping of vibrations in optical structures. *Applied Optics* 18, 690–697. doi:10.1364/AO.18.000690.
- Frioui, N., Bezazi, A., Remillat, C., Scarpa, F., Gomez, J., 2010. Viscoelastic and compression fatigue properties of closed cell PVDF foam. *Mechanics of Materials* 42, 189–195. URL: <http://www.sciencedirect.com/science/article/pii/S0167663609001963>, doi:<http://dx.doi.org/10.1016/j.mechmat.2009.11.009>.
- Fritzen, F., Kochmann, D.M., 2014. Material instability-induced extreme damping in composites: A computational study. *International Journal of Solids and Structures* 51, 4101–4112. URL: <http://>

[//www.sciencedirect.com/science/article/pii/S0020768314003047](http://www.sciencedirect.com/science/article/pii/S0020768314003047), doi:<http://dx.doi.org/10.1016/j.ijsolstr.2014.07.028>.

Fu, R., Zhang, T.Y., 2000a. Effects of an electric field on the fracture toughness of poled lead zirconate titanate ceramics. *Journal of the American Ceramic Society* 83, 1215–1218. URL: <http://dx.doi.org/10.1111/j.1151-2916.2000.tb01356.x>, doi:10.1111/j.1151-2916.2000.tb01356.x.

Fu, R., Zhang, T.Y., 2000b. Influences of temperature and electric field on the bending strength of lead zirconate titanate ceramics. *Acta Materialia* 48, 1729–1740. URL: <http://www.sciencedirect.com/science/article/pii/S1359645400000100>, doi:[http://dx.doi.org/10.1016/S1359-6454\(00\)00010-0](http://dx.doi.org/10.1016/S1359-6454(00)00010-0).

Gadaud, P., Guisolan, B., Kulik, A., Schaller, R., 1990. Apparatus for high-temperature internal friction differential measurements. *Review of Scientific Instruments* 61, 2671–2675. URL: <http://scitation.aip.org/content/aip/journal/rsi/61/10/10.1063/1.1141858>, doi:<http://dx.doi.org/10.1063/1.1141858>.

Gaynutdinov, R., Minnekaev, M., Mitko, S., Tolstikhina, A., Zenkevich, A., Ducharme, S., Fridkin, V., 2013. Polarization switching kinetics in ultrathin ferroelectric barium titanate film. *Physica B: Condensed Matter* 424, 8–12. URL: <http://www.sciencedirect.com/science/article/pii/S0921452613002901>, doi:<http://dx.doi.org/10.1016/j.physb.2013.04.056>.

Genenko, Y.A., Wehner, J., von Seggern, H., 2013. Self-consistent model of polarization switching kinetics in disordered ferroelectrics. *Journal of Applied Physics* 114, 084101. URL: <http://scitation.aip.org/content/aip/journal/jap/114/8/10.1063/1.4818951>, doi:<http://dx.doi.org/10.1063/1.4818951>.

Gentner, J.O., Gerthsen, P., Schmidt, N.A., Send, R.E., 1978. Dielectric losses in ferroelectric ceramics produced by domain-wall motion. *Journal of Applied Physics* 49, 4485–4489. URL: <http://link.aip.org/link/?JAP/49/4485/1>, doi:10.1063/1.325453.

Gilbert, T.L., 2004. A phenomenological theory of damping in ferromagnetic materials. *Magnetics, IEEE Transactions on* 40, 3443–3449. doi:10.1109/TMAG.2004.836740.

- Goff, A., 2003. Modeling and Synthesis of a Piezoelectric Ceramic-Reinforced Metal Matrix Composite. Master's thesis. Virginia Polytechnic Institute and State University. URL: <http://scholar.lib.vt.edu/theses/available/etd-05212003-205819/unrestricted/finalthesis.pdf>.
- Goff, A.C., Aning, A.O., Kampe, S.L., 2004. A model to predict the damping potential of piezoelectric-reinforced metal matrix composites. *TMS Letters* 1, 59–60.
- Gottenberg, W., Christensen, R., 1964. An experiment for determination of the mechanical property in shear for a linear, isotropic viscoelastic solid. *International Journal of Engineering Science* 2, 45–57. URL: <http://www.sciencedirect.com/science/article/pii/0020722564900102>, doi:[http://dx.doi.org/10.1016/0020-7225\(64\)90010-2](http://dx.doi.org/10.1016/0020-7225(64)90010-2).
- Granato, A., Lücke, K., 2004. Theory of mechanical damping due to dislocations. *Journal of Applied Physics* 27, 583–593. URL: <http://scitation.aip.org/content/aip/journal/jap/27/6/10.1063/1.1722436>, doi:<http://dx.doi.org/10.1063/1.1722436>.
- le Graverend, J.B., Wojnar, C., Kochmann, D., 2015. Broadband Electromechanical Spectroscopy: Characterizing the dynamic mechanical response of viscoelastic materials under temperature and electric field control in a vacuum environment. *Journal of Materials Science* 50, 3656–3685. URL: <http://dx.doi.org/10.1007/s10853-015-8928-x>, doi:[10.1007/s10853-015-8928-x](http://dx.doi.org/10.1007/s10853-015-8928-x).
- Gribb, T.T., Cooper, R.F., 1998. A high-temperature torsion apparatus for the high-resolution characterization of internal friction and creep in refractory metals and ceramics: Application to the seismic-frequency, dynamic response of earths upper mantle. *Review of Scientific Instruments* 69, 559–564. URL: <http://scitation.aip.org/content/aip/journal/rsi/69/2/10.1063/1.1148694>, doi:<http://dx.doi.org/10.1063/1.1148694>.
- Gridnev, S.A., 2007. Low-frequency shear elasticity and mechanical losses in ferroelastics. *Ferroelectrics* 360, 1–24. URL: <http://dx.doi.org/10.1080/00150190701515840>, doi:[10.1080/00150190701515840](http://dx.doi.org/10.1080/00150190701515840).
- Grindlay, J., Haar, D., 2013. An Introduction to the Phenomenological Theory of Ferroelectricity: International Series of Monographs In: Natural Philosophy. International series of monographs in natural philosophy, Elsevier Science. URL: <https://books.google.com/books?id=Y88gBQAAQBAJ>.

- Guyomar, D., Richard, C., Mohammadi, S., 2008. Damping behavior of semi-passive vibration control using shunted piezoelectric materials. *Journal of Intelligent Material Systems and Structures* 19, 977–985. doi:[10.1177/1045389X07083122](https://doi.org/10.1177/1045389X07083122).
- Haertling, G.H., 1999. Ferroelectric ceramics: History and technology. *Journal of the American Ceramic Society* 82, 797–818. URL: <http://dx.doi.org/10.1111/j.1151-2916.1999.tb01840.x>, doi:[10.1111/j.1151-2916.1999.tb01840.x](https://doi.org/10.1111/j.1151-2916.1999.tb01840.x).
- Hagood, N., von Flotow, A., 1991. Damping of structural vibrations with piezoelectric materials and passive electrical networks. *Journal of Sound and Vibration* 146, 243–268. URL: <http://www.sciencedirect.com/science/article/pii/0022460X91907629>, doi:[10.1016/0022-460X\(91\)90762-9](https://doi.org/10.1016/0022-460X(91)90762-9).
- Hanagud, S., Obal, M.W., Calise, A.J., 1992. Optimal vibration control by the use of piezoceramic sensors and actuators. *Journal of Guidance Control and Dynamics* 15, 1199–1206. doi:[10.2514/3.20969](https://doi.org/10.2514/3.20969).
- Hao, Z., Erbil, A., Ayazi, F., 2003. An analytical model for support loss in micromachined beam resonators with in-plane flexural vibrations. *Sensors and Actuators A: Physical* 109, 156–164. URL: <http://www.sciencedirect.com/science/article/pii/S0924424703004898>, doi:<http://dx.doi.org/10.1016/j.sna.2003.09.037>.
- Harrison, R.J., Redfern, S.A.T., 2002. The influence of transformation twins on the seismic-frequency elastic and anelastic properties of perovskite: Dynamical mechanical analysis of single crystal LaAlO₃. *Physics of the Earth and Planetary Interiors* 134, 253–272. URL: <http://www.sciencedirect.com/science/article/pii/S0031920102001905>, doi:[http://dx.doi.org/10.1016/S0031-9201\(02\)00190-5](http://dx.doi.org/10.1016/S0031-9201(02)00190-5).
- Herbiet, R., Robels, U., Dederichs, H., Arlt, G., 1989. Domain wall and volume contributions to material properties of PZT ceramics. *Ferroelectrics* 98, 107–121. URL: <http://dx.doi.org/10.1080/00150198908217575>, doi:[10.1080/00150198908217575](https://doi.org/10.1080/00150198908217575).
- Holland, R., 1967. Representation of dielectric, elastic, and piezoelectric losses by complex coefficients. *Sonics and Ultrasonics, IEEE Transactions on* 14, 18–20. doi:[10.1109/T-SU.1967.29405](https://doi.org/10.1109/T-SU.1967.29405).

- Hooker, M.W., 1998. Properties of PZT-based Piezoelectric Ceramics Between-150 and 250°C. Book CR-1998-208708. National Aeronautics and Space Administration. URL: <http://ntrs.nasa.gov/archive/nasa/casi.ntrs.nasa.gov/19980236888.pdf>.
- Hosaka, H., Ito, K., Kuroda, S., 1995. Damping characteristics of beam-shaped micro-oscillators. *Sensors and Actuators A: Physical* 49, 87–95. URL: <http://www.sciencedirect.com/science/article/pii/092442479501003J>, doi:[http://dx.doi.org/10.1016/0924-4247\(95\)01003-J](http://dx.doi.org/10.1016/0924-4247(95)01003-J).
- Hourdakis, E., Simonds, B.J., Zimmerman, N.M., 2006. Submicron gap capacitor for measurement of breakdown voltage in air. *Review of Scientific Instruments* 77, 034702–034702. URL: <http://scitation.aip.org/content/aip/journal/rsi/77/3/10.1063/1.2185149>, doi:<http://dx.doi.org/10.1063/1.2185149>.
- Huber, J.E., 2005. Micromechanical modelling of ferroelectrics. *Current Opinion in Solid State and Materials Science* 9, 100–106. URL: <http://www.sciencedirect.com/science/article/pii/S1359028606000404>, doi:<http://dx.doi.org/10.1016/j.cossms.2006.05.001>.
- Huber, J.E., Fleck, N.A., 2001. Multi-axial electrical switching of a ferroelectric: Theory versus experiment. *Journal of the Mechanics and Physics of Solids* 49, 785–811. URL: <http://www.sciencedirect.com/science/article/pii/S0022509600000521>, doi:[http://dx.doi.org/10.1016/S0022-5096\(00\)00052-1](http://dx.doi.org/10.1016/S0022-5096(00)00052-1).
- Hwang, S.C., Huber, J.E., McMeeking, R.M., Fleck, N.A., 1998. The simulation of switching in polycrystalline ferroelectric ceramics. *Journal of Applied Physics* 84, 1530–1540. URL: <http://scitation.aip.org/content/aip/journal/jap/84/3/10.1063/1.368219>, doi:<http://dx.doi.org/10.1063/1.368219>.
- Hwang, S.C., Lynch, C.S., McMeeking, R.M., 1995. Ferroelectric/ferroelastic interactions and a polarization switching model. *Acta Metallurgica et Materialia* 43, 2073–2084. URL: <http://www.sciencedirect.com/science/article/pii/095671519400379V>, doi:[http://dx.doi.org/10.1016/0956-7151\(94\)00379-V](http://dx.doi.org/10.1016/0956-7151(94)00379-V).
- Ishibashi, Y., 1989. Phenomenological theory of domain walls. *Ferroelectrics* 98, 193–205. URL: <http://dx.doi.org/10.1080/00150198908217582>, doi:[10.1080/00150198908217582](http://dx.doi.org/10.1080/00150198908217582).

- Ishibashi, Y., 1990. Structure and physical properties of domain walls. *Ferroelectrics* 104, 299–310. URL: <http://dx.doi.org/10.1080/00150199008223831>, doi:10.1080/00150199008223831.
- Ishibashi, Y., Salje, E., 2004. Theoretical consideration on the 90° domain walls in tetragonal ferroelectrics. *Ferroelectrics* 303, 9–13. URL: <http://dx.doi.org/10.1080/00150190490456394>, doi:10.1080/00150190490456394.
- Iwata, M., Morishita, T., Aoyagi, R., Maeda, M., Suzuki, I., Yasuda, N., Ishibashi, Y., 2007. Observations and simulations of polarization reversals with the 90° domain wall structure in Bi₄Ti₃O₁₂. *Ferroelectrics* 355, 28–36. URL: <http://dx.doi.org/10.1080/00150190701515873>, doi:10.1080/00150190701515873.
- Iyer, S., Alkhader, M., Venkatesh, T.A., 2014. Electromechanical response of piezoelectric honeycomb foam structures. *Journal of the American Ceramic Society* 97, 826–834. URL: <http://dx.doi.org/10.1111/jace.12699>, doi:10.1111/jace.12699.
- Jaffe, B., Jaffe, H., Cook, W., 1971. *Piezoelectric Ceramics*. Non-metallic solids, Academic Press. URL: <https://books.google.com/books?id=a1v7cQAACAAJ>.
- Jaglinski, T., Kochmann, D., Stone, D., Lakes, R.S., 2007. Composite materials with viscoelastic stiffness greater than diamond. *Science* 315, 620–622. URL: <http://www.sciencemag.org/content/315/5812/620.abstract>, doi:10.1126/science.1135837.
- James, R., 2002. Configurational forces in magnetism with application to the dynamics of a small-scale ferromagnetic shape memory cantilever. *Continuum Mechanics and Thermodynamics* 14, 55–86. URL: <http://dx.doi.org/10.1007/s001610100072>, doi:10.1007/s001610100072.
- Jiménez, B., Vicente, J., 1998. The low-frequency Young modulus and internal friction in Pb-Ca and Pb-Zr titanate ceramics. *Journal of Physics D: Applied Physics* 31, 130. URL: <http://stacks.iop.org/0022-3727/31/i=1/a=016>.
- Jiménez, B., Vicente, J., 2000. Influence of mobile 90° domains on the complex elastic modulus of PZT ceramics. *Journal of Physics D: Applied Physics* 33, 1525. URL: <http://stacks.iop.org/0022-3727/33/i=12/a=315>.
- Jona, F., 1962. *Ferroelectric Crystals*. International Series of Monographs on Solid State Physics, V.1, Macmillan. URL: <https://books.google.com/books?id=FhQntWAACAAJ>.

- Kamiya, T., Tsurumi, T., Mishima, R., Sakai, E., Daimon, M., 1997. Frequency, electric field and temperature dependence of piezoelectric constant of $\text{Pb}(\text{Zr,Ti})\text{O}_3$ based ceramics under high electric field. *Ferroelectrics* 196, 277–280. URL: <http://dx.doi.org/10.1080/00150199708224179>, doi:10.1080/00150199708224179.
- Kamlah, M., 2001. Ferroelectric and ferroelastic piezoceramics - modeling of electromechanical hysteresis phenomena. *Continuum Mechanics and Thermodynamics* 13, 219–268. URL: <http://dx.doi.org/10.1007/s001610100052>, doi:10.1007/s001610100052.
- Kampe, S., Schultz, J., Aning, A., Goff, A., Franklin, J., 2006. Piezoelectric ceramic-reinforced metal-matrix composites. Patent.
- Kanata, T., Yoshikawa, T., Kubota, K., 1987. Grain-size effects on dielectric phase transition of BaTiO_3 ceramics. *Solid State Communications* 62, 765–767. URL: <http://www.sciencedirect.com/science/article/pii/0038109887900445>, doi:[http://dx.doi.org/10.1016/0038-1098\(87\)90044-5](http://dx.doi.org/10.1016/0038-1098(87)90044-5).
- Kawai, H., 1969. The piezoelectricity of poly (vinylidene fluoride). *Japanese Journal of Applied Physics* 8, 975. URL: <http://stacks.iop.org/1347-4065/8/i=7/a=975>.
- Kê, T.S., 1947. Experimental evidence of the viscous behavior of grain boundaries in metals. *Physical Review* 71, 533–546. URL: <http://link.aps.org/doi/10.1103/PhysRev.71.533>, doi:10.1103/PhysRev.71.533.
- Kim, S.J., 2011. A constitutive model for thermo-electro-mechanical behavior of ferroelectric polycrystals near room temperature. *International Journal of Solids and Structures* 48, 1318–1329. URL: <http://www.sciencedirect.com/science/article/pii/S0020768311000278>, doi:<http://dx.doi.org/10.1016/j.ijsolstr.2011.01.018>.
- Kinderlehrer, D., 1987. Twinning of crystals (ii), in: Antman, S., Ericksen, J., Kinderlehrer, D., Müller, I. (Eds.), *Metastability and Incompletely Posed Problems*. Springer New York. volume 3 of *The IMA Volumes in Mathematics and Its Applications*, pp. 185–211. URL: http://dx.doi.org/10.1007/978-1-4613-8704-6_12, doi:10.1007/978-1-4613-8704-6_12.
- King, P.C., Zahiri, S.H., Jahedi, M., Friend, J., 2007. Cold spray electroding of piezoelectric ceramic. *Materials Forum* 31, 116–119. © Institute of Materials Engineering Australasia Ltd.

- Kliem, H., Kuehn, M., 2011. Modeling the switching kinetics in ferroelectrics. *Journal of Applied Physics* 110, 114106. URL: <http://scitation.aip.org/content/aip/journal/jap/110/11/10.1063/1.3660680>, doi:<http://dx.doi.org/10.1063/1.3660680>.
- Kontsos, A., Landis, C.M., 2009. Computational modeling of domain wall interactions with dislocations in ferroelectric crystals. *International Journal of Solids and Structures* 46, 1491–1498. URL: <http://www.sciencedirect.com/science/article/pii/S0020768308004939>, doi:<http://dx.doi.org/10.1016/j.ijsolstr.2008.11.021>.
- Koppelman, J., 1958. Über die bestimmung des dynamischen elastizitätsmoduls und des dynamischen schubmoduls im frequenzbereich von 10^{-5} bis 10^{-1} Hz. *Rheologica Acta* 1, 20–28. URL: <http://dx.doi.org/10.1007/BF01982279>, doi:[10.1007/BF01982279](http://dx.doi.org/10.1007/BF01982279).
- Kruger, G., 1976. Domain wall motion concept to describe ferroelectric rhombohedral PLZT ceramics. *Ferroelectrics* 11, 417–422. URL: <http://dx.doi.org/10.1080/00150197608237773>, doi:[10.1080/00150197608237773](http://dx.doi.org/10.1080/00150197608237773).
- Kumar, N., Singh, S.P., 2009. Vibration and damping characteristics of beams with active constrained layer treatments under parametric variations. *Materials & Design* 30, 4162–4174. URL: <http://www.sciencedirect.com/science/article/pii/S0261306909001836>, doi:<http://dx.doi.org/10.1016/j.matdes.2009.04.044>.
- Kuokkala, V.T., Schwarz, R.B., 1992. The use of magnetostrictive film transducers in the measurement of elastic moduli and ultrasonic attenuation of solids. *Review of Scientific Instruments* 63, 3136–3142. URL: <http://scitation.aip.org/content/aip/journal/rsi/63/5/10.1063/1.1142566>, doi:<http://dx.doi.org/10.1063/1.1142566>.
- Lakes, R., 1998. *Viscoelastic Solids*. Mechanical and Aerospace Engineering Series, CRC Press. URL: <https://books.google.com/books?id=soZZl17sm5IC>.
- Lakes, R., Lee, T., Bersie, A., Wang, Y., 2001. Extreme damping in composite materials with negative-stiffness inclusions. *Nature* 410, 565–567. URL: <http://www.ncbi.nlm.nih.gov/pubmed/11279490>.
- Lakes, R., Quackenbusch, J., 1996. Viscoelastic behavior in indium tin alloys over a wide range of

- frequency and time. *Philosophical Magazine Letters* 74, 227–238. URL: <http://silver.neep.wisc.edu/~lakes/gInSn.pdf>.
- Lakes, R.S., 2004. Viscoelastic measurement techniques. *Review of Scientific Instruments* 75, 797–810. URL: <http://link.aip.org/link/?RSI/75/797/1>, doi:10.1063/1.1651639.
- Landau, L., 1937. On the theory of phase transitions (in russian). *Zhurnal Eksperimental'noi i Teoreticheskoi Fiziki* 7, 19–32.
- Landau, L., Bell, J., Kearsley, J., Pitaevskii, L., Lifshitz, E., Sykes, J., 1984. *Electrodynamics of Continuous Media. Course of Theoretical Physics*, Elsevier Science. URL: <http://books.google.com/books?id=jedbAwwAAQBAJ>.
- Landis, C.M., 2002. Fully coupled, multi-axial, symmetric constitutive laws for polycrystalline ferroelectric ceramics. *Journal of the Mechanics and Physics of Solids* 50, 127–152. URL: <http://www.sciencedirect.com/science/article/pii/S0022509601000217>, doi:[http://dx.doi.org/10.1016/S0022-5096\(01\)00021-7](http://dx.doi.org/10.1016/S0022-5096(01)00021-7).
- Landis, C.M., 2004. Non-linear constitutive modeling of ferroelectrics. *Current Opinion in Solid State and Materials Science* 8, 59–69. URL: <http://www.sciencedirect.com/science/article/pii/S1359028604000397>, doi:<http://dx.doi.org/10.1016/j.cossms.2004.03.010>.
- Lee, T., Aksay, I.A., 2001. Hierarchical structure-ferroelectricity relationships of barium titanate particles. *Crystal Growth & Design* 1, 401–419. URL: <http://dx.doi.org/10.1021/cg010012b>, doi:10.1021/cg010012b.
- Lee, T., Lakes, R., Lal, A., 2000. Resonant ultrasound spectroscopy for measurement of mechanical damping: Comparison with broadband viscoelastic spectroscopy. *Review of Scientific Instruments* 71, 2855. URL: <http://link.aip.org/link/RSINAK/v71/i7/p2855/s1&Agg=doi>.
- Li, F.M., Kishimoto, K., Wang, Y.S., Chen, Z.B., Huang, W.H., 2008. Vibration control of beams with active constrained layer damping. *Smart Materials and Structures* 17, 065036. URL: <http://stacks.iop.org/0964-1726/17/i=6/a=065036>.
- Lieberman, M., Lichtenberg, A., 2005. *Principles of Plasma Discharges and Materials Processing*. Wiley. URL: <https://books.google.com/books?id=m0i0ga2XE5wC>.

- Liepmann, H., Roshko, A., 1957. Elements of Gasdynamics. Dover Books on Aeronautical Engineering Series, Dover Publications. URL: <https://books.google.com/books?id=6zcolViQHIYC>.
- Lin, Q., Ermanni, P., 2004. Semi-active damping of a clamped plate using PZT. International Journal of Solids and Structures 41, 1741–1752. URL: <http://e-citations.ethbib.ethz.ch/view/pub:75334>, doi:10.1016/j.ijsolstr.2003.11.023.
- Lines, E., Glass, A., 1977. Principles and Applications of Ferroelectrics and Related Materials. International series of monographs on physics, Oxford University Press. URL: <https://books.google.com/books?id=p6ruJH8C84kC>.
- Little, E.A., 1955. Dynamic behavior of domain walls in barium titanate. Physical Review 98, 978–984. URL: <http://link.aps.org/doi/10.1103/PhysRev.98.978>.
- Liu, Y., Sanchez, A., Zogg, M., Ermanni, P., 2010. A comparative experimental study on structural and interface damping approaches for vibration suppression purposes. Proceedings of SPIE 7643, 764335. URL: <http://dx.doi.org/10.1117/12.848062>, doi:10.1117/12.848062.
- Lu, S.W., Lee, B.I., Wang, Z.L., Samuels, W.D., 2000. Hydrothermal synthesis and structural characterization of BaTiO₃ nanocrystals. Journal of Crystal Growth 219, 269–276. URL: <http://www.sciencedirect.com/science/article/pii/S0022024800006199>, doi:[http://dx.doi.org/10.1016/S0022-0248\(00\)00619-9](http://dx.doi.org/10.1016/S0022-0248(00)00619-9).
- Luo, L., Wang, H., Tang, Y., Zhao, X., Feng, Z., Lin, D., Luo, H., 2006. Ultrahigh transverse strain and piezoelectric behavior in $(1 - x)\text{Pb}(\text{Mg}_{1/3}\text{Nb}_{2/3})\text{O}_{3-x}\text{PbTiO}_3$ crystals. Journal of Applied Physics 99, 024104. URL: <http://scitation.aip.org/content/aip/journal/jap/99/2/10.1063/1.2161947>, doi:<http://dx.doi.org/10.1063/1.2161947>.
- Lupascu, D.C., 2004. Fatigue in Ferroelectric Ceramics and Related Issues. volume 61 of *Springer Series in Materials Science*. 1 ed., Springer-Verlag, Berlin Heidelberg. URL: <http://www.springer.com/us/book/9783540402350>, doi:10.1007/978-3-662-07189-2.
- Lynch, C., 1996. The effect of uniaxial stress on the electro-mechanical response of 8/65/35 PLZT. Acta Materialia 44, 4137–4148. URL: <http://www.sciencedirect.com/science/article/pii/S1359645496000626>, doi:[http://dx.doi.org/10.1016/S1359-6454\(96\)00062-6](http://dx.doi.org/10.1016/S1359-6454(96)00062-6).

- Mason, W., 2013. *Physical Acoustics: Principles and Methods*. v. 1, pt. 1, Elsevier Science. Ch. 3: Piezoelectric and Piezomagnetic Materials and their Function in Transducers.
- Meirovitch, L., 1997. *Principles and Techniques of Vibrations*. Prentice Hall. URL: <https://books.google.com/books?id=qg1RAAAAMAAJ>.
- Merz, W.J., 1954. Domain formation and domain wall motions in ferroelectric BaTiO₃ single crystals. *Physical Review* 95, 690–698. URL: <http://link.aps.org/doi/10.1103/PhysRev.95.690>, doi:10.1103/PhysRev.95.690.
- Merz, W.J., 1956. Switching time in ferroelectric BaTiO₃ and its dependence on crystal thickness. *Journal of Applied Physics* 27, 938–943. URL: <http://dx.doi.org/10.1063/1.1722518>.
- Miehe, C., Rosato, D., 2011. A rate-dependent incremental variational formulation of ferroelectricity. *International Journal of Engineering Science* 49, 466–496. URL: <http://www.sciencedirect.com/science/article/pii/S0020722510002466>, doi:<http://dx.doi.org/10.1016/j.ijengsci.2010.11.003>.
- Migliori, A., Sarrao, J., Visscher, V., Bell, T., Lei, M., Fisk, Z., Leisure, R., 1993. Resonant ultrasound spectroscopic techniques for measurement of the elastic moduli of solids. *Physica B: Condensed Matter* 183, 1–24. URL: <http://www.sciencedirect.com/science/article/pii/092145269390048B>, doi:10.1016/0921-4526(93)90048-B.
- Miller, R.C., 1958. Some experiments on the motion of 180° domain walls in BaTiO₃. *Physical Review* 111, 736–739. URL: <http://link.aps.org/doi/10.1103/PhysRev.111.736>, doi:10.1103/PhysRev.111.736.
- Miller, R.C., Savage, A., 1958. Velocity of sidewise 180° domain-wall motion in BaTiO₃ as a function of the applied electric field. *Physical Review* 112, 755. URL: <http://link.aps.org/doi/10.1103/PhysRev.112.755>, doi:10.1103/PhysRev.112.755.
- Miller, R.C., Savage, A., 1959a. Direct observation of antiparallel domains during polarization reversal in single-crystal barium titanate. *Physical Review Letters* 2, 294–296. URL: <http://link.aps.org/doi/10.1103/PhysRevLett.2.294>, doi:10.1103/PhysRevLett.2.294.

- Miller, R.C., Savage, A., 1959b. Further experiments on the sidewise motion of 180° domain walls in BaTiO_3 . *Physical Review*. 115, 1176–1180. URL: <http://link.aps.org/doi/10.1103/PhysRev.115.1176>, doi:10.1103/PhysRev.115.1176.
- Miller, R.C., Savage, A., 1960. Motion of 180° domain walls in metal electroded barium titanate crystals as a function of electric field and sample thickness. *Journal of Applied Physics* 31, 662–669. URL: <http://link.aip.org/link/?JAP/31/662/1>, doi:<http://dx.doi.org/10.1063/1.1735663>.
- Miller, R.C., Savage, A., 1961. Motion of 180° domain walls in BaTiO_3 under the application of a train of voltage pulses. *Journal of Applied Physics* 32, 714–721. URL: <http://scitation.aip.org/content/aip/journal/jap/32/4/10.1063/1.1736077>, doi:<http://dx.doi.org/10.1063/1.1736077>.
- Moulson, A., Herbert, J., 2003. *Electroceramics: Materials, Properties, Applications*. Wiley. URL: <https://books.google.com/books?id=FbMfaqSgOxsC>.
- Nagaoka, H., 1909. The inductance coefficients of solenoids. *Journal of the College of Science* 27, 18–33.
- Newnham, R., Dogan, A., Xu, Q., Onitsuka, K., Tressler, J., Yoshikawa, S., 1993. Flexensional “moonie” actuators, in: *Ultrasonics Symposium, 1993., Proceedings of the IEEE*, pp. 509–513. doi:10.1109/ULTSYM.1993.339557.
- Ng, N., Ahluwalia, R., Su, H.B., Boey, F., 2009. Lateral size and thickness dependence in ferroelectric nanostructures formed by localized domain switching. *Acta Materialia* 57, 2047–2054. URL: <http://www.sciencedirect.com/science/article/pii/S1359645408007374>, doi:<http://dx.doi.org/10.1016/j.actamat.2008.10.022>.
- Ngo, E., Northwang, W.D., Cole, M.W., Hubbard, C., Hirsch, G., Mohanchandra, K.P., Carman, G.P., 2004. *Fabrication of active thin films for vibration damping in MEMS devices for the next generation army munition systems*. Army Research Laboratories, Aberdeen Technical Publication.
- Ooi, P.C., Ishibashi, Y., Lim, S.C., Osman, J., 2007. Numerical investigation of polarization

- reversal characteristics in a ferroelectric thin film. *Ferroelectrics* 355, 216–222. URL: <http://dx.doi.org/10.1080/00150190701521392>, doi:10.1080/00150190701521392.
- Ortiz, M., Stainier, L., 1999. The variational formulation of viscoplastic constitutive updates. *Computer Methods in Applied Mechanics and Engineering* 171, 419–444. URL: <http://www.sciencedirect.com/science/article/pii/S0045782598002199>, doi:[http://dx.doi.org/10.1016/S0045-7825\(98\)00219-9](http://dx.doi.org/10.1016/S0045-7825(98)00219-9).
- Pan, W.Y., Dam, C.Q., Zhang, Q.M., Cross, L.E., 1989. Large displacement transducers based on electric field forced phase transitions in the tetragonal $(\text{Pb}_{0.97}\text{La}_{0.02})(\text{Ti,Zr,Sn})\text{O}_3$ family of ceramics. *Journal of Applied Physics* 66, 6014–6023. URL: <http://scitation.aip.org/content/aip/journal/jap/66/12/10.1063/1.343578>, doi:<http://dx.doi.org/10.1063/1.343578>.
- Park, S.E., Shrout, T.R., 1997. Ultrahigh strain and piezoelectric behavior in relaxor based ferroelectric single crystals. *Journal of Applied Physics* 82, 1804–1811. URL: <http://scitation.aip.org/content/aip/journal/jap/82/4/10.1063/1.365983>, doi:<http://dx.doi.org/10.1063/1.365983>.
- Paschen, F., 1889. Ueber die zum funkenübergang in luft, wasserstoff und kohlendioxid bei verschiedenen drucken erforderliche potentialdifferenz. *Annalen der Physik* 273, 69–96. URL: <http://dx.doi.org/10.1002/andp.18892730505>, doi:10.1002/andp.18892730505.
- Pasco, Y., Berry, A., 2004. A hybrid analytical/numerical model of piezoelectric stack actuators using a macroscopic nonlinear theory of ferroelectricity and a Preisach model of hysteresis. *Journal of Intelligent Material Systems and Structures* 15, 375–386. URL: <http://jim.sagepub.com/content/15/5/375.abstract>, doi:10.1177/1045389X04040907.
- Patterson, K.D., 2014. Lightweight Deformable Mirrors for Future Space Telescopes. Ph.D. thesis. California Institute of Technology. URL: <http://resolver.caltech.edu/CaltechTHESIS:12182013-094108778>.
- Perkin Elmer, 2014. DMA 8000 – Dynamic Mechanical Analyzer. URL: http://www.perkinelmer.com/CMSResources/Images/44-74431BRO_DMA8000.pdf.
- Peters, W.H., Ranson, W.F., 1982. Digital imaging techniques in experimental stress analysis.

- Optical Engineering 21, 213427. URL: <http://dx.doi.org/10.1117/12.7972925>, doi:10.1117/12.7972925.
- Picot, P., 2000. La coupure du courant lectrique dans le vide. Technical Report 198. Schneider Electric.
- Poquette, B.D., 2005. Damping Behavior in Ferroelectric Reinforced Metal Matrix Composites. Ph.D. thesis. Virginia Polytechnic Institute and State University. URL: http://scholar.lib.vt.edu/theses/available/etd-10022007-124455/unrestricted/Dissertation_Final_10-4-07.pdf.
- Poquette, B.D., Asare, T.A., Schultz, J.P., Brown, D.W., Kampe, S.L., 2011. Domain reorientation as a damping mechanism in ferroelastic-reinforced metal matrix composites. Metallurgical and Materials Transactions A 42, 2833–2842. URL: <http://dx.doi.org/10.1007/s11661-011-0676-1>, doi:10.1007/s11661-011-0676-1.
- Ramesh, R., 1997. Thin Film Ferroelectric Materials and Devices. Electronic Materials: Science & Technology, Springer US. URL: <https://books.google.com/books?id=iWpTAAAMAAJ>.
- Rayleigh, J.W.S., 1945. The Theory of Sound. volume 2. 2 ed., Dover Publications New York.
- Richard, C., Guyomar, D., Audigier, D., Ching, G., 1999. Semi-passive damping using continuous switching of a piezoelectric device. Proceedings of SPIE 3672, 104–111. URL: <http://dx.doi.org/10.1117/12.349773>, doi:10.1117/12.349773.
- Robels, U., Herbiet, R., Arlt, G., 1989. Coupled losses in PZT near the morphotropic phase boundary. Ferroelectrics 93, 95–103. URL: <http://dx.doi.org/10.1080/00150198908017329>, doi:10.1080/00150198908017329.
- Savage, A., Miller, R.C., 1960. Temperature dependence of the velocity of sidewise 180° domain-wall motion in BaTiO₃. Journal of Applied Physics 31, 1546–1549. URL: <http://link.aip.org/link/?JAP/31/1546/1>, doi:<http://dx.doi.org/10.1063/1.1735890>.
- Sawyer, C.B., Tower, C.H., 1930. Rochelle salt as a dielectric. Physical Review 35, 269–273. URL: <http://link.aps.org/doi/10.1103/PhysRev.35.269>, doi:10.1103/PhysRev.35.269.

- Schmidt, N.A., 1981. Coercive force and 90° domain wall motion in ferroelectric PLZT ceramics with square hysteresis loops. *Ferroelectrics* 31, 105–111. URL: <http://www.tandfonline.com/doi/abs/10.1080/00150198108201980>, doi:10.1080/00150198108201980.
- Schrade, D., Mueller, R., Gross, D., Utschig, T., Shur, V., Lupascu, D., 2007. Interaction of domain walls with defects in ferroelectric materials. *Mechanics of Materials* 39, 161–174. URL: <http://www.sciencedirect.com/science/article/pii/S0167663606000561>, doi:<http://dx.doi.org/10.1016/j.mechmat.2006.04.002>.
- Scott, J., 2000. *Ferroelectric Memories*. Advanced Microelectronics, Springer. URL: <https://books.google.com/books?id=9FT06UFHWzC>.
- Seffen, K., Toews, E., 2004. Hyperhelical actuators: Coils and coiled-coils, in: 45th AIAA/ASME/ASCE/AHS/ASC Structures, Structural Dynamics & Materials Conference. URL: <http://arc.aiaa.org/doi/abs/10.2514/6.2004-1814>.
- Setter, N., Damjanovic, D., Eng, L., Fox, G., Gevorgian, S., Hong, S., Kingon, A., Kohlstedt, H., Park, N.Y., Stephenson, G.B., Stolitchnov, I., Taganstev, A.K., Taylor, D.V., Yamada, T., Streiffer, S., 2006. Ferroelectric thin films: Review of materials, properties, and applications. *Journal of Applied Physics* 100, 051606. URL: <http://link.aip.org/link/?JAP/100/051606/1>, doi:10.1063/1.2336999.
- Sharma, S.K., Gaur, H., Kulkarni, M., Patil, G., Bhattacharya, B., Sharma, A., 2013. PZT-PDMS composite for active damping of vibrations. *Composite Science and Technology* 77, 42–51. doi:10.1016/j.compscitech.2013.01.004.
- Shih, W.Y., Shih, W.H., Aksay, I.A., 1994. Size dependence of the ferroelectric transition of small BaTiO₃ particles: Effect of depolarization. *Physical Review B* 50, 15575–15585. URL: <http://link.aps.org/doi/10.1103/PhysRevB.50.15575>, doi:10.1103/PhysRevB.50.15575.
- Shu, Y.C., Bhattacharya, K., 2001. Domain patterns and macroscopic behaviour of ferroelectric materials. *Philosophical Magazine Part B* 81, 2021–2054. URL: <http://www.tandfonline.com/doi/abs/10.1080/13642810108208556>, doi:10.1080/13642810108208556.
- Simpson, J., Schweiger, J., 1998. Industrial approach to piezoelectric damping of large fighter

- aircraft components. *Proceedings of SPIE* 3326, 34–46. URL: <http://dx.doi.org/10.1117/12.310669>, doi:10.1117/12.310669.
- Sinha, J., 1965. Modified sawyer and tower circuit for the investigation of ferroelectric samples. *Journal of Scientific Instruments* 42, 696. URL: <http://stacks.iop.org/0950-7671/42/i=9/a=308>, doi:10.1088/0950-7671/42/9/308.
- Snoek, J., 1941. Effect of small quantities of carbon and nitrogen on the elastic and plastic properties of iron. *Physica* 8, 711–733. URL: <http://www.sciencedirect.com/science/article/pii/S0031891441905177>, doi:[http://dx.doi.org/10.1016/S0031-8914\(41\)90517-7](http://dx.doi.org/10.1016/S0031-8914(41)90517-7).
- Sodano, H.A., 2003. Macro-Fiber Composites for Sensing, Actuation and Power Generation. Ph.D. thesis. Virginia Polytechnic Institute and State University. URL: http://scholar.lib.vt.edu/theses/available/etd-08012003-105114/unrestricted/Complete_Thesis.pdf.
- Song, T.K., Yang, S.M., 2009. Phenomenological calculation of the domain-size-dependent ferroelectric domain-wall velocity. *Journal of the Korean Physical Society* 55, 618–621. URL: http://www.kps.or.kr/jkps/abstract_view.asp?articleid=EEF620BD-0F83-449B-AAB6-CA3BA2981696, doi:10.3938/jkps.55.618.
- Stephens, D.G., Scavullo, M.A., 1965. Investigation of air damping of circular and rectangular plates, a cylinder, and a sphere. Technical Report NASA-TN-D-1865. National Aeronautics and Space Administration. URL: <http://ntrs.nasa.gov/archive/nasa/casi.ntrs.nasa.gov/19650010805.pdf>.
- Su, Y., Landis, C.M., 2007. Continuum thermodynamics of ferroelectric domain evolution: Theory, finite element implementation, and application to domain wall pinning. *Journal of the Mechanics and Physics of Solids* 55, 280–305. URL: <http://www.sciencedirect.com/science/article/pii/S0022509606001256>, doi:<http://dx.doi.org/10.1016/j.jmps.2006.07.006>.
- Sutton, M., Orteu, J., Schreier, H., 2009. Image Correlation for Shape, Motion and Deformation Measurements: Basic Concepts, Theory and Applications. Springer US. URL: <https://books.google.com/books?id=AlkqMxpQMLsC>.
- TA Instruments, 2015. URL: <http://www.tainstruments.com/product.aspx?siteid=11&id=25&n=3>.

- Takashige, M., Hirotsu, S., Ishibashi, Y., Sawada, S., Hamano, K., 1982. Piezoelectric and elastic properties in a two-sublattice model. *Ferroelectrics* 40, 133–140. URL: <http://dx.doi.org/10.1080/00150198208218164>, doi:10.1080/00150198208218164.
- Takeuchi, T., Ado, K., Asai, T., Kageyama, H., Saito, Y., Masquelier, C., Nakamura, O., 1994. Thickness of cubic surface phase on barium titanate single-crystalline grains. *Journal of the American Ceramic Society* 77, 1665–1668. URL: <http://dx.doi.org/10.1111/j.1151-2916.1994.tb09774.x>, doi:10.1111/j.1151-2916.1994.tb09774.x.
- Takeuchi, T., Tabuchi, M., Ado, K., Honjo, K., Nakamura, O., Kageyama, H., Suyama, Y., Ohtori, N., Nagasawa, M., 1997. Grain size dependence of dielectric properties of ultrafine BaTiO₃ prepared by a sol-crystal method. *Journal of Materials Science* 32, 4053–4060. URL: <http://dx.doi.org/10.1023/A:1018697706704>, doi:10.1023/A:1018697706704.
- Tamura, M., Ogasawara, K., Ono, N., Hagiwara, S., 1974. Piezoelectricity in uniaxially stretched poly(vinylidene fluoride). *Journal of Applied Physics* 45, 3768–3771. URL: <http://scitation.aip.org/content/aip/journal/jap/45/9/10.1063/1.1663857>, doi:<http://dx.doi.org/10.1063/1.1663857>.
- Taranath, B., 1988. *Structural Analysis and Design of Tall Buildings*. Monografia (Politechnika Krakowska): Civil Engineering Series, McGraw-Hill. URL: <https://books.google.com/books?id=k2N00gAACAAJ>.
- Tatara, G., Kohno, H., 2004. Theory of current-driven domain wall motion: Spin transfer versus momentum transfer. *Physical Review Letters* 92, 086601. URL: <http://link.aps.org/doi/10.1103/PhysRevLett.92.086601>, doi:10.1103/PhysRevLett.92.086601.
- Tremaine, K., 2012. *Modal Analysis of Composite Structures with Damping Material*. Ph.D. thesis. California Polytechnic State University. URL: <http://digitalcommons.calpoly.edu/cgi/viewcontent.cgi?article=1867&context=theses>.
- Trindade, M.A., Benjeddou, A., 2002. Hybrid active-passive damping treatments using viscoelastic and piezoelectric materials: Review and assessment. *Journal of Vibration and Control* 8, 699–745. URL: <http://jvc.sagepub.com/content/8/6/699.abstract>, doi:10.1177/1077546029186.

- Tsurumi, T., Kumano, Y., Ohashi, N., Takenaka, T., Fukunaga, O., 1997. 90° domain reorientation and electric-field-induced strain of tetragonal lead zirconate titanate ceramics. *Japanese Journal of Applied Physics* 36, 5970. URL: <http://stacks.iop.org/1347-4065/36/i=9S/a=5970>.
- Tura, V., Mitoseriu, L., Papusoi, C., Osaka, T., Okuyama, M., 1997. Investigation of grain-size influence on the ferroelectric-to-paraelectric phase transition in BaTiO₃ ceramics by means of ac calorimetry. *Japanese Journal of Applied Physics* 37, 1950–1954. URL: <http://stacks.iop.org/1347-4065/37/i=4R/a=1950>, doi:10.1143/JJAP.37.1950.
- Uchino, K., 1997. *Piezoelectric Actuators and Ultrasonic Motors*. *Electronic Materials: Science & Technology*, Springer. URL: https://books.google.com/books?id=gocBhXFRv_kC.
- Ueda, J., Secord, T., Asada, H., 2008. Static lumped parameter model for nested PZT cellular actuators with exponential strain amplification mechanisms, in: *Robotics and Automation. ICRA 2008*. *IEEE International Conference on*, pp. 3582–3587. doi:10.1109/ROBOT.2008.4543759.
- Ueda, J., Secord, T., Asada, H., 2010. Large effective-strain piezoelectric actuators using nested cellular architecture with exponential strain amplification mechanisms. *Mechatronics, IEEE/ASME Transactions on* 15, 770–782. doi:10.1109/TMECH.2009.2034973.
- Valadez, J.C., Pisani, D.M., Lynch, C.S., 2013. Coupled effects of hydrostatic pressure and bipolar electric field on the FE-AFE phase transformation in 95/5 PZT, in: *Behavior and Mechanics of Multifunctional Materials and Composites*, p. 868907. URL: <http://dx.doi.org/10.1117/12.2013753>, doi:10.1117/12.2013753.
- Valasek, J., 1921. Piezo-electric and allied phenomena in rochelle salt. *Physical Review* 17, 475–481. URL: <http://link.aps.org/doi/10.1103/PhysRev.17.475>, doi:10.1103/PhysRev.17.475.
- Venkatesh, T.A., Challagulla, K.S., 2013. Piezoelectric foam structures and hydrophone utilizing the same. URL: <http://appft1.uspto.gov/netacgi/nph-Parser?Sect1=PT01&Sect2=HITOFF&d=PG01&p=1&u=/netahtml/PT0/srchnum.html&r=1&f=G&l=50&s1=20130126774.PGNR..> Patent.
- Viehland, D., Chen, Y.H., 2000. Random-field model for ferroelectric domain dynamics and polarization reversal. *Journal of Applied Physics* 88, 6696–6707. URL: <http://scitation.aip.org/content/aip/journal/jap/88/11/10.1063/1.1325001>, doi:10.1063/1.1325001.

- Vinogradov, A., Holloway, F., 2000. Dynamic mechanical testing of the creep and relaxation properties of polyvinylidene fluoride. *Polymer Testing* 19, 131–142. URL: <http://www.sciencedirect.com/science/article/pii/S0142941898000798>, doi:[http://dx.doi.org/10.1016/S0142-9418\(98\)00079-8](http://dx.doi.org/10.1016/S0142-9418(98)00079-8).
- Wang, H., Lee, S.M., Wang, J.L., Lin, H.T., 2014. Fatigue of extracted lead zirconate titanate multilayer actuators under unipolar high field electric cycling. *Journal of Applied Physics* 116, 234101. URL: <http://scitation.aip.org/content/aip/journal/jap/116/23/10.1063/1.4904352>, doi:<http://dx.doi.org/10.1063/1.4904352>.
- Wang, J., Neaton, J.B., Zheng, H., Nagarajan, V., Ogale, S.B., Liu, B., Viehland, D., Vaithyanathan, V., Schlom, D.G., Waghmare, U.V., Spaldin, N.A., Rabe, K.M., Wuttig, M., Ramesh, R., 2003a. Epitaxial BiFeO₃ multiferroic thin film heterostructures. *Science* 299, 1719–1722. URL: <http://www.sciencemag.org/content/299/5613/1719.abstract>, doi:[10.1126/science.1080615](https://doi.org/10.1126/science.1080615).
- Wang, Q.M., Zhang, T., Chen, Q., Du, X.H., 2003b. Effect of DC bias field on the complex materials coefficients of piezoelectric resonators. *Sensors and Actuators A: Physical* 109, 149–155. URL: <http://www.sciencedirect.com/science/article/pii/S0924424703004229>, doi:<http://dx.doi.org/10.1016/j.sna.2003.08.008>.
- Wang, Z., Blendell, J.E., White, G.S., Jiang, Q., 2003c. Atomic force microscope observations of domains in fine-grained bulk lead zirconate titanate ceramics. *Smart Materials and Structures* 12, 217. URL: <http://stacks.iop.org/0964-1726/12/i=2/a=309>.
- Wegener, M., 2008. Polarization-electric field hysteresis of ferroelectric PVDF films: Comparison of different measurement regimes. *Review of Scientific Instruments* 79, 106103. URL: <http://scitation.aip.org/content/aip/journal/rsi/79/10/10.1063/1.2972169>, doi:<http://dx.doi.org/10.1063/1.2972169>.
- Wetton, R.E., 1979. *Elastomers: Criteria for Engineering Design*. Applied Science Publishers. chapter 3. URL: <https://books.google.com/books?id=GutTAAAMA AJ>.
- Wilkie, W., Bryant, R., Fox, R., Hellbaum, R., High, J., Jalink, A., Little, B., Mirick, P., 2003. Positioning monolithic wafers on backing sheets, joining using adhesives, then slicing into fibers

- and covering with conductive films having electrodes patterns; strain activators. URL: <http://www.google.com/patents/US6629341>. US Patent 6,629,341.
- Woïrgard, J., Sarrazin, Y., Chaumet, H., 1977. Apparatus for the measurement of internal friction as a function of frequency between 10^{-5} and 10 Hz. *Review of Scientific Instruments* 48, 1322–1325. URL: <http://scitation.aip.org/content/aip/journal/rsi/48/10/10.1063/1.1134874>, doi:<http://dx.doi.org/10.1063/1.1134874>.
- Wojnar, C.S., le Graverend, J.B., Kochmann, D.M., 2014. Broadband control of the viscoelasticity of ferroelectrics via domain switching. *Applied Physics Letters* 105, 162912. URL: <http://scitation.aip.org/content/aip/journal/apl/105/16/10.1063/1.4899055>, doi:<http://dx.doi.org/10.1063/1.4899055>.
- Wojnar, C.S., Kochmann, D.M., 2014a. A negative-stiffness phase in elastic composites can produce stable extreme effective dynamic but not static stiffness. *Philosophical Magazine* 94, 532–555. URL: <http://dx.doi.org/10.1080/14786435.2013.857795>, doi:[10.1080/14786435.2013.857795](http://dx.doi.org/10.1080/14786435.2013.857795).
- Wojnar, C.S., Kochmann, D.M., 2014b. Stability of extreme static and dynamic bulk moduli of an elastic two-phase composite due to a non-positive-definite phase. *Physica Status Solidi (b)* 251, 397–405. URL: <http://dx.doi.org/10.1002/pssb.201384241>, doi:[10.1002/pssb.201384241](http://dx.doi.org/10.1002/pssb.201384241).
- Wood, R., Steltz, E., Fearing, R., 2005. Optimal energy density piezoelectric bending actuators. *Sensors and Actuators A: Physical* 119, 476–488. URL: <http://www.sciencedirect.com/science/article/pii/S0924424704007757>, doi:<http://dx.doi.org/10.1016/j.sna.2004.10.024>.
- Wuensch, B., 2005. Symmetry, structure, and tensor properties of materials. URL: <http://ocw.mit.edu/courses/materials-science-and-engineering/3-60-symmetry-structure-and-tensor-properties-of-materials-fall-2005/index.htm>. accessed 2014.
- Wuttig, M., Su, Q., Masson, F., Quandt, E., Ludwig, A., 1998. Magnetomechanical instability in FeTb/Fe multilayers. *Journal of Applied Physics* 83, 7264–7266. URL: <http://scitation.aip.org/content/aip/journal/jap/83/11/10.1063/1.367753>, doi:<http://dx.doi.org/10.1063/1.367753>.

- Xu, B., Schrade, D., Müller, R., Gross, D., Granzow, T., Rödel, J., 2010. Phase field simulation and experimental investigation of the electro-mechanical behavior of ferroelectrics. *ZAMM - Journal of Applied Mathematics and Mechanics / Zeitschrift für Angewandte Mathematik und Mechanik* 90, 623–632. URL: <http://dx.doi.org/10.1002/zamm.200900344>, doi:10.1002/zamm.200900344.
- Xu, F., Trolier-McKinstry, S., Ren, W., Xu, B., Xie, Z.L., Hemker, K., 2001. Domain wall motion and its contribution to the dielectric and piezoelectric properties of lead zirconate titanate films. *Journal of Applied Physics* 89, 1336–1348. URL: <http://scitation.aip.org/content/aip/journal/jap/89/2/10.1063/1.1325005>, doi:<http://dx.doi.org/10.1063/1.1325005>.
- Xu, Y., 2013. *Ferroelectric Materials and Their Applications*. Elsevier Science. URL: <https://books.google.com/books?id=dWkhBQAAQBAJ>.
- Yang, G., Ren, W., Liu, S.F., Masys, A., Mukherjee, B., 2000. Effects of uniaxial stress and DC bias field on the piezoelectric, dielectric, and elastic properties of piezoelectric ceramics, in: *Ultrasonics Symposium, 2000 IEEE*, pp. 1005–1008. doi:10.1109/ULTSYM.2000.921494.
- Yao, J., Yang, Y., Ge, W., Li, J., Viehland, D., 2011. Domain evolution in $\text{PbMg}_{1/3}\text{Nb}_{2/3}\text{O}_3$ -60at% PbTiO_3 with temperature and electric field. *Journal of the American Ceramic Society* 94, 2479–2482. URL: <http://dx.doi.org/10.1111/j.1551-2916.2010.04380.x>, doi:10.1111/j.1551-2916.2010.04380.x.
- Yin, J., Cao, W., 2001. Polarization reversal study using ultrasound. *Applied Physics Letters* 79, 4556–4558. URL: <http://scitation.aip.org/content/aip/journal/apl/79/27/10.1063/1.1428629>, doi:<http://dx.doi.org/10.1063/1.1428629>.
- Yin, J., Cao, W., 2002. Coercive field of $0.955\text{Pb}(\text{Zn}_{1/3}\text{Nb}_{2/3})\text{O}_3$ - 0.045PbTiO_3 single crystal and its frequency dependence. *Applied Physics Letters* 80, 1043–1045. URL: <http://scitation.aip.org/content/aip/journal/apl/80/6/10.1063/1.1448385>, doi:<http://dx.doi.org/10.1063/1.1448385>.
- Yu, Y., Naganathan, N., Dukkupati, R., 2002. Preisach modeling of hysteresis for piezo-ceramic actuator system. *Mechanism and Machine Theory* 37, 49–59. URL: <http://www.sciencedirect.com/science/article/pii/S0094114X01000659>, doi:[http://dx.doi.org/10.1016/S0094-114X\(01\)00065-9](http://dx.doi.org/10.1016/S0094-114X(01)00065-9).

- Zadler, B.J., Le Rousseau, J.H.L., Scales, J.A., Smith, M.L., 2004. Resonant Ultrasound Spectroscopy: Theory and application. *Geophysical Journal International* 156, 154–169. URL: <http://gji.oxfordjournals.org/content/156/1/154.abstract>, doi:10.1111/j.1365-246X.2004.02093.x.
- Zener, C., 1937. Internal friction in solids. I. Theory of internal friction in reeds. *Physical Review* 52, 230–235. URL: <http://link.aps.org/doi/10.1103/PhysRev.52.230>, doi:10.1103/PhysRev.52.230.
- Zener, C., 1938. Internal friction in solids II. General theory of thermoelastic internal friction. *Physical Review* 53, 90–99. URL: <http://link.aps.org/doi/10.1103/PhysRev.53.90>, doi:10.1103/PhysRev.53.90.
- Zener, C., 1948. *Elasticity and Anelasticity of Metals*. University of Chicago Press, Chicago. URL: <http://dx.doi.org/10.1021/j150474a017>, doi:10.1021/j150474a017.
- Zhang, H., Sorbello, R.S., Hucho, C., Herro, J., Feller, J.R., Beck, D.E., Levy, M., Isaak, D., Carnes, J.D., Anderson, O., 1998. Radiation impedance of resonant ultrasound spectroscopy modes in fused silica. *The Journal of the Acoustical Society of America* 103, 2385–2394. URL: <http://scitation.aip.org/content/asa/journal/jasa/103/5/10.1121/1.422757>, doi:<http://dx.doi.org/10.1121/1.422757>.
- Zhang, Q., 2004. *Atomistic Simulations of Barium Titanate*. Ph.D. thesis. California Institute of Technology. URL: <http://resolver.caltech.edu/CaltechETD:etd-10292004-152709>.
- Zhang, W., Bhattacharya, K., 2005a. A computational model of ferroelectric domains. Part I: Model formulation and domain switching. *Acta Materialia* 53, 185–198. URL: <http://www.sciencedirect.com/science/article/pii/S1359645404005580>, doi:<http://dx.doi.org/10.1016/j.actamat.2004.09.016>.
- Zhang, W., Bhattacharya, K., 2005b. A computational model of ferroelectric domains. Part II: Grain boundaries and defect pinning. *Acta Materialia* 53, 199–209. URL: <http://www.sciencedirect.com/science/article/pii/S1359645404005579>, doi:<http://dx.doi.org/10.1016/j.actamat.2004.09.015>.

- Zheng, L., Zhang, D., Wang, Y., 2011. Vibration and damping characteristics of cylindrical shells with active constrained layer damping treatments. *Smart Materials and Structures* 20, 025008. URL: <http://stacks.iop.org/0964-1726/20/i=2/a=025008>.
- Zhou, D., 2003. Experimental Investigation of Non-Linear Constitutive Behavior of PZT Piezoceramics. Ph.D. thesis. Universität Karlsruhe. URL: <http://digbib.ubka.uni-karlsruhe.de/volltexte/documents/1389>.
- Zhou, D., Kamlah, M., 2006. Room-temperature creep of soft PZT under static electrical and compressive stress loading. *Acta Materialia* 54, 1389–1396. URL: <http://www.sciencedirect.com/science/article/pii/S1359645405006853>, doi:<http://dx.doi.org/10.1016/j.actamat.2005.11.010>.
- Zhou, D., Kamlah, M., Munz, D., 2001. Rate dependence of soft PZT ceramics under electric field loading, in: SPIE's 8th Annual International Symposium on Smart Structures and Materials, pp. 64–70. URL: <http://dx.doi.org/10.1117/12.432740>, doi:[10.1117/12.432740](http://dx.doi.org/10.1117/12.432740).
- Zhou, D., Kamlah, M., Munz, D., 2005a. Effects of bias electric fields on the non-linear ferroelastic behavior of soft lead zirconate titanate piezoceramics. *Journal of the American Ceramic Society* 88, 867–874. URL: <http://dx.doi.org/10.1111/j.1551-2916.2005.00139.x>, doi:[10.1111/j.1551-2916.2005.00139.x](http://dx.doi.org/10.1111/j.1551-2916.2005.00139.x).
- Zhou, D., Kamlah, M., Munz, D., 2005b. Effects of uniaxial prestress on the ferroelectric hysteretic response of soft PZT. *Journal of the European Ceramic Society* 25, 425–432. URL: <http://www.sciencedirect.com/science/article/pii/S0955221904000706>, doi:<http://dx.doi.org/10.1016/j.jeurceramsoc.2004.01.016>.